

**DOTTORATO DI RICERCA IN
GEOFISICA
Ciclo XXX**

Settore Concorsuale di afferenza:

04/A4 - GEOFISICA

Settore Scientifico disciplinare:

GEO/10 - GEOFISICA DELLA TERRA SOLIDA

**Discrete fault models:
the dynamical role of asperities
and their interaction**

Presentata da: Emanuele Lorenzano

Coordinatore Dottorato:

Prof. Nadia Pinardi

Supervisore:

Prof. Michele Dragoni

Esame finale anno 2018

Contents

Abstract	1
1 Introduction	3
2 Seismic source dynamics	5
2.1 Fault mechanics	5
2.1.1 Frictional resistance	6
2.1.2 Interaction between faults	8
2.2 Rheology of the lithosphere	9
2.2.1 The Maxwell body	10
2.3 Post-seismic phenomena	12
2.3.1 Afterslip	12
2.3.2 Post-seismic fluid flow	13
3 Discrete fault models	15
3.1 Dynamical systems - selected topics	15
3.2 Faults as discrete dynamical systems	17
3.3 Asperity models of faults	20
3.3.1 A two-asperity fault model with elastic coupling	22
3.4 Reference model	24
4 A fault with a single asperity	26
4.1 The model	26
4.2 Dynamic modes	29
4.2.1 Sticking mode	29
4.2.2 Slipping mode	29
4.3 Orbits in the phase space	31
4.4 Seismic moment rate and spectrum	33

4.5	Energy budget	35
4.6	Choice of the parameters	38
4.7	An application: the 2004 Sumatra-Andaman earthquake	39
5	A fault exhibiting seismic slip and afterslip	43
5.1	The model	43
5.2	Solutions of dynamic modes	47
5.2.1	Interseismic interval	47
5.2.2	Seismic slip	48
5.2.3	Afterslip	52
5.3	Afterslip vs. viscoelastic relaxation	59
5.4	Choice of the parameters	60
5.5	An application: the 2011 Tohoku-Oki earthquake	62
6	A fault with two asperities of different areas and strengths	68
6.1	The model	68
6.1.1	The sticking region	71
6.2	Solutions of dynamic modes	73
6.2.1	Stationary asperities (mode 00)	73
6.2.2	Slip of asperity 1 (mode 10)	74
6.2.3	Slip of asperity 2 (mode 01)	76
6.2.4	Simultaneous slip of asperities (mode 11)	77
6.3	Slip in a seismic event	78
6.4	Source functions and seismic moment	79
6.5	Moment rate spectrum	83
6.6	The difference between the asperity areas	85
6.6.1	Forces on the asperities	85
6.6.2	Slip duration and amplitude	85
6.6.3	The sticking region and its subsets	87
6.6.4	Radiation of elastic waves	89
6.7	Choice of the parameters	93
6.8	An application: the 2007 Pisco, Peru, earthquake	94
7	A two-asperity fault in the presence of viscoelastic relaxation	98
7.1	The model	98

7.1.1	The sticking region	101
7.2	Solutions of dynamic modes	103
7.2.1	Stationary asperities (mode 00)	104
7.2.2	Slip of asperity 1 (mode 10)	105
7.2.3	Slip of asperity 2 (mode 01)	106
7.2.4	Simultaneous slip of asperities (mode 11)	108
7.3	Slip in a seismic event	108
7.3.1	Dependence on the state at the onset of the event	109
7.3.2	Dependence on the state at the beginning of the interseismic interval	110
7.4	Source functions and seismic moment	113
7.5	Forces on the asperities	116
7.5.1	Interseismic interval	116
7.5.2	Onset of a seismic event	117
7.5.3	Static force drops	120
7.6	Influence of seismic efficiency on events due to the consecutive slips of the asperities	120
7.7	Choice of the parameters	123
7.8	An application: the 1964 Alaska earthquake	124
7.8.1	Refinement according to the seismic history to date	126
7.8.2	Future earthquakes	128
7.8.3	Comparison with the purely elastic case	129

8 Stress perturbations on a two-asperity fault in the presence of viscoelastic relaxation **132**

8.1	Modelling stress perturbations	132
8.2	Effects of the perturbation	135
8.2.1	Changes in Coulomb forces	137
8.2.2	Changes in the duration of the interseismic interval	138
8.2.3	Comparison with the elastic case	139
8.3	An application: perturbation of the 1992 Landers fault by the 1999 Hector Mine earthquake	140
8.3.1	Stress perturbation by the 1999 Hector Mine earthquake	143
8.3.2	Constraints due to the seismic history to date	146
8.3.3	Effects of the stress perturbation on future earthquakes	147

9	Seismic sequences originated by a fault system	151
9.1	The model	151
9.1.1	A particular case: coplanar faults	156
9.2	Evolution of the system	157
9.3	Retrieval of the initial and final states	158
9.4	The order of events	160
9.4.1	Subsequent evolution	161
9.5	Discussion of the model	162
9.5.1	Constraints on the state of the system	162
9.5.2	Stress drops vs. stress transfers: a special case	163
9.6	Applications	164
9.6.1	The 2012 Emilia sequence	164
9.6.2	The 1997 - 1998 Umbria-Marche sequence	170
	Conclusions	176
	Appendices	183
A	Stress rates in different tectonic settings	185
B	Traction due to different dislocation sources	187
B.1	Point-like source in an unbounded medium	187
B.2	Point-like source in a half-space	188
B.3	Finite square source in an unbounded medium	189
B.4	Finite square source in a half-space	189
B.5	Comparison	190
C	Constants in mode 11 - Chapter 6	193
C.1	Case 10 \rightarrow 11	193
C.2	Case 01 \rightarrow 11	193
C.3	Case 00 \rightarrow 11	194
D	Events resulting from $p = p_1$ and $p = p_2$ - Chapter 6	195
E	Constants in mode 11 - Chapter 7	199
E.1	Case 10 \rightarrow 11	199
E.2	Case 01 \rightarrow 11	200

E.3	Case $00 \rightarrow 11$	200
F	Details of the faces $AECD$ and $BCDF$ - Chapter 7	202
G	Particular events generated on segments s_1 and s_2 - Chapter 7	206
G.1	Three-mode events 10-01-10	206
G.2	Three-mode events 01-10-01	207
G.3	Four-mode events 01-10-01-10	207
H	Stress perturbations between neighbouring faults	209
I	Poroelastic effect	213
	Bibliography	214
	Acknowledgements	230

Abstract

The present thesis focuses on the mechanics of the seismic source, in the framework of asperity models of faults. Thanks to the major role played by asperities in the dynamics of the seismic source, faults have been treated as dynamical systems made of a small number of asperities, weak regions or fault segments. The state of the system is described by the slip deficits or Coulomb stresses associated with the regions of the fault. Five cases are illustrated, differing for the number of asperities, weak regions or fault segments and for the mechanical processes investigated. In a model of a fault with a single asperity, the dynamics is described by two dynamic modes, corresponding to asperity loading and asperity failure, respectively. In a model of a fault with an asperity and a weak region, the dynamics is studied in terms of three dynamic modes, corresponding to interseismic intervals, seismic slip of the asperity and afterslip in the weak region. In a model of a two-asperity fault with purely elastic coupling, the dynamics is described by a sticking mode, associated with stationary asperities, and three slipping modes, corresponding to the slip of one or both asperities at a time. If viscoelastic coupling between the asperities is assumed, the model allows to highlight the role of rock rheology in the duration of the interseismic intervals of the fault and in the response to stress perturbations from neighbouring faults. In a model of a system of n faults generating a seismic sequence, it is possible to retrieve the state of the system at any time during the sequence. Also, the order of fault activation is described by a permutation of the first n natural numbers. In each case, applications to real faults are presented.

Chapter 1

Introduction

Several aspects of fault mechanics can be effectively investigated by devising discrete models that reduce fault dynamics to its essentials. From a macroscopic point of view, this is accomplished by modelling faults (or fault systems) as made of a small number of regions, namely asperities and weak regions (or fault segments). Asperities on a fault are identified as regions with a high static friction and a velocity-weakening dynamic friction; therefore, they can be also referred to as strong regions (Lay et al., 1982; Ruff, 1983; Scholz, 1990). On the other hand, weak (or stable) fault regions are characterized as regions with a negligible static friction and a velocity-strengthening dynamic friction.

In the present thesis, faults are treated as discrete dynamical systems whose basic elements are asperities, weak region or fault segments. This study method presents several benefits. First of all, the number of degrees of freedom required to describe fault dynamics is reduced, thus allowing the analytical solution of the evolution equations. What is more, it is possible to analyse the evolution of the system from a geometrical point of view, following its orbit in the phase space. Finally, this approach allows to focus on the main features of the seismic source (e.g. stick-slip mechanism, stress transfers, post-seismic deformation) while avoiding the more complicated description of continuum mechanics.

Chapter 2 serves as an introduction to the most relevant aspects of fault mechanics, with particular emphasis on the description of friction on a fault, the interaction between neighbouring faults, the rheology of lithospheric rocks and two important post-seismic phenomena.

Chapter 3 presents the main achievements in the field of discrete modelling of fault dynamics, focusing on asperity models of faults and the relevant theory of dynamical systems. At the end of the chapter, the reference fault model for all the studies presented in the thesis is illustrated.

The subsequent chapters present five fault models, differing for the number of asperities, weak regions or fault segments and for the mechanical processes investigated.

The simplest case is considered in Chapter 4, where it is assumed that the fault activity is dominated by the evolution of one large asperity on its surface. The system has one degree of freedom and its dynamics is described in terms of two dynamic modes. The main features of a seismic event (e.g. moment rate function, seismic spectrum, energy budget) are discussed. In Chapter 5, a fault containing an asperity and a weak region is considered. The system has two degrees of freedom and its dynamics is studied by means of three dynamic modes. The interaction between seismic and aseismic slip on the fault is discussed. In Chapter 6, a two-asperity fault is considered, assuming purely elastic coupling between the asperities. The system has two degrees of freedom and its dynamics is described in terms of four dynamic modes. The role of asperity size on various aspects of the model (e.g. sticking region, slip amplitude, duration and moment rate spectrum of a seismic event) is investigated. In Chapter 7, the evolution of a two-asperity fault in the presence of viscoelastic relaxation is discussed. The system has three degrees of freedom and its dynamics is studied by means of the same four dynamic modes as in the purely elastic case. The interplay between viscoelastic relaxation and stress perturbations in the evolution of a two-asperity fault is investigated in Chapter 8. The complications with respect to the case of a purely elastic rock rheology are presented. Finally, a model for the evolution of a system of n faults during a seismic sequence is illustrated in Chapter 9. The role played by stress drops and stress transfers in governing the order of fault activation during a seismic sequence is discussed.

In each case, applications to real faults are presented, showing the potential to shed some light on the essential aspects of complex geophysical observations.

Chapter 2

Seismic source dynamics

The goal of the present chapter is to provide an overview of the main aspects of the seismic source dynamics this thesis focuses on. First, the general features of fault mechanics are presented, discussing the phases of the seismic cycle, the role of friction in the process of earthquake generation and the complications arising from the interaction between neighbouring faults. Afterwards, the rheological properties of lithospheric rocks are considered, with particular reference to the characteristics of viscoelasticity. Finally, I provide a description of two significant phenomena often observed in the aftermath of an earthquake, namely afterslip and pore fluid diffusion.

2.1 Fault mechanics

It is a geological evidence that lithospheric rocks exhibit a certain degree of fracturing at any scale of observation. As a consequence of the relative motion of tectonic plates, lithospheric rocks undergo a continual process of deformation. The stress thus accumulated in the medium is preferably released by the relative motion of the sides of a pre-existing fracture, instead of by the formation of a new one, in order to minimize the expenditure of energy. We call fault any large fracture showing signs of a dislocation, i.e., the relative motion of its sides.

According to seismic and geodetic observations, faults can accommodate tectonic motion in two different ways. Some fault regions exhibit a slow, quasi-static creep, with slip rates comparable to tectonic rates; other fault regions remain locked for most of the time and eventually undergo a sudden failure, catastrophically releasing the deformation energy stored in the medium with the emission of

elastic waves. The former is known as aseismic (stable) slip, the latter as seismic (unstable) slip. In the case of seismogenic faults, the process of stress build-up takes place over time intervals of tens or hundredths of years, whereas the duration of seismic slip is of the order of tens of seconds. This mechanism is referred to as “stick-slip” (where the “stick” corresponds to the interseismic period of elastic strain accumulation and the “slip” identifies the earthquake) and is related to the frictional properties of seismogenic faults (§2.1.1).

In fact, the dynamical behaviour of a fault is governed by two factors, both functions of time and space: the frictional resistance and the stress applied to the fault. As for the stress field, it is the result of the combined action of lithostatic pressure and tectonic stress: the former is associated with a purely normal, compressive contribution, whereas the latter is generally made of two components, one normal to the fault plane and the other tangential to it. This tangential component is the one responsible for earthquake generation: according to Amonton’s law (Turcotte and Schubert, 2002), slip on a fault initiates when the shear stress on the fault reaches the threshold

$$\tau_s = k_s(p - \sigma_n - p') \quad (2.1)$$

where k_s is known as static friction coefficient, σ_n is the tectonic normal stress on the fault, p is the lithostatic pressure and p' is the pore fluid pressure. According to Eq. (2.1), the condition for the onset of slip may change both in space and time, as a consequence of a variation in any of the four components in its right-hand side. In fact: k_s is a property of the rocks embedding the fault; σ_n depends on tectonic loading and on the interaction with neighbouring faults (§2.1.2); p is a function of the depth and the orientation of the fault; p' depends on the concentration of pore fluids in lithospheric rocks.

2.1.1 Frictional resistance

As already stated, earthquakes rarely occur as a consequence of the formation of a new crack, but instead they take place on a pre-existing fault. Accordingly, it is crucial to underline that earthquakes are a frictional, rather than a fracture, phenomenon (Scholz, 1998). Nonetheless, an increase in the contact points of the sides of a fault and chemical interactions between rocks (welding) may cause the static friction coefficient on a fault to grow larger over long interseismic intervals, typically as a logarithmic function of time: this process is known as fault healing

(Dieterich, 1972).

To date, the most accurate description of frictional resistance is provided by the rate- and state-dependent friction laws. In the Dieterich-Ruina formulation (Ruina, 1983; Dieterich, 1994), they express the static friction coefficient as

$$\begin{cases} k_s(V, \zeta) = k_s^* + a \ln\left(\frac{V}{V^*}\right) + \zeta \\ \dot{\zeta} = -\frac{V}{L} [\zeta + b \ln\left(\frac{V}{V^*}\right)] \end{cases} \quad (2.2)$$

where: V is the slip velocity; V^* is a reference slip velocity, corresponding to the steady-state friction coefficient k_s^* ; the nondimensional coefficients a and b depend on the material; ζ is a nondimensional variable representing the state of the contact surface; L is the critical slip distance required for friction to change value following a variation in the slip velocity. This formulation points out that friction depends on the sliding velocity and on the “history” of the sliding surface. Frictional stability is governed by the difference $(a - b)$: if $(a - b) \geq 0$, the material is said to be velocity-strengthening (stable), so that an increase in the slip velocity entails an increase in friction; the opposite holds if $(a - b) < 0$, so that the material is said to be velocity-weakening (unstable). In the Earth’s interior, the parameter $(a - b)$ shows a dependence upon temperature and depth (Stesky et al., 1974). Furthermore, it is affected by the presence of wear detritus on the fault surface (the so-called fault gouge), resulting from previous episodes of slip (Marone et al., 1990). To sum up, earthquakes can only take place on faults located where unstable sliding conditions are fulfilled, whereas aseismic slip is a characteristic feature of faults lying in a velocity-strengthening environment. Furthermore, modelling and experimental observations have pointed out that instability is attained only if the slipping patch reaches a critical size L_c , known as nucleation length (Dieterich, 1992).

As a matter of fact, the typical stick-slip behaviour associated with the dynamics of a seismogenic fault can be also reproduced adopting a simplified version of the rate- and state-dependent friction laws: the Coulomb friction law. It describes the friction coefficient k as a function of the slip velocity V in the form

$$k(V) = \begin{cases} k_s & V = 0 \\ k_d & V \neq 0 \end{cases} \quad (2.3)$$

where $k_d < k_s$ is called dynamic friction coefficient. Typical values of k_s range

between 0.6 and 0.8 for most crustal rocks, whereas a representative value for the ratio k_d/k_s is 0.7 (Jaeger and Cook, 1976; Scholz, 1990).

2.1.2 Interaction between faults

A dramatic complication in studying the evolution of a fault arises from the fact that no fault can be considered isolated; in fact, any fault is subject to the stress perturbations associated with earthquakes on neighbouring faults (Harris, 1998; Steacy et al., 2005). We refer to system of faults when considering a set of two or more faults that are close enough to be significantly affected by each other. Whenever a fault slips, the stress field in the surrounding medium is altered. Focusing on the coseismic effects, static and dynamic stress changes can be distinguished: the former take place instantaneously, as the result of the dislocation on the slipping fault, whereas the latter are associated with the propagation of elastic waves and are as such oscillatory. The magnitude of stress changes decays with the distance from the dislocation source; however, static stress changes attenuate more rapidly than dynamic stress changes, which then dominate at large distances (Belardinelli et al., 2003). The stress field on a fault can be further altered owing to post-seismic processes (§2.3).

As a result of stress perturbations, the stress field on a fault can be enhanced or weakened, the net effect depending on the relative orientations and locations of the interacting faults. What is more, contributions from different faults of the same system may partially cancel each other out. Accordingly, the occurrence time of future earthquakes on the perturbed fault may change with respect to the unperturbed condition, which is governed by tectonic loading. The interaction between neighbouring faults and the problem of stress perturbations are considered in the discrete models presented in §8 and §9.

Coulomb stress

An effective way to characterize the interaction between faults is provided by the concept of Coulomb stress (Stein, 1999). On a given fault, it is defined as the difference between the shear stress σ_t in the direction of fault slip and the static friction τ_s on the fault surface:

$$\sigma_C = \sigma_t - \tau_s. \quad (2.4)$$

Accordingly, σ_C is negative during an interseismic interval and a seismic event occurs when σ_C vanishes.

After the occurrence of an earthquake in the surroundings, a perturbing stress field is superimposed to the fault. This additional stress results in the fault being brought closer to or farther from the failure, depending on its position and orientation relative to the dislocation source. Generally speaking, the coseismic traction transferred to the fault consists in a normal component $\Delta\sigma_n$ and a tangential component $\Delta\sigma_t$: the former modifies the frictional resistance of the fault, while the latter promotes or prevents the slip on the fault, depending on its orientation relative to the tectonic stress loading the fault. The change in static friction is

$$\Delta\tau_s = -k_s \Delta\sigma_n \quad (2.5)$$

where k_s is the effective static friction coefficient on the perturbed fault (i.e., the friction coefficient corresponding to the net effect of lithostatic and pore fluid pressures). We conclude that the frictional resistance of the fault is increased if $\Delta\sigma_n < 0$ (compressional) or decreased if $\Delta\sigma_n > 0$ (extensional). As for $\Delta\sigma_t$, it is defined as positive if it promotes the slip of the fault as driven by tectonic loading, while it is defined as negative if it counteracts the effect of tectonic motion, thus obstructing fault slip.

The net effect of the stress perturbation can be estimated from the variation in Coulomb stress, given by

$$\Delta\sigma_C = \Delta\sigma_t - \Delta\tau_s. \quad (2.6)$$

The slip of the perturbed fault is anticipated if $\Delta\sigma_C > 0$, whereas it is delayed if $\Delta\sigma_C < 0$.

2.2 Rheology of the lithosphere

The rheological properties of lithospheric rocks play a crucial role in the long-term evolution of a fault. They can be inferred from seismological and geodetic surveys, from the observations of post-seismic deformations following large earthquakes and from the constitutive equations (strain vs. stress relations) derived from experimental data (Kirby and Kronenberg, 1987; Nishimura and Tatcher, 2003; Bürgmann and Dresen, 2008). The rheological behaviour of rocks is a consequence

not only of their composition, but also of a number of external (environmental) factors, such as pressure and temperature (Kusznir et al., 1991).

It must also be borne in mind that the rheology of lithospheric rocks strongly depends on the time scale of the observations. Accordingly, it is possible to discriminate between a short-term, elastic behaviour and a long-term, viscous behaviour (Carter, 1976). The former is associated with the typical time scales of seismic waves propagation, whereas the latter only appears on time scales several orders of magnitude larger. As a result, a viscoelastic rheology is generally attributed to lithospheric rocks (Ranalli, 1995).

This degree of anelasticity has a significant impact on the post-seismic deformation of the medium in which the dislocation source is located. In fact, the static stress field produced by an earthquake undergoes a certain amount of relaxation during the interseismic intervals; in turn, this process alters the stress distribution on surrounding faults, thus modifying the occurrence times of future seismic events (Piombo et al., 2007; Ding and Lin, 2014). With similar considerations as in §2.1.2, earthquakes can be anticipated or delayed by viscoelastic relaxation, depending on the net effect of the stress redistribution.

2.2.1 The Maxwell body

One of the most common models employed to reproduce the viscoelastic rheology of lithospheric rocks is the Maxwell body (e.g. Dragoni et al., 1982, Turcotte and Schubert, 2002).

Many rheological models are graphically represented as combinations of basic mechanical elements, such as springs and dashpots. In this description, the Maxwell body is composed by the series of a Hooke elastic solid (spring) of rigidity μ and a Newtonian viscous element (dashpot) of viscosity η ; it is shown in Fig. (2.1).

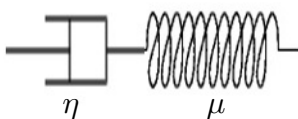


Figure 2.1: Graphical representation of the Maxwell body.

In the series of multiple mechanical elements, the overall strain is equal to the sum of the strains associated with the single elements. The strain-stress relation for the Hooke solid is

$$e_H = \frac{\sigma}{2\mu}, \quad (2.7)$$

whereas the constitutive equation for the Newtonian fluid is

$$\dot{e}_N = \frac{\sigma}{2\eta}. \quad (2.8)$$

Deriving Eq. (2.7) with respect to time and setting

$$\dot{e} = \dot{e}_H + \dot{e}_N, \quad (2.9)$$

we end up with the constitutive equation for the Maxwell body:

$$2\dot{e} = \frac{\dot{\sigma}}{\mu} + \frac{\sigma}{\eta}. \quad (2.10)$$

In view of the following application, let us introduce the characteristic relaxation time

$$\theta = \frac{\eta}{\mu}. \quad (2.11)$$

Relaxation at constant strain

Let us consider the case in which the Maxwell body is subject to a constant strain for times $t > 0$:

$$e(t) = e_0 H(t) \quad (2.12)$$

where H is the Heaviside function. At first, the medium reacts in a purely elastic way, as there is not enough time for the dashpot to react to the instantaneous strain. Hence, the initial stress is

$$\sigma(t = 0^+) = 2\mu e_0. \quad (2.13)$$

From Eq. (2.10) we get the ODE (Ordinary Differential Equation)

$$\frac{\dot{\sigma}}{\mu} + \frac{\sigma}{\eta} = 0. \quad (2.14)$$

Integrating with the initial condition (2.13), we obtain the solution

$$\sigma(t) = 2\mu e_0 H(t) e^{-t/\theta}. \quad (2.15)$$

The initial elastic stress is therefore gradually relaxed and gets substantially negligible for times $t \gg \theta$. The situation discussed here reproduces the long-term

effect of an earthquake in a viscoelastic medium, as anticipated beforehand. The strain (2.12) can be interpreted as the result of the coseismic slip on a fault: thus, according to Eq. (2.15), the static stress field produced by the seismic event undergoes a certain degree of relaxation during the subsequent interseismic interval. This phenomenon is taken into account in the discrete model of a fault presented in §7.

2.3 Post-seismic phenomena

Here, two post-seismic processes are considered, namely afterslip and poroelastic deformation, which often contribute to the stress redistribution on faults, thus altering their subsequent evolution.

2.3.1 Afterslip

Afterslip is defined as the aseismic slip of a fault that is frequently observed after an earthquake and that may last up to several months, depending on the magnitude of the seismic event. This phenomenon takes place at a decreasing rate and has been ascribed to elementary creep events triggered by the stress perturbation caused by the mainshock (Belardinelli and Bonafede, 1993). If afterslip can be clearly observed at the Earth surface, geodetic measurements allow to estimate the extension of the creeping zone. Several studies pointed out that the final amplitude of afterslip is proportional to that of seismic slip. Also, it can produce an amount of aseismic slip comparable with the coseismic slip at seismogenic depths (e.g. Kenner and Segall, 2000).

Marone et al. (1991) studied the relationship between afterslip and the presence of scarcely consolidated sediments at shallow depths by means of a mechanical model of the upper crust, under the hypothesis that fault rocks exhibit rate- and state-variable frictional behaviour (§2.1.1). They considered an elastic lithosphere containing a fault zone with a velocity-strengthening (stable) region overlying a velocity-weakening (unstable) region. As a result of the stress perturbation due to the sudden increase in slip velocity associated with a seismic event in the lower region, the fault starts slipping aseismically at the surface. Accordingly, afterslip can be interpreted as the relaxation of coseismic stress within a velocity-strengthening region that has been loaded by the coseismic slip of a velocity-weakening region.

The authors also showed that a thicker layer of superficial sediments would result in reduced coseismic surface slip and increased afterslip, in good agreement with field observations.

Several empirical relationships have been suggested in order to describe the evolution of aseismic slip as a function of the time elapsed since an earthquake (Barbot et al., 2009). Nason and Weertman (1973) proposed an exponential function approaching a constant value. The theoretical analysis of Marone et al. (1991) suggested a logarithmic function of time. In many cases, this functional form reproduces field observations reasonably well; however, it entails a slip amplitude increasing indefinitely with time and must be truncated ad hoc. In §5, a discrete model of a fault with two mechanically different regions and another formulation of the temporal evolution of afterslip are proposed.

2.3.2 Post-seismic fluid flow

Due to the presence of fluids (the most abundant of which is water), the Earth's crust cannot be considered as a purely elastic medium, but it is more properly to be treated as a fluid-filled poroelastic medium (Detournay and Cheng, 1993; Wang, 2000). If an earthquake takes place in a fluid-filled medium, the subsequent perturbation in the stress field causes the compression or dilation of the volume of rocks surrounding the seismic source. As a result, pore fluid pressure gradients are generated, thus triggering the diffusion of interstitial fluids. This transient phenomenon can last up to times in the order of 1 year (Jónsson et al., 2003) and can play an important role in the stress interaction between neighbouring faults and in post-seismic deformation.

The governing equations for a linear elastic, fluid-filled porous medium were first derived by Biot (1941). The effect of migrating fluids can be taken into account by distinguishing between two limit regimes, known as undrained and drained conditions, governed by the Poisson's moduli ν_u and ν , respectively. These regimes correspond to the short- and long-term responses of the medium to a abrupt pore pressure change, respectively. At the occurrence of an earthquake, the interstitial fluids can be considered stationary and their diffusive flow can be reasonably neglected: the medium is then said to be in the undrained state and the stress field correspond to the elastic solution with undrained moduli. As time

goes by, fluid flow takes place until the pore pressure gradients are cancelled out: the medium is then said to be in a drained condition and the stress field is given by the elastic solution with drained moduli. The timescale of fluid migration is controlled by the hydraulic diffusivity c of the medium: its value depends on the position and the composition of rocks, spanning over a wide range, from 10^{-11} to $10^5 \text{ m}^2 \text{ s}^{-1}$ (Roeloffs, 1996).

Theoretical considerations and laboratory data (Rice and Cleary, 1976) show that, under undrained conditions, the Poisson modulus is larger than under drained condition, that is, $\nu_u \geq \nu$. It was already mentioned that the two regimes correspond to the coseismic and post-seismic response of the medium, respectively. Therefore, we conclude that fluid migration in a porous medium can be a source of post-seismic ground deformation: this effect is called poroelastic rebound.

Furthermore, pore pressure relaxation and the related diffusive processes have been proposed as a possible cause of aftershock migration, induced seismicity and triggered seismicity (Steacy et al., 2005). For instance, Piombo et al. (2005) studied the effect of post-seismic fluid flow on the coseismic Coulomb stress change field due to an earthquake: they found that the migration of fluids can delay the occurrence of earthquakes in regions where a positive change in Coulomb stress has been inferred, and vice-versa. The role of pore fluid diffusion in the stress redistribution within a system of faults is discussed in Appendix I.

Chapter 3

Discrete fault models

In this chapter, an overview of the most significant aspects of discrete modelling of fault dynamics is presented. In this framework, faults are treated as dynamical systems: therefore, I begin by mentioning the properties of such systems that are most relevant to the present work. Afterwards, the advantages granted by this study approach and the categories in which discrete fault models can be classified into are illustrated, with particular reference to asperity models.

3.1 Dynamical systems - selected topics

A dynamical system is any system whose behaviour can be described by means of an evolution operator

$$\Phi^t : X \rightarrow X \tag{3.1}$$

defined on a space X for all times $t \in T$, such that, given any initial condition $\mathbf{x}_0 \in X$ and any $t, s \in T$, we have

$$\Phi^0(\mathbf{x}_0) = \mathbf{x}_0, \tag{3.2}$$

$$\Phi^{t+s}(\mathbf{x}_0) = \Phi^t(\Phi^s(\mathbf{x}_0)). \tag{3.3}$$

The first condition identifies the initial state of the system, whereas the second entails the deterministic nature of the evolution of the system.

Generally speaking, X is a subset of \mathbb{R}^n : it is known as the state space of the system. The state of the system at any instant t in time is described by the n -dimensional vector $\mathbf{x}(t)$: its n components are the state variables of the system. As for the space T , we can distinguish between two cases, corresponding to $T = \mathbb{R}$

and $T = \mathbb{Z}$: in the former case, the dynamical system is said to be a continuous time system, while in the latter case it is said to be a discrete time system. In the present thesis, only systems of the first kind are dealt with. On the whole, a dynamical system is often identified as $\{X, \Phi\}$ (e.g. Stewart and Thompson, 1986; Strogatz, 2014).

A continuous time system of dimension n is defined by a set of n autonomous ODEs in the form

$$\dot{\mathbf{x}} = \frac{d\mathbf{x}}{dt} = f(\mathbf{x}) \quad (3.4)$$

where $f : X \rightarrow \mathbb{R}^n$ is the vector field associated with the dynamical system. The evolution operator Φ^t describes the flow of the vector field, that is,

$$\mathbf{x}(t) = \Phi^t(\mathbf{x}_0). \quad (3.5)$$

The system is called linear if Eq. (3.4) can be written in the form

$$\dot{\mathbf{x}} = \mathbf{A}\mathbf{x} \quad (3.6)$$

where \mathbf{A} is a $n \times n$ matrix of constant components. Furthermore, the system is defined as conservative in the absence of any forms of energy dissipation; otherwise, it is said to be dissipative and its total mechanical energy changes with time.

The evolution of a dynamical system can be studied by following its orbit in the state space: it is defined as the set

$$\{\Phi^t(\mathbf{x}_0) \mid t \in T\} \quad (3.7)$$

representing the complete history of the system, starting from the initial state \mathbf{x}_0 .

A dynamical system is said to be smooth of order r if the first r time derivatives of the associated vector field f exist and are continuous $\forall \mathbf{x} \in X$. A particular case of great significance is represented by piecewise-smooth dynamical systems: they are defined as systems exhibiting phases of smooth evolution interrupted by sudden transitions (di Bernardo et al., 2008). Such are the systems whose behaviour is governed by a friction threshold, known as stick-slip systems. For such systems, the transitions between phases of smooth evolution are not associated with a discontinuity in the state vector \mathbf{x} , but instead in the accelerations and in the equations describing the dynamics, i.e., in the vector field f .

Nonlinear, dissipative, piecewise-smooth dynamical systems with a discontinuous right-hand side are called Filippov systems (Filippov, 1988). For such systems, it is possible to define a sticking region as the set of the state space corresponding to a phase of global stick. The system enters a phase of slip when its orbits intersects a geometric set known as failure locus.

Another significant feature in the characterization of a dynamical system is its sensitivity to initial conditions and to perturbations in the boundary conditions. Accordingly, a dynamical system is said to be predictable when its long-term evolution is not affected by small variations in initial and/or boundary conditions, whereas it is named chaotic if its long-term evolution strongly depends on the initial and/or boundary conditions. Notice that these definitions are referred to deterministic (non stochastic) dynamical systems.

3.2 Faults as discrete dynamical systems

It has long been acknowledged that fault dynamics can be fruitfully investigated by discrete models made of blocks connected through springs (Pelletier, 2000). Such an approach has the advantage of reducing the number of degrees of freedom required to describe the dynamics of the seismic source.

Discrete fault models can be classified into two categories, corresponding to a micro- and a macroscopic characterization of fault dynamics, respectively.

In the first case, a large number n of blocks is used to represent the contact points between the two sides of a fault. As $n \rightarrow \infty$, these models simulate the behaviour of a continuous elastic medium. The precursor of this methodology can be found in the work of Burridge and Knopoff (1967). The authors considered an array of blocks placed on a horizontal rough plane, connected to each other by springs and pulled by an external driver (Fig. 3.1).

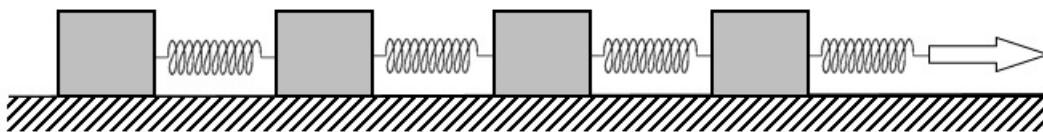


Figure 3.1: Sketch of the spring-block system due to Burridge and Knopoff (1967).

As for friction on the blocks, a piecewise constant function of the slip velocity as the one in Eq.(2.3) was assumed. This way, the authors were able to reproduce the characteristic stick-slip behaviour of seismic sources, as well as the typical Gutenberg-Richter distribution of earthquake sizes (e.g. Scholz, 1990). Owing to the nonlinear dependence of friction on the slip velocity, the system is nonlinear and dissipative. Models of this first category have been subsequently developed by a number of authors (e.g. Carlson and Langer, 1989a,b; Nakanishi, 1990; Carlson et al., 1991; Nakanishi, 1991; Huang et al., 1992; Hainzl et al., 1999; Weatherley and Abe, 2004).

Models of the second kind make use of a small number of blocks to analyse the main aspects of the dynamics of the seismic source (e.g. seismic slip, stress transfers, post-seismic deformation) with little regard to a minute description of these processes. In this framework, blocks represent multiple coplanar faults or asperities on the same fault (§3.3). In a way, this approach is similar to the characterization of a physical system by means of macroscopic thermodynamic quantities, instead of through the microscopic concepts of statistical mechanics. These models allow the study of the evolution of a fault by means of orbits in the phase space: via this geometrical analysis, it is possible to better appreciate and visualize the different aspects of the dynamics of the system. On the whole, these discrete fault models allow to focus on the main features of the seismic source (e.g. the stick-slip mechanism governed by the system of forces on the fault) and avoid the more complicated characterization based on continuum mechanics. The present thesis deals with models of this category.

The first example of such spring-block models is due to Nussbaum and Ruina (1987), who considered the elastic rebound of two blocks placed on a horizontal rough plane. The blocks are coupled to each other and to an external driver by means of springs of different stiffnesses (Fig. 3.2). The following correspondence rules hold: the blocks represent two asperities on the same fault plane or two coplanar faults; the external driver corresponds to the motion of the tectonic plates; the deformation of the springs represent the elastic deformation of crustal rocks; the forces applied to the blocks reproduce the tractions on the asperities/faults; friction on the horizontal support represents the frictional resistance on the asperity/fault surface; the motion of a block corresponds to the seismic slip; the coupling spring accounts for the coseismic stress transfer between the asperities/faults.

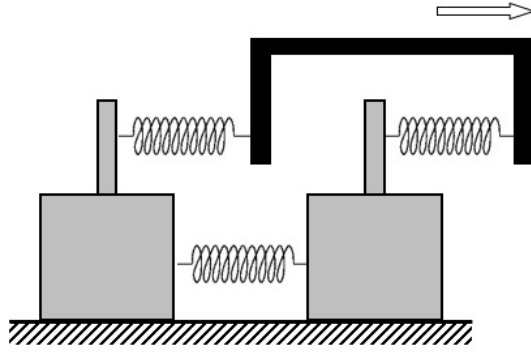


Figure 3.2: Sketch of the two-block model devised by Nussbaum and Ruina (1987).

The analysis was carried out under the hypothesis of complete spatial symmetry, i.e., assuming for the two blocks the same mass, frictional resistance and coupling with the external driver. Most of the seismic events resulted from the motion of a single block at a time, even though the simultaneous motion of the two blocks was observed as well. According to its properties, the two-block system can be classified as a Filippov stick-slip system (§3.1). During a phase of global stick, the state of the system can be described in terms of the difference p between the positions of the two blocks with respect to the external driver. As a seismic event occurs, p takes a new value. Accordingly, the evolution of the system can be described by means of an event map $p_{k+1} = f(p_k)$, where every iteration corresponds to a seismic event.

The hypothesis of spatial symmetry was later relaxed by Huang and Turcotte (1990a): under the assumption of a simple static/dynamic friction law as the one in Eq. (2.3), the authors showed that a two-block asymmetric system may exhibit chaotic behaviour (§3.1) in correspondence with higher coupling stiffness between the blocks. Furthermore, Huang and Turcotte (1990b) found that the chaotic behaviour may reproduce some features of interacting fault systems (§2.1.2), such as the pattern of seismicity observed on real faults. More recently, He (2003) showed that chaos in a two-block asymmetric system also depends on the particular formulation of friction adopted. In fact, if a rate- and state-friction law as the one in Eq. (2.2) is assumed, a chaotic evolution is fostered by smaller coupling intensities, corresponding to blocks moving more independently from each other, in contrast with the results obtained by Huang and Turcotte (1990a) with a simpler static/dynamic friction law. Hence, the crucial influence of friction on the specific properties of spring-block systems was acknowledged.

3.3 Asperity models of faults

Asperity models were first proposed by Scholz and Engelder (1976) and Byerlee (1978) as a means to explain some experimental results on the frictional resistance of rock samples. Later on, they were introduced in the field of fault mechanics (Lay et al., 1982; Ruff, 1983; Scholz, 1990). In the framework of asperity models, it is assumed that the fault is characterized by the presence of one or more strong regions with a high static friction and a velocity-weakening dynamic friction (§2.1.1). As a consequence of tectonic loading, the stress acting on the asperities is gradually increased, eventually leading to their sudden slip and to a seismic event. Thus, asperity failures account for the unstable, stick-slip sliding regime of seismogenic faults (§2.1). This characteristic behaviour can be fruitfully described by means of the concept of slip deficit: at any instant t in time, the slip deficit of an asperity is defined as the amount of slip that asperity should undergo in order to recover the relative displacement of tectonic plates occurred up to time t . Accordingly, the slip deficit increases when the asperity is at rest and decreases when it slips.

The number of asperities involved in an earthquake is generally small (from 1 to 3) and can be inferred from the analysis of the moment rate (source function), which yields the features of the far-field displacement due to the seismic event. Examples of earthquakes that can be ascribed to the failure of two asperities are the 1964 Alaska earthquake (Christensen and Beck, 1994), the 1992 Landers, California, earthquake (Kanamori et al., 1992), the 2004 Parkfield, California, earthquake (Twardzik et al., 2012), the 2007 Pisco, Peru, earthquake (Sladen et al., 2010) and the 2010 Maule, Chile, earthquake (Delouis et al., 2010).

Kanamori (1978) studied the role of asperity distribution and size in the spatial and temporal patterns of earthquake generation. If the asperities on the same fault plane have similar extension and frictional resistance, the slip of a first asperity is in general capable of triggering the slip of neighbouring asperities, thus giving rise to an earthquake of larger size. The opposite holds if asperities have different size and frictional resistance: in this case, the stress coupling between the asperities is less efficient, so that the slip of a first asperity mainly yield the failure of the smaller and weaker surrounding regions of the fault.

When considering asperity models, stress accumulation on the asperities, slip at the asperities and stress transfer between asperities are factors of crucial relevance. It is therefore appropriate to describe the fault as a dynamical system whose essential components are the asperities (Ruff, 1992; Turcotte, 1997).

It must be stressed that the discrete dynamical systems considered in the present work are much more general than the simple spring-block system shown in Fig. (3.2). Systems where each asperity is a compact and simply connected subset of the fault surface are considered. Therefore, asperities may have any geometrical shape and they may be different from each other as to their shapes and areas. Each asperity is subject to a tectonic traction that may have any direction, with both normal and tangential components with respect to the fault surface. Asperity slip takes place in the direction of the tangential traction and can reproduce any kind of source mechanism (Fig. 3.3).

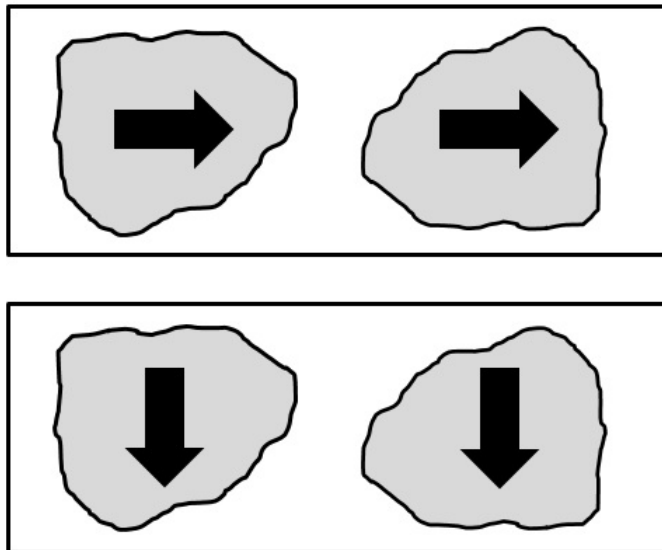


Figure 3.3: Slip of a two-asperity fault with strike-slip mechanism (above) and dip-slip normal mechanism (below). The rectangular frame is the fault border.

Since asperities are considered as single units of the fault, details of slip distribution on asperities are not considered, but a uniform slip is assumed to take place when an asperity moves. Therefore, asperity motions are similar to Volterra (or translation) dislocations, which are commonly employed in describing seismic sources (e.g. Okada, 1992).

3.3.1 A two-asperity fault model with elastic coupling

I summarize the main results of a series of works addressed to the analysis of a two-asperity fault model, on which much of the present thesis is based upon. In these works, it is assumed that the coupling between the asperities is purely elastic and that the fault is subject to a uniform and constant strain rate due to the motion of tectonic plates. The fault is treated as a dynamical system whose state variables are the slip deficits of the asperities (§3.3). As a result, the model has two degrees of freedom and the phase space is 4-dimensional. Furthermore, the dynamics of the system can be described in terms of four dynamic modes: one sticking mode, corresponding to stationary asperities, and three slipping modes, associated with the separate or simultaneous failures of the asperities.

A model of a fault with two asperities of equal areas and frictional resistances (symmetric system) was considered by Dragoni and Santini (2010, 2011). The authors showed that the evolution of the system is governed by a quantity related to the inhomogeneity of the stress applied to the asperities. This quantity corresponds to the quantity p (§3.2) governing the evolution of the two-block system considered by Nussbaum and Ruina (1987). Within a narrow range of stress distributions, the system follows a limit cycle, corresponding to a periodic behaviour, with the alternate slips of the asperities. There exists an uncountable infinity of such cycles, each one corresponding to a particular pattern of seismicity. The orbit of the system enters a limit cycle if, at the beginning of an interseismic interval, its representative point belongs to a specific subset L of the state space. If an external perturbation alters the stress distribution, so that the representative point lies outside of L , earthquakes associated with the simultaneous slips of the asperities take place. Due to the interaction between the asperities, the seismic moment released during such events is larger than the sum of the moments released by the asperities when they slip separately. Therefore, earthquakes due to the simultaneous failures of the asperities are the largest events that the fault can generate. Over time, a stress distribution compatible with the aforementioned periodic behaviour is restored: hence, the long-term evolution of the fault is always a limit cycle. The previous considerations point out that the system is sensitive to small perturbations: this observation is particularly significant, since no fault can be considered isolated, being subject to stress transfers due to earthquakes on surrounding faults (§2.1.2).

Dragoni and Santini (2012, 2014) studied the properties of a two-asperity asymmetric fault model. Complete analytical solutions for the four dynamic modes of the system were presented; furthermore, in order to apply the model to a real fault, the authors devised a set of correspondence rules between the discrete model and a model based on continuum mechanics. It was found that, when a single asperity is involved in a seismic event, the subsequent earthquake is very often due to the failure of the other asperity, although it may take place on the same asperity. The authors also investigated the source functions of all the possible seismic events predicted by the model, showing the dependence of their shape (number of humps and amplitude) on the sequence of slipping modes involved in the earthquake, which is in turn univocally determined by the state of the system before the earthquake. As for the rise time, duration and amplitude of the source functions, they are affected by the degree of coupling between the asperities and by the frictional resistance on them.

The effect of stress perturbations due to earthquakes on neighbouring faults was considered by Dragoni and Piombo (2015) in the case of an asymmetric model. The presence of two asperities entails that stress perturbations may not only change the occurrence time of the next earthquake on the fault, but also its hypocentre, seismic moment and duration: in fact, stress transfers may alter the sequence of dynamic modes in the earthquake. This circumstance was proposed by the authors as an explanation of the fact that earthquakes produced by a given fault are not only an aperiodic phenomenon, but are also different from one other in magnitude, slip distribution and duration. The effect of stress perturbations was discussed in terms of the variation of the Coulomb stress on each asperity (§2.1.2). Specifically, the authors found that the change in the difference between Coulomb stresses on the asperities determines which asperity will fail the first in the next earthquake; furthermore, the variation in the duration of the preceding interseismic interval is directly proportional to the change in the Coulomb stress associated with the asperity that fails the first in the earthquake.

The radiation of seismic waves during earthquakes generated by a two-asperity fault was studied by Dragoni and Santini (2015) in the framework of an asymmetric model. They included the seismic radiation by introducing an additional term proportional to the slip rate of the asperities in the equations of motion. Assuming

that this rate-dependent term gives a smaller contribution than dynamic friction during a seismic event, the authors illustrated the influence of seismic radiation on the earthquakes generated by the fault. Specifically, they showed that the slip amplitude and, in turn, the seismic moment are smaller, while the slip duration is larger in the presence of elastic waves. Furthermore, they calculated the moment rate spectra predicted by the model, which were found to be in agreement with the classic high-frequency trend found by Brune (1970). The model was further investigated by Dragoni and Tallarico (2016), who focused on the dynamic interplay between the asperities during seismic events made up of two or more slipping modes. The authors pointed out how such events require an heterogeneous stress distribution on the fault to be generated. Also, they discussed the seismic moment release, source functions and seismic spectra associated with these events, whose features may change dramatically as a function of the initial stress distribution on the fault.

In the models listed above, it was assumed that the asperities on the fault have equal areas. This assumption is relaxed in Chapter 6.

3.4 Reference model

In this section, I describe the fault model on which all the different studies presented in the following chapters are based on.

A plane fault (or a fault system) enclosed by two tectonic plates moving at constant relative velocity v is considered. The fault lies in an elastic shear zone that is a homogeneous and isotropic Poisson solid with rigidity μ . As a consequence of tectonic motion, the fault is subject to a uniform and constant strain rate $\dot{\epsilon}$.

It is assumed that the fault contains one or more asperities and possibly one or more weak regions (i.e., regions associated with a negligible static friction and a velocity-strengthening dynamic friction). Following the assumptions of asperity models, the production of earthquakes on the fault and the release of seismic moment are ascribed to the failure of the sole asperities. The slips of the different regions on the fault are treated as Volterra dislocations and thus assumed uniform over their areas.

Instead of focusing on the values of friction, slip and stress at every point on the fault, only the average values of these quantities on the asperities and weak regions are considered.

The fault is treated as a dynamical system whose state is described by the state of the asperities and weak regions (or the fault segments in the fault system). The state variables are the slip deficits (§3.3) or the Coulomb stresses (§2.1.2) associated with the regions on the fault.

Chapter 4

A fault with a single asperity

In this chapter, a discrete model of a fault containing a single asperity is considered. This configuration represents the simplest expression of a discrete fault model and provides as such a useful means to replicate the essential features of the seismic source (§3). The present chapter is based on the fault model devised by Dragoni and Piombo (2011).

4.1 The model

The fault model described in §3.4 is adopted and a fault containing a strong region (asperity) with area A is considered. The asperity is responsible for the bulk of seismic moment release during an earthquake: any contribution from the remaining weaker region of the fault is assumed to be negligible. A sketch of the model is shown in Fig. (4.1).

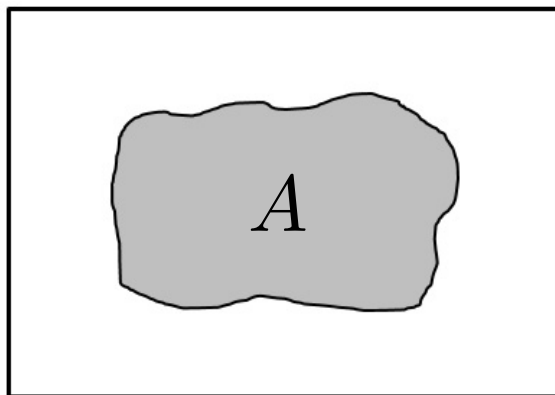


Figure 4.1: A plane fault containing a single asperity of area A . The rectangular frame is the fault border.

The fault is treated as a dynamical system whose state is described by the slip deficit $x(t)$ associated with the asperity, where t is time. Since the system has one degree of freedom, the phase-space is a 2-manifold.

The simplest form of rate-dependent friction is considered, characterizing the asperity by a static friction threshold f_s and a dynamic friction f_d defined as the average value of friction during asperity slip. This description of friction yields the typical stick-slip behaviour of fault dynamics.

Since the asperity moves as a rigid surface, it is easier to use forces instead of tractions. During the sticking mode, the asperity is subject to the loading action of tectonic motion, corresponding to the tangential force

$$f = -Kx, \quad (4.1)$$

where the coupling constant K can be calculated from the values of A, v and the tangential stress rate on the fault (§4.6). The equation of motion for the sticking mode is

$$\ddot{x} = 0 \quad (4.2)$$

where a dot indicates differentiation with respect to t . As a result, the slip deficit x increases steadily with time. A seismic event takes place as soon as the condition

$$f = -f_s \quad (4.3)$$

is reached. During the slipping mode, the asperity is subject to the additional tangential force

$$f_t = -\iota\dot{x} \quad (4.4)$$

where ι is an impedance introduced to take into account the radiation of elastic waves during asperity slip. The equation of motion during the slipping mode is

$$\mu_1\ddot{x} + Kx + \iota\dot{x} - f_d = 0 \quad (4.5)$$

where μ_1 is the mass associated with the asperity.

For the sake of simplicity, the analysis is carried out in nondimensional form. I introduce the nondimensional parameters

$$\gamma = \frac{\iota}{\sqrt{K\mu_1}}, \quad \epsilon = \frac{f_d}{f_s}, \quad V = \frac{\sqrt{K\mu_1}}{f_s}v \quad (4.6)$$

where: γ is a function of the seismic efficiency of the fault; ϵ is the ratio between dynamic and static frictions on the asperity; V is the nondimensional velocity of tectonic plates. The parameters are subject to the constraints $\gamma \geq 0$, $0 < \epsilon < 1$ and $V > 0$. I also define the nondimensional slip deficit and time

$$X = \frac{Kx}{f_s}, \quad T = \sqrt{\frac{K}{\mu_1}}t. \quad (4.7)$$

Accordingly, the equation of motion (4.2) for the sticking mode can be rewritten as

$$\ddot{X} = 0, \quad (4.8)$$

while the equation of motion (4.5) for the slipping mode becomes

$$\ddot{X} + X + \gamma\dot{X} - \epsilon = 0 \quad (4.9)$$

where a dot now denotes differentiation with respect to T .

Introducing the nondimensional force

$$F = \frac{f}{f_s}, \quad (4.10)$$

the loading action (4.1) of tectonic motion can be rewritten as

$$F = -X \quad (4.11)$$

and the condition (4.3) for the onset of a seismic event becomes

$$F = -1 \quad (4.12)$$

or, in terms of the slip deficit,

$$X = 1. \quad (4.13)$$

A condition of no overshooting is assumed: accordingly, it is required that $X \geq 0$ and that the tangential force on the asperity is always in the same direction as the velocity of tectonic plates, that is, $F \leq 0$.

To sum up, the system is described by the set of three parameters γ, ϵ and V . At any instant T in time, the state of the system may be univocally expressed by the slip deficit X or by the force F .

4.2 Dynamic modes

The dynamics of the system is characterized by two dynamic modes: the sticking and the slipping mode. In the following, the solution of the equations of motion for these modes is provided. I shall make use of the characteristic frequency

$$\omega_0 = \sqrt{1 - \frac{\gamma^2}{4}}. \quad (4.14)$$

During a slipping mode, it is assumed that the velocity dependent term (4.4) in the equation of motion is small with respect to dynamic friction. This choice is suggested by the observation that the seismic efficiency of faults is small (Kanamori, 2001). Accordingly, the case of weak damping is considered, so that $\gamma \leq 2$.

The effect of wave radiation is described by the quantity

$$\kappa_0 = \frac{1}{2} \left(1 + e^{-\frac{\pi\gamma}{2\omega_0}} \right) \quad (4.15)$$

which is a decreasing function of γ , equal to 1 in the absence of radiation ($\gamma = 0$).

4.2.1 Sticking mode

The equation of motion is (4.8). With initial conditions

$$X(0) = \bar{X}, \quad \dot{X}(0) = V \quad (4.16)$$

the solution is

$$X(T) = \bar{X} + VT. \quad (4.17)$$

Accordingly, the slip deficit of the asperity increases linearly with time, as a consequence of tectonic motion at constant relative velocity V .

4.2.2 Slipping mode

The equation of motion is (4.9). With initial conditions

$$X(0) = 1, \quad \dot{X}(0) = 0 \quad (4.18)$$

the solution is

$$X(T) = \epsilon + \frac{U}{2} \left(\cos \omega_0 T + \frac{\gamma}{2\omega_0} \sin \omega_0 T \right) e^{-\frac{\gamma T}{2}} \quad (4.19)$$

where

$$U = 2(1 - \epsilon). \quad (4.20)$$

The evolution of the slip deficit is shown in Fig. (4.2), together with the slip velocity $\dot{X}(T)$, for given values of γ and ϵ .

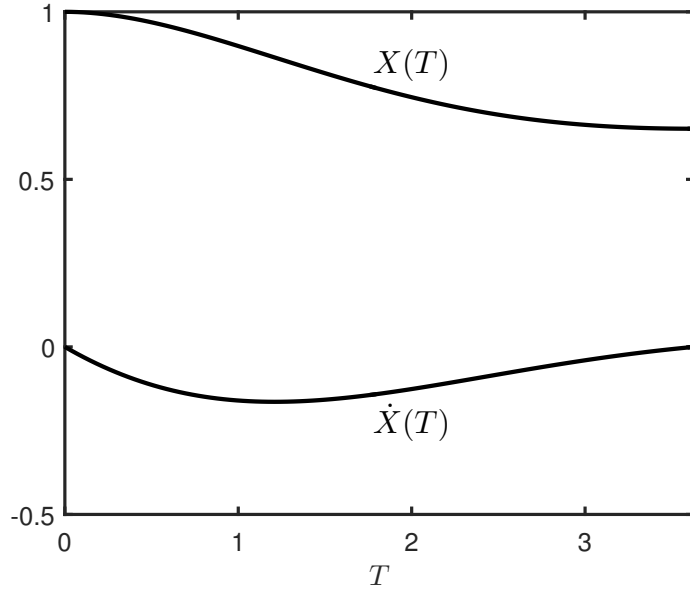


Figure 4.2: Evolution of the slip deficit $X(T)$ and the slip velocity $\dot{X}(T)$ during an earthquake generated by the fault ($\gamma = 1, \epsilon = 0.7$).

In choosing the initial conditions, I set $V = 0$. This is a reasonable assumption, since the ratio between the velocity of tectonic plates and the slip rate of a fault is in the order of 10^{-9} .

The duration of slip T_s can be evaluated from the condition $\dot{X}(T) = 0$, yielding

$$T_s = \frac{\pi}{\omega_0} \quad (4.21)$$

which reduces to π in the limit case $\gamma = 0$. The slip amplitude is

$$\Delta X(T) = X(0) - X(T). \quad (4.22)$$

It is shown in Fig. (4.3) for a particular choice of the parameters γ and ϵ . The graph shows the typical features of the source function of an earthquake, with a rise time T_s and a final slip amplitude

$$U_s = \Delta X(T_s) = \kappa_0 U. \quad (4.23)$$

In the limit case $\gamma = 0$, we have $U_s = U$.

Finally, the slip rate is

$$\Delta \dot{X}(T) = \frac{U}{2\omega_0} e^{-\frac{\gamma T}{2}} \sin \omega_0 T. \quad (4.24)$$

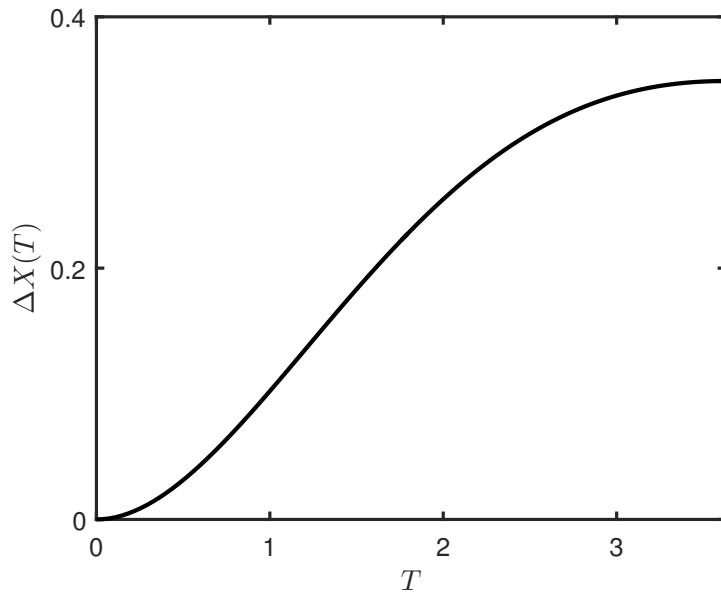


Figure 4.3: Evolution of the slip amplitude during an earthquake generated by the fault ($\gamma = 1, \epsilon = 0.7$).

Figure (4.4) shows the graphs of slip duration and amplitude as functions of the parameter γ , in units of the values assumed in the limit case $\gamma = 0$. As the radiation of elastic waves becomes more and more significant, the slip duration increases, whereas the slip amplitude is reduced. The former effect is a direct consequence of the smaller slip rate $\Delta\dot{X}(T)$ determined by the presence of radiation, in accordance with Eq. (4.24). The effect on the slip amplitude is instead due to the more and more important contribution of wave radiation to the energy budget of the system as γ increases. This issue will be further discussed in §4.5.

4.3 Orbits in the phase space

In this section, the orbit of the system in the phase space (X, \dot{X}) is described, distinguishing between the two dynamic modes.

During the sticking mode, it is assumed that $\dot{X} = 0$, as discussed before. The solution (4.17) is then a line segment lying on the X axis. The system evolves on this line until the point $(1, 0)$ is reached, corresponding to the condition (4.13) for the onset of failure. Here, the system enters the slipping mode.

As for the slipping mode, the solution (4.19) describes a damped Lissajous curve

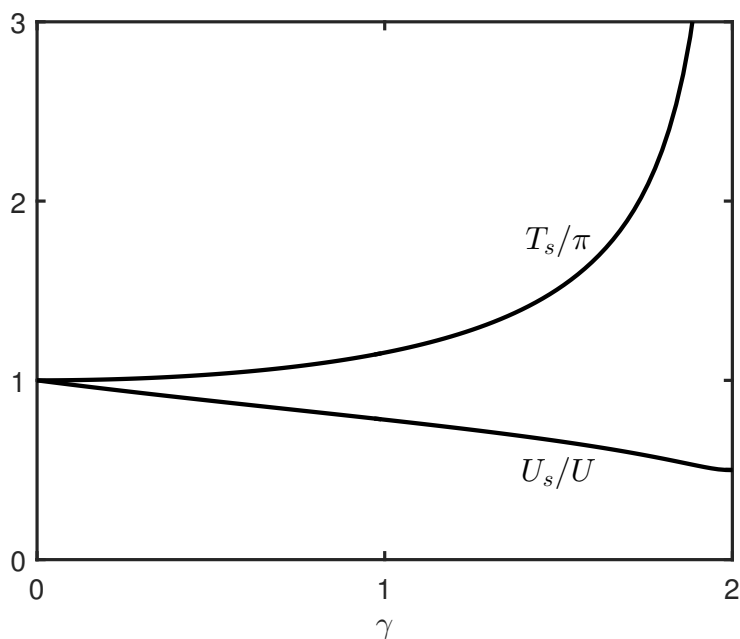


Figure 4.4: Slip duration T_s and slip amplitude U_s as functions of the parameter γ . They are normalized to the values assumed in the limit case $\gamma = 0$.

(Lawrence, 1972) in the phase space. The representative point of the system moves in the half-plane $\dot{X} < 0$ until its orbit crosses the X axis at the point $(1 - U_s, 0)$, where the system goes back in the sticking mode. In the limit case $\gamma = 0$, the orbit is a half circumference centered in $(\epsilon, 0)$ with radius $U/2$. The no overshooting condition $X \geq 0$ entails the constraint

$$1 - U_s \geq 0 \Rightarrow \epsilon \geq 1 - \frac{1}{2\kappa_0}. \quad (4.25)$$

Summing up, the system is characterized by a periodic orbit that is displayed in Fig. (4.5) for a given choice of the parameters γ and ϵ . The possible initial states are the points $(X, 0)$ with $0 \leq X \leq 1$. All orbits eventually enter the periodic orbit, giving rise to a limit cycle with period

$$\Delta T = \frac{U_s}{V} \quad (4.26)$$

whose specific value depends on the parameters γ, ϵ and V .

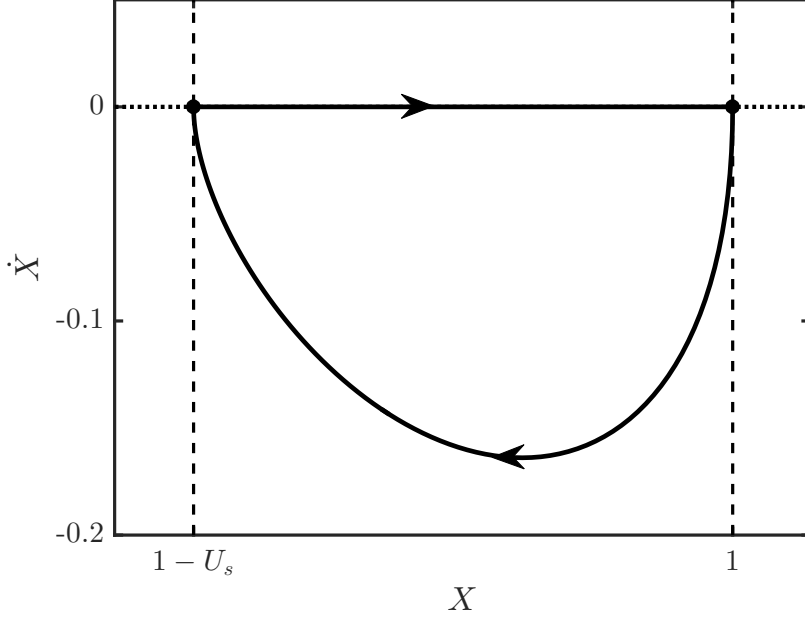


Figure 4.5: Orbit of the system in the phase space ($\gamma = 1, \epsilon = 0.7$).

An alternative visualization of the evolution of the system is provided by the graph of the tangential force on the asperity during the seismic cycle, which can be calculated exploiting Eq. (4.11). The modulus of the force increases linearly in time with rate V during the sticking mode, until the failure condition $|F| = 1$ is reached. The slip of the asperity is associated with a fixed stress drop

$$|\Delta F| = 1 - (1 - U_s) = U_s. \quad (4.27)$$

Afterwards, the force resumes increasing linearly until the failure condition is reached again, and so on. As a result, the tangential force exhibits a saw tooth shape with period ΔT . It is shown in Fig. (4.6).

4.4 Seismic moment rate and spectrum

The moment rate associated with an earthquake originated by the fault can be evaluated as

$$\dot{M}(T) = \frac{M_1}{U} \Delta \dot{X}(T) = \frac{M_1}{2\omega_0} e^{-\frac{\gamma T}{2}} \sin \omega_0 T \quad (4.28)$$

where M_1 is the seismic moment associated with the seismic event in the limit case $\gamma = 0$. Figure (4.7) shows the moment rate $\dot{M}(T)$ for different values of γ and for a given choice of the parameter ϵ .

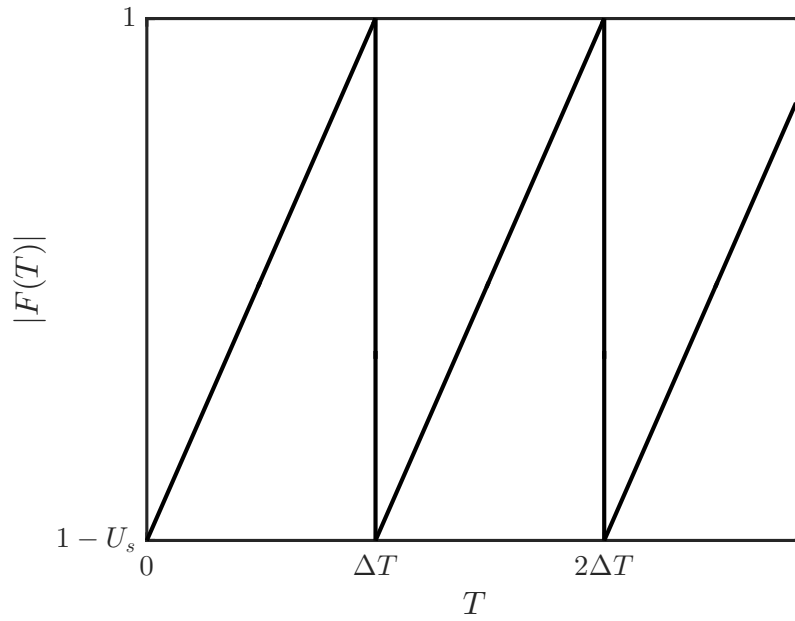


Figure 4.6: Evolution of the tangential force on the asperity during the seismic cycle ($\gamma = 1, \epsilon = 0.7, V = 10^{-9}$).

In the absence of wave radiation, the graph is a symmetric hump and presents a maximum at $T = T_s/2$. As wave radiation gets more and more significant, the graph becomes more and more asymmetric; also, its maximum is displaced towards earlier times and gets smaller and smaller.

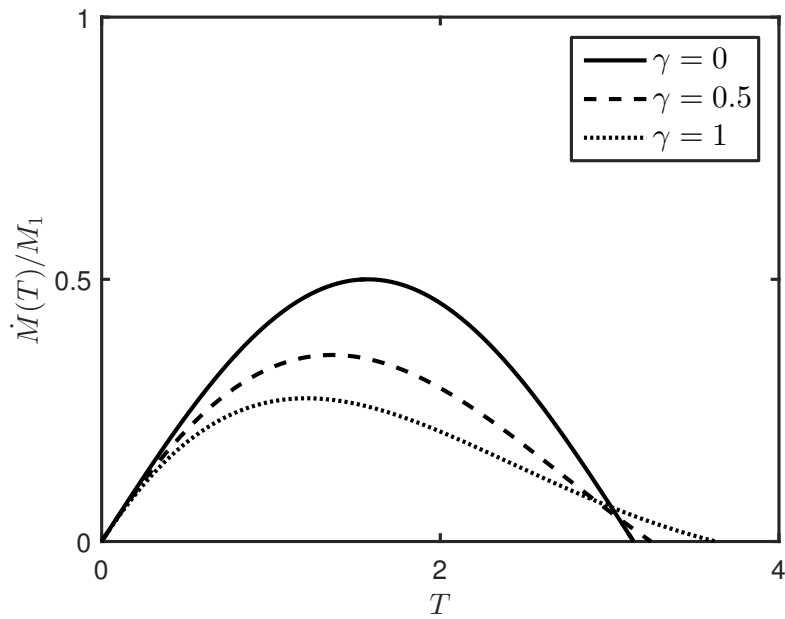


Figure 4.7: Moment rate associated with an earthquake originated by the fault ($\epsilon = 0.7$).

The final seismic moment is

$$M_0 = \frac{M_1}{U} \Delta X(T_s) = \kappa_0 M_1 \quad (4.29)$$

which is a decreasing function of γ , owing to its dependence on the factor κ_0 .

In order to calculate the moment rate spectrum associated with a seismic event, let us consider the Fourier transform

$$H(\Omega) = \int_0^{T_s} \dot{M}(T) e^{-i\Omega T} dT \quad (4.30)$$

where Ω is a nondimensional frequency defined from the frequency ω of the seismic waves as

$$\Omega = \sqrt{\frac{\mu_1}{K}} \omega. \quad (4.31)$$

The nondimensional spectrum is then given by

$$S(\Omega) = |H(\Omega)| = \frac{M_1}{2} \sqrt{\frac{1 + 2e^{-\frac{\pi\gamma}{2\omega_0}} \cos \Omega T_s + e^{-\frac{\pi\gamma}{\omega_0}}}{(1 - \Omega^2)^2 + \gamma^2 \Omega^2}}. \quad (4.32)$$

It takes the value M_0 for $\Omega = 0$, while its envelope for $\Omega \rightarrow \infty$ is M_0/Ω^2 . Thus, the seismic spectrum is inversely proportional to Ω^2 at high frequencies, in accordance with the classical spectrum described by Brune (1970). The corner frequency, corresponding to the intersection of the asymptotic trends at low and high frequencies, is

$$\Omega_c = 1. \quad (4.33)$$

The spectrum $S(\Omega)$ is shown in Fig. (4.8) in the case $\gamma = 1$.

4.5 Energy budget

As a result of tectonic loading, the slip deficit of the asperity increases with time, resulting in a build up of potential energy in the system. Such energy is dissipated into heat and wave radiation during a seismic event. Let $w(t)$ be the mechanical energy of the system at a time t , while $q(t)$ and $r(t)$ are the heat and radiation produced by the slip of the asperity after a time t from the onset of the earthquake. Their nondimensional equivalents are defined as

$$W = \frac{Kw}{f_s^2}, \quad Q = \frac{Kq}{f_s^2}, \quad R = \frac{Kr}{f_s^2}. \quad (4.34)$$

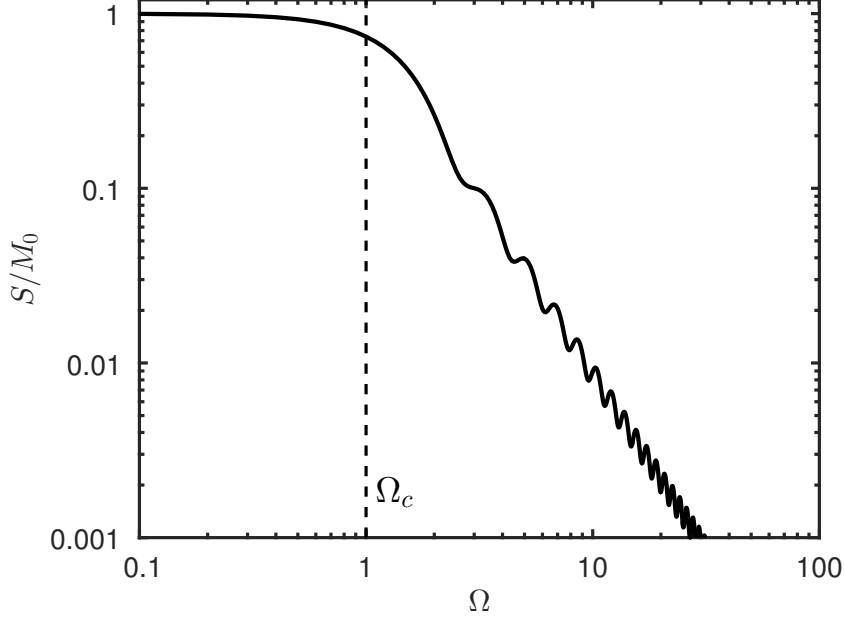


Figure 4.8: The moment rate spectrum associated with an earthquake generated by the fault ($\gamma = 1$). The dashed line indicates the corner frequency Ω_c , corresponding to the intersection of the low and high-frequency asymptotes.

During a sticking mode, the energy of the system is given by

$$W(X) = \frac{1}{2}X^2. \quad (4.35)$$

The slip of the asperity begins at $X = 1$ and ends at $X = 1 - U_s$. The consequent energy change is

$$\Delta W = W(1 - U_s) - W(1) = -\frac{1}{2}U_s(2 - U_s) \quad (4.36)$$

which reduces to

$$\Delta W_0 = 2\epsilon(\epsilon - 1) \quad (4.37)$$

in the limit case $\gamma = 0$. As for the heat and seismic energy released during the earthquake, we have

$$\Delta Q = \int_0^{T_s} \dot{Q}(T)dT, \quad \Delta R = \int_0^{T_s} \dot{R}(T)dT, \quad (4.38)$$

with rates

$$\dot{Q} = \epsilon\dot{X}, \quad \dot{R} = -\gamma\dot{X}^2. \quad (4.39)$$

Accordingly, we obtain

$$\Delta Q = -\epsilon U_s, \quad \Delta R = -\frac{1}{8}U^2(1 - e^{-\frac{\pi\gamma}{2\omega_0}}). \quad (4.40)$$

The energy budget of the fault is shown in Fig. (4.9) as a function of the impedance γ . In the limit case $\gamma = 0$, no seismic waves are radiated and all the energy is dissipated into heat, while the contribution of elastic radiation increases with γ .

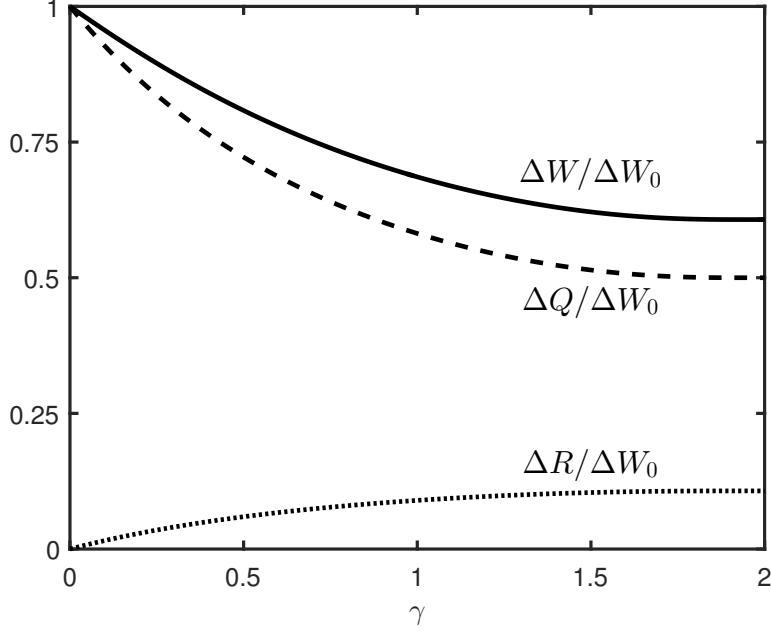


Figure 4.9: Energy budget for an earthquake generated by the fault, as a function of the impedance γ with $\epsilon = 0.7$. The change in mechanical energy ΔW , the heat release ΔQ and the radiated energy ΔR are normalised with respect to ΔW_0 , the total energy change in the limit case $\gamma = 0$.

The seismic efficiency of the fault is defined as

$$\eta = \frac{\Delta R}{\Delta W}. \quad (4.41)$$

Hence, we find

$$\eta = \bar{\eta} \frac{1 - e^{-\frac{\pi\gamma}{2\omega_0}}}{1 - \bar{\eta}e^{-\frac{\pi\gamma}{2\omega_0}}}, \quad (4.42)$$

where

$$\bar{\eta} = \frac{1 - \epsilon}{1 + \epsilon} \quad (4.43)$$

is the seismic efficiency in the limit case $\gamma = 2$, which decreases from 1 to 0 as ϵ increases. Figure (4.10) shows the seismic efficiency η as a function of γ for different values of the parameter ϵ .

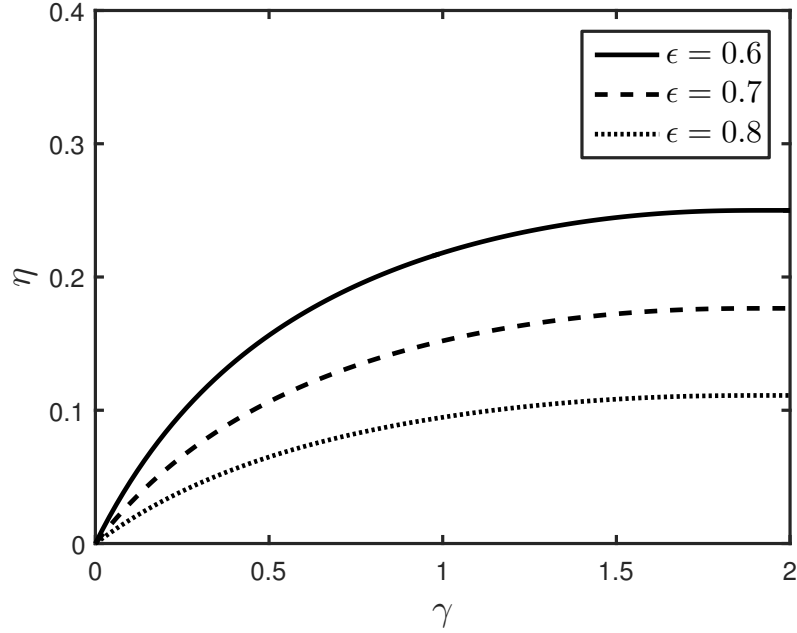


Figure 4.10: Seismic efficiency η of the fault, as a function of the impedance γ .

4.6 Choice of the parameters

In order to apply the model to a real fault, it is necessary to assign appropriate values to the three parameters γ , ϵ and V .

The impedance γ is related to the seismic efficiency of the fault: from Eq. (4.42), it is easy to obtain

$$\gamma = \frac{2 \ln \zeta}{\sqrt{\pi^2 + \ln^2 a}}, \quad (4.44)$$

with

$$\zeta = \frac{(1 - \eta)(1 - \epsilon)}{1 - \epsilon - \eta(1 + \epsilon)}. \quad (4.45)$$

However, the seismic efficiency cannot be determined from seismological data (Kanamori, 2001); therefore, the value of γ can be inferred on the basis of the fit with the observed source function of the earthquake.

The parameter ϵ depends on the properties of crustal rocks and can be chosen on the basis of experimental data (e.g. Jaeger and Cook, 1976). Finally, the rate V can be calculated from the observed plate velocity v , the duration t_s and the average slip amplitude u_s of the seismic event generated by the fault:

$$V = \frac{U_s t_s}{u_s T_s} v. \quad (4.46)$$

As for the constant K in Eq. (4.1), it can be evaluated from the tectonic shear force f accumulating on the asperity over a time t , given by

$$f = \dot{\sigma}_t A t \quad (4.47)$$

where $\dot{\sigma}_t$ is the tangential stress rate on the fault. Its expression is calculated from the strain rate $\dot{\epsilon}$ in Appendix A, distinguishing between strike-slip and dip-slip faults. In the discrete model, the force associated with tectonic loading over a time t is Kvt . By comparison, we obtain

$$K = \frac{\dot{\sigma}_t A}{v}. \quad (4.48)$$

Hence, the intensity of coupling between the asperity and the tectonic plates increases with the area of the asperity and with the tangential stress rate acting on the fault, while it decreases with the velocity of the tectonic plates.

4.7 An application: the 2004 Sumatra-Andaman earthquake

The great Sumatra-Andaman earthquake of 26 December 2004 occurred as the result of combined reverse dip-slip and right-lateral strike-slip faulting, with a moment magnitude ranging between 9.1 and 9.3 (Chlieh et al., 2007). The rupture involved a fault segment at the boundary between the Indo-Australian plate and the southeastern portion of the Eurasian plate, with an extension of about 1300 km from Northern Sumatra to the northern Andaman islands (Lay et al., 2005). The duration of the seismic event was about 600 s, with a moment release concentrated in a time interval $t_s = 460$ s (Ammon et al., 2005). I characterize the event averaging the data available in the SRCMOD database and assume an asperity area $A = 400,000 \text{ km}^2$ and a seismic moment $m = 5.4 \times 10^{22} \text{ Nm}$. With an average rigidity $\mu = 25 \text{ GPa}$ (Lorito et al., 2010), the average slip of the asperity is $u_s = 5.4 \text{ m}$. Finally, I take $v = 4.5 \text{ cm a}^{-1}$ (McCaffrey, 2009) for the relative velocity of tectonic plates at the Sumatra-Andaman subduction zone. A sketch of the tectonic setting is shown in Fig. (4.11).

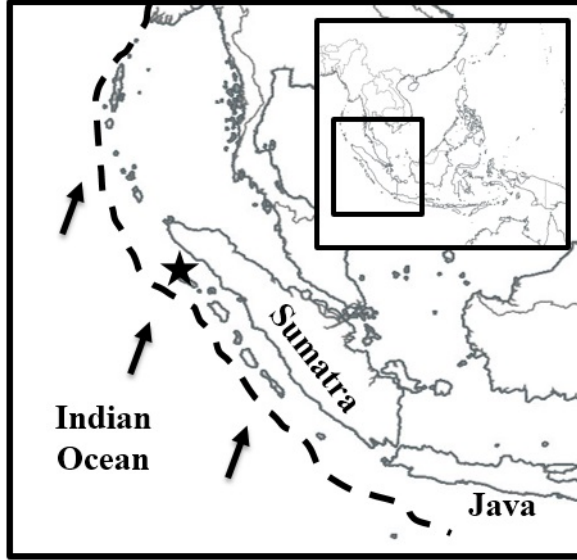


Figure 4.11: Geographic location of the 2004 Sumatra-Andaman earthquake. The star denotes the epicenter. Black arrows indicate the relative motion of the Indo-Australian plate with respect to the Eurasian plate, whereas the thick dashed line identifies the boundary between the tectonic plates.

For the sake of the present application, I assume $\epsilon = 0.7$ (e.g. Jaeger and Cook, 1976) and take $\gamma = 1.4$, a value yielding the best fit with the observed source function of the earthquake.

First, the observed seismic moment rate is reproduced, focusing on the time interval $t_1 \leq t \leq t_2$ where the main contribution to seismic moment is generated, with $t_1 = 40$ s and $t_2 = 500$ s. In dimensional form, the moment rate (4.28) becomes

$$\dot{m}(t) = \frac{m_1}{2\omega_0} \chi e^{-\frac{\gamma\chi(t-t_1)}{2}} \sin \omega_0 \chi (t - t_1) \quad (4.49)$$

where

$$\chi = \frac{T_s}{t_s} \quad (4.50)$$

and

$$m_1 = \mu A u \quad (4.51)$$

is the seismic moment released by the fault in the limit case $\gamma = 0$: accordingly, we have $u = u_s/\kappa_0$. The modelled moment rate is shown in Fig. (4.12) together with the observed moment rate reported by Ammon et al. (2005). The central peak of the source function and its shape are reasonably well fit by the model.

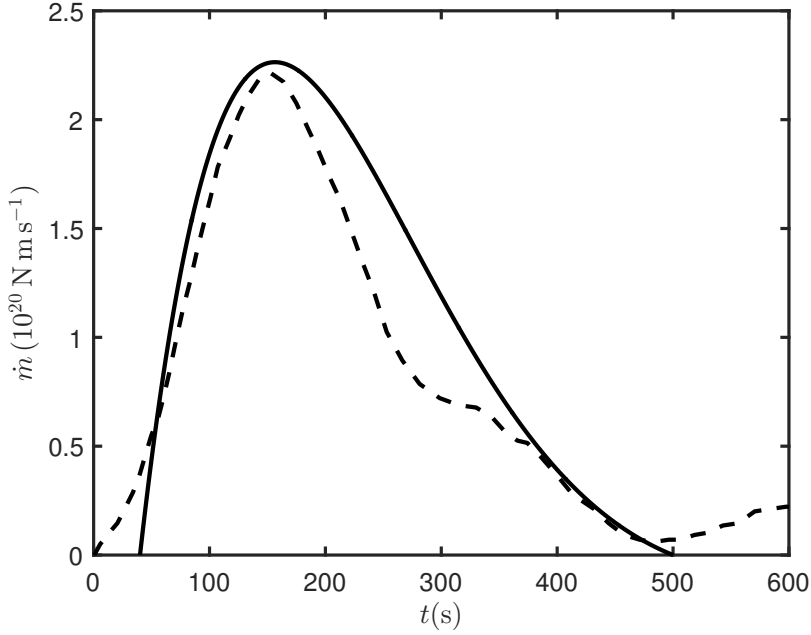


Figure 4.12: Modelled source function (solid line) of the 2004 Sumatra-Andaman earthquake, compared with the observed source function (dashed line) given by Ammon et al. (2005).

The final seismic moment provided by the model is

$$m_0 = \kappa_0 m_1 = 5.4 \times 10^{22} \text{ Nm} \quad (4.52)$$

consistent with the average value given beforehand.

The moment rate spectrum can be obtained as

$$s(\omega) = \int_{t_1}^{t_2} \dot{m}(t) e^{-i\omega t} dt \quad (4.53)$$

with $\dot{m}(t)$ given by Eq. (4.49). The spectrum is shown in Fig. (4.13).

The dimensional form of the corner frequency (4.33) can be retrieved taking the definition of the nondimensional frequency Ω into account. According to Eq. (4.31), we have

$$\omega_c = \frac{\omega}{\Omega} \Omega_c = \sqrt{\frac{K}{\mu_1}}. \quad (4.54)$$

Bearing in mind the definition (4.7) of the nondimensional time T , we can write

$$\sqrt{\frac{K}{\mu_1}} = \frac{T_s}{t_s} \quad (4.55)$$

where T_s is the slip duration predicted by the model, given by Eq. (4.21). Hence, the dimensional corner frequency can be estimated from the parameter γ and the source duration t_s as

$$\omega_c = \frac{1}{t_s} \frac{2\pi}{\sqrt{4 - \gamma^2}}. \quad (4.56)$$

With the values of γ and t_s listed above, we get $\omega_c \simeq 0.01 \text{ rad s}^{-1}$. This result is in very good agreement with the corner frequency $\omega_c \simeq 2 \text{ mHz}$ that can be estimated graphically from the seismic spectrum reported by Lay et al. (2005).

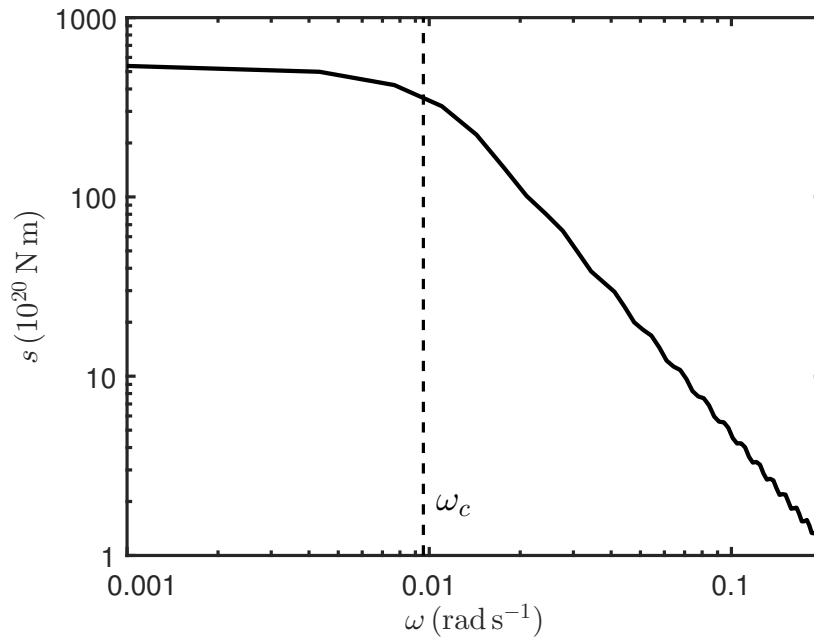


Figure 4.13: Modelled seismic spectrum for the 2004 Sumatra-Andaman earthquake. The dashed line indicates the corner frequency ω_c , corresponding to the intersection of the low and high-frequency asymptotes.

Chapter 5

A fault exhibiting seismic slip and afterslip

In this chapter, I consider a discrete model of a fault containing two regions differing for their mechanical behaviour: an unstable, velocity-weakening region and a stable, velocity-strengthening region (§2.1.1). The separation of the fault surface into two such regions allows to replicate the generation of earthquakes, associated with the slip of the unstable region, and the occurrence of afterslip in the aftermath of an earthquake, taking place in the stable region (§2.3.1). This chapter presents the results discussed by Dragoni and Lorenzano (2017).

5.1 The model

Adopting the fault model described in §3.4, I consider a fault containing two regions differing for their mechanical behaviours (Fig. 5.1): a strong region (asperity) of area A_1 , characterized by a high static friction and a velocity-weakening dynamic friction, and a weak region of area A_2 , associated with a negligible static friction and a velocity-strengthening dynamic friction. Let a be the distance between the centres of the two regions.

A simplified form of the general rate- and state-dependent friction law (§2.1.1) is adopted. For the asperity, a constant static friction f_s and a dynamic friction f_d that is the average value of friction during slip are assumed. For the weak region, a dynamic friction \tilde{f}_d described by the velocity-strengthening law

$$\tilde{f}_d = f_0 - \Lambda \dot{y} \tag{5.1}$$

is assumed, where f_0 is the steady-state dynamic friction and Λ is a constant. In writing the velocity-dependent term, it was taken into account that $\dot{y} < 0$ during a slip phase.

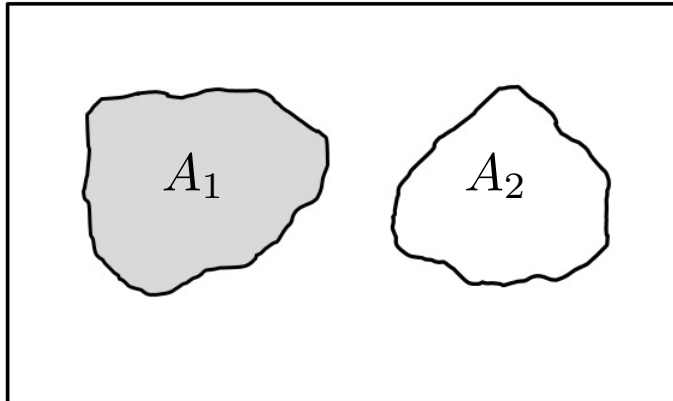


Figure 5.1: Model of a fault with two mechanically different regions: an asperity of area A_1 and a weak region of area A_2 . The rectangular frame is the fault border.

The fault is characterized as a dynamical system whose state variables are the slip deficits $x(t)$ and $y(t)$ of the asperity and of the weak region, respectively, as functions of time t . Since the system has two degrees of freedom, the phase-space is a 4-manifold.

As the two regions move as rigid surfaces, it is simpler to use forces instead of tractions. Let f_1 and f_2 be the tangential forces applied to the asperity and to the weak region, respectively, in the slip direction. They can be written as

$$f_1 = -K_1x + K_c(y - x) - \iota\dot{x}, \quad f_2 = -K_2y - K_c(y - x). \quad (5.2)$$

The terms $-K_1x$ and $-K_2y$ represent the effect of tectonic loading; the terms $\pm K_c(y - x)$ are the contributions of stress transfer between the two regions; the term $-\iota\dot{x}$ is only present during seismic slip and is due to radiation damping, where ι is an impedance and the dot indicates differentiation with respect to t . The constants K_1 , K_2 and K_c can be retrieved from the values of A_1 , A_2 , μ , v , the tangential stress rate acting on the fault and the tangential stress transferred by the slip of one region to the other (§5.4). Specifically, the ratio K_2/K_1 results equal to the ratio A_2/A_1 .

The dynamics of the system can be characterized in terms of three dynamic modes, each one associated with a different system of autonomous ODEs. They

correspond to: evolution during an interseismic interval, seismic slip of the asperity and afterslip within the weak region. In the following, the masses associated with the asperity and the weak region are denoted as μ_1 and μ_2 , respectively.

During an interseismic interval, the slip deficit x of the asperity increases steadily due to tectonic loading. As for the weak region, a steady-state creep at constant stress is allowed, so that its slip deficit y increases with time, but at a slower rate than x . Accordingly, the equations of motion during an interseismic interval are

$$\ddot{x} = 0 \quad (5.3)$$

$$(K_2 + K_c)y - K_c x = f_0. \quad (5.4)$$

The slip of the asperity occurs when

$$f_1 = -f_s. \quad (5.5)$$

Asperity slip takes place over a time interval very short with respect to the interseismic interval: accordingly, both tectonic loading and steady-state creep can be neglected during a seismic event. As a result, the slip deficit y of the weak region can be assumed as constant during asperity slip. The equations of motion are then

$$\mu_1 \ddot{x} + \iota \dot{x} + (K_1 + K_c)x - K_c y - f_d = 0 \quad (5.6)$$

$$\dot{y} = 0. \quad (5.7)$$

Following an earthquake, afterslip takes place in the weak region, while the asperity remains stationary. Since afterslip is characterized by a much shorter duration than typical interseismic intervals, tectonic loading can be reasonably neglected during this mode. The equations of motion are then

$$\dot{x} = 0 \quad (5.8)$$

$$\mu_2 \ddot{y} + \Lambda \dot{y} + (K_2 + K_c)y - K_c x - f_0 = 0. \quad (5.9)$$

For the sake of simplicity, the analysis is carried out in nondimensional form. I introduce the nondimensional parameters

$$\alpha = \frac{K_c}{K_1}, \quad \beta = \frac{f_0}{f_s}, \quad \gamma = \frac{\iota}{\sqrt{K_1 \mu_1}} \quad (5.10)$$

$$\epsilon = \frac{f_d}{f_s}, \quad \lambda = \frac{\Lambda}{\sqrt{K_1 \mu_1}}, \quad \xi = \frac{A_2}{A_1}, \quad V = \frac{\sqrt{K_1 \mu_1}}{f_s} v \quad (5.11)$$

where: α expresses the degree of coupling between the asperity and the weak region; β is the ratio between the steady-state dynamic friction on the weak region and the static friction on the asperity; γ is a function of the seismic efficiency of the fault; ϵ is the ratio between the dynamic and static frictions of the asperity; λ is a measure of the intensity of velocity strengthening in the weak region; ξ is the ratio between the areas of the two regions; V is the nondimensional velocity of tectonic plates. These parameters are subject to the following constraints: $\alpha \geq 0$, $0 < \beta < 1$, $\gamma \geq 0$, $\lambda > 0$, $0 < \epsilon < 1$, $\xi > 0$, $V > 0$. Furthermore, it is assumed that the masses associated with the two regions are proportional to their areas, so that

$$\frac{\mu_2}{\mu_1} = \frac{K_2}{K_1} = \xi. \quad (5.12)$$

Finally, I introduce the nondimensional slip deficits and time

$$X = \frac{K_1 x}{f_s}, \quad Y = \frac{K_1 y}{f_s}, \quad T = \sqrt{\frac{K_1}{\mu_1}} t \quad (5.13)$$

and the nondimensional forces

$$F_1 = \frac{f_1}{f_s}, \quad F_2 = \frac{f_2}{f_s}. \quad (5.14)$$

Making use of Eq. (5.2), we get

$$F_1 = -X + \alpha(Y - X) - \gamma \dot{X}, \quad F_2 = -\xi Y - \alpha(Y - X) \quad (5.15)$$

where a dot now indicates differentiation with respect to T . These forces reduce to

$$F_1 = -X + \alpha(Y - X), \quad F_2 = -\xi Y - \alpha(Y - X) \quad (5.16)$$

during an interseismic interval and afterslip. To sum up, the system is described by the set of seven parameters $\alpha, \beta, \gamma, \epsilon, \lambda, \xi$ and V . At any instant T in time, the state of the system can be univocally expressed by the couple (X, Y) or by the couple (F_1, F_2) .

In nondimensional form, the equations of motion (5.3)-(5.4) for the interseismic intervals can be rewritten as

$$\ddot{X} = 0 \quad (5.17)$$

$$(\alpha + \xi)Y - \alpha X = \beta. \quad (5.18)$$

The equations of motion (5.6) and (5.7) for the seismic mode become

$$\ddot{X} + \gamma \dot{X} + (1 + \alpha)X - \alpha Y - \epsilon = 0 \quad (5.19)$$

$$\dot{Y} = 0. \quad (5.20)$$

Finally, the equations of motion (5.8) and (5.9) for the afterslip mode become

$$\dot{X} = 0 \quad (5.21)$$

$$\xi\ddot{Y} + \lambda\dot{Y} + (\alpha + \xi)Y - \alpha X - \beta = 0. \quad (5.22)$$

5.2 Solutions of dynamic modes

The analytical solutions to the equations of motion for the three dynamic modes of the system are provided. I shall make use of the frequencies

$$\omega_1 = \sqrt{1 + \alpha - \frac{\gamma^2}{4}}, \quad \omega_2 = \sqrt{\frac{\lambda^2}{4\xi^2} - 1 - \frac{\alpha}{\xi}}. \quad (5.23)$$

The maximum slip amplitude of the asperity in the absence of radiation ($\gamma = 0$) is defined as

$$U = 2\frac{1 - \epsilon}{1 + \alpha}. \quad (5.24)$$

Finally, the effect of wave radiation is described by the quantity

$$\kappa_1 = \frac{1}{2} \left(1 + e^{-\frac{\pi\gamma}{2\omega_1}} \right), \quad (5.25)$$

which is a decreasing function of γ , equal to 1 in the absence of radiation ($\gamma = 0$).

5.2.1 Interseismic interval

The equations of motion are given by Eq. (5.17) and Eq. (5.18). With initial conditions

$$X(0) = X_0, \quad \dot{X}(0) = V, \quad Y(0) = Y_0 \quad (5.26)$$

the solution is

$$X(T) = X_0 + VT \quad (5.27)$$

$$Y(T) = Y_0 + \frac{\alpha}{\alpha + \xi} VT \quad (5.28)$$

where, according to Eq. (5.18),

$$Y_0 = \frac{\alpha X_0 + \beta}{\alpha + \xi}. \quad (5.29)$$

We conclude that, during an interseismic interval, the representative point of the system moves along the line

$$Y = \frac{\beta + \alpha X}{\alpha + \xi}. \quad (5.30)$$

The solution shows that the slip deficit X of the asperity increases in time with the velocity V of tectonic plates. The slip deficit Y of the weak region increases in time as well, but with a slower rate

$$\dot{Y} = \frac{\alpha}{\alpha + \xi} V \quad (5.31)$$

implying a steady creep $\Delta Y(T)$ with constant rate

$$\Delta \dot{Y} = V - \dot{Y} = \frac{\xi}{\alpha + \xi} V \quad (5.32)$$

that is smaller than plate velocity. Combining Eq. (5.27) - (5.28) with Eq. (5.16), the evolution of the tangential forces on the two regions during an interseismic interval is expressed by

$$F_1(T) = F_1(0) - \frac{\alpha + \alpha\xi + \xi}{\alpha + \xi} VT \quad (5.33)$$

$$F_2 = -\beta \quad (5.34)$$

where

$$F_1(0) = -X_0 + \alpha(Y_0 - X_0). \quad (5.35)$$

Accordingly, stress increases linearly with time on the asperity, while it remains constant on the weak region.

5.2.2 Seismic slip

The asperity starts to slip at $T = T_1$, when the forces have the values

$$F_1 = -1, \quad F_2 = -\beta \quad (5.36)$$

where Eq. (5.5) and Eq. (5.34) were taken into account. By combination with Eq. (5.16), we obtain the equations of two lines

$$(1 + \alpha)X - \alpha Y = 1 \quad (5.37)$$

$$(\alpha + \xi)Y - \alpha X = \beta \quad (5.38)$$

whose intersection yields the state of the fault at the beginning of the seismic event:

$$X_1 = \frac{\alpha + \alpha\beta + \xi}{\alpha + \alpha\xi + \xi}, \quad Y_1 = \frac{\alpha + \alpha\beta + \beta}{\alpha + \alpha\xi + \xi}. \quad (5.39)$$

The equations of motion are given in Eq. (5.19) and Eq. (5.20). Eq. (5.19) is solved in the case of weak damping, implying that the velocity dependent term is small

with respect to the other forces (§4.2). For the sake of simplicity, I set $T_1 = 0$. With initial conditions

$$X(0) = X_1, \quad \dot{X}(0) = 0, \quad Y(0) = Y_1 \quad (5.40)$$

the solution is

$$X(T) = X_1 - \frac{U}{2} \left[1 - \left(\cos \omega_1 T + \frac{\gamma}{2\omega_1} \sin \omega_1 T \right) e^{-\frac{\gamma}{2} T} \right] \quad (5.41)$$

$$Y = Y_1. \quad (5.42)$$

Accordingly, the slip deficit of the asperity decreases with time, whereas the slip deficit of the weak region remains unchanged. The duration of the seismic event, calculated from the condition $\dot{X}(T) = 0$, is

$$T_s = \frac{\pi}{\omega_1}. \quad (5.43)$$

Defining the slip amplitude of the asperity as

$$\Delta X(T) = X_1 - X(T), \quad (5.44)$$

the final slip amplitude is

$$U_s = \Delta X(T_s) = \kappa_1 U. \quad (5.45)$$

The slip amplitude $\Delta X(T)$ is shown in Fig. (5.2) for a given choice of the parameters α, γ and ϵ .

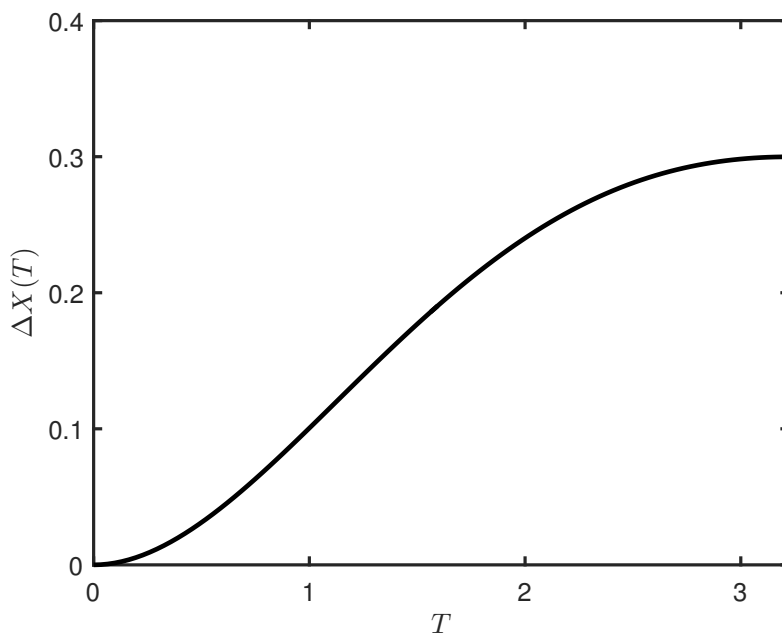


Figure 5.2: Evolution of the slip amplitude of the asperity during a seismic event ($\alpha = 0.2, \gamma = 1, \epsilon = 0.7$).

The moment rate associated with the seismic event can be calculated as

$$\dot{M}_s(T) = M_1 \frac{\Delta \dot{X}(T)}{U} \quad (5.46)$$

where M_1 is the seismic moment corresponding to the slip U . From Eq. (5.41) and Eq. (5.44), we obtain

$$\dot{M}_s(T) = M_1 \frac{1 + \alpha}{2\omega_1} \sin \omega_1 T e^{-\frac{\gamma}{2}T}. \quad (5.47)$$

The final seismic moment is

$$M_s = M_1 \frac{U_s}{U} = \kappa_1 M_1. \quad (5.48)$$

The seismic moment rate $\dot{M}_s(T)$ is shown in Fig. (5.3) for a given choice of the parameters α, γ and ϵ .

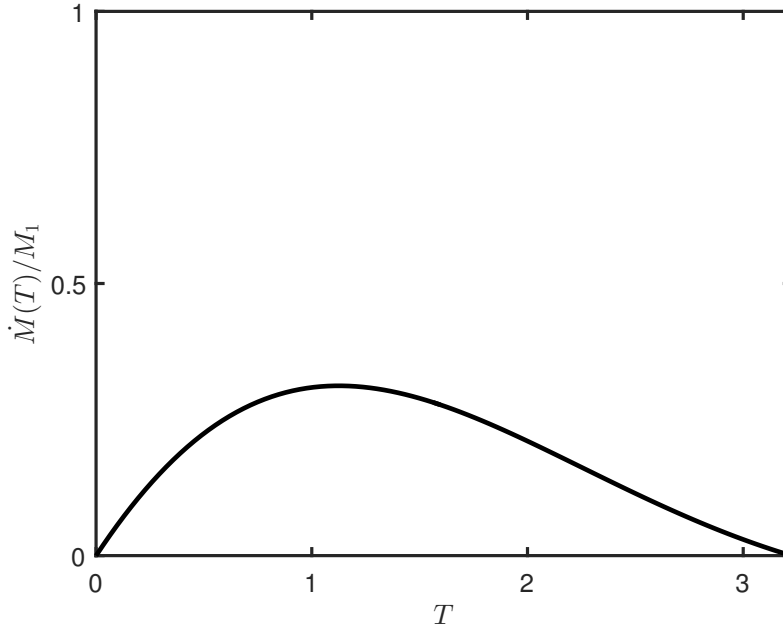


Figure 5.3: Moment rate associated with an earthquake on the fault ($\alpha = 0.2, \gamma = 1, \epsilon = 0.7$).

From Eq. (5.15), the forces on the asperity and on the weak region during the earthquake are, respectively,

$$F_1(T) = -X(T) + \alpha [Y_1 - X(T)] - \gamma \dot{X}(T) \quad (5.49)$$

$$F_2(T) = -\xi Y_1 - \alpha [Y_1 - X(T)]. \quad (5.50)$$

They are shown in Fig. (5.4) for a given choice of the parameters α, γ and ϵ .

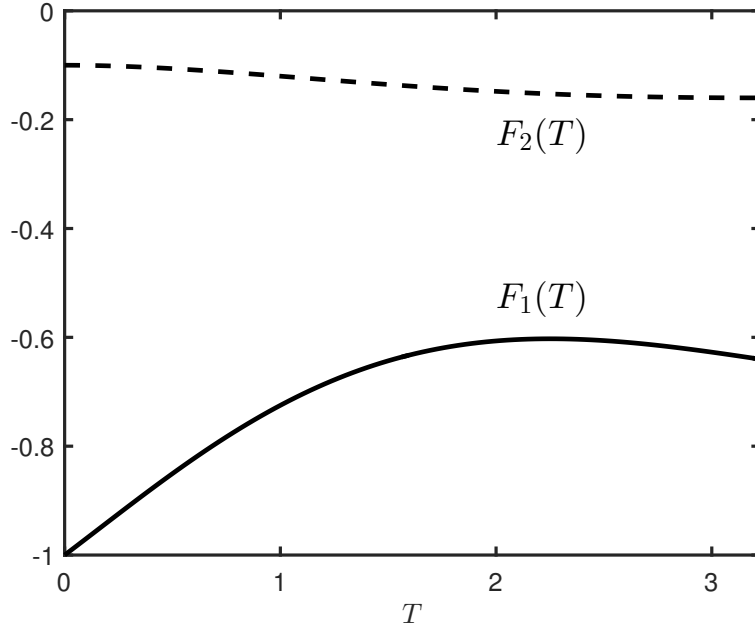


Figure 5.4: Evolution of the tangential forces on the asperity (solid line) and on the weak region (dashed line) during a seismic event ($\alpha = 0.2, \gamma = 1, \epsilon = 0.7$).

At the end of the event ($T = T_2$), the slip deficits of the two regions are

$$X_2 = X_1 - U_s, \quad Y_2 = Y_1. \quad (5.51)$$

In order to exclude overshooting during the earthquake, the condition $X_2 \geq 0$ is required. Making use of Eq. (5.39), we obtain the constraint

$$\beta \geq \frac{U_s(\alpha + \alpha\xi + \xi) - \alpha - \xi}{\alpha}. \quad (5.52)$$

Introducing the expressions of X_2 and Y_2 into Eq. (5.49) and Eq. (5.50), we conclude that the forces at the end of the slipping mode are

$$F_1(T_2) = -1 + (1 + \alpha)U_s \quad (5.53)$$

$$F_2(T_2) = -\beta - \alpha U_s. \quad (5.54)$$

A comparison with Eq. (5.36) indicates that the force F_1 on the asperity has decreased in magnitude, with a force drop $(1 + \alpha)U_s$. Conversely, the force F_2 on the weak region has increased in magnitude by an amount αU_s : this drives the region out of the steady-state creep and initiates the afterslip.

5.2.3 Afterslip

The equations of motion are given in Eq. (5.21) and Eq. (5.22). As a matter of fact, afterslip is characterized by a longer duration than seismic slip: thus, a high value of λ is expected and it is reasonable to consider the overdamped solution of Eq. (5.22). For the sake of simplicity, I set $T_2 = 0$ for the origin time of the afterslip mode. With initial conditions

$$X(0) = X_2, \quad Y(0) = Y_2, \quad \dot{Y}(0) = 0 \quad (5.55)$$

the solution is

$$X = X_2 \quad (5.56)$$

$$Y(T) = \bar{Y} - (\bar{Y} - Y_1) \left[\cosh \omega_2 T + \frac{\lambda}{2\xi\omega_2} \sinh \omega_2 T \right] e^{-\frac{\lambda}{2\xi} T} \quad (5.57)$$

where

$$\bar{Y} = \frac{\alpha X_2 + \beta}{\alpha + \xi}. \quad (5.58)$$

Defining the afterslip amplitude as

$$\Delta Y(T) = Y_2 - Y(T), \quad (5.59)$$

the final afterslip amplitude is

$$U_a = Y_2 - \bar{Y} = \frac{\alpha}{\alpha + \xi} U_s \quad (5.60)$$

where Eq. (5.39), Eq. (5.45), Eq. (5.51) and Eq. (5.58) were used. This result points out that afterslip in the weak region is proportional to the seismic slip of the asperity, in agreement with observations (Scholz, 1990). The afterslip amplitude $\Delta Y(T)$ is shown in Fig. (5.5) for a particular choice of the parameters α , ϵ , λ and ξ .

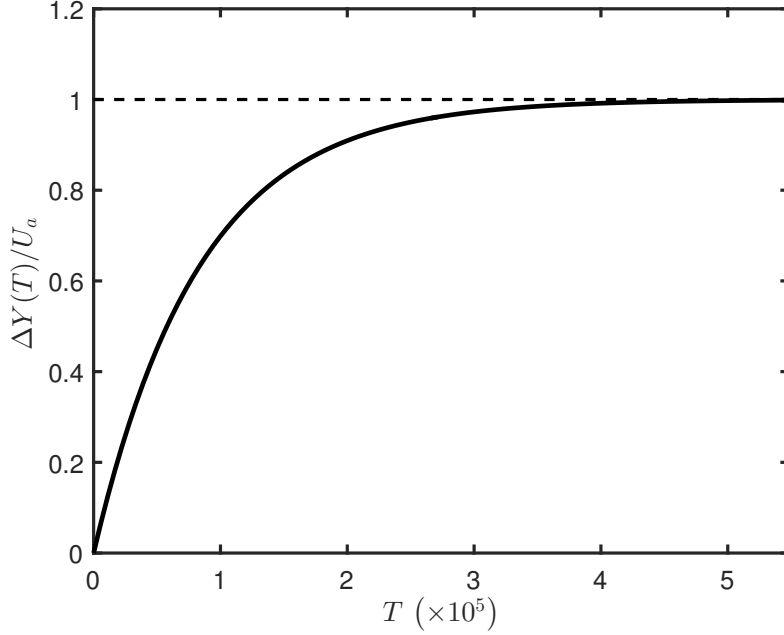


Figure 5.5: Evolution of the afterslip amplitude of the weak region following a seismic event ($\alpha = 0.2, \epsilon = 0.7, \lambda = 10^5, \xi = 1$).

The afterslip rate is

$$\Delta\dot{Y}(T) = \frac{(\alpha + \xi)U_a}{\xi\omega_2} \sinh \omega_2 T e^{-\frac{\lambda}{2\xi}T}. \quad (5.61)$$

Strictly speaking, this expression suggests that the final value U_a of the afterslip amplitude is reached only as $T \rightarrow \infty$. However, the slip rate $\Delta\dot{Y}$ is exponentially decreasing and, after some time, afterslip becomes indistinguishable from the steady-state creep taking place during interseismic intervals. Therefore, it is possible to assign a finite duration to afterslip, defined as the time interval T_a after which the afterslip rate (5.61) lowers below the creep rate (5.32):

$$\Delta\dot{Y}(T_a) = \frac{\xi}{\alpha + \xi} V. \quad (5.62)$$

This equation can be easily solved for T_a noticing that, for large values of T , it is possible to write to a very good approximation

$$\Delta\dot{Y}(T) \approx \frac{(\alpha + \xi)U_a}{2\xi\omega_2} e^{-T/\Theta_a} \quad (5.63)$$

with

$$\Theta_a = \left(\frac{\lambda}{2\xi} - \omega_2 \right)^{-1}. \quad (5.64)$$

Thus, Eq. (5.62) yields

$$T_a = \Theta_a \ln \frac{\alpha U_s (\alpha + \xi)}{2\xi^2 \omega_2 V}. \quad (5.65)$$

Afterslip duration T_a is remarkably affected by the degree of coupling between the two regions of the fault. This is illustrated in Fig. (5.6), where T_a is shown as a function of the coupling parameter α for different values of the parameter ξ . The graph shows an initial steep growth for smaller values of α , reaching a maximum value that depends on the particular combination of the parameters of the system; finally, it decreases for higher values of α .

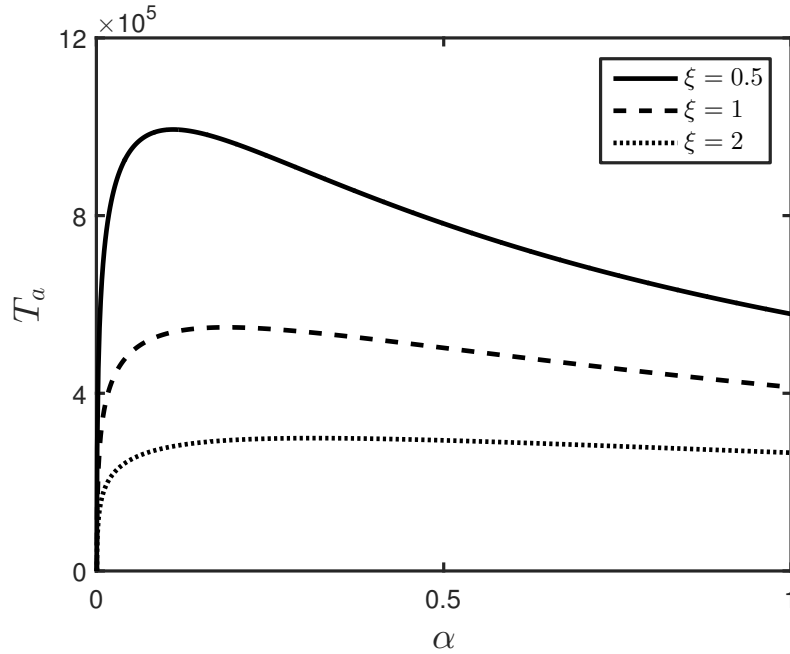


Figure 5.6: Afterslip duration (5.65) as a function of the coupling parameter α for different values of the parameter ξ . Other parameters are $\epsilon = 0.7, \gamma = 1, \lambda = 10^5$ and $V = 10^{-9}$.

The geodetic moment rate associated with afterslip can be calculated as

$$\dot{M}_a(T) = \xi M_1 \frac{\Delta \dot{Y}(T)}{U}. \quad (5.66)$$

Using Eq. (5.60) and Eq. (5.61), we obtain

$$\dot{M}_a(T) = M_1 \frac{\alpha \kappa_1}{\omega_2} \sinh \omega_2 T e^{-\frac{\lambda}{2\xi} T}. \quad (5.67)$$

The final moment is

$$M_a = \xi M_1 \frac{U_a}{U} = \frac{\alpha \xi}{\alpha + \xi} \kappa_1 M_1 \quad (5.68)$$

differing from the seismic moment (5.48) by a factor $\alpha\xi/(\alpha + \xi)$. The geodetic moment rate $\dot{M}_a(T)$ is shown in Fig. (5.7) for a particular choice of the parameters $\alpha, \epsilon, \lambda$ and ξ .

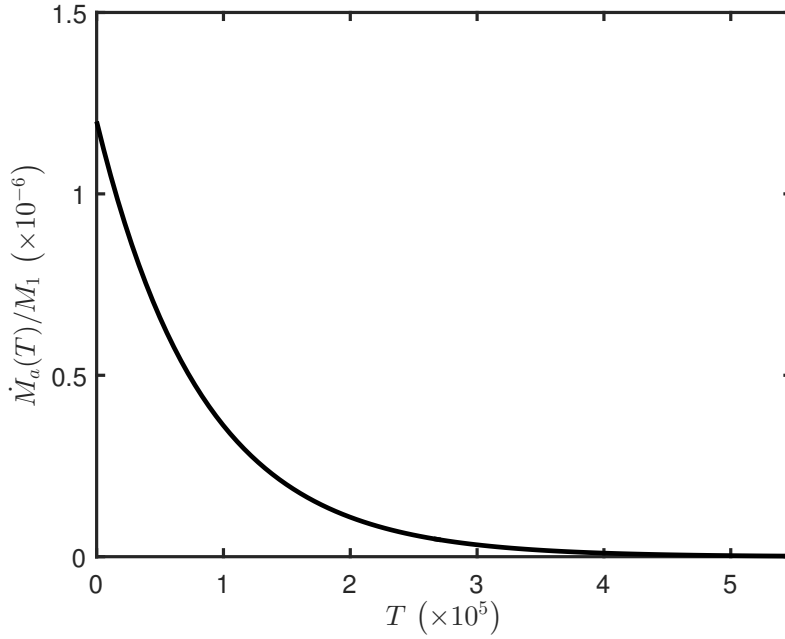


Figure 5.7: Geodetic moment rate associated with afterslip on the fault ($\alpha = 0.2, \epsilon = 0.7, \lambda = 10^5, \xi = 1$).

From Eq. (5.16), the forces acting on the asperity and on the weak region during afterslip are, respectively,

$$F_1(T) = -X_2 + \alpha [Y(T) - X_2] \quad (5.69)$$

$$F_2(T) = -\xi Y(T) - \alpha [Y(T) - X_2]. \quad (5.70)$$

They are shown in Fig. (5.8) for a given choice of the parameters $\alpha, \epsilon, \lambda$ and ξ .

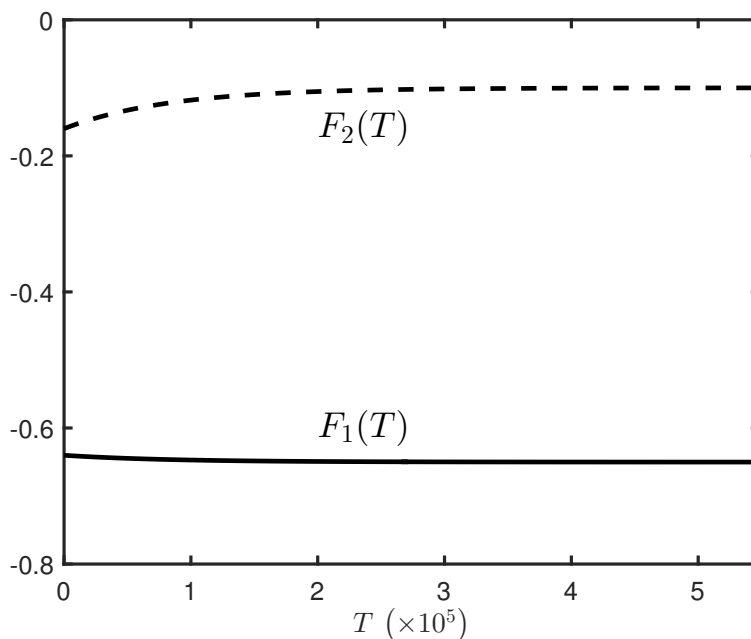


Figure 5.8: Evolution of the tangential forces on the asperity (solid line) and on the weak region (dashed line) during afterslip on the fault ($\alpha = 0.2$, $\epsilon = 0.7$, $\lambda = 10^5$, $\xi = 1$).

At the end of afterslip, the state of the fault is

$$X_3 = X_2, \quad Y_3 = Y_2 - U_a = \bar{Y}. \quad (5.71)$$

If we introduce these values in Eq. (5.69) and Eq. (5.70), we obtain the forces at the end of afterslip ($T = T_3$)

$$F_1(T_3) = -1 + \frac{\alpha + \alpha\xi + \xi}{\alpha + \xi} U_s \quad (5.72)$$

$$F_2(T_3) = -\beta. \quad (5.73)$$

The force F_1 on the asperity has increased (in magnitude) by an amount αU_a with respect to its value (5.53) at the end of the earthquake ($T = T_2$), since afterslip has transferred stress to the asperity. Therefore, the asperity is closer to the failure condition. The amount of stress transferred to the asperity significantly increases with the coupling parameter α ; however, $F_1(T_3) > -1$, which guarantees that afterslip never triggers asperity failure. Nevertheless, the amount of stress that afterslip transfers to the asperity will produce a time advance of the next earthquake. This is illustrated in Fig. (5.9), where $F_1(T_3)$ is shown as a function of α for different values of the parameter ξ . As for the weak region, Eq. (5.73) points out that the condition for steady-state creep has been recovered.

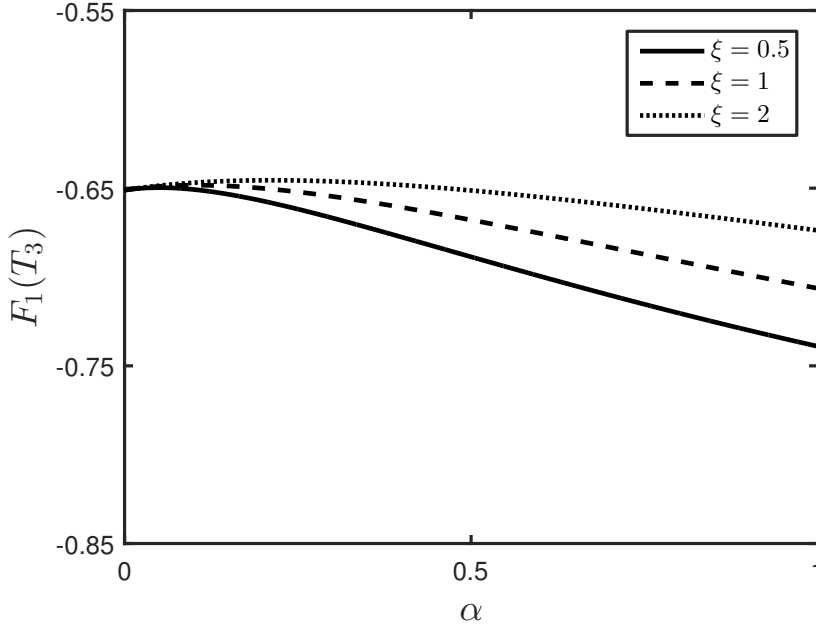


Figure 5.9: Tangential force (5.72) on the asperity at the end of afterslip, as a function of the coupling parameter α for different values of the parameter ξ . Other parameters are $\epsilon = 0.7$ and $\gamma = 1$.

Notice that the state (5.71) at the end of the afterslip mode satisfies the equation of line (5.30). Under the assumption (5.52), the no overshooting condition $Y_3 \geq 0$ is then always satisfied and no additional constraint is required. Hence, in the absence of perturbations due to earthquakes on nearby faults, the orbit of the system describes a cycle made of a sequence of the three dynamic modes. During the interseismic interval, the representative point of the system moves on line (5.30). When it reaches the point P_1 with coordinates (5.39), a seismic event takes place. The point moves by a quantity U_s given by Eq. (5.45), reducing the value of the slip deficit X and reaching the point P_2 with coordinates (5.51). Here afterslip begins and lowers the value of Y by a quantity U_a given by Eq. (5.60), driving the system to the point P_3 with coordinates (5.71). This state belongs again to line (5.30), so that a new interseismic interval begins. This orbit is independent of λ and describes the right-angled triangle $P_1P_2P_3$ shown in Fig. (5.10).

The duration T_{is} of the new interseismic interval can be calculated considering the expression (5.72) of the force acting on the asperity at the end of the afterslip mode, that is, when the system is at point P_3 . In order to reach the unit value

and give rise to a new earthquake, F_1 must increase in magnitude by an amount

$$\Delta F_1 = \frac{\alpha + \alpha\xi + \xi}{\alpha + \xi} U_s. \quad (5.74)$$

This force is accumulated over a time interval

$$T_{is} = \frac{\Delta F_1}{|\dot{F}_1|} \quad (5.75)$$

where \dot{F}_1 is the interseismic rate of increase of F_1 that can be calculated from Eq. (5.33). We obtain

$$T_{is} = \frac{U_s}{V}. \quad (5.76)$$

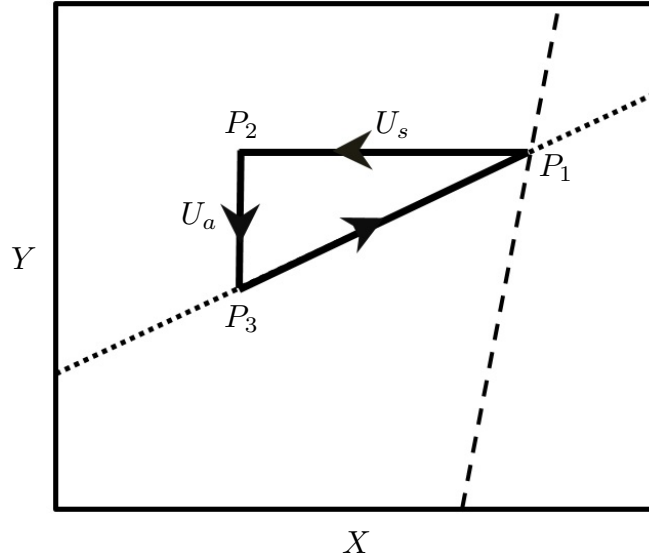


Figure 5.10: Geometrical illustration of the cycle made of interseismic creep, seismic slip and afterslip. The dashed and dotted lines represent the conditions for the failure of the asperity and for the interseismic fault creep, respectively. The state of the fault is P_1 at the beginning of a seismic event, P_2 at the end of the event, P_3 at the end of afterslip. In the triangle $P_1P_2P_3$, the lengths of the catheti are the amplitudes U_s of seismic slip and U_a of afterslip, respectively. From P_3 to P_1 , the fault is subject to tectonic loading and steady-state creep. Arrows indicate the motion of the representative point of the system during the cycle.

In order to enlighten the role of afterslip, the duration of the interseismic interval T'_{is} that would be observed in the absence of afterslip is calculated next. In this case, at the beginning of the interseismic interval, the force on the asperity remains fixed to the value (5.53) reached at the end of seismic event ($T = T_2$). Accordingly,

F_1 must increase in magnitude by an amount

$$\Delta F'_1 = (1 + \alpha) U_s \quad (5.77)$$

for the next earthquake to take place. Thus, we get

$$T'_{is} = \frac{\Delta F'_1}{|\dot{F}_1|} = \frac{(1 + \alpha)(\alpha + \xi)}{\alpha + \alpha\xi + \xi} \frac{U_s}{V}. \quad (5.78)$$

The ratio

$$\frac{T_{is}}{T'_{is}} = 1 - \frac{\alpha^2}{(1 + \alpha)(\alpha + \xi)} \quad (5.79)$$

is always smaller than 1, since α and ξ are defined as positive. Hence, the occurrence of afterslip anticipates the next earthquake produced by the fault.

From Eq. (5.32) and Eq. (5.76), the cumulative creep in the interseismic interval is

$$U_{is} = \Delta \dot{Y} \cdot T_{is} = \frac{\xi}{\alpha + \xi} U_s, \quad (5.80)$$

corresponding to a geodetic moment

$$M_{is} = \xi M_1 \frac{U_{is}}{U} = \frac{\xi^2}{\alpha + \xi} M_s. \quad (5.81)$$

Comparing this result with Eq. (5.48) and Eq. (5.68), we conclude that, in a cycle including the three dynamic modes, the total geodetic moment ($M_a + M_{is}$) is a fraction ξ of the seismic moment M_s and the total moment released is

$$M = (1 + \xi) M_s. \quad (5.82)$$

5.3 Afterslip vs. viscoelastic relaxation

The present model provides a possible means to discriminate between afterslip and viscoelastic relaxation as sources of postseismic deformation.

Let us begin by noticing that, since λ is much larger than $(1 - \alpha/\xi)$, the expression (5.59) for the afterslip amplitude

$$\Delta Y(T) = U_a \left[1 - \left(\cosh \omega_2 T + \frac{\lambda}{2\xi\omega_2} \sinh \omega_2 T \right) e^{-\frac{\lambda}{2\xi} T} \right] \quad (5.83)$$

can be rewritten in a simpler form. Expressing the hyperbolic functions by exponentials, one easily finds

$$\Delta Y(T) \approx U_a (1 - e^{-T/\Theta_a}) \quad (5.84)$$

to a very good approximation, with Θ_a given by Eq. (5.64).

The surface displacement associated with postseismic deformation has been often modelled as

$$s(t) = b \ln\left(1 + \frac{t}{\tau}\right) \quad (5.85)$$

where b is a constant and τ is a characteristic time (Scholz, 1990; Marone et al., 1991; Heki et al., 1997; Barbot et al., 2009). This function becomes arbitrarily large as $t \rightarrow \infty$, even though its derivative tends to zero. In many cases, it fits the postseismic deformation data over finite time intervals reasonably well. On the contrary, Eq. (5.84) entails an afterslip approaching a maximum value U_a in a finite time T_a , with an associated surface displacement

$$s_a(t) = \bar{s}_a(1 - e^{-t/\theta_a}) \quad (5.86)$$

where \bar{s}_a is the asymptotic value and θ_a can be calculated from the observed duration of afterslip t_a as

$$\theta_a = \frac{t_a}{T_a} \cdot \Theta_a \quad (5.87)$$

Let us assume that the lithosphere is a Maxwell body with a characteristic time θ . Accordingly, the surface displacement associated with viscoelastic relaxation can be written as

$$s_v(t) = \bar{s}_v(1 - e^{-t/\theta}) \quad (5.88)$$

where \bar{s}_v is the asymptotic value. Owing to the high value of the lithospheric viscosity, viscoelastic relaxation typically occurs over a timescale much longer than the one associated with afterslip, i.e. $\theta \gg \theta_a$. Thus, if we focus on the time interval $0 \leq t \leq t_a$ during which afterslip is observed, it results $t \ll \theta$ and the displacement $s_v(t)$ can be approximated with its first-order expansion. The total displacement can then be written as

$$s(t) = s_a(1 - e^{-t/\theta_a}) + ct \quad (5.89)$$

with $c = \bar{s}_v/\theta$. The slope of this function decreases much slower than the slope of $s_a(t)$, thus resembling the logarithmic function (5.85).

5.4 Choice of the parameters

I show how to assign appropriate values to the parameters of the system.

The coupling parameter α can be calculated from the area A_2 of the weak region, the rigidity μ of the elastic medium, the velocity v of the tectonic plates, the tangential stress rate $\dot{\sigma}_t$ acting on the fault and the tangential traction (per unit moment) s imposed on one region by a dislocation of the other, calculated as the average value at the centre of the receiving region. With the same considerations as in §4.6, the coupling constants K_1 and K_2 can be evaluated as

$$K_1 = \frac{\dot{\sigma}_t A_1}{v}, \quad K_2 = \frac{\dot{\sigma}_t A_2}{v} \quad (5.90)$$

where the proper expression for $\dot{\sigma}_t$ is provided in Appendix A. In the discrete model, the tangential force imposed on the weak region by the slip of the asperity by an amount u is $K_c u$. The corresponding tangential traction (per unit moment) is

$$s = \frac{K_c u}{\mu A_1 A_2 u} = \frac{K_c}{\mu A_1 A_2} \quad (5.91)$$

from which we obtain

$$K_c = \mu A_1 A_2 s. \quad (5.92)$$

Hence, the coupling parameter α is given by

$$\alpha = \frac{K_c}{K_1} = \frac{\mu A_2 s v}{\dot{\sigma}_t}. \quad (5.93)$$

For nonoverlapping regions satisfying the condition $a \geq 1.5\sqrt{A_1}$, the traction produced by a point-like dislocation source placed at the centre of the asperity is a good approximation for s (Appendix B). Specifically, we have

$$s = \frac{5}{12\pi} a^{-3} \quad (5.94)$$

for strike-slip faulting and

$$s = \frac{1}{6\pi} a^{-3} \quad (5.95)$$

for dip-slip faulting. We conclude that the coupling between the two regions of the fault increases with the area of the weak region, the rigidity of the medium and the velocity of the tectonic plates, whereas it is inversely proportional to the distance between the centres of the two regions and to the tangential stress rate on the fault.

The parameter β is always smaller than 1: in fact, by definition, the steady-state dynamic friction f_0 on the weak region is much smaller than the static friction f_s on the asperity. In applications to real cases, the value of β can be chosen in order that the model gives the best fit with observations.

As already stated in §4.6, γ is chosen in order to obtain the best fit with the observed source function of a given earthquake, while ϵ is inferred from experimental data.

The evaluation of the parameter λ requires the knowledge of the observed durations t_a and t_s of the afterslip and of the seismic event, respectively. In fact, λ can be obtained as the numerical solution of Eq. (5.65) with the substitution

$$T_a = \frac{t_a}{t_s} T_s. \quad (5.96)$$

Finally, the parameter ξ is determined from the areas of the strong and the weak region on the fault, which are in turn inferred from the spatial distribution of coseismic slip and afterslip, respectively. As for the parameter V , it can be calculated by means of Eq. (4.46) from the observed plate velocity v , the duration t_s and the slip amplitude u_s of the seismic event.

5.5 An application: the 2011 Tohoku-Oki earthquake

The 11 March 2011 M_w 9.0 Tohoku-Oki (Japan) earthquake took place as a result of thrust faulting at the Japan trench, where the Pacific plate subducts below the Eurasia plate at a rate $v = 8 \text{ cm a}^{-1}$ (Simons et al., 2011). With a seismic moment $m_s = 3.5 \times 10^{22} \text{ Nm}$ (Maercklin et al., 2012; Bletery et al., 2014), this event will be certainly included as one of the largest earthquakes of the current century. A sketch of the tectonic setting is shown in Fig. (5.11).

The event lasted for about 160 s, with a moment release concentrated in a time interval $t_s = 80 \text{ s}$ (Wei et al., 2012). The coseismic slip distribution suggests a compact area of large slip extending from the trench to about 50 km of depth (Lay et al., 2012), whereas afterslip was mostly observed in an area located downdip of the coseismic slip, reaching a depth of about 100 km (Silverii et al., 2014). Accordingly, it is assumed that the fault is made of a shallower, velocity-weakening region and a deeper, velocity-strengthening region. The two regions are assumed to be rectangles with sides 400 and 150 km long, so that their areas are $A_1 = A_2 = 60,000 \text{ km}^2$, with a distance $a = 150 \text{ km}$ between their centres. An average dip angle $\delta = 20^\circ$ is assumed (Lay et al., 2012). With an

average rigidity $\mu = 40$ GPa (Ozawa et al., 2011), the average seismic slip was $u_s = 15$ m. With a strain rate $\dot{\epsilon} = 10^{-14}$ s $^{-1}$ (Kato et al., 1998) and a Poisson modulus $\nu = 0.25$, the tangential stress rate on the fault is $\dot{\sigma}_t \simeq 3.4 \times 10^{-4}$ Pa s $^{-1}$ (Eq. A.4).

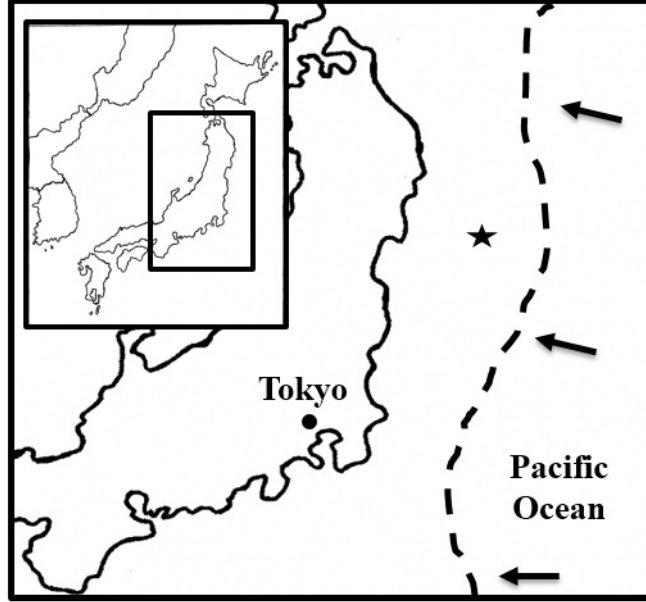


Figure 5.11: Geographic location of the 2011 Tohoku-Oki (Japan) earthquake. The star denotes the epicenter. Black arrows indicate the relative motion of the Pacific plate with respect to the Eurasia plate, whereas the thick dashed line identifies the boundary between the tectonic plates.

With the data listed above, the parameters of the model are calculated. From Eq. (5.93), we get $\alpha \simeq 0.3$. The best fit with the observed source function of the earthquake is obtained with $\gamma = 1.5$. I assume $\epsilon = 0.7$ (e.g. Jaeger and Cook, 1976). The value of λ will be evaluated on the basis of the assumed afterslip duration. Finally, we have $\xi = 1$. Notice that only the seismic slip and afterslip phases associated with the event are investigated here; their evolutions are independent of β (as shown in §5.2.2 and §5.2.3), so that there is no need to assign a value to this parameter.

First, the observed source function is reproduced over the time interval $t_1 \leq t \leq t_2$ where the dominant contribution to seismic moment is generated, with $t_1 = 50$ s and $t_2 = 130$ s. In dimensional form, the moment rate (5.47) becomes

$$\dot{m}_s(t) = m_1 \frac{1 + \alpha}{2\omega_1} \chi \sin \omega_1 \chi (t - t_1) e^{-\frac{\gamma}{2}\chi(t-t_1)} \quad (5.97)$$

where

$$\chi = \frac{T_s}{t_s} \quad (5.98)$$

and

$$m_1 = \mu A_1 u \quad (5.99)$$

where u is the slip of the asperity in the limit case $\gamma = 0$, so that $u = u_s/\kappa_1$. The moment rate (5.97) is shown in Fig. (5.12). It is superimposed to the observed moment rate reported by Montagner et al. (2016) and fits its central peak reasonably well.

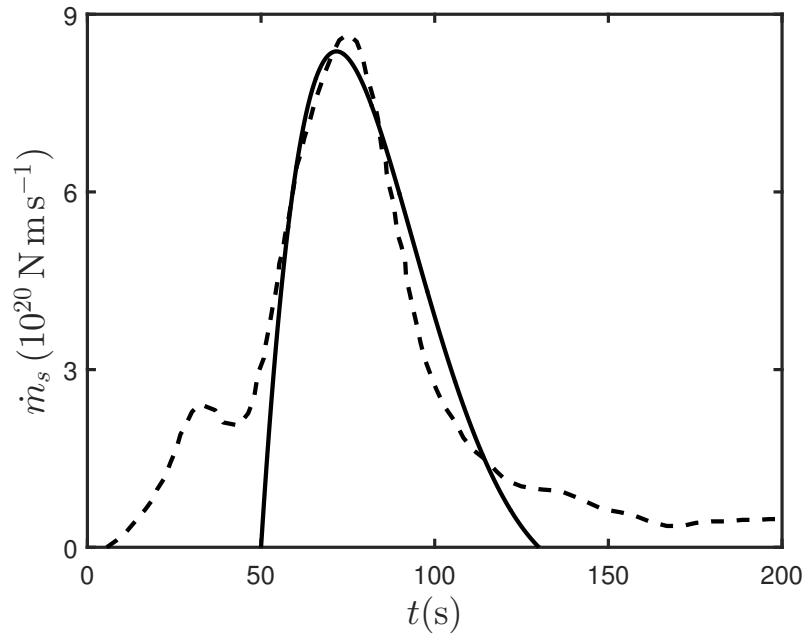


Figure 5.12: Modelled source function (solid line) of the 2011 Tohoku-Oki (Japan) earthquake, compared with the observed source function (dashed line) given by Montagner et al. (2016).

According to the model, the final seismic moment is

$$m_s = \kappa_1 m_1 = 3.6 \times 10^{22} \text{ Nm} \quad (5.100)$$

in agreement with the observations.

Let us now focus on the postseismic evolution of the fault. Equation (5.60) yields an average afterslip amplitude in the weak region equal to $u_a = 0.23 u_s \simeq 3.5$ m. Also, from Eq. (5.68), the geodetic moment associated with afterslip is $m_a = 0.23 m_s \simeq 8.3 \times 10^{21}$ Nm.

Let s_s be the coseismic ground displacement. According to Ozawa et al. (2011), a postseismic displacement $s'_a = 0.09 s_s$ was reached at a time $t'_a = 15$ d after the seismic event. We can ascribe s'_a entirely to afterslip, because viscoelastic relaxation takes place over much longer times: in fact, with a viscosity of the lower crust equal to 10^{19} Pa s (Wang et al., 2012; Sun et al., 2014), the Maxwell relaxation time is $\theta = 8$ a. By means of Eq. (5.86) and taking into account that surface displacement is proportional to fault slip, we find $\theta_a \simeq 30$ d $\ll \theta$, as anticipated.

The surface displacement generated by afterslip is shown in Fig. (5.13) as a function of time. The curve is consistent with data from Diao et al. (2013) and Silverii et al. (2014), according to whom postseismic ground displacement reached the value \bar{s}_a after a time from 120 to 150 d from the event. We conclude that afterslip reached the asymptotic value u_a after a time t_a of about four months. Following the procedure described in §5.4, we find $\lambda \simeq 10^5$.

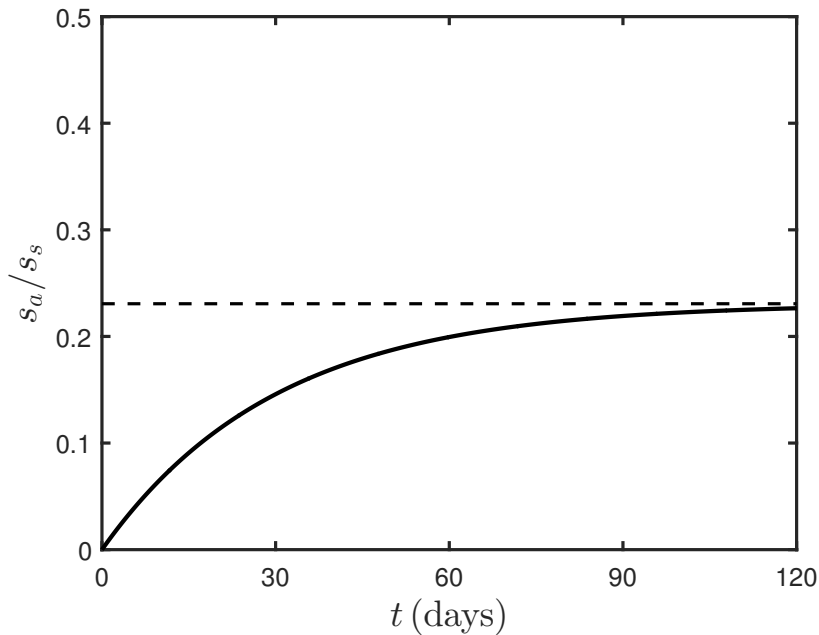


Figure 5.13: Surface displacement generated by afterslip during a time interval of 120 d following the 2011 Tohoku-Oki (Japan) earthquake, according to the model. It is normalized to the coseismic surface displacement s_s .

The ground displacement produced by afterslip has been calculated making use of Okada's (1985) formulae. The graphs of the horizontal and vertical displacement components are shown in Fig. (5.14).

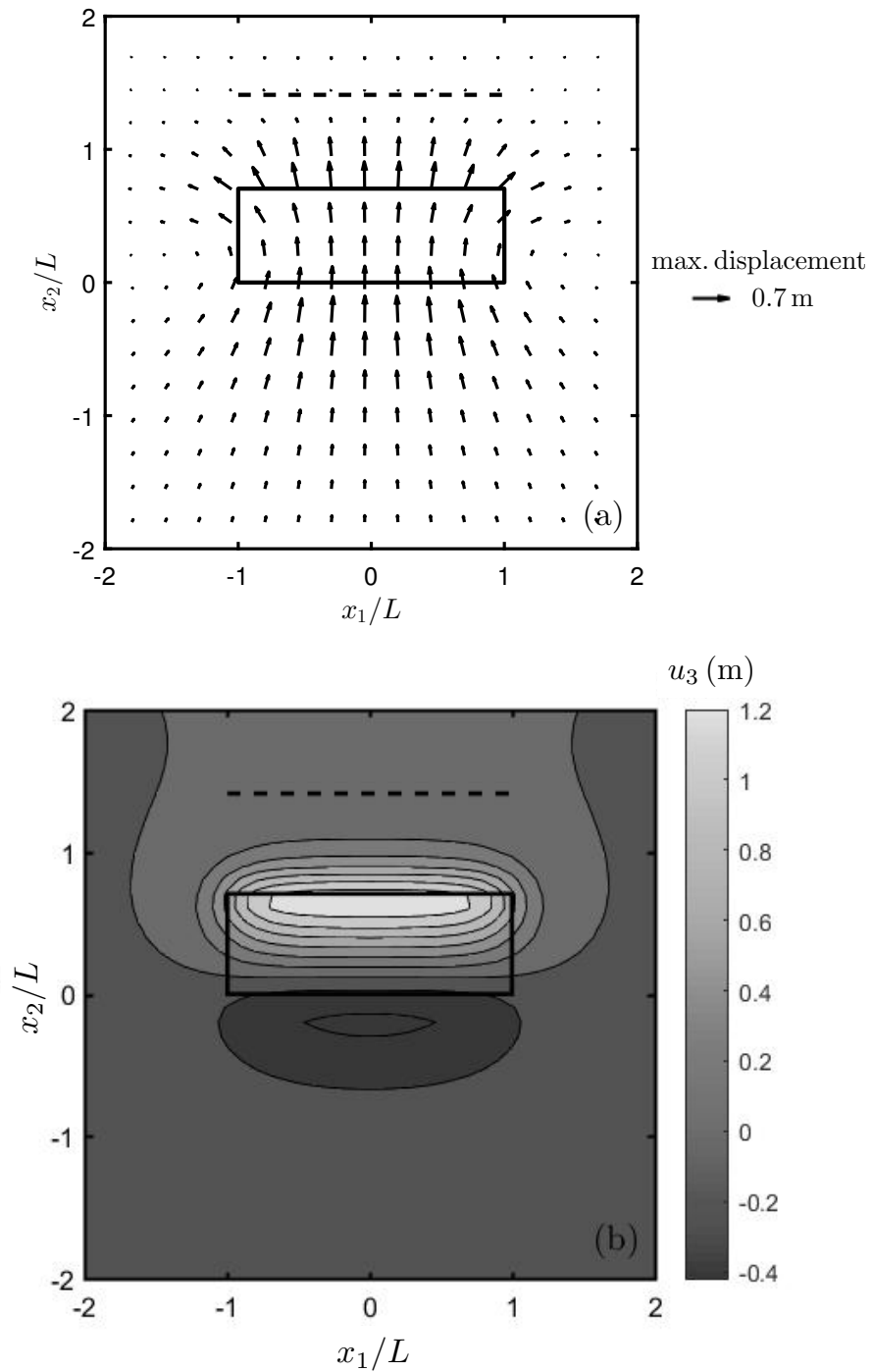


Figure 5.14: Ground displacement produced by afterslip following the 2011 Tohoku-Oki (Japan) earthquake, according to the present model: (a) horizontal component; (b) vertical component u_3 . The rectangle is the projection of the weak fault region on the Earth's surface and the dashed segment is the fault trace. The x_1 and x_2 axes are parallel to the strike direction of the fault and to the direction normal to strike, respectively. Distances are measured in units of the half-side of the fault along the strike direction, namely $L = 200$ km.

The direction and magnitude of the calculated displacement are broadly comparable with displacements obtained from GPS data over a time interval comparable with t_a . For instance, Silverii et al. (2014) reported a maximum horizontal displacement of the order of 1 m at the eastern coasts of the Iwate/Miyagi prefectures of Japan and a maximum vertical displacement of about 20 cm in the same area. These figures are in good agreement with the results shown in Fig. (5.14), where the eastern coasts of the Iwate/Miyagi prefectures approximately correspond with the projection of the lower margin of the weak fault region on the Earth's surface. According to this analysis, the remainder of postseismic deformation should be ascribed to viscoelastic relaxation in the lithosphere.

Chapter 6

A fault with two asperities of different areas and strengths

In this chapter, a discrete model of a fault with two asperities of different areas and strengths is considered, assuming purely elastic coupling between the asperities. This model represents a further development of the models illustrated in §3.3.1.

6.1 The model

The fault model described in §3.4 is adopted and a fault containing two asperities (named asperity 1 and asperity 2) with areas A_1 and A_2 , respectively, is considered (Fig. 6.1). Let a be the distance between the centres of the asperities.

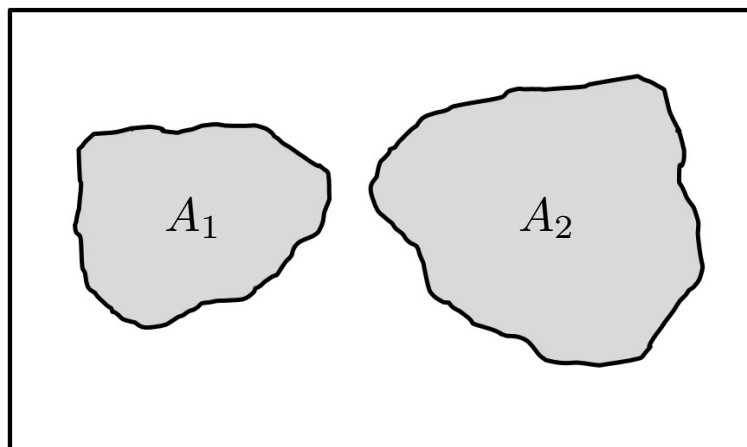


Figure 6.1: Model of a fault with two asperities of different areas, namely A_1 and A_2 . The rectangular frame is the fault border.

The fault is treated as a dynamical system with two state variables, functions of time t : the slip deficits $x(t)$ and $y(t)$ of asperity 1 and 2, respectively. Since the system has two degrees of freedom, the phase-space is a 4-manifold.

The simplest form of rate-dependent friction is assumed, associating the asperities with constant static and dynamic frictions, the latter considered as the average value during slip. Let f_{s1} and f_{d1} be the static and dynamic friction forces on asperity 1, respectively, whereas f_{s2} and f_{d2} are the static and dynamic friction forces on asperity 2, respectively. Letting β be the ratio between the frictional stresses of the asperities, we have

$$\frac{f_{s2}}{f_{s1}} = \frac{f_{d2}}{f_{d1}} = \beta\xi \quad (6.1)$$

where the nondimensional parameter

$$\xi = \frac{A_2}{A_1} \quad (6.2)$$

was introduced. It is assumed that $f_{s1} > f_{s2}$ and $f_{d1} > f_{d2}$, i.e., asperity 1 is stronger than asperity 2. Accordingly, it results $0 < \beta < 1$.

Since the asperities move as rigid surfaces, it is easier to use forces instead of tractions. The tangential forces applied to the asperities in the slip direction are

$$f_1 = -K_1x + K_c(y - x) - \iota_1\dot{x}, \quad f_2 = -K_2y - K_c(y - x) - \iota_2\dot{y}. \quad (6.3)$$

In these expressions, the terms $-K_1x$ and $-K_2y$ represent the effect of tectonic loading, whereas the terms $\pm K_c(y - x)$ are the contributions of stress transfer between the asperities; finally, the terms $-\iota_1\dot{x}$ and $-\iota_2\dot{y}$ are forces due to radiation damping, where ι_1 and ι_2 are impedances. Assuming that the impedance per unit area is the same for both asperities, it results

$$\frac{\iota_2}{\iota_1} = \xi. \quad (6.4)$$

The constants K_1 , K_2 and K_c can be retrieved from the values of A_1 , A_2 , μ , v , the tangential stress rate acting on the fault and the tangential stress transferred from one asperity to the other during a seismic event, as it was shown in §5.4.

During a sticking mode, the slip deficits x and y increase steadily due to tectonic motion. Accordingly, the equations of motion during a sticking mode are

$$\ddot{x} = 0, \quad \ddot{y} = 0 \quad (6.5)$$

where a dot indicates differentiation with respect to t . The slip of asperity 1 occurs when

$$f_1 = -f_{s1}, \quad (6.6)$$

while the slip of asperity 2 takes place when

$$f_2 = -f_{s2}. \quad (6.7)$$

The equations of motion during a slipping mode are

$$\mu_1 \ddot{x} + \iota_1 \dot{x} + (K_1 + K_c) x - K_c y - f_{d1} = 0 \quad (6.8)$$

$$\mu_2 \ddot{y} + \iota_2 \dot{y} + (K_2 + K_c) y - K_c x - f_{d2} = 0 \quad (6.9)$$

where μ_1 and μ_2 are the masses associated with the asperities.

For the sake of simplicity, the analysis is carried out in nondimensional form. I introduce the additional nondimensional parameters

$$\alpha = \frac{K_c}{K_1}, \quad \gamma = \frac{\iota_1}{\sqrt{K_1 \mu_1}} \quad (6.10)$$

$$\epsilon = \frac{f_{d1}}{f_{s1}} = \frac{f_{d2}}{f_{s2}}, \quad V = \frac{\sqrt{K_1 \mu_1}}{f_{s1}} v \quad (6.11)$$

where: α is a measure of the degree of coupling between the asperities; γ is a function of the seismic efficiency of the fault; ϵ is the ratio between dynamic and static frictions on the asperities; V is the nondimensional velocity of tectonic plates. The parameters are subject to the following constraints: $\alpha \geq 0$, $\gamma \geq 0$, $0 < \epsilon < 1$, $V > 0$. Furthermore, it is assumed that the masses associated with the two asperities are proportional to their areas, so that

$$\frac{\mu_2}{\mu_1} = \frac{K_2}{K_1} = \xi. \quad (6.12)$$

I also define the nondimensional slip deficits and time

$$X = \frac{K_1 x}{f_{s1}}, \quad Y = \frac{K_1 y}{f_{s1}}, \quad T = \sqrt{\frac{K_1}{\mu_1}} t. \quad (6.13)$$

Accordingly, the equations of motion (6.5) for the sticking mode can be rewritten as

$$\ddot{X} = 0, \quad \ddot{Y} = 0 \quad (6.14)$$

where a dot now indicates differentiation with respect to T . The equations of motion (6.8)-(6.9) for the slipping mode become

$$\ddot{X} + \gamma \dot{X} + (1 + \alpha)X - \alpha Y - \epsilon = 0 \quad (6.15)$$

$$\ddot{Y} + \gamma\dot{Y} + (1 + \alpha')Y - \alpha'X - \beta\epsilon = 0 \quad (6.16)$$

where the parameter

$$\alpha' = \frac{\alpha}{\xi} \quad (6.17)$$

was introduced.

Finally, I introduce the nondimensional forces

$$F_1 = \frac{f_1}{f_{s1}}, \quad F_2 = \frac{f_2}{f_{s1}}. \quad (6.18)$$

Making use of Eq. (6.3), it results

$$F_1 = -(1 + \alpha)X + \alpha Y - \gamma\dot{X}, \quad F_2 = -(\alpha + \xi)Y + \alpha X - \gamma\xi\dot{Y}. \quad (6.19)$$

To sum up, the system is described by the set of six parameters $\alpha, \beta, \gamma, \epsilon, \xi$ and V . At any instant T in time, the state of the system can be univocally expressed by one of the couples (X, Y) or (F_1, F_2) .

The dynamics of the system can be characterized in terms of four dynamic modes, each one described by a different system of autonomous ODEs: a sticking mode (00), corresponding to stationary asperities, and three slipping modes, associated with the slip of asperity 1 alone (mode 10), the slip of asperity 2 alone (mode 01) and the simultaneous slip of the asperities (mode 11). A seismic event generally consists in n slipping modes and involves one or both the asperities.

6.1.1 The sticking region

The sticking region is defined as the set of states corresponding to a phase of global stick of the system. When both asperities are stationary (mode 00), the rates \dot{X} and \dot{Y} are negligible with respect to their values when the asperities are slipping; thus, the sticking region is a subset \mathbf{Q} of the state space XY . It can be determined as follows.

During a global stick phase, the forces (6.19) reduce to

$$F_1 = -(1 + \alpha)X + \alpha Y, \quad F_2 = -(\alpha + \xi)Y + \alpha X. \quad (6.20)$$

In nondimensional form, the conditions (6.6) and (6.7) for the onset of motion of asperity 1 and 2 become, respectively,

$$F_1 = -1, \quad F_2 = -\beta\xi. \quad (6.21)$$

Combining these conditions with Eq. (6.20), we obtain two lines in the XY plane,

$$Y = \frac{1 + \alpha}{\alpha}X - \frac{1}{\alpha} \quad (6.22)$$

$$Y = \frac{\alpha}{\alpha + \xi}X + \frac{\beta\xi}{\alpha + \xi} \quad (6.23)$$

which I name line 1 and line 2, respectively.

Overshooting during a slipping mode is excluded: accordingly, it is assumed that $X \geq 0$ and $Y \geq 0$. As a consequence, the tangential forces on the asperities must always be in the same direction as the velocity of tectonic plates, i.e. $F_1 \leq 0$ and $F_2 \leq 0$. From Eq. (6.20), the limit cases $F_1 = 0$ and $F_2 = 0$ define two more lines in the XY plane,

$$Y = \frac{1 + \alpha}{\alpha}X \quad (6.24)$$

$$Y = \frac{\alpha}{\alpha + \xi}X, \quad (6.25)$$

which I call line 3 and line 4, respectively.

Let P_a be the intersection of line 1 with line 4 and P_b be the intersection of line 2 with line 3. The coordinates of points P_a and P_b are

$$X_a = \frac{\alpha + \xi}{\alpha + \alpha\xi + \xi}, \quad Y_a = \frac{\alpha}{\alpha + \alpha\xi + \xi} \quad (6.26)$$

$$X_b = \frac{\alpha\beta\xi}{\alpha + \alpha\xi + \xi}, \quad Y_b = \frac{(1 + \alpha)\beta\xi}{\alpha + \alpha\xi + \xi} \quad (6.27)$$

Lines 1 and 2 meet at point P with coordinates

$$X_P = X_a + X_b, \quad Y_P = Y_a + Y_b. \quad (6.28)$$

To sum up, the sticking region \mathbf{Q} of the system is the parallelogram enclosed by the four lines, with vertices at the origin, P_a , P_b and P . It is shown in Fig. (6.2) for a particular choice of the parameters α , β and ξ . Its area is

$$A_{\mathbf{Q}} = \frac{\beta\xi}{\alpha + \alpha\xi + \xi}. \quad (6.29)$$

Accordingly, the subset of state space corresponding to stationary asperities decreases with the degree of coupling between the asperities and with the asymmetry of the system ($\beta \rightarrow 0$). By definition, every orbit of mode 00 is enclosed within \mathbf{Q} and eventually reaches line 1 or line 2, where a seismic event starts. In these cases, the system switches from mode 00 to mode 10 or mode 01, respectively. In the particular case in which the orbit of mode 00 reaches point P , the system passes from mode 00 to mode 11.

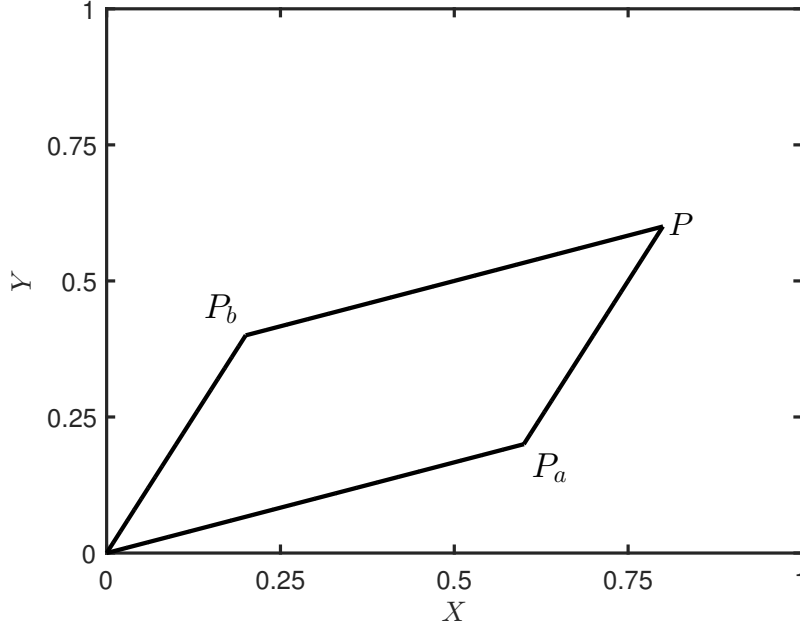


Figure 6.2: The sticking region of the system: a parallelogram \mathbf{Q} ($\alpha = 1, \beta = 0.5, \xi = 2$).

6.2 Solutions of dynamic modes

The solutions to the equations of motion for each of the four dynamic modes of the system are presented. I shall make use of the frequencies ω_0 and ω_1 defined in Eq. (4.14) and Eq. (5.23), respectively, and

$$\omega_2 = \sqrt{1 + \alpha' - \frac{\gamma^2}{4}}, \quad \omega_3 = \sqrt{1 + \alpha + \alpha' - \frac{\gamma^2}{4}}. \quad (6.30)$$

The case of weak damping is considered, i.e. $\gamma \leq 2$ (§4.2).

6.2.1 Stationary asperities (mode 00)

The equations of motion are given in Eq. (6.14). With initial conditions

$$X(0) = \bar{X}, \quad Y(0) = \bar{Y}, \quad \dot{X}(0) = V, \quad \dot{Y}(0) = V \quad (6.31)$$

the solutions are

$$X(T) = \bar{X} + VT, \quad Y(T) = \bar{Y} + VT \quad (6.32)$$

where $T \geq 0$. Equations (6.32) are the parametric equations of the line

$$Y = X + p \quad (6.33)$$

where

$$p = \bar{Y} - \bar{X}. \quad (6.34)$$

This line is the orbit of the system in the sticking region \mathbf{Q} during mode 00.

Let $P_1 = (X_1, Y_1)$ and $P_2 = (X_2, Y_2)$ be the points where the orbit of mode 00 intersects line 1 and line 2, respectively, and let T_1 and T_2 be the corresponding instants in time. The coordinates of P_1 must satisfy the equation (6.22) of line 1: thus, by combination with Eq. (6.32), we get the condition

$$\bar{Y} + VT_1 = \frac{1 + \alpha}{\alpha} (\bar{X} + VT_1) - \frac{1}{\alpha}. \quad (6.35)$$

Accordingly, the slip of asperity 1 will start after a time

$$T_1 = \frac{1 + \alpha p - \bar{X}}{V}. \quad (6.36)$$

Analogously, the coordinates of P_2 must satisfy the equation (6.23) of line 2: exploiting Eq. (6.32) again, we get the condition

$$\bar{Y} + VT_2 = \frac{\alpha}{\alpha + \xi} (\bar{X} + VT_2) + \frac{\beta\xi}{\alpha + \xi}. \quad (6.37)$$

Thus, the slip of asperity 2 will take place at time

$$T_2 = \frac{\beta - \alpha'p - \bar{Y}}{V}. \quad (6.38)$$

6.2.2 Slip of asperity 1 (mode 10)

The equations of motion are

$$\ddot{X} + \gamma\dot{X} + (1 + \alpha)X - \alpha Y - \epsilon = 0 \quad (6.39)$$

$$\ddot{Y} = 0 \quad (6.40)$$

The fault can enter mode 10 from mode 11 or from mode 00.

Case 11 \rightarrow 10

Let us assume that the asperities are both initially in motion and that, at $T = 0$, asperity 2 stops, while asperity 1 continues to slip. Thus, the initial conditions are

$$X(0) = \bar{X}, \quad Y(0) = \bar{Y}, \quad \dot{X}(0) = \bar{V}, \quad \dot{Y}(0) = 0 \quad (6.41)$$

and the solutions are

$$X(T) = \bar{X} - \frac{\bar{U}_1}{2} + \left[\frac{\bar{U}_1}{2} \cos \omega_1 T + \frac{1}{\omega_1} \left(\frac{\gamma}{4} \bar{U}_1 + \bar{V} \right) \sin \omega_1 T \right] e^{-\frac{\gamma}{2} T} \quad (6.42)$$

$$Y(T) = \bar{Y} \quad (6.43)$$

where

$$\bar{U}_1 = 2 \left(\bar{X} - \frac{\alpha \bar{Y} + \epsilon}{1 + \alpha} \right). \quad (6.44)$$

Accordingly, the slip deficit of asperity 1 decreases with time, whereas the slip deficit of asperity 2 remains unchanged. If the orbit does not reach line 2 during the mode, the slip duration can be calculated from the condition $\dot{X}(T) = 0$, yielding

$$T_{1a} = \frac{1}{\omega_1} \left[\pi + \arctan \frac{2\omega_1 \bar{V}}{(1 + \alpha)\bar{U}_1 + \gamma \bar{V}} \right]. \quad (6.45)$$

The final slip amplitude is then

$$U_{1a} = \bar{X} - X(T_{1a}) = \frac{\bar{U}_1}{2} + \sqrt{\frac{\bar{U}_1^2}{4} + \frac{\bar{V}^2}{1 + \alpha} + \frac{\gamma \bar{U}_1 \bar{V}}{2(1 + \alpha)}} e^{-\frac{\gamma}{2} T_{1a}}. \quad (6.46)$$

If instead the orbit reaches line 2 during the mode, the system enters again mode 11. The slip duration is then obtained by solving the equation (6.23) of line 2 for the unknown T .

Case 00 \rightarrow 10

Let us assume that the asperities are both initially stationary and that, at $T = 0$, the condition for the failure of asperity 1 is reached. Accordingly, the initial point of the orbit of mode 10 belongs to line 1 given by Eq. (6.22) and $\bar{V} = 0$; from Eq. (6.44), we have $\bar{U}_1 = U$ defined in Eq. (5.24). The solutions reduce to

$$X(T) = \bar{X} - \frac{U}{2} \left[1 - \left(\cos \omega_1 T + \frac{\gamma}{2\omega_1} \sin \omega_1 T \right) e^{-\frac{\gamma}{2} T} \right] \quad (6.47)$$

$$Y(T) = \bar{Y}. \quad (6.48)$$

If the orbit does not reach line 2 during the mode, the slip duration is

$$T_{1b} = \frac{\pi}{\omega_1} \quad (6.49)$$

and the final slip amplitude is

$$U_{1b} = \kappa_1 U \quad (6.50)$$

with κ_1 defined in Eq. (5.25). If instead the orbit reaches line 2 before time T_{1b} has elapsed, the system passes to mode 11. In this case, the slip duration is again obtained by solving the equation (6.23) of line 2 for the unknown T .

6.2.3 Slip of asperity 2 (mode 01)

The equations of motion are

$$\ddot{X} = 0 \quad (6.51)$$

$$\ddot{Y} + \gamma\dot{Y} + (1 + \alpha')Y - \alpha'X - \beta\epsilon = 0. \quad (6.52)$$

The fault can enter mode 01 from mode 11 or from mode 00.

Case 11 \rightarrow 01

Let us assume that the asperities are both initially in motion and that, at $T = 0$, asperity 1 stops, while asperity 2 continues to slip. Thus, the initial conditions are

$$X(0) = \bar{X}, \quad Y(0) = \bar{Y}, \quad \dot{X}(0) = 0, \quad \dot{Y}(0) = \bar{V} \quad (6.53)$$

and the solutions are

$$X(T) = \bar{X} \quad (6.54)$$

$$Y(T) = \bar{Y} - \frac{\bar{U}_2}{2} + \left[\frac{\bar{U}_2}{2} \cos \omega_2 T + \frac{1}{\omega_2} \left(\frac{\gamma}{4} \bar{U}_2 + \bar{V} \right) \sin \omega_2 T \right] e^{-\frac{\gamma}{2} T} \quad (6.55)$$

where

$$\bar{U}_2 = 2 \left(\bar{Y} - \frac{\alpha' \bar{X} + \beta\epsilon}{1 + \alpha'} \right). \quad (6.56)$$

Accordingly, the slip deficit of asperity 2 decreases with time, whereas the slip deficit of asperity 1 remains unchanged. If the orbit does not reach line 1 during the mode, the slip duration can be calculated from the condition $\dot{Y}(T) = 0$, yielding

$$T_{2a} = \frac{1}{\omega_2} \left[\pi + \arctan \frac{2\omega_2 \bar{V}}{(1 + \alpha') \bar{U}_2 + \gamma \bar{V}} \right]. \quad (6.57)$$

The final slip amplitude is then

$$U_{2a} = \bar{Y} - Y(T_{2a}) = \frac{\bar{U}_2}{2} + \sqrt{\frac{\bar{U}_2^2}{4} + \frac{\bar{V}^2}{1 + \alpha'} + \frac{\gamma \bar{U}_2 \bar{V}}{2(1 + \alpha')}} e^{-\frac{\gamma}{2} T_{2a}}. \quad (6.58)$$

If instead the orbit reaches line 1 during the mode, the system enters again mode 11. The slip duration is then obtained by solving the equation (6.22) of line 1 for the unknown T .

Case 00 \rightarrow 01

Let us assume that the asperities are both initially stationary and that, at $T = 0$, the condition for the failure of asperity 2 is reached. Accordingly, the initial point

of the orbit of mode 01 belongs to line 2 given by Eq. (6.23) and $\bar{V} = 0$; from Eq. (6.56), we have $\bar{U}_2 = \beta U'$, where

$$U' = 2 \frac{1 - \epsilon}{1 + \alpha'}. \quad (6.59)$$

The solutions reduce to

$$X(T) = \bar{X} \quad (6.60)$$

$$Y(T) = \bar{Y} - \frac{\beta U'}{2} \left[1 - \left(\cos \omega_2 T + \frac{\gamma}{2\omega_2} \sin \omega_2 T \right) e^{-\frac{\gamma}{2} T} \right]. \quad (6.61)$$

If the orbit does not reach line 1 during the mode, the slip duration is

$$T_{2b} = \frac{\pi}{\omega_2} \quad (6.62)$$

and the final slip amplitude is

$$U_{2b} = \beta \kappa_2 U' \quad (6.63)$$

where

$$\kappa_2 = \frac{1}{2} \left(1 + e^{-\frac{\pi\gamma}{2\omega_2}} \right). \quad (6.64)$$

If instead the orbit reaches line 1 before time T_{2b} has elapsed, the system passes to mode 11. In this case, the slip duration is again obtained by solving the equation (6.22) of line 1 for the unknown T .

6.2.4 Simultaneous slip of asperities (mode 11)

The equations of motion are

$$\ddot{X} + \gamma \dot{X} + (1 + \alpha)X - \alpha Y - \epsilon = 0 \quad (6.65)$$

$$\ddot{Y} + \gamma \dot{Y} + (1 + \alpha')Y - \alpha' X - \beta \epsilon = 0 \quad (6.66)$$

and the solution is

$$X(T) = \epsilon X_P + (A \sin \omega_0 T + B \cos \omega_0 T + C \sin \omega_3 T + D \cos \omega_3 T) e^{-\frac{\gamma}{2} T} \quad (6.67)$$

$$Y(T) = \epsilon Y_P + (A \sin \omega_0 T + B \cos \omega_0 T - \frac{1}{\xi} C \sin \omega_3 T - \frac{1}{\xi} D \cos \omega_3 T) e^{-\frac{\gamma}{2} T} \quad (6.68)$$

showing that the slip deficits of both asperities decrease with time. The constants A , B , C and D depend on the initial conditions and are listed in Appendix C.

The duration T_{11} of mode 11 must be evaluated numerically: letting T_x and T_y be the smallest positive solutions of the equations $\dot{X}(T) = 0$ and $\dot{Y}(T) = 0$,

respectively, we have $T_{11} = \min(T_x, T_y)$. Notice that T_x and T_y always differ, owing to the asymmetry of the system ($\beta \neq 1$). If $T_x < T_y$, asperity 1 stops the first and the system enters mode 01; if instead $T_y < T_x$, asperity 2 stops the first and the system enters mode 10. In both cases, the final slip amplitudes of the asperities in mode 11 are given by $\bar{X} - X(T_{11})$ and $\bar{Y} - Y(T_{11})$ for asperity 1 and 2, respectively.

6.3 Slip in a seismic event

A seismic event is generally made up of n slipping modes and can involve only one or both asperities. More specifically, it is possible to distinguish three kinds of events, namely (i) events due to the slip of a single asperity, (ii) events associated with the separate (i.e., not simultaneous) slips of both asperities and (iii) events involving the simultaneous slip of asperities. The number and sequence of dynamic modes in a seismic event can be univocally determined from the knowledge of the state of the system at the beginning of the interseismic interval preceding the event. This state is identified by the value of the variable p defined in Eq. (6.34): different subsets of the sticking region of the system can be identified accordingly, as discussed in the following.

Let $P_0 \in \mathbf{Q}$ be the representative point of the system at the beginning of an interseismic interval. The orbit of mode 00 starting at P_0 eventually reaches line 1 or line 2, where an earthquake begins. The kind of seismic event generated by the fault depends on the subset of \mathbf{Q} which P_0 belongs to. Specifically, it depends exclusively on the value of the variable p .

A major subdivision of \mathbf{Q} is determined by the orbit through P , driving the fault from mode 00 to mode 11. This orbit belongs to the line

$$Y = X + p_0 \tag{6.69}$$

with

$$p_0 = Y_P - X_P = \frac{(\beta - 1)\xi}{\alpha + \alpha\xi + \xi} \tag{6.70}$$

where Eq. (6.28) was taken into account. Line (6.69) divides \mathbf{Q} in two subsets producing events starting with mode 10 ($p < p_0$) and mode 01 ($p > p_0$), respectively. In the particular case $p = p_0$, the fault produces a two-mode event 11-01: this is

the largest seismic event predicted by the model.

Next, the subset \mathbf{S} of \mathbf{Q} from which the fault generates events starting with the slip of one asperity followed by the simultaneous motion of both of them is determined. This subset is defined by the values of p belonging to the interval $[p_1, p_2]$, where

$$p_1 = \frac{(\beta - 1)\xi - \alpha\kappa_1 U}{\alpha + \xi + \alpha\xi}, \quad p_2 = \frac{(\beta - 1)\xi + \alpha\beta\xi\kappa_2 U'}{\alpha + \xi + \alpha\xi} \quad (6.71)$$

as shown in Appendix D. Specifically, the lower margin of \mathbf{S} is the line

$$Y = X + p_1 \quad (6.72)$$

causing asperity 1 to trigger the motion of asperity 2 after completing mode 10, whereas the upper margin of \mathbf{S} is the line

$$Y = X + p_2 \quad (6.73)$$

causing asperity 2 to trigger the motion of asperity 1 after completing mode 01. Initial states that are outside \mathbf{S} produce one-mode events 10 or 01, corresponding to $p < p_1$ and $p > p_2$, respectively.

The subset \mathbf{S} is shown in Fig. (6.3) for a particular choice of the parameters of the system. For later use, let \mathbf{S}_1 and \mathbf{S}_2 be the subsets of \mathbf{S} below and above line (6.69), respectively. By definition, seismic events resulting from $p = p_1$ and $p = p_2$ are two-mode events 10-01 and 01-10, respectively. A further discussion of the events generated by these stress distributions is provided in Appendix D.

6.4 Source functions and seismic moment

The number and sequence of slipping modes in a seismic event yield a specific shape of the source function associated with the earthquake. Let us consider a seismic event made up of n slipping modes and call $P_i = (X_i, Y_i)$ the representative point of the system at $T = T_i$, when the system enters the i -th mode ($i = 1, 2, \dots, n$). The duration of the event is then

$$\Delta T = T_{n+1} - T_1. \quad (6.74)$$

Let $X_i(T)$ and $Y_i(T)$ be the slip deficits of asperities 1 and 2 respectively in the i -th mode. The slip functions of the asperities in the i -th mode are then

$$\Delta X_i(T) = X_i - X_i(T - T_i), \quad \Delta Y_i(T) = Y_i - Y_i(T - T_i) \quad (6.75)$$

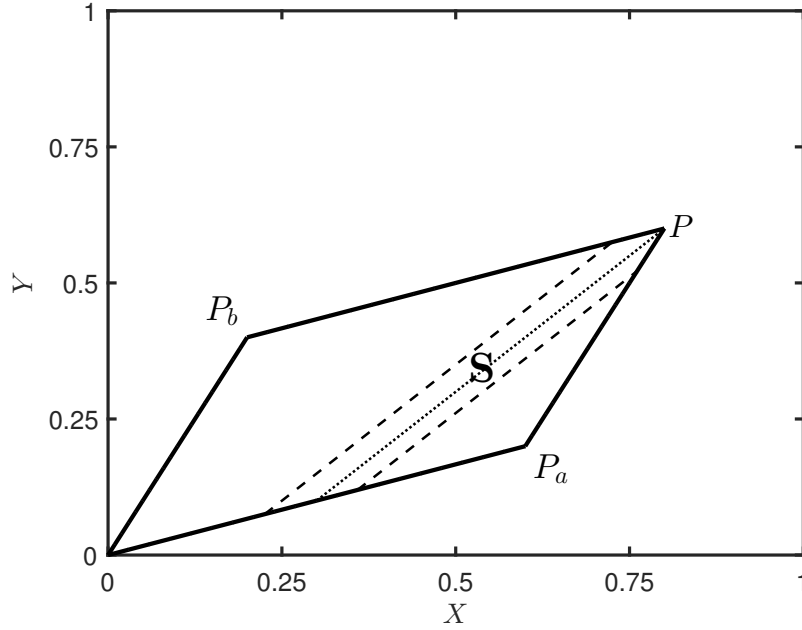


Figure 6.3: The subset \mathbf{S} of the sticking region \mathbf{Q} from which events involving the simultaneous slip of the asperities take place ($\alpha = 1, \beta = 0.5, \gamma = 1, \epsilon = 0.7, \xi = 2$). The dashed lines correspond to $p = p_1$ (right) and $p = p_2$ (left), the dotted line to $p = p_0$.

and the slip rates are

$$\Delta \dot{X}_i(T) = -\dot{X}_i(T - T_i), \quad \Delta \dot{Y}_i(T) = -\dot{Y}_i(T - T_i). \quad (6.76)$$

Of course, the appropriate expressions of $X_i(T)$ and $Y_i(T)$ must be used (§6.2).

Each event corresponds to a seismic moment $m(t)$ or, in nondimensional form,

$$M(T) = \frac{K_1}{f_{s1}^2} m(t). \quad (6.77)$$

As a reference, the seismic moment M_1 that is released in a one-mode event 10 in the limit case $\gamma = 0$ is considered. Accordingly, the moment rate associated with a n -mode event is given by

$$\dot{M}(T) = \frac{M_1}{U} \sum_{i=1}^n (\Delta \dot{X}_i + \Delta \dot{Y}_i) [H(T - T_i) - H(T - T_{i+1})] \quad (6.78)$$

where $H(T)$ is the Heaviside function. Slip rates can be calculated analytically, while the instants T_i are known a priori only for events involving the separate slips of the asperities; in any other case, they must be calculated numerically. The final seismic moment is

$$M_0 = M_1 \frac{U_1 + U_2}{U} \quad (6.79)$$

where

$$U_1 = \sum_{i=1}^n \Delta X_i = X_1 - X_{n+1}, \quad U_2 = \sum_{i=1}^n \Delta Y_i = Y_1 - Y_{n+1} \quad (6.80)$$

are the final slip amplitudes of the asperities.

As an example, events involving the failure of a single asperity or the consecutive, but separate, failures of the asperities are considered: these are the only events predicted by the model for which completely analytical expressions of the source functions and final seismic moment can be obtained.

1) One-mode events. If the earthquake is produced by the failure of asperity 1, Eq. (6.78) yields

$$\dot{M}(T) = M_1 \frac{1 + \alpha}{2\omega_1} \sin \omega_1 T e^{-\frac{\gamma}{2}T} \quad (6.81)$$

with $0 \leq T \leq T_{1b}$. The final seismic moment is

$$M_0 = \kappa_1 M_1. \quad (6.82)$$

If the earthquake is produced by the failure of asperity 2, Eq. (6.78) yields

$$\dot{M}(T) = M_1 \frac{1 + \alpha}{2\omega_2} \beta \sin \omega_2 T e^{-\frac{\gamma}{2}T} \quad (6.83)$$

with $0 \leq T \leq T_{2b}$. The final seismic moment is

$$M_0 = \frac{1 + \alpha}{1 + \alpha'} \beta \kappa_2 M_1. \quad (6.84)$$

The source functions associated with such events are shown in Fig. (6.4) for a particular choice of the parameters of the system.

2) Two-mode events 10-01/01-10. If the sequence of slipping modes is 10-01, the moment rate is

$$\dot{M}(T) = M_1 \frac{1 + \alpha}{2} \begin{cases} \frac{1}{\omega_1} \sin \omega_1 T e^{-\frac{\gamma}{2}T}, & 0 \leq T \leq T_{1b} \\ \frac{\beta}{\omega_2} \sin \omega_2 (T - T_{1b}) e^{-\frac{\gamma}{2}(T - T_{1b})}, & T_{1b} \leq T \leq \Delta T \end{cases} \quad (6.85)$$

where

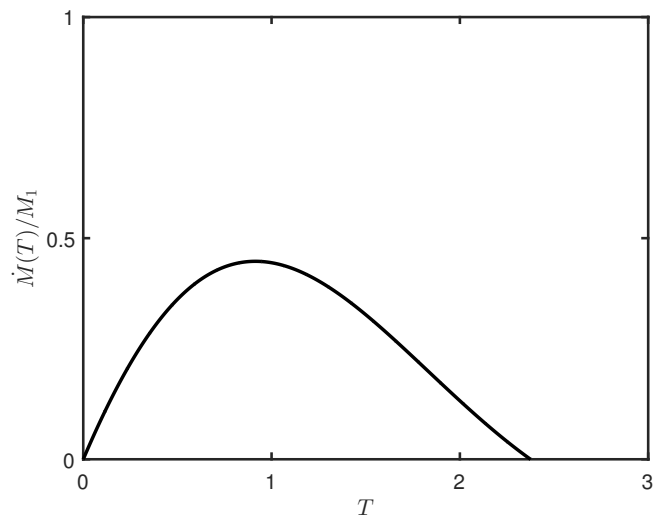
$$\Delta T = T_{1b} + T_{2b}. \quad (6.86)$$

If the sequence is 01-10, the expression is straightforward. In both cases, the final seismic moment is

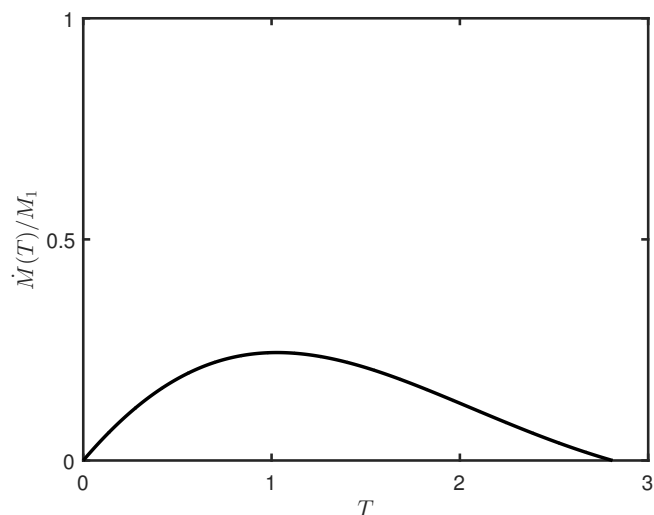
$$M_0 = \left(\kappa_1 + \frac{1 + \alpha}{1 + \alpha'} \beta \kappa_2 \right) M_1. \quad (6.87)$$

The source functions associated with such events are shown in Fig. (6.5) for a particular choice of the parameters of the system.

To sum up, the number and sequence of dynamic modes involved in a seismic event can be determined from the number and the amplitudes of the humps in its source function. In turn, the knowledge of the source function of the seismic event allows to set constraints on the state of the fault that generated it (§6.3). An example will be shown in §6.8 for a real fault.

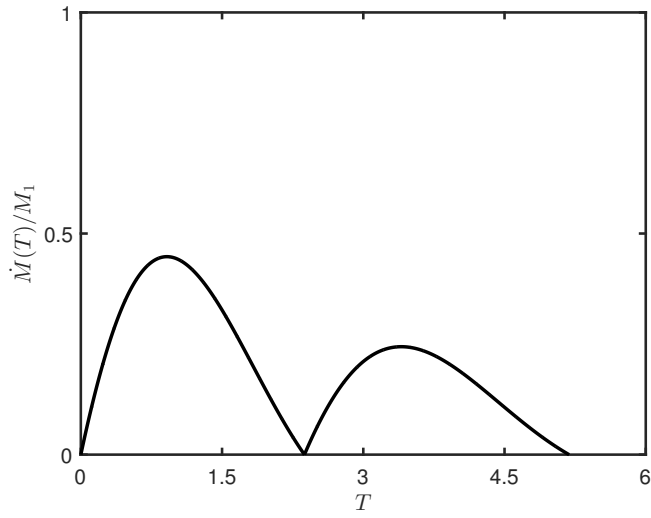


(a) One-mode event 10.

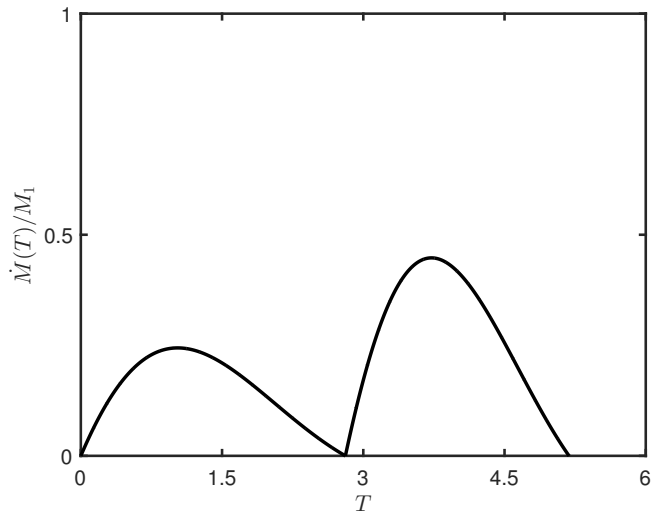


(b) One-mode event 01.

Figure 6.4: Source functions associated with the one-mode events predicted by the model ($\alpha = 1, \beta = 0.5, \gamma = 1, \epsilon = 0.7, \xi = 2$).



(a) Two-mode event 10-01.



(b) Two-mode event 01-10.

Figure 6.5: Source functions associated with two-mode events involving the consecutive slips of the asperities ($\alpha = 1, \beta = 0.5, \gamma = 1, \epsilon = 0.7, \xi = 2$).

6.5 Moment rate spectrum

As in §4.4, the nondimensional moment rate spectrum of a seismic event can be calculated as

$$S(\Omega) = \left| \int_0^{\Delta T} \dot{M}(T) e^{-i\Omega T} dT \right| \quad (6.88)$$

where ΔT is the duration of the event given in Eq. (6.74) and Ω is a nondimensional frequency, defined from the angular frequency ω of the emitted waves as

$$\Omega = \sqrt{\frac{\mu_1}{K_1}} \omega. \quad (6.89)$$

The spectrum can be calculated analytically for one-mode events 10 or 01 and for two-mode events 10-01 or 01-10: for the sake of simplicity, only the spectrum of one-mode events is shown.

1) For a one-mode event 10, $\Delta T = T_{1b}$ and we obtain

$$S(\Omega) = M_1 \frac{1 + \alpha}{2} \sqrt{\frac{1 + 2e^{-\frac{\gamma}{2}T_{1b}} \cos \Omega T_{1b} + e^{-\gamma T_{1b}}}{(1 + \alpha - \Omega^2)^2 + \gamma^2 \Omega^2}}. \quad (6.90)$$

Its value for $\Omega = 0$ is

$$S_0 = M_0 \quad (6.91)$$

where M_0 is given by Eq. (6.82), and its envelope for $\Omega \rightarrow \infty$ is

$$S_\infty(\Omega) = \frac{1 + \alpha}{\Omega^2} M_0. \quad (6.92)$$

The nondimensional corner frequency is

$$\Omega_c = \sqrt{1 + \alpha} \quad (6.93)$$

and its dimensional value is

$$\omega_c = \frac{T_{1b}}{t'} \Omega_c \quad (6.94)$$

where t' is the observed event duration.

2) For a one-mode event 01, $\Delta T = T_{2b}$ and the spectrum is

$$S(\Omega) = M_1 \frac{1 + \alpha}{2} \beta \sqrt{\frac{1 + 2e^{-\frac{\gamma}{2}T_{2b}} \cos \Omega T_{2b} + e^{-\gamma T_{2b}}}{(1 + \alpha' - \Omega^2)^2 + \gamma^2 \Omega^2}} \quad (6.95)$$

Its value for $\Omega = 0$ is

$$S_0 = \frac{1 + \alpha}{1 + \alpha'} \beta \kappa_2 M_1 = M_0 \quad (6.96)$$

where M_0 is given by Eq. (6.84), and its envelope for $\Omega \rightarrow \infty$ is

$$S_\infty(\Omega) = \frac{1 + \alpha'}{\Omega^2} M_0. \quad (6.97)$$

The nondimensional corner frequency is

$$\Omega_c = \sqrt{1 + \alpha'} \quad (6.98)$$

and its dimensional value is

$$\omega_c = \frac{T_{2b}}{t'} \Omega_c. \quad (6.99)$$

6.6 The difference between the asperity areas

In this section, the influence of the difference between the asperity areas on several features of the model is considered. For the sake of the present discussion, it is assumed that the size of asperity 1 remains fixed, whereas asperity 2 can be smaller ($\xi < 1$) or larger ($\xi > 1$).

6.6.1 Forces on the asperities

The evolution of the tangential forces on the asperities during a global stick phase is considered. Combining Eq. (6.20) with Eq. (6.32), the forces F_1 and F_2 during mode 00 are

$$F_1(T) = -\bar{X} + \alpha p - VT, \quad F_2(T) = -\xi\bar{Y} - \alpha p - \xi VT. \quad (6.100)$$

Accordingly, the forces on the asperities do not evolve with the same rate, since

$$\dot{F}_1 = -V, \quad \dot{F}_2 = -\xi V. \quad (6.101)$$

We conclude that $|\dot{F}_2| > |\dot{F}_1|$ if asperity 2 is larger than asperity 1, and vice-versa.

A significant implication of Eq. (6.100) concerns the meaning of the variable p defined in Eq. (6.34). In fact, the difference

$$F_1(T) - F_2(T) = -\bar{X} + \xi\bar{Y} + 2\alpha p + (\xi - 1)VT \quad (6.102)$$

does not remain constant during an interseismic interval, except for the limit case $\xi = 1$, in which we have

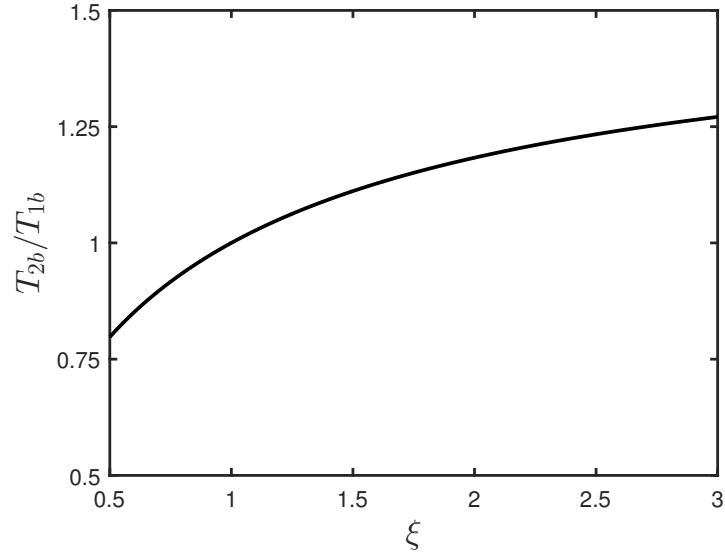
$$F_1 - F_2 = (1 + 2\alpha)p. \quad (6.103)$$

As a result, the variable p no longer describes the stress inhomogeneity on the fault in a univocal way (Dragoni and Santini, 2012). Nevertheless, it still controls which asperity fails the first in a seismic event, as shown in §6.3.

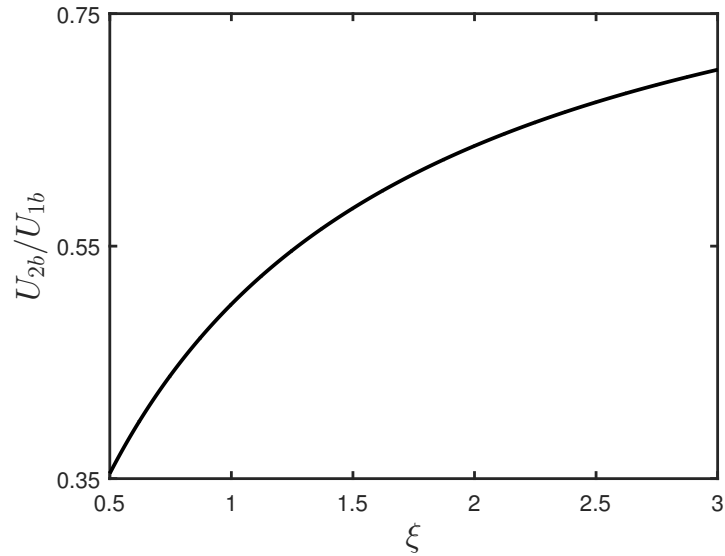
6.6.2 Slip duration and amplitude

The dependence of slip duration and amplitude on the size of the asperities is discussed. The parameter ξ appears in the solutions of dynamic modes involving the slip of asperity 2, as shown in §6.2.3 and §6.2.4. For the sake of simplicity, only one-mode events 01 are considered here. Figure (6.6) shows the slip duration (6.62) and final slip amplitude (6.63) in a one-mode event 01, as functions of ξ .

They are expressed in units of the slip duration (6.49) and final slip amplitude (6.50) associated with a one-mode event 10, respectively.



(a) Slip duration.



(b) Final slip amplitude.

Figure 6.6: Slip duration and final slip amplitude in a one-mode event 01, as functions of ξ ($\alpha = 1, \beta = 0.5, \gamma = 1, \epsilon = 0.7$). They are normalized to the slip duration and final slip amplitude associated with a one-mode event 10, respectively.

As asperity 2 gets larger, its inertia grows as well. Therefore, the slip duration is increased and, in turn, the final slip amplitude increases too. Notice that the slip durations T_{1b} and T_{2b} coincide in the limit case $\xi = 1$ (asperities of equal areas),

whereas $U_{2b} < U_{1b}$ for any value of ξ , since asperity 2 is assumed to be weaker than asperity 1. In turn, the source function of the event is affected by ξ : for larger values of this parameter, the source function reaches a larger maximum value that is delayed in time, as shown in Fig. (6.7).

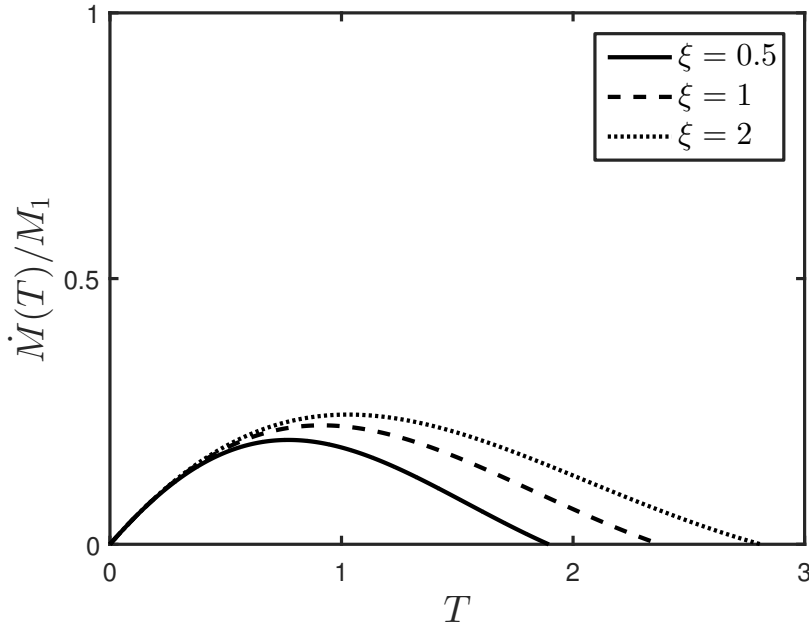


Figure 6.7: Source function of a one-mode event 01 for different values of the parameter ξ ($\alpha = 1, \beta = 0.5, \gamma = 1, \epsilon = 0.7$).

6.6.3 The sticking region and its subsets

I discuss the influence of the parameter ξ on the sticking region \mathbf{Q} . Its area $A_{\mathbf{Q}}$ was given in Eq. (6.29): it is shown in Fig. (6.8) as a function of ξ , in units of the area $A_{\mathbf{Q}}^*$ corresponding to the limit case $\xi = 1$ (asperities of equal areas). The graph clearly shows that the area $A_{\mathbf{Q}}$ is smaller than the area $A_{\mathbf{Q}}^*$ for $\xi < 1$; the opposite holds for $\xi > 1$. As a matter of fact, the overall inertia of the system decreases when $\xi < 1$ and the set of states corresponding to stationary asperities is reduced in turn; the opposite holds when $\xi > 1$.

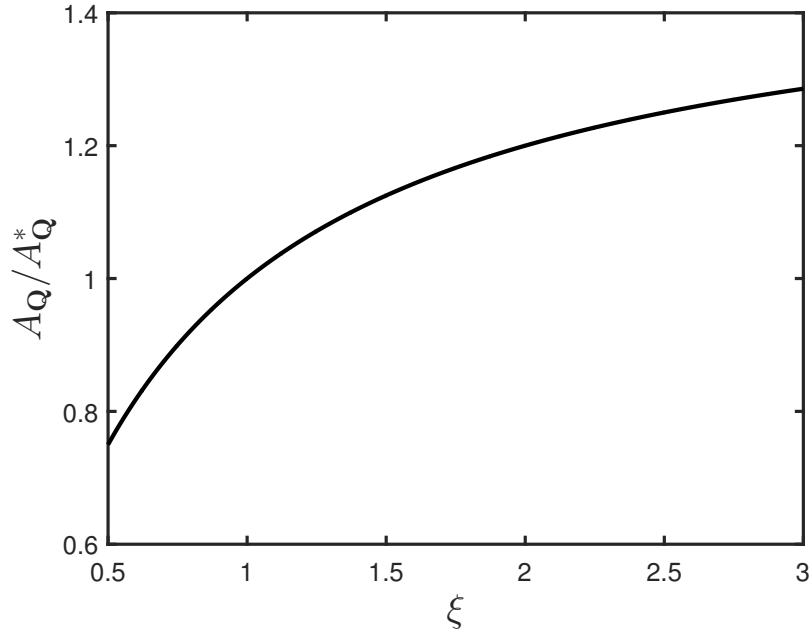
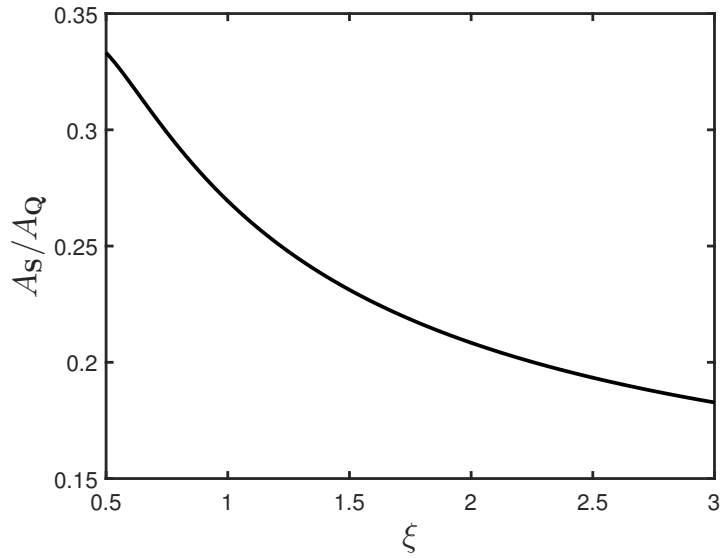
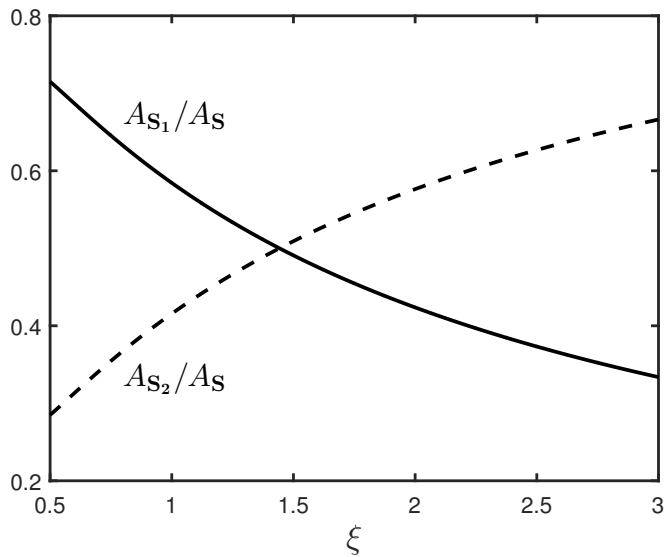


Figure 6.8: The area $A_{\mathbf{Q}}$ of the sticking region \mathbf{Q} , as a function of the parameter ξ ($\alpha = 1, \beta = 0.5$). It is normalized to the area $A_{\mathbf{Q}}^*$ corresponding to $\xi = 1$.

Next, the effect of ξ on events involving the simultaneous slip of the asperities is discussed. Figure (6.9)-(a) shows the area $A_{\mathbf{S}}$ of the subset \mathbf{S} of the sticking region from which events involving mode 11 take place, as a function of ξ . A deeper insight is presented in Figure (6.9)-(b), showing the dependence on ξ of the areas $A_{\mathbf{S}_1}$ and $A_{\mathbf{S}_2}$ of the subsets \mathbf{S}_1 and \mathbf{S}_2 (§6.3). On the whole, as the overall size of the asperities gets larger, the probability that the system gives rise to events involving the simultaneous slip of the asperities is reduced. More specifically, the subset \mathbf{S}_1 decreases with ξ , since the slip of asperity 1 is less likely to trigger the failure of asperity 2 if its size grows. On the contrary, the subset \mathbf{S}_2 increases with ξ , since a larger size entails a larger slip amplitude of asperity 2 and, in turn, a larger stress transfer to asperity 1; as a result, it is easier for the slip of asperity 2 to trigger the failure of asperity 1. Notice that there exists a particular value of ξ in correspondence to which \mathbf{S}_1 and \mathbf{S}_2 are equal to each other. This value must be evaluated numerically and depends on the particular combination of the parameters α, β, γ and ϵ .



(a) Area of \mathbf{S} , normalized to the area of the sticking region \mathbf{Q} .



(b) Areas of subsets \mathbf{S}_1 and \mathbf{S}_2 .

Figure 6.9: The area A_S of the subset \mathbf{S} of the sticking region and the areas A_{S_1} and A_{S_2} of its subsets \mathbf{S}_1 and \mathbf{S}_2 , as functions of the parameter ξ ($\alpha = 1, \beta = 0.5, \gamma = 1, \epsilon = 0.7$).

6.6.4 Radiation of elastic waves

In order to show the influence of the asperity area on the radiation of elastic waves during fault slip, let us first consider the moment rate spectrum (6.95) associated with one-mode events 01. It is shown in Fig. (6.10) for different values of the parameter ξ . As asperity 2 gets larger, the corner frequency (6.98) diminishes, so

that the content of relatively high frequencies is reduced.

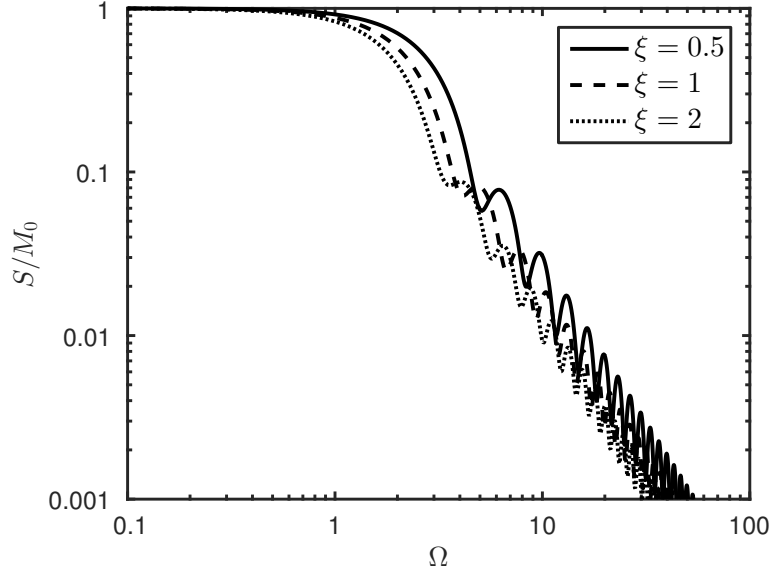


Figure 6.10: Moment rate spectrum of a one-mode event 01 for different values of the parameter ξ ($\alpha = 1, \beta = 0.5, \gamma = 1$).

Next, the seismic efficiency of the fault is discussed. As in §4.5, it is defined as the ratio

$$\eta = \frac{\Delta R}{\Delta W} \quad (6.104)$$

between the nondimensional seismic energy ΔR and the nondimensional total energy change ΔW associated with a seismic event. Let us consider a seismic event made up of n slipping modes starting at time T_i ($i = 1, 2, \dots, n$), when the state of the system is (X_i, Y_i) . The seismic energy released during the event can be calculated as

$$\Delta R = -\gamma \sum_{i=1}^n \int_{T_i}^{T_{i+1}} (\dot{X}_i^2 + \xi \dot{Y}_i^2) dT \quad (6.105)$$

where \dot{X}_i and \dot{Y}_i are the slip rates of the asperities during the event. During a sticking mode, the total energy of the system is

$$W(X, Y) = \frac{1}{2}(X^2 + \xi Y^2) + \frac{1}{2}\alpha(X - Y)^2. \quad (6.106)$$

Accordingly, the total energy change in the seismic event is given by

$$\Delta W = W(X_1 - U_1, Y_1 - U_2) - W(X_1, Y_1) \quad (6.107)$$

where U_1 and U_2 are the final slip amplitudes (6.80) of the asperities.

In the case of a one-mode event 10, we have

$$\dot{Y} = 0, \quad T_1 = 0, \quad T_2 = T_{1b} \quad (6.108)$$

$$U_1 = U_{1b}, \quad U_2 = 0 \quad (6.109)$$

with T_{1b} and U_{1b} given by Eq. (6.49) and Eq. (6.50), respectively. In the case of a one-mode event 01, we have

$$\dot{X} = 0, \quad T_1 = 0, \quad T_2 = T_{2b} \quad (6.110)$$

$$U_1 = 0, \quad U_2 = U_{2b} \quad (6.111)$$

with T_{2b} and U_{2b} given by Eq. (6.62) and Eq. (6.63), respectively. As a result, the seismic efficiency is

$$\eta_1 = \bar{\eta} \frac{1 - e^{-\frac{\gamma T_{1b}}{2}}}{1 - \bar{\eta} e^{-\frac{\gamma T_{1b}}{2}}} \quad (6.112)$$

for a one-mode event 10 and

$$\eta_2 = \bar{\eta} \frac{1 - e^{-\frac{\gamma T_{2b}}{2}}}{1 - \bar{\eta} e^{-\frac{\gamma T_{2b}}{2}}} \quad (6.113)$$

for a one-mode event 01, with $\bar{\eta}$ defined in Eq. (4.43). The ratio η_2/η_1 is shown in Fig. (6.11) as a function of ξ .

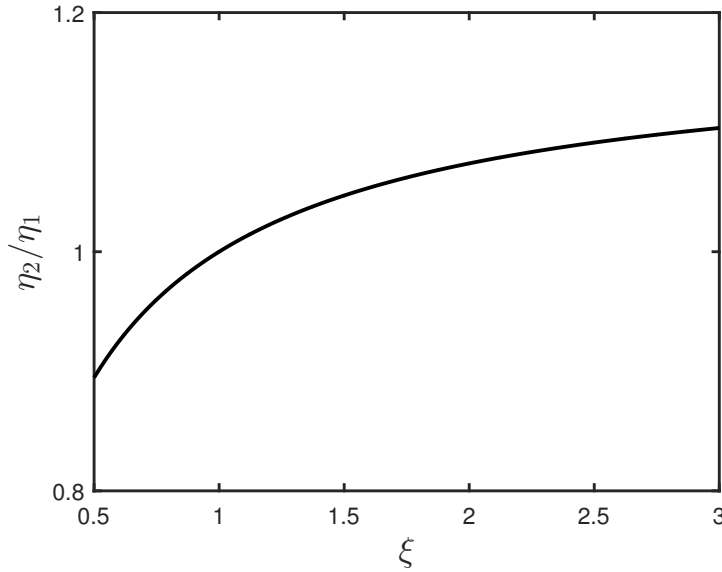


Figure 6.11: Ratio η_2/η_1 between the seismic efficiencies associated with one-mode events 01 and 10, respectively, as a function of the parameter ξ ($\alpha = 1, \gamma = 1, \epsilon = 0.7$).

If asperity 2 is larger than asperity 1, we have $\eta_2 > \eta_1$, and vice-versa. The seismic efficiencies coincide in the limit case $\xi = 1$, since this circumstance yields $T_{1b} = T_{2b}$. As pointed out by Dragoni and Santini (2015), the seismic efficiency does not depend on the relative strength of asperity 2 with respect to asperity 1.

Finally, events associated with the consecutive, but separate, failures of the asperities are considered. In the case of a two-mode event 10-01, we have

$$T_1 = 0, \quad T_2 = T_{1b}, \quad T_3 = T_{1b} + T_{2b} \quad (6.114)$$

$$U_1 = U_{1b}, \quad U_2 = U_{2b} \quad (6.115)$$

and the initial state is given by (D.1) with $p = p_1$ defined in Eq. (D.3). In the case of a two-mode event 01-10, we have

$$T_1 = 0, \quad T_2 = T_{2b}, \quad T_3 = T_{1b} + T_{2b} \quad (6.116)$$

$$U_1 = U_{1b}, \quad U_2 = U_{2b} \quad (6.117)$$

and the initial state is given by (D.4) with $p = p_2$ defined in Eq. (D.6). The seismic efficiency is the same for the two events. Its analytical expression is too complicated to be reported here: I only show its dependence on ξ in Fig. (6.12).

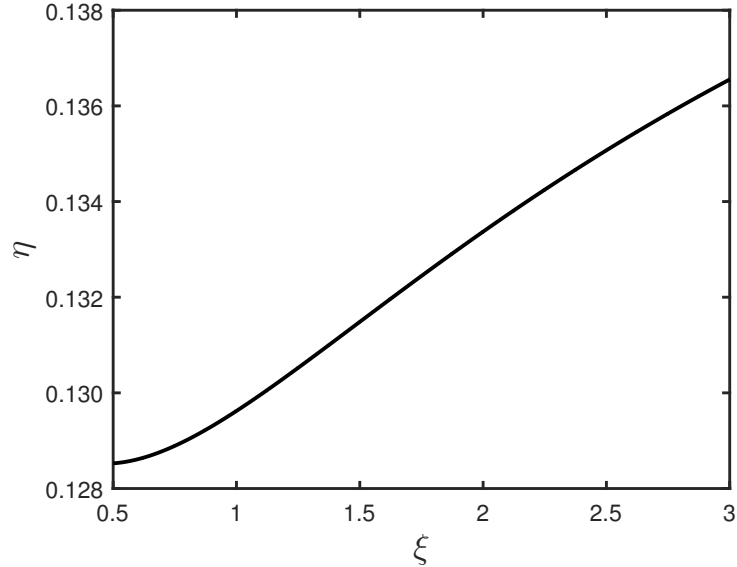


Figure 6.12: Seismic efficiency associated with two-mode events 10-01 and 01-10, as a function of the parameter ξ ($\alpha = 1, \beta = 0.5, \gamma = 1, \epsilon = 0.7$).

The graph points out that the seismic efficiency associated with events due to the consecutive, but separate, failures of the asperities increases with the overall size of the asperities.

It is noteworthy to point out that the seismic efficiency η shown in Fig. (6.12) has two horizontal asymptotes, whose existence can be verified numerically:

$$\lim_{\xi \rightarrow 0} \eta = \eta_1, \quad \lim_{\xi \rightarrow \infty} \eta = \eta_2 \quad (6.118)$$

with η_1 and η_2 given by Eq. (6.112) and Eq. (6.113), respectively.

6.7 Choice of the parameters

With the same consideration as in §5.4, the coupling parameter α can be calculated as

$$\alpha = \frac{\mu A_2 s v}{\dot{\sigma}_t} \quad (6.119)$$

where s is the tangential traction (per unit moment) imposed on an asperity by the slip of the other and $\dot{\sigma}_t$ is the tangential stress rate acting on the fault. The expression of s has been given in Eq. (5.94) and Eq. (5.95) for strike-slip and dip-slip faulting, respectively, while the proper expression for $\dot{\sigma}_t$ is provided in Appendix A.

The parameter β conveying the degree of asymmetry of the system can be estimated from the knowledge of the slip amplitudes u_1 and u_2 of the asperities when they slip separately. In the framework of the elastic rebound model of a fault, these slips are given by

$$u_1 = v \frac{\sigma_{s1} - \sigma_{d1}}{\dot{\sigma}_t}, \quad u_2 = v \frac{\sigma_{s2} - \sigma_{d2}}{\dot{\sigma}_t} \quad (6.120)$$

where the difference $\sigma_{si} - \sigma_{di}$ is the stress drop associated with the failure of the i -th asperity. Accordingly, we have

$$\frac{u_2}{u_1} = \frac{\sigma_{s2} - \sigma_{d2}}{\sigma_{s1} - \sigma_{d1}} = \frac{\sigma_{s2}}{\sigma_{s1} - \sigma_{d1}} - \frac{\sigma_{d2}}{\sigma_{s1} - \sigma_{d1}} = \frac{\beta}{1 - \epsilon} - \frac{\epsilon\beta}{1 - \epsilon} = \beta \quad (6.121)$$

where the definition of the parameter ϵ given in Eq. (6.11) was taken into account. As for the parameters γ and ϵ , the same considerations discussed in §4.6 hold.

6.8 An application: the 2007 Pisco, Peru, earthquake

The M_w 8.0 Pisco (Peru) earthquake of 15 August 2007 occurred as the result of thrust faulting at the interface between the Nazca and South American plates, with a seismic moment estimated between 1.8 and 2×10^{21} Nm (Lay et al., 2010). A sketch of the tectonic setting is shown in Fig. (6.13).

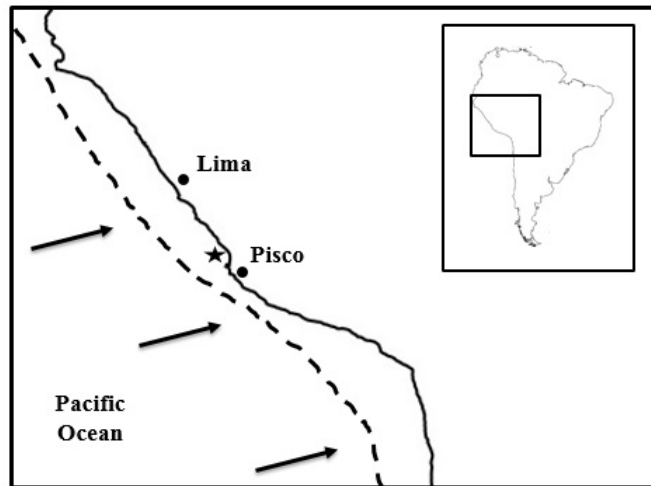


Figure 6.13: Geographic location of the 2007 Pisco, Peru, earthquake. The star denotes the epicenter. Black arrows indicate the relative motion of the Nazca plate with respect to the South American plate, whereas the thick dashed line identifies the boundary between the tectonic plates.

The slip distribution inferred from the joint inversion of teleseismic body waves and InSAR data indicates the presence of two distinct asperities (Sladen et al., 2010): a shallower, larger one (asperity 1), where the maximum coseismic slip was attained, and a deeper, smaller one (asperity 2). The earthquake initiated with the slip of asperity 2, followed by the slip of asperity 1 after a brief time interval. The two phases of the earthquake were treated as distinct events by Lay et al. (2010), who estimated seismic moments of 1.2×10^{21} Nm and 3.5×10^{20} Nm for the slip of asperity 1 and 2, respectively. With an average rigidity $\mu = 30$ GPa (Wang and Liu, 2007) and assuming $A_1 = 4200$ km² and $A_2 = 2400$ km² for the area of asperity 1 and 2, respectively, we obtain average slips $u_1 = 9.5$ m and $u_2 = 4.8$ m for asperity 1 and 2, respectively. Finally, we take $v = 6$ cm a⁻¹ (Sladen et al., 2010) as the relative velocity of tectonic plates at the Peru trench and assume that the fault is subject to a tangential strain rate $\dot{\epsilon} = 10^{-15}$ s⁻¹.

With the data listed above, we evaluate the parameters of the model. From Eq. (6.119) and Eq. (6.121), we obtain $\alpha = 0.2$ and $\beta = 0.5$. We take $\gamma = 1.3$, a value yielding the best fit with the observed source function of the earthquake and corresponding to a seismic efficiency $\eta \simeq 0.16$, and assume $\epsilon = 0.7$ (e.g. Jaeger and Cook, 1976). Finally, the ratio A_2/A_1 yields $\xi = 0.6$.

In terms of the present model, the 2007 earthquake can be described as a two-mode event 01-10 with a finite time interval between the slips of the asperities. Specifically, it is assumed that the slip of asperity 2 takes place over the time interval $t_1 \leq t \leq t_2$, with $t_1 = 0$ s and $t_2 = 38$ s, whereas the slip of asperity 1 takes place over the time interval $t_3 \leq t \leq t_4$, with $t_3 = 60$ s and $t_4 = 105$ s. The action of tectonic loading during the time gap of 22 s that separates the slips of the asperities is excluded, since its effect is negligible over such a short time. Accordingly, the state of the fault at the onset of the earthquake ($t = t_1$) is

$$X_1 = \beta - \frac{\alpha + \xi}{\xi} p_2, \quad Y_1 = \beta - \frac{\alpha}{\xi} p_2 \quad (6.122)$$

where $p_2 \simeq -0.31$ from Eq. (D.6). At the end of mode 01 ($t = t_2$), the state is

$$X_2 = X_1, \quad Y_2 = Y_1 - \beta \kappa_2 U'. \quad (6.123)$$

In accordance with the previous assumptions, this is also the state of the fault at the onset of mode 10 ($t = t_3$). Finally, the state is

$$X_3 = X_2 - \kappa_1 U, \quad Y_3 = Y_2 \quad (6.124)$$

at the end of the event ($t = t_4$). The orbit of the system during the earthquake is shown in Fig. (6.14).

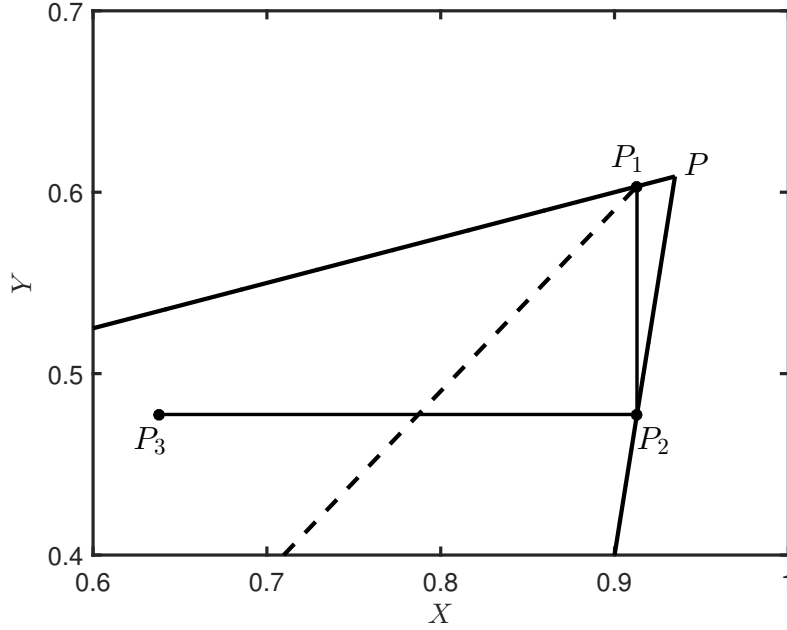


Figure 6.14: Orbit of the Pisco (Peru) fault during the 2007 earthquake. The dashed line corresponds to $p = p_2$. The event starts at point P_1 with the slip of asperity 2; the orbit then reaches line 1 at point P_2 , triggering the slip of asperity 1 up to point P_3 , where the event terminates. For reference, the point P defined in Eq. (6.28) is also shown.

Next, the observed seismic moment rate is reproduced. In dimensional form, the moment rate predicted by the model is

$$\dot{m}(t) = m_1 \frac{1 + \alpha}{2} \begin{cases} \frac{\beta \chi_2}{\omega_2} \sin \omega_2 \chi_2 (t - t_1) e^{-\frac{\gamma}{2} \chi_2 (t - t_1)}, & t_1 \leq t \leq t_2 \\ \frac{\chi_1}{\omega_1} \sin \omega_1 \chi_1 (t - t_3) e^{-\frac{\gamma}{2} \chi_1 (t - t_3)}, & t_3 \leq t \leq t_4 \end{cases} \quad (6.125)$$

where

$$\chi_1 = \frac{T_{1b}}{t_4 - t_3}, \quad \chi_2 = \frac{T_{2b}}{t_2 - t_1} \quad (6.126)$$

and

$$m_1 = \mu A_1 u \quad (6.127)$$

is the seismic moment released by asperity 1 in the limit case $\gamma = 0$: accordingly, we have $u = u_1/\kappa_1$. The modelled moment rate is shown in Fig. (6.15) together with the observed moment rate reported by Sladen et al. (2010). The two main peaks of the source function and its shape are reasonably well fit by the model.

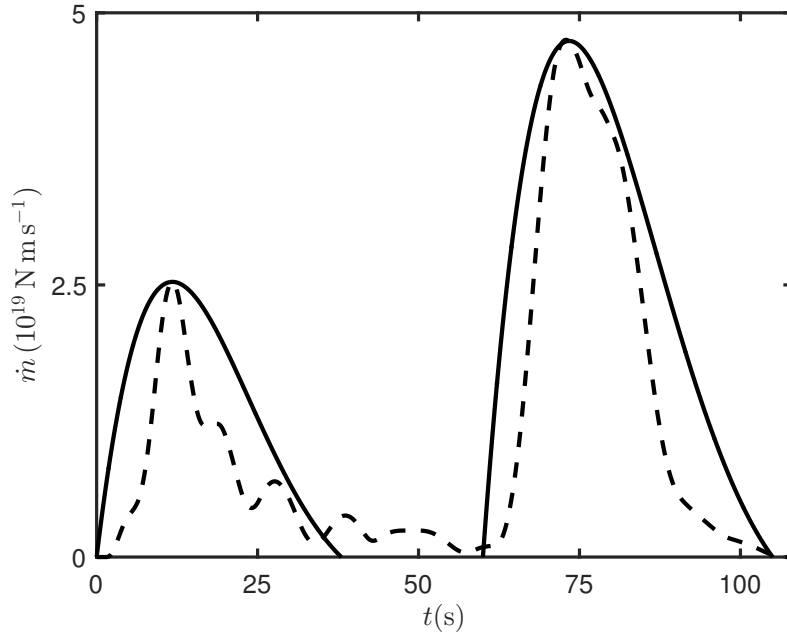


Figure 6.15: Modelled source function (solid line) of the 2007 Pisco (Peru) earthquake, compared with the observed source function (dashed line) reported by Sladen et al. (2010).

According to Eq. (6.87), the final seismic moment provided by the model is

$$m_0 = \left(\kappa_1 + \frac{1 + \alpha}{1 + \alpha'} \beta \kappa_2 \right) m_1 \simeq 1.7 \times 10^{21} \text{ Nm} \quad (6.128)$$

in good agreement with the observations.

Chapter 7

A two-asperity fault in the presence of viscoelastic relaxation

In this chapter, a discrete model of a fault with two asperities is considered and it is assumed that the static stress field produced by earthquakes on the fault undergoes a certain amount of relaxation in the following interseismic interval, as a result of the rheological properties of lithospheric rocks (§2.2). This model has first been studied by Amendola and Dragoni (2013) and then further investigated by Dragoni and Lorenzano (2015).

7.1 The model

The fault model described in §3.4 is adopted and a fault with two asperities of equal areas A and different strengths, named asperity 1 and asperity 2, is considered (Fig. 7.1). Let a be the distance between the centres of the asperities. As for the rheology of lithospheric rocks, a Maxwell viscoelastic behaviour with a characteristic relaxation time θ is assumed. Accordingly, the static stress fields produced by the slip of the asperities undergo a certain amount of relaxation during the subsequent interseismic interval.

The fault is treated as a dynamical system with three state variables, functions of time t : the slip deficits $x(t)$ and $y(t)$ of asperity 1 and 2, respectively, and a variable $z(t)$ representing the variation of the difference between the slip deficits of the asperities, owing to the viscoelastic rheology of lithospheric rocks. Since the system has three degrees of freedom, the phase-space is a 6-manifold. Notice that tectonic loading is assumed to occur under purely elastic rheological conditions:

in fact, viscoelastic coupling between the fault and the tectonic plates would cause the stress imposed to the fault to approach a constant value, thus preventing the occurrence of earthquakes. Accordingly, the characteristic relaxation time associated with tectonic loading is assumed to be much longer than the typical duration of interseismic intervals.

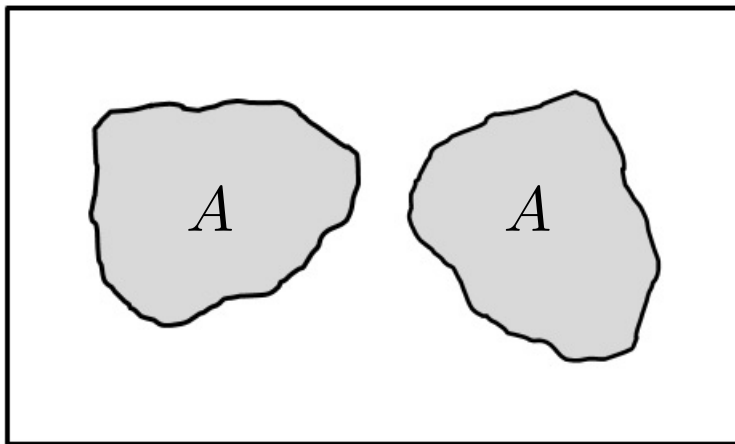


Figure 7.1: Model of a fault with two asperities of equal areas A . The rectangular frame is the fault border.

The simplest form of rate-dependent friction is assumed, associating the asperities with constant static and dynamic frictions, the latter considered as the average values during slip. Let f_{s1} and f_{d1} be the static and dynamic frictions on asperity 1, respectively, whereas f_{s2} and f_{d2} are the static and dynamic frictions on asperity 2, respectively. It is assumed that $f_{s1} > f_{s2}$ and $f_{d1} > f_{d2}$, i.e., asperity 1 is stronger than asperity 2.

Since the asperities move as rigid surfaces, it is easier to use forces instead of tractions. The tangential forces applied to the asperities in the slip direction are

$$f_1 = -Kx + K_c z - \iota \dot{x}, \quad f_2 = -Ky - K_c z - \iota \dot{y}. \quad (7.1)$$

In these expressions, the terms $-Kx$ and $-Ky$ represent the effect of tectonic loading, whereas the terms $\pm K_c z$ are the contributions of stress transfer between the asperities, in the presence of viscoelastic relaxation; finally, the terms $-\iota \dot{x}$ and $-\iota \dot{y}$ are forces due to radiation damping, where ι is an impedance. The constants K and K_c can be retrieved from the values of A, μ, v , the tangential stress rate acting on the fault and the tangential stress transferred from one asperity to the other during a seismic event, as it was shown in §5.4 (bearing in mind that, in

the framework of the present model, $K = K_1 = K_2$).

During a sticking mode, the slip deficits x and y increase steadily due to tectonic motion, while the variable z is governed by the Maxwell constitutive equation (§2.2.1). Accordingly, the equations of motion during a sticking mode are

$$\ddot{x} = 0, \quad \ddot{y} = 0, \quad \ddot{z} = \frac{z}{\theta^2} \quad (7.2)$$

where a dot indicates differentiation with respect to t . The slip of asperity 1 occurs when

$$f_1 = -f_{s1}, \quad (7.3)$$

while the slip of asperity 2 takes place when

$$f_2 = -f_{s2}. \quad (7.4)$$

During a seismic event, viscoelastic relaxation is negligible, since it takes place over times much longer than the duration of seismic slip. Hence, asperity slip can be studied as in the case of purely elastic coupling between the asperities (§6.1), corresponding to $z = y - x$ and $\theta \rightarrow \infty$. Accordingly, the equations of motion for x and y are

$$\mu_1 \ddot{x} + \iota \dot{x} + Kx - K_c z - f_{d1} = 0 \quad (7.5)$$

$$\mu_1 \ddot{y} + \iota \dot{y} + Ky + K_c z - f_{d2} = 0 \quad (7.6)$$

where μ_1 is the mass associated with both asperities, while z changes according to the equation

$$\ddot{z} = \ddot{y} - \ddot{x}. \quad (7.7)$$

For the sake of simplicity, the analysis is carried out in nondimensional form. I introduce the nondimensional parameters

$$\alpha = \frac{K_c}{K}, \quad \beta = \frac{f_{s2}}{f_{s1}} = \frac{f_{d2}}{f_{d1}}, \quad \gamma = \frac{\iota}{\sqrt{K\mu_1}} \quad (7.8)$$

$$\epsilon = \frac{f_{d1}}{f_{s1}} = \frac{f_{d2}}{f_{s2}}, \quad \Theta = \sqrt{\frac{K}{\mu_1}}\theta, \quad V = \frac{\sqrt{K\mu_1}}{f_{s1}}v \quad (7.9)$$

where Θ is the nondimensional Maxwell relaxation time, while the same interpretation as it was given in §6.1 hold for the remaining parameters. These parameters are subject to the constraints $\alpha \geq 0$, $0 < \beta < 1$, $\gamma \geq 0$, $0 < \epsilon < 1$, $\Theta > 0$ and $V > 0$.

I also define the nondimensional slip deficits and time

$$X = \frac{Kx}{f_{s1}}, \quad Y = \frac{Ky}{f_{s1}}, \quad Z = \frac{Kz}{f_{s1}}, \quad T = \sqrt{\frac{K}{\mu_1}}t. \quad (7.10)$$

Accordingly, the equations of motion (7.2) for the sticking mode can be rewritten as

$$\ddot{X} = 0, \quad \ddot{Y} = 0, \quad \ddot{Z} = \frac{Z}{\Theta^2} \quad (7.11)$$

where a dot now indicates differentiation with respect to T , while the equations of motion (7.5)-(7.6)-(7.7) for the slipping mode become

$$\ddot{X} + \gamma\dot{X} + X - \alpha Z - \epsilon = 0 \quad (7.12)$$

$$\ddot{Y} + \gamma\dot{Y} + Y + \alpha Z - \beta\epsilon = 0 \quad (7.13)$$

$$\ddot{Z} = \ddot{Y} - \ddot{X} \quad (7.14)$$

I introduce the nondimensional forces

$$F_1 = \frac{f_1}{f_{s1}} = -X + \alpha Z - \gamma\dot{X}, \quad F_2 = \frac{f_2}{f_{s1}} = -Y - \alpha Z - \gamma\dot{Y} \quad (7.15)$$

which reduce to

$$F_1 = -X + \alpha Z, \quad F_2 = -Y - \alpha Z \quad (7.16)$$

during a global stick phase. To sum up, the system is described by the set of six parameters $\alpha, \beta, \gamma, \epsilon, \Theta$ and V . At any instant T in time, the state of the system can be univocally expressed by the tern (X, Y, Z) or by the couple (F_1, F_2) .

The dynamics of the system can be characterized in terms of four dynamic modes, each one described by a different system of autonomous ODEs: a sticking mode (00), corresponding to stationary asperities, and three slipping modes, associated with the slip of asperity 1 alone (mode 10), the slip of asperity 2 alone (mode 01) and the simultaneous slip of the asperities (mode 11). A seismic event generally consists in n slipping modes and involves one or both the asperities.

7.1.1 The sticking region

The sticking region is defined as the set of states corresponding to a phase of global stick of the system. When both asperities are stationary (mode 00), the rates \dot{X}, \dot{Y} and \dot{Z} are negligible with respect to their values when the asperities

are slipping; thus, the sticking region is a subset of the state space XYZ . It can be determined as follows.

In nondimensional form, the conditions (7.3) and (7.4) for the onset of motion of asperity 1 and 2 become, respectively,

$$F_1 = -1, \quad F_2 = -\beta. \quad (7.17)$$

Combining these conditions with Eq. (7.16), we obtain two planes in the XYZ space,

$$X - \alpha Z - 1 = 0 \quad (7.18)$$

$$Y + \alpha Z - \beta = 0, \quad (7.19)$$

which I name Π_1 and Π_2 , respectively.

Overshooting during asperity slip is excluded: accordingly, it is assumed that $X \geq 0$ and $Y \geq 0$. As a consequence, the tangential forces on the asperities must always be in the same direction as the velocity of tectonic plates, i.e. $F_1 \leq 0$ and $F_2 \leq 0$. From Eq. (7.16), the limit cases $F_1 = 0$ and $F_2 = 0$ define two more planes in the XYZ space,

$$X - \alpha Z = 0 \quad (7.20)$$

$$Y + \alpha Z = 0, \quad (7.21)$$

which I name Γ_1 and Γ_2 , respectively.

To sum up, the sticking region of the system is the subset of the XYZ space enclosed by the planes $X = 0, Y = 0, \Gamma_1, \Gamma_2, \Pi_1$ and Π_2 : a convex hexahedron \mathbf{H} . Its vertices are the origin $(0, 0, 0)$ and the points

$$A = \left(0, 1, -\frac{1}{\alpha}\right), \quad B = \left(\beta, 0, \frac{\beta}{\alpha}\right), \quad C = \left(\beta + 1, 0, \frac{\beta}{\alpha}\right) \quad (7.22)$$

$$D = \left(0, \beta + 1, -\frac{1}{\alpha}\right), \quad E = (1, 0, 0), \quad F = (0, \beta, 0). \quad (7.23)$$

The sticking region is shown in Fig. (7.2) for a particular choice of the parameters α and β . Its volume can be expressed as a function of the parameters of the system as $\beta(\beta + 1)/2\alpha$. Accordingly, the subset of the state space corresponding to stationary asperities decreases with the degree of coupling between the asperities and with the asymmetry of the system ($\beta \rightarrow 0$).

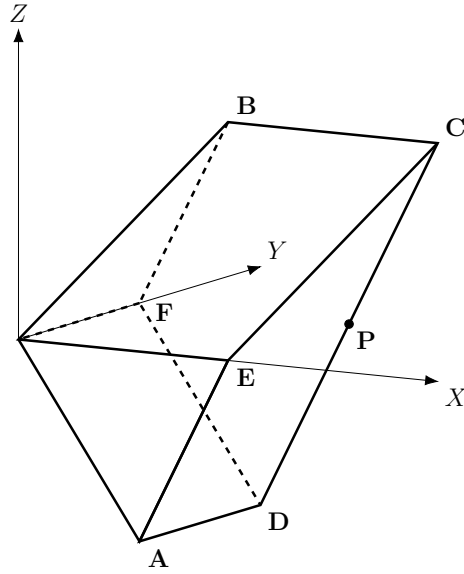


Figure 7.2: The sticking region of the system: a convex hexahedron \mathbf{H} ($\alpha = 1, \beta = 1$). The point P , corresponding to purely elastic coupling between the asperities, is shown. Seismic events take place on the faces $AECD$ and $BCDF$.

By definition, every orbit of mode 00 is enclosed within \mathbf{H} and eventually reaches one of its faces $AECD$ or $BCDF$, belonging to the planes Π_1 and Π_2 , respectively, where a seismic event starts. In these cases, the system switches from mode 00 to mode 10 or mode 01, respectively. In the particular case in which the orbit of mode 00 reaches the edge CD , the system passes from mode 00 to mode 11.

For later use, I introduce a point P with coordinates

$$X_P = \frac{\alpha + \alpha\beta + 1}{1 + 2\alpha}, \quad Y_P = \frac{\alpha + \alpha\beta + \beta}{1 + 2\alpha}, \quad Z_P = -\frac{1 - \beta}{1 + 2\alpha} \quad (7.24)$$

belonging to the edge CD and corresponding to a condition of purely elastic coupling, since $Z_P = Y_P - X_P$.

7.2 Solutions of dynamic modes

The solutions of the equations of motion for each of the four dynamic modes are presented. I shall make use of the frequencies ω_0 and ω_1 defined in Eq. (4.14) and Eq. (5.23), respectively, and

$$\omega_2 = \sqrt{1 + 2\alpha - \frac{\gamma^2}{4}} \quad (7.25)$$

The case of weak damping is considered, i.e. $\gamma \leq 2$ (§4.2).

7.2.1 Stationary asperities (mode 00)

The equations of motion are given in Eq. (7.11). With initial conditions

$$X(0) = \bar{X}, \quad Y(0) = \bar{Y}, \quad Z(0) = \bar{Z} \quad (7.26)$$

$$\dot{X}(0) = V, \quad \dot{Y}(0) = V, \quad \dot{Z}(0) = -\frac{\bar{Z}}{\Theta} \quad (7.27)$$

the solutions are

$$X(T) = \bar{X} + VT, \quad Y(T) = \bar{Y} + VT, \quad Z(T) = \bar{Z}e^{-T/\Theta} \quad (7.28)$$

with $T \geq 0$. The equations (7.28) are the parametric equations of a curve lying on the plane

$$X - Y + \bar{Y} - \bar{X} = 0 \quad (7.29)$$

that is parallel to the Z axis.

The orbit of mode 00 lies inside \mathbf{H} and eventually reaches one of its faces $AECD$ or $BCDF$, belonging to the planes Π_1 and Π_2 , respectively, where a seismic event takes place. Let $P_1 = (X_1, Y_1, Z_1)$ and $P_2 = (X_2, Y_2, Z_2)$ be the points where the orbit of mode 00 intersects the planes Π_1 and Π_2 , respectively, and let T_1 and T_2 be the corresponding instants in time. The coordinates of P_1 must satisfy the equation (7.18) of Π_1 : thus, exploiting Eq. (7.28), we get the condition

$$\bar{X} + VT_1 - \alpha\bar{Z}e^{-T_1/\Theta} - 1 = 0. \quad (7.30)$$

Accordingly, the slip of asperity 1 starts at time

$$T_1 = \Theta W(\gamma_1) + \frac{1 - \bar{X}}{V}, \quad (7.31)$$

where W is the Lambert function with argument

$$\gamma_1 = \frac{\alpha\bar{Z}}{V\Theta} e^{-\frac{1-\bar{X}}{V\Theta}}. \quad (7.32)$$

Analogously, the coordinates of P_2 must satisfy the equation (7.19) of Π_2 : again from Eq. (7.28), we get the condition

$$\bar{Y} + VT_2 + \alpha\bar{Z}e^{-T_2/\Theta} - \beta = 0. \quad (7.33)$$

Thus, the slip of asperity 2 starts at time

$$T_2 = \Theta W(\gamma_2) + \frac{\beta - \bar{Y}}{V}, \quad (7.34)$$

with

$$\gamma_2 = -\frac{\alpha\bar{Z}}{V\Theta} e^{-\frac{\beta-\bar{Y}}{V\Theta}}. \quad (7.35)$$

7.2.2 Slip of asperity 1 (mode 10)

The equations of motion are

$$\ddot{X} + \gamma\dot{X} + X - \alpha Z - \epsilon = 0 \quad (7.36)$$

$$\ddot{Y} = 0 \quad (7.37)$$

$$\ddot{Z} - \gamma\dot{Z} - Z + \alpha X + \epsilon = 0. \quad (7.38)$$

The fault can enter mode 10 from mode 11 or from mode 00.

Case 11 \rightarrow 10

Let us assume that the asperities are both initially in motion and that, at $T = 0$, asperity 2 stops, while asperity 1 continues to slip. Thus, the initial conditions are

$$X(0) = \bar{X}, \quad Y(0) = \bar{Y}, \quad Z(0) = \bar{Z} \quad (7.39)$$

$$\dot{X}(0) = \bar{V}, \quad \dot{Y}(0) = 0, \quad \dot{Z}(0) = -\bar{V}. \quad (7.40)$$

The solutions are

$$X(T) = \bar{X} - \frac{\bar{U}_1}{2} + \left[\frac{\bar{U}_1}{2} \cos \omega_1 T + \frac{1}{\omega_1} \left(\frac{\gamma}{4} \bar{U}_1 + \bar{V} \right) \sin \omega_1 T \right] e^{-\frac{\gamma}{2} T} \quad (7.41)$$

$$Y(T) = \bar{Y} \quad (7.42)$$

$$Z(T) = \bar{Z} + \bar{X} - X(T) \quad (7.43)$$

where

$$\bar{U}_1 = 2 \frac{\bar{X} - \alpha \bar{Z} - \epsilon}{1 + \alpha}. \quad (7.44)$$

Accordingly, the slip deficit of asperity 1 decreases with time, whereas the slip deficit of asperity 2 remains unchanged. If the orbit does not reach the plane Π_2 during the mode, the slip duration can be calculated from the condition $\dot{X}(T) = 0$, yielding

$$T_{1a} = \frac{1}{\omega_1} \left[\pi + \arctan \frac{2\omega_1 \bar{V}}{(1 + \alpha)\bar{U}_1 + \gamma\bar{V}} \right]. \quad (7.45)$$

The final slip amplitude is then

$$U_{1a} = \bar{X} - X(T_{1a}) = \frac{\bar{U}_1}{2} + \sqrt{\frac{\bar{U}_1^2}{4} + \frac{\bar{V}^2}{1 + \alpha} + \frac{\gamma\bar{U}_1\bar{V}}{2(1 + \alpha)}} e^{-\frac{\gamma}{2} T_{1a}}. \quad (7.46)$$

If instead the orbit reaches the plane Π_2 during the mode, the system enters again mode 11. The slip duration is then obtained by solving the equation (7.19) of plane Π_2 for the unknown T .

Case 00 \rightarrow 10

Let us assume that the asperities are both initially stationary and that, at $T = 0$, the condition for the failure of asperity 1 is reached. Accordingly, the initial point of the orbit of mode 10 belongs to plane Π_1 , so that

$$\bar{X} - \alpha\bar{Z} = 1 \quad (7.47)$$

and $\bar{V} = 0$; from Eq. (7.44), we have $\bar{U}_1 = U$ defined in Eq. (5.24). The solutions reduce to

$$X(T) = \bar{X} - \frac{U}{2} \left[1 - \left(\cos \omega_1 T + \frac{\gamma}{2\omega_1} \sin \omega_1 T \right) e^{-\frac{\gamma}{2} T} \right] \quad (7.48)$$

$$Y(T) = \bar{Y} \quad (7.49)$$

$$Z(T) = \bar{Z} + \bar{X} - X(T). \quad (7.50)$$

If the orbit does not reach the plane Π_2 during the mode, the slip duration is

$$T_{1b} = \frac{\pi}{\omega_1}, \quad (7.51)$$

while the final slip amplitude is

$$U_{1b} = \kappa_1 U \quad (7.52)$$

with κ_1 defined in Eq. (5.25). If instead the orbit reaches the plane Π_2 before time T_{1b} has elapsed, the system passes to mode 11. In this case, the slip duration is again obtained by solving the equation (7.19) of plane Π_2 for the unknown T .

7.2.3 Slip of asperity 2 (mode 01)

The equations of motion are

$$\ddot{X} = 0 \quad (7.53)$$

$$\ddot{Y} + \gamma\dot{Y} + Y + \alpha Z - \beta\epsilon = 0 \quad (7.54)$$

$$\ddot{Z} + \gamma\dot{Z} + Z + \alpha Y - \beta\epsilon = 0. \quad (7.55)$$

The fault can enter mode 01 from mode 11 or from mode 00.

Case 11 \rightarrow 01

Let us assume that the asperities are both initially in motion and that, at $T = 0$, asperity 1 stops, while asperity 2 continues to slip. Thus, the initial conditions are

$$X(0) = \bar{X}, \quad Y(0) = \bar{Y}, \quad Z(0) = \bar{Z} \quad (7.56)$$

$$\dot{X}(0) = 0, \quad \dot{Y}(0) = \bar{V}, \quad \dot{Z}(0) = \bar{V}. \quad (7.57)$$

The solutions are

$$X(T) = \bar{X} \quad (7.58)$$

$$Y(T) = \bar{Y} - \frac{\bar{U}_2}{2} + \left[\frac{\bar{U}_2}{2} \cos \omega_1 T + \frac{1}{\omega_1} \left(\frac{\gamma}{4} \bar{U}_2 + \bar{V} \right) \sin \omega_1 T \right] e^{-\frac{\gamma}{2} T} \quad (7.59)$$

$$Z(T) = \bar{Z} - \bar{Y} + Y(T) \quad (7.60)$$

where

$$\bar{U}_2 = 2 \frac{\bar{Y} + \alpha \bar{Z} - \beta \epsilon}{1 + \alpha}. \quad (7.61)$$

Accordingly, the slip deficit of asperity 2 decreases with time, whereas the slip deficit of asperity 1 remains unchanged. If the orbit does not reach the plane Π_1 during the mode, the slip duration can be calculated from the condition $\dot{Y}(T) = 0$, yielding

$$T_{2a} = \frac{1}{\omega_1} \left[\pi + \arctan \frac{2\omega_1 \bar{V}}{(1 + \alpha) \bar{U}_2 + \gamma \bar{V}} \right]. \quad (7.62)$$

The final slip amplitude is then

$$U_{2a} = \bar{Y} - Y(T_{2a}) = \frac{\bar{U}_2}{2} + \sqrt{\frac{\bar{U}_2^2}{4} + \frac{\bar{V}^2}{1 + \alpha} + \frac{\gamma \bar{U}_2 \bar{V}}{2(1 + \alpha)}} e^{-\frac{\gamma}{2} T_{2a}}. \quad (7.63)$$

If instead the orbit reaches the plane Π_1 during the mode, the system enters again mode 11. The slip duration is then obtained by solving the equation (7.18) of plane Π_1 for the unknown T .

Case 00 \rightarrow 01

Let us assume that the asperities are both initially stationary and that, at $T = 0$, the condition for the failure of asperity 2 is reached. Accordingly, the initial point of the orbit of mode 01 belongs to the plane Π_2 , so that

$$\bar{Y} + \alpha \bar{Z} = \beta \quad (7.64)$$

and $\bar{V} = 0$; from Eq. (7.61), we have $\bar{U}_2 = \beta U$. The solutions reduce to

$$X(T) = \bar{X} \quad (7.65)$$

$$Y(T) = \bar{Y} - \frac{\beta U}{2} \left[1 - \left(\cos \omega_1 T + \frac{\gamma}{2\omega_1} \sin \omega_1 T \right) e^{-\frac{\gamma}{2} T} \right] \quad (7.66)$$

$$Z(T) = \bar{Z} - \bar{Y} + Y(T). \quad (7.67)$$

If the orbit does not reach the plane Π_1 during the mode, the slip duration is the same as in Eq. (7.51), while the final slip amplitude is

$$U_{2b} = \beta \kappa_1 U. \quad (7.68)$$

If instead the orbit reaches the plane Π_1 before time T_{1b} has elapsed, the system passes to mode 11. In this case, the slip duration is again obtained by solving the equation (7.18) of plane Π_1 for the unknown T .

7.2.4 Simultaneous slip of asperities (mode 11)

The equations of motion are

$$\ddot{X} + \gamma \dot{X} + X - \alpha Z - \epsilon = 0 \quad (7.69)$$

$$\ddot{Y} + \gamma \dot{Y} + Y + \alpha Z - \beta \epsilon = 0 \quad (7.70)$$

$$\ddot{Z} + \gamma (\dot{Y} - \dot{X}) - X + Y + 2\alpha Z + (1 - \beta)\epsilon = 0 \quad (7.71)$$

and the solutions are

$$X(T) = E_1 + (A \sin \omega_0 T + B \cos \omega_0 T + C \sin \omega_2 T + D \cos \omega_2 T) e^{-\frac{\gamma}{2} T} \quad (7.72)$$

$$Y(T) = E_2 + (A \sin \omega_0 T + B \cos \omega_0 T - C \sin \omega_2 T - D \cos \omega_2 T) e^{-\frac{\gamma}{2} T} \quad (7.73)$$

$$Z(T) = E_3 - 2(C \sin \omega_2 T + D \cos \omega_2 T) e^{-\frac{\gamma}{2} T} \quad (7.74)$$

showing that the slip deficits of both asperities decrease with time. The constants A , B , C , D , E_1 , E_2 and E_3 depend on initial conditions and are listed in Appendix E. As for the slip duration and amplitude, the same considerations as in §6.2.4 hold.

7.3 Slip in a seismic event

A seismic event is generally made up of n slipping modes and can involve only one or both asperities. More specifically, it is possible to distinguish three kinds of events, namely (i) events due to the slip of a single asperity, (ii) events associated with the separate (i.e., not simultaneous) slips of both asperities and (iii) events

involving the simultaneous slip of asperities. In the following, the connection between these three kinds of events with the state of the system at the beginning of the earthquake are first discussed. Afterwards, it is shown how the number and the sequence of slipping modes in a seismic event can be univocally determined from the knowledge of the state of the system at the beginning of the interseismic interval preceding the event, in the absence of stress perturbations.

7.3.1 Dependence on the state at the onset of the event

It was showed that the conditions for the onset of motion for asperity 1 and 2 are reached on the face $AECD$ and $BCDF$ of the sticking region \mathbf{H} , respectively. Here, I discuss the different subsets in which these faces can be divided, according to the number and sequence of dynamic modes involved in a seismic event.

Let us consider an orbit of mode 00 starting at a point P_0 inside \mathbf{H} and reaching one of the faces $AECD$ or $BCDF$ at a point P_1 , where the earthquake begins. With reference to Fig. (7.3), let us first focus on the face $AECD$. If P_1 belongs to the trapezoid \mathbf{Q}_1 , the earthquake will be a one-mode event 10; if P_1 belongs to the segment \mathbf{s}_1 , the earthquake will be a two-mode event 10-01; finally, if P_1 belongs to the trapezoid \mathbf{R}_1 , the earthquake will be a three-mode event 10-11-01 or 10-11-10, where the specific sequence must be evaluated numerically and depends on the particular combination of the parameters α, β, γ and ϵ . The remaining portion of the face would lead to overshooting. Analogous considerations can be made for subsets $\mathbf{Q}_2, \mathbf{s}_2$ and \mathbf{R}_2 on the face $BCDF$. In the particular case in which P_1 belongs to the edge CD , the earthquake will be a two-mode event 11-01: this is the largest seismic event predicted by the model.

The boundaries of the subsets of the faces $AECD$ and $BCDF$ can be identified taking into account the no overshooting conditions and the constraint on the orientation of the tangential forces on the asperities discussed beforehand (§7.1). The details are provided in Appendix F.

By definition, seismic events taking place on the segments \mathbf{s}_1 and \mathbf{s}_2 are two-mode events 10-01 and 01-10, respectively. A further discussion of the events generated on these subsets is reported in Appendix G.

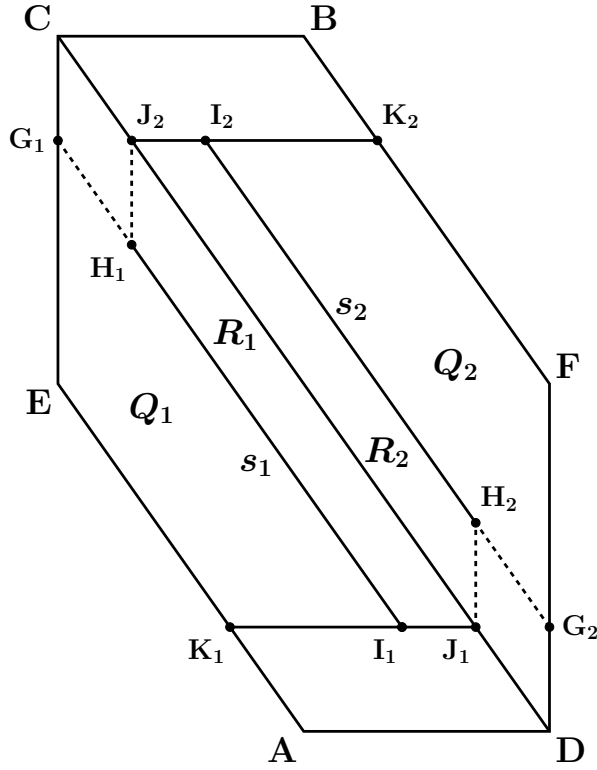


Figure 7.3: The faces $AECD$ and $BCDF$ of the sticking region and their subsets, which determine the number and the sequence of dynamic modes in a seismic event ($\alpha = 1, \beta = 1, \gamma = 1, \epsilon = 0.7$). The events taking place on the face $AECD$ ($BCDF$) start with mode 10 (01).

7.3.2 Dependence on the state at the beginning of the interseismic interval

I now discuss how the location of the initial point P_0 of any orbit of mode 00 affects the number and the sequence of slipping modes in the seismic event.

To begin with, a way to discriminate the first slipping mode involved in the earthquake is devised. Every orbit of mode 00, if prolonged outside the sticking region, intersects both planes Π_1 and Π_2 . The expressions of the times T_1 and T_2 required to the orbit for reaching these planes were provided in Eq. (7.31) and Eq. (7.34), respectively. The condition

$$T_1 - T_2 = 0 \quad (7.75)$$

identifies a transcendental surface Σ in the state space, with equation

$$V\Theta [W(\gamma_1) - W(\gamma_2)] + Y - X + 1 - \beta = 0. \quad (7.76)$$

This surface divides the sticking region \mathbf{H} in two connected, open subsets \mathbf{H}_1 and \mathbf{H}_2 . It is shown in Fig. (7.4) for a particular choice of the parameters α, β, V and Θ . Given any initial state $P_0 \in \mathbf{H}$, the seismic event starts with mode 10 if $P_0 \in \mathbf{H}_1$ or with mode 01 if $P_0 \in \mathbf{H}_2$. By definition, the edge CD belongs to Σ and no orbit of mode 00 can cross it; thus, if $P_0 \in \Sigma$, its orbit remains on Σ and reaches the edge CD , so that the seismic event starts with mode 11. Notice from Eq. (7.76) that the surface Σ does not depend on the parameter γ ; thus, it is not affected by the seismic efficiency of the fault.

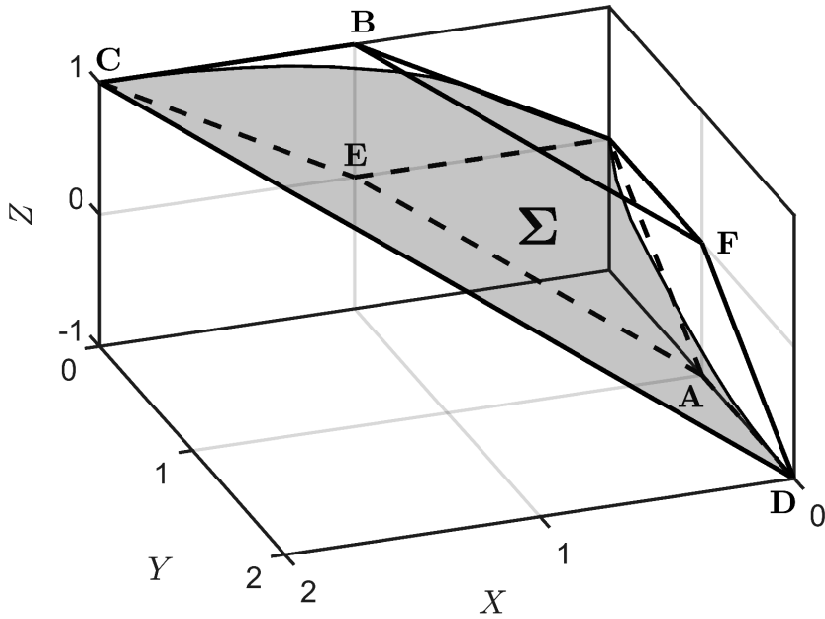


Figure 7.4: The surface Σ dividing the sticking region in the subsets \mathbf{H}_1 (below) and \mathbf{H}_2 (above) that discriminate the first slipping mode in a seismic event ($\alpha = 1, \beta = 1, V\Theta = 1$).

I now describe an additional surface inside each of the subsets \mathbf{H}_1 and \mathbf{H}_2 , allowing to distinguish the number of slipping modes in the seismic event.

Let P_1 be the point where the orbit of mode 00 starting at $P_0 \in \mathbf{H}_1$ reaches the face $AECD$. In order that P_1 belongs to the segment \mathbf{s}_1 , its coordinates must satisfy Eq. (F.13). Introducing the solutions (7.28) of mode 00 in Eq. (F.13) and replacing T with T_1 given in Eq. (7.31), we obtain the equation of a transcendental surface Σ_1

$$X - Y - 2\alpha Z e^{-W(\gamma) - \frac{1-X}{V\Theta}} + \beta - \alpha\kappa_1 U - 1 = 0. \quad (7.77)$$

The surface Σ_1 is shown in Fig. (7.5) for a given choice of the six parameters of

the system. It lies beneath the surface Σ , so that the subset \mathbf{H}_1 is divided into two sections \mathbf{H}_1^- and \mathbf{H}_1^+ , respectively below and above Σ_1 . If $P_0 \in \mathbf{H}_1^-$, then $P_1 \in \mathbf{Q}_1$ and the earthquake will be a one-mode event 10, whereas if $P_0 \in \mathbf{H}_1^+$, then $P_1 \in \mathbf{R}_1$ and the earthquake will be a three-mode event 10-11-10 or 10-11-01, as discussed in §7.3.1. By definition, the segment \mathbf{s}_1 belongs to Σ_1 and no orbit can cross Σ_1 : accordingly, if $P_0 \in \Sigma_1$, its orbit remains on Σ_1 and reaches the segment \mathbf{s}_1 , giving rise to a two-mode event 10-01.

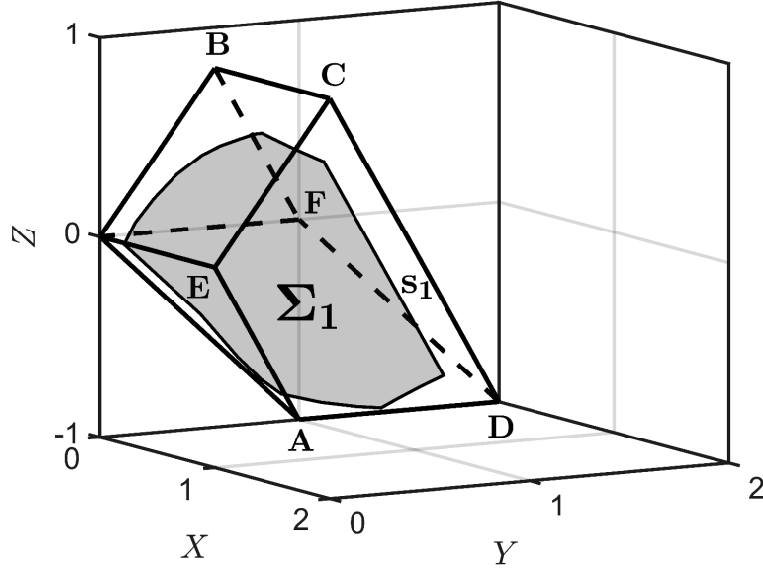


Figure 7.5: The surface Σ_1 in the subset \mathbf{H}_1 of the sticking region, discriminating the number of slipping modes in a seismic event starting when the orbit of the system reaches the face $AECD$ ($\alpha = 1$, $\beta = 1$, $\gamma = 1$, $\epsilon = 0.7$, $V\Theta = 1$).

Let us now repeat the analysis for the subset \mathbf{H}_2 . Let P_2 be the point where the orbit of mode 00 starting at $P_0 \in \mathbf{H}_2$ reaches the face $BCDF$. In order that P_2 belongs to the segment \mathbf{s}_2 , its coordinates must satisfy Eq. (F.28). Introducing the solutions (7.28) of mode 00 in Eq. (F.28) and replacing T with T_2 given in Eq. (7.34), we obtain the equation of a transcendental surface Σ_2

$$X - Y - 2\alpha Z e^{-W(\gamma_2) - \frac{\beta - Y}{V\Theta}} + \beta + \alpha\beta\kappa_1 U - 1 = 0. \quad (7.78)$$

The surface Σ_2 is shown in Fig. (7.6) for a given choice of the six parameters of the system. It lies above the surface Σ , so that the subset \mathbf{H}_2 is divided into two sections \mathbf{H}_2^- and \mathbf{H}_2^+ , respectively below and above Σ_2 . If $P_0 \in \mathbf{H}_2^-$, then $P_2 \in \mathbf{R}_2$ and the earthquake will be a three-mode event 01-11-10 or 01-11-01, whereas if $P_0 \in \mathbf{H}_2^+$, then $P_2 \in \mathbf{Q}_2$ and the earthquake will be a one-mode event

01 (§7.3.1). By definition, the segment s_2 belongs to Σ_2 and no orbit can cross Σ_2 : accordingly, if $P_0 \in \Sigma_2$, its orbit remains on Σ_2 and reaches the segment s_2 , giving rise to a two-mode event 01-10.

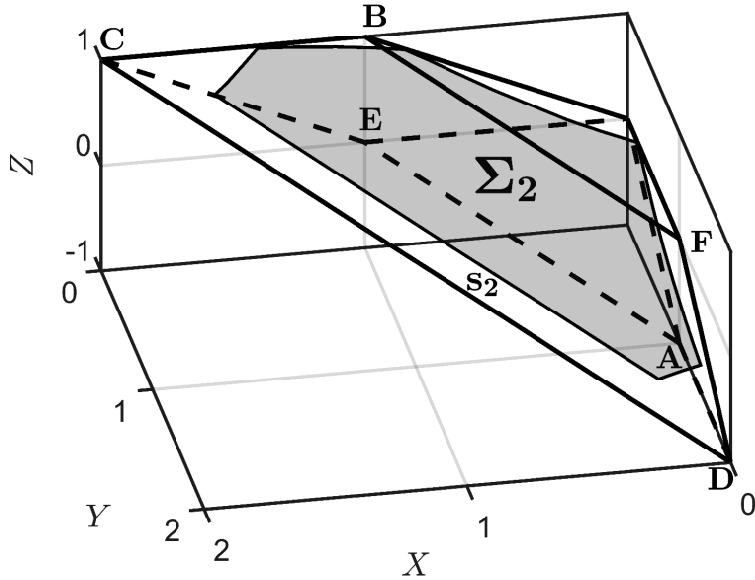
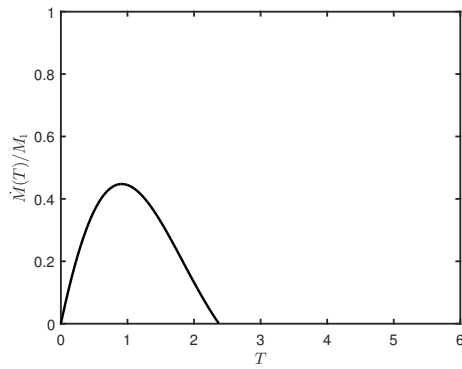


Figure 7.6: The surface Σ_2 in the subset H_2 of the sticking region, discriminating the number of slipping modes in a seismic event starting when the orbit of the system reaches the face $BCDF$ ($\alpha = 1$, $\beta = 1$, $\gamma = 1$, $\epsilon = 0.7$, $V\Theta = 1$).

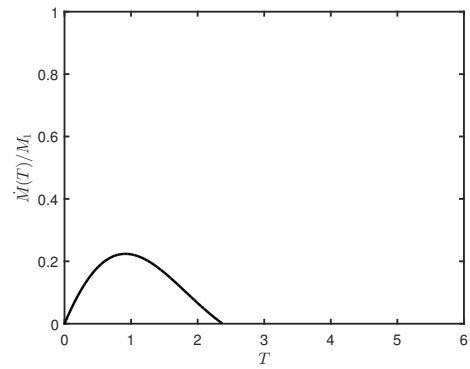
It is clear from their definitions (7.77) and (7.78) that both Σ_1 and Σ_2 depend on κ_1 introduced in Eq. (5.25). Therefore, their position inside the sticking region changes as a function of the seismic efficiency of the fault. For larger values of γ , they are both closer to Σ , so that the subsets H_1^+ and H_2^- are smaller. This feature shows that higher values of γ reduce the possibility of simultaneous slip of the asperities, in agreement with the results obtained by Dragoni and Santini (2015) in the purely elastic case.

7.4 Source functions and seismic moment

The source functions and seismic moment of a seismic event can be determined with the same procedure as it was described in §6.4 for the purely elastic case. Figures (7.7), (7.8) and (7.9) show the source functions associated with the different seismic events predicted by the model for a given choice of the parameters α , β , γ and ϵ .

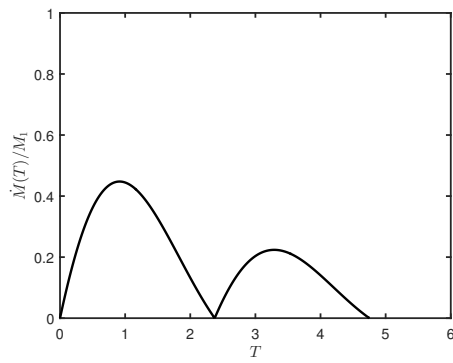


(a) One-mode event 10.

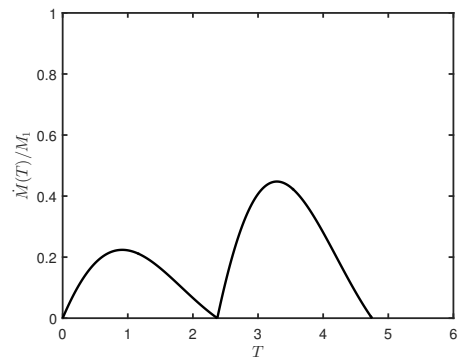


(b) One-mode event 01.

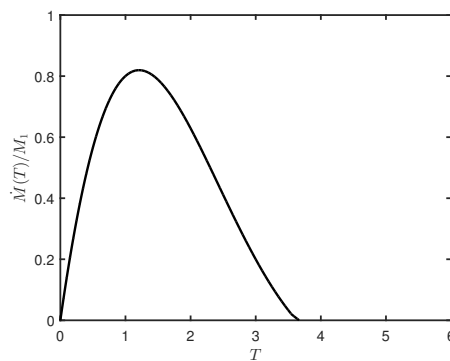
Figure 7.7: Source functions associated with the one-mode events predicted by the model ($\alpha = 1, \beta = 0.5, \gamma = 1, \epsilon = 0.7$).



(a) Two-mode event 10-01.

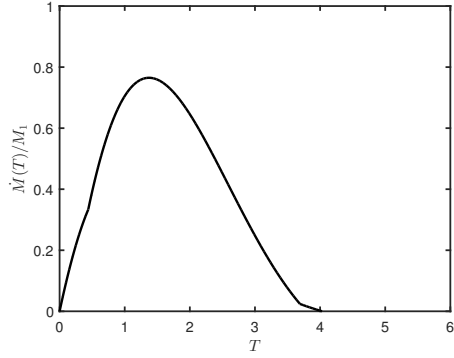


(b) Two-mode event 01-10.

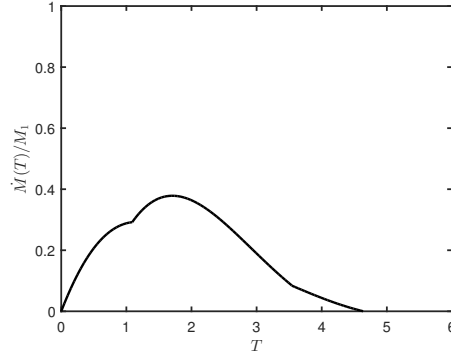


(c) Two-mode event 11-01.

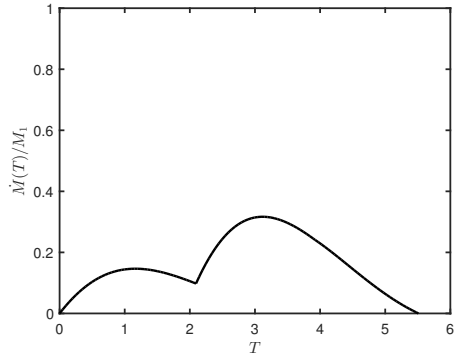
Figure 7.8: Source functions associated with the two-mode events predicted by the model ($\alpha = 1, \beta = 0.5, \gamma = 1, \epsilon = 0.7$).



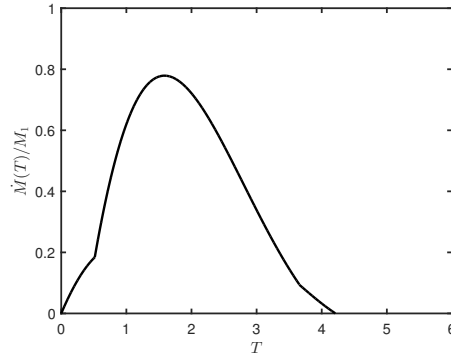
(a) Three-mode event 10-11-10 ($\alpha = 1$).



(b) Three-mode event 10-11-01 ($\alpha = 0.1$).



(c) Three-mode event 01-11-10 ($\alpha = 0.1$).



(d) Three-mode event 01-11-01 ($\alpha = 1$).

Figure 7.9: Source functions associated with the three-mode events predicted by the model ($\beta = 0.5, \gamma = 1, \epsilon = 0.7$).

The values of the final slip amplitudes of the asperities (namely U_1 and U_2) and the final seismic moment M_0 in a seismic event can be discriminated according to the state P_0 at the beginning of the interseismic interval preceding the event and, in turn, according to the state P_1 where the seismic event starts: this is summarized in Table (7.1).

In conclusion, the number and the amplitudes of the humps in the source function of a seismic event allow to derive the number and sequence of dynamic modes involved; in turn, the state of the fault that generated the event can be constrained. Subsequently, it is possible to reduce the uncertainty on the future evolution of the system. An example will be shown in §7.8 for a real fault.

Table 7.1: Final slip amplitudes U_1 and U_2 of asperity 1 and 2 and seismic moment M_0 during an earthquake made up of n slipping modes, as functions of the states P_0 at the beginning of the interseismic interval preceding the event and P_1 where the event started. The entry *e.n.* is the abbreviation for *evaluated numerically*.

P_0	P_1	n	U_1	U_2	M_0
$P_0 \in \mathbf{H}_1^-$	$P_1 \in \mathbf{Q}_1$	1	$\kappa_1 U$	0	$\kappa_1 M_1$
$P_0 \in \mathbf{H}_2^+$	$P_1 \in \mathbf{Q}_2$	1	0	$\beta \kappa_1 U$	$\beta \kappa_1 M_1$
$P_0 \in \Sigma$	$P_1 \in CD$	2	<i>e.n.</i>	<i>e.n.</i>	<i>e.n.</i>
$P_0 \in \Sigma_1 \vee P_0 \in \Sigma_2$	$P_1 \in \mathbf{s}_1 \vee P_1 \in \mathbf{s}_2$	2	$\kappa_1 U$	$\beta \kappa_1 U$	$\kappa_1 M_1 (1 + \beta)$
$P_0 \in \mathbf{H}_1^+ \vee P_0 \in \mathbf{H}_2^-$	$P_1 \in \mathbf{R}_1 \vee P_1 \in \mathbf{R}_2$	3	<i>e.n.</i>	<i>e.n.</i>	<i>e.n.</i>

7.5 Forces on the asperities

In the following, the evolution of the tangential forces on the asperities during the seismic cycle of the fault is discussed. First, I focus on the interseismic intervals and show the main differences with respect to the case of purely elastic coupling between the asperities. Then, the sequence of dynamic modes involved in an earthquake is related with the force distribution on the fault at the onset of the event. Finally, the static force drops on the asperities following the different seismic events predicted by the model are evaluated.

7.5.1 Interseismic interval

In order to discuss the influence of viscoelastic relaxation on the duration of the interseismic intervals of the fault, let us first focus on the case of purely elastic coupling between the asperities, corresponding to $Z = Y - X$ and $\Theta \rightarrow \infty$. Combining Eq. (7.16) with Eq. (7.28), the temporal evolution of the tangential forces on the asperities during mode 00 is expressed by

$$F_1(T) = -\bar{X} - VT + \alpha(\bar{Y} - \bar{X}), \quad F_2(T) = -\bar{Y} - VT - \alpha(\bar{Y} - \bar{X}) \quad (7.79)$$

where (\bar{X}, \bar{Y}) is the state of the fault at the beginning of the interseismic interval. Accordingly, the forces evolve with the same rate

$$\dot{F}_1 = \dot{F}_2 = -V \quad (7.80)$$

and their difference remains constant in time. If instead we introduce the viscoelastic deformation, the temporal evolution of the tangential forces on the asperities during mode 00 is given by

$$F_1(T) = -\bar{X} - VT + \alpha\bar{Z}e^{-T/\Theta}, \quad F_2(T) = -\bar{Y} - VT - \alpha\bar{Z}e^{-T/\Theta} \quad (7.81)$$

where $(\bar{X}, \bar{Y}, \bar{Z})$ is the state of the fault at the beginning of the interseismic interval. These forces evolve with rates

$$\dot{F}_1(T) = -V - \frac{\alpha\bar{Z}}{\Theta}e^{-T/\Theta}, \quad \dot{F}_2(T) = -V + \frac{\alpha\bar{Z}}{\Theta}e^{-T/\Theta}. \quad (7.82)$$

Some significant divergences with respect to the elastic case stand out. First, the difference $F_1 - F_2$ changes as tectonic loading takes place, so that the stress distribution on the asperities varies during an interseismic interval. Furthermore, the rate of evolution of the tangential force on asperity 1 is not the same as for asperity 2. Also, these rates are not constant in time and depend on the state of the fault at the beginning of the interseismic interval: if $\bar{Z} > 0$, the rate $|\dot{F}_1|$ is larger than in the purely elastic case, so that the failure of asperity 1 can be anticipated, and vice-versa if $\bar{Z} < 0$; the opposite holds for asperity 2.

7.5.2 Onset of a seismic event

The relationship between the sequence of dynamic modes in an earthquake generated by the fault and the different subsets in which the faces $AECD$ or $BCDF$ of the sticking region \mathbf{H} can be divided was discussed in §7.3.1. I now show the correlation existing between these sequences and the distribution of forces on the fault at the onset of a seismic event.

Let us consider an earthquake involving n slipping modes starting with mode 10, i.e., on the face $AECD$. Let $P_i = (X_i, Y_i, Z_i)$ be the representative point of the system at $T = T_i$, when the system enters the i -th mode ($i = 1, 2, \dots, n$). Finally, let d be the distance of the starting point P_1 from the edge CD . At the beginning of the event ($T = T_1$), the force acting on asperity 2 is

$$F_2(T_1) = -Y_1 - \alpha Z_1 \quad (7.83)$$

where Eq. (7.16) was used. The magnitude $|F_2(T_1)|$ decreases linearly with d , as shown in Fig. (7.10)-(a), whereas the magnitude of the force F_1 acting on asperity 1 is the same everywhere ($|F_1| = 1$). At $T = T_2$, the force on asperity 2 is

$$F_2(T_2) = -Y_2 - \alpha Z_2 = F_2(T_1) - \alpha(Z_2 - Z_1), \quad (7.84)$$

where it was taken into account that $Y_2 = Y_1$, since the first slipping mode in the event is associated with the sole slip of asperity 1. The difference

$$F_2(T_2) - F_2(T_1) = -\alpha(Z_2 - Z_1) \quad (7.85)$$

represents the stress transfer from asperity 1. If the magnitude of $F_2(T_1)$ is large enough that $|F_2(T_2)| = \beta$, the slip of asperity 1 triggers the slip of asperity 2, so that mode 10 is followed by mode 01 or 11. This condition is verified by states $P_1 \in \mathbf{s}_1$ and $P_1 \in \mathbf{R}_1$, respectively, as shown in Fig. (7.10)-(b); conversely, $|F_2(T_2)| < \beta$ for states $P_1 \in \mathbf{Q}_1$ and mode 10 is followed by mode 00.

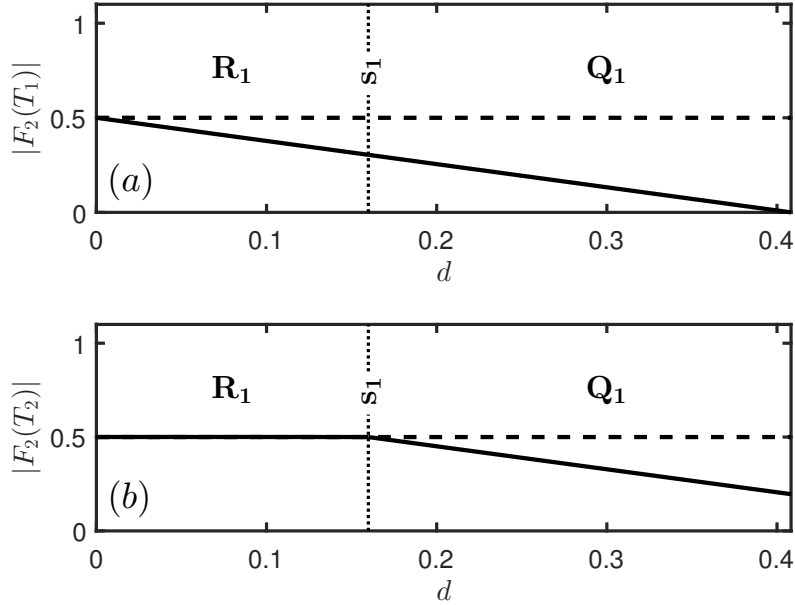


Figure 7.10: Force F_2 on asperity 2 during an earthquake involving n slipping modes and starting with mode 10, as a function of the distance d of the initial state P_1 , measured on the face $AECD$ from the edge CD of the sticking region \mathbf{H} ($\alpha = 1$, $\beta = 0.5$, $\gamma = 1$, $\epsilon = 0.7$): (a) magnitude of F_2 at the onset of the event ($T = T_1$); (b) magnitude of F_2 after the initial slip of asperity 1 ($T = T_2$). The labels indicate the subsets of the face $AECD$ corresponding to different intervals of d . The dashed line indicates the condition for the slip of asperity 2 ($|F_2| = \beta$), which is reached only for states $P_1 \in \mathbf{s}_1$ and $P_1 \in \mathbf{R}_1$.

Similar considerations hold on the face $BCDF$. In this case, the n -mode event starts with mode 01. At the beginning of the event ($T = T_1$), the force acting on asperity 1 is

$$F_1(T_1) = -X_1 + \alpha Z_1 \quad (7.86)$$

where Eq. (7.16) was employed. The magnitude $|F_1(T_1)|$ decreases linearly with d , while $|F_2| = \beta$ everywhere. At $T = T_2$, the force on asperity 1 is

$$F_1(T_2) = -X_2 + \alpha Z_2 = F_1(T_1) + \alpha(Z_2 - Z_1), \quad (7.87)$$

where it was taken into account that $X_2 = X_1$, since the first slipping mode in the event is associated with the sole slip of asperity 2. The difference

$$F_1(T_2) - F_1(T_1) = \alpha(Z_2 - Z_1) \quad (7.88)$$

represents the stress transfer from asperity 2. If the magnitude of $F_1(T_1)$ is large enough that $|F_1(T_2)| = 1$, the slip of asperity 2 triggers the slip of asperity 1 and mode 01 is followed by mode 10 or 11. This condition is verified by states $P_1 \in \mathbf{s}_2$ and $P_1 \in \mathbf{R}_2$, respectively. On the contrary, $|F_1(T_2)| < 1$ for states $P_1 \in \mathbf{Q}_2$, so that mode 01 is followed by mode 00. This is shown in Fig. (7.11).

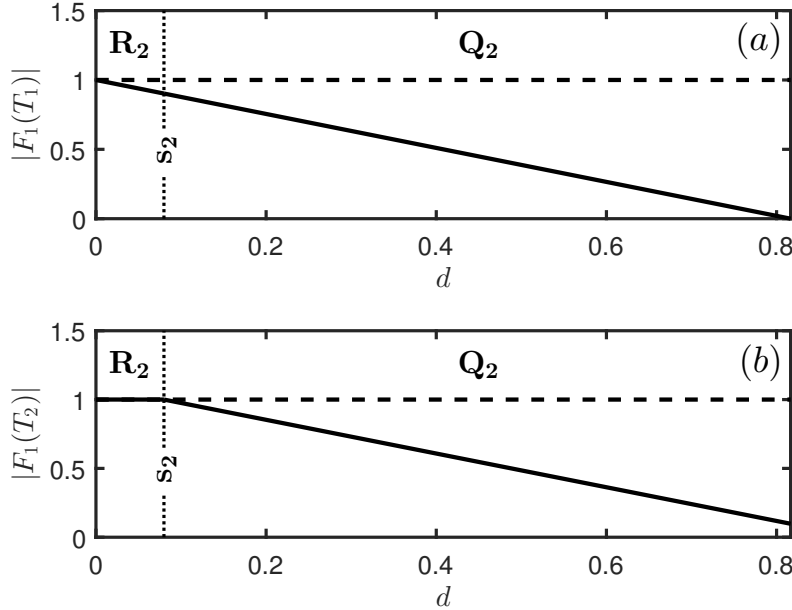


Figure 7.11: Force F_1 on asperity 1 during an earthquake involving n slipping modes and starting with mode 01, as a function of the distance d of the initial state P_1 , measured on the face $BCDF$ from the edge CD of the sticking region \mathbf{H} ($\alpha = 1$, $\beta = 0.5$, $\gamma = 1$, $\epsilon = 0.7$) : (a) magnitude of F_1 at the onset of the event ($T = T_1$); (b) magnitude of F_1 after the initial slip of asperity 2 ($T = T_2$). The labels indicate the subsets of the face $BCDF$ corresponding to different intervals of d . The dashed line indicates the condition for the slip of asperity 1 ($|F_1| = 1$), which is reached only for states $P_1 \in \mathbf{s}_2$ and $P_1 \in \mathbf{R}_2$.

7.5.3 Static force drops

The static force drops on the asperities can be calculated from the knowledge of the slip amplitudes (6.80) of the asperities and the stress transferred from one asperity to the other.

Once again, I consider a seismic event involving n slipping modes and call $P_i = (X_i, Y_i, Z_i)$ the representative point of the system at $T = T_i$, when the system enters the i -th mode ($i = 1, 2, \dots, n$). At the end of the event, the force drop on asperity 1 is

$$F_1(T_{n+1}) - F_1(T_1) = U_1 + \alpha(Z_{n+1} - Z_1). \quad (7.89)$$

Analogously, the force drop on asperity 2 is

$$F_2(T_{n+1}) - F_2(T_1) = U_2 - \alpha(Z_{n+1} - Z_1). \quad (7.90)$$

Combining these expressions with the details of Table (7.1), the values of the force drops associated with the different seismic events predicted by the model can be calculated. They are listed in Table (7.2). For events involving the slip of a single asperity, the force drop on the stationary asperity is negative, since stress is accumulated on it.

Table 7.2: Static force drops on the asperities, following the different seismic events predicted by the model. The entry *e.n.* is the abbreviation for *evaluated numerically*.

Kind of event	Force drop on asperity 1	Force drop on asperity 2
one-mode 10	$2\kappa_1(1 - \epsilon)$	$-\alpha\kappa_1U$
one-mode 01	$-\alpha\beta\kappa_1U$	$2\kappa_1\beta(1 - \epsilon)$
two-mode 10-01/01-10	$\kappa_1U(1 + \alpha - \alpha\beta)$	$\kappa_1U(\beta - \alpha + \alpha\beta)$
involving mode 11	<i>e.n.</i>	<i>e.n.</i>

7.6 Influence of seismic efficiency on events due to the consecutive slips of the asperities

In this section, I focus on two-mode events starting on segments \mathbf{s}_1 and \mathbf{s}_2 and discuss how they are affected by the radiation of elastic waves. To this aim, the effect of a variation of the parameter γ in the interval $[0, 2]$ is studied. In the

following, a superscript ⁰ shall be used when referring to quantities corresponding to no wave radiation ($\gamma = 0$).

The lengths l_1 and l_2 of segments \mathbf{s}_1 and \mathbf{s}_2 , respectively, as well as their distances d_1 and d_2 from the edge CD are provided in Appendix F. In the limit case $\gamma = 0$, the maximum amount of slip $\kappa_1 U$ of asperity 1 that is present in their expressions must be replaced by U defined in Eq. (5.24), where $U \geq \kappa_1 U$. In Fig. (7.12) the ratios l_1/l_1^0 and l_2/l_2^0 are plotted as functions of γ . The trends clearly point out that an increase in γ entails a lengthening of both segments \mathbf{s}_1 and \mathbf{s}_2 . As a matter of fact, the lengths of these segments depend on the coordinates of their end points, which are in turn constrained by the no overshooting conditions. Since wave radiation reduces the maximum amount of slip allowed to the asperities, the number of states satisfying the no overshooting conditions is increased and more states are included in the segments \mathbf{s}_1 and \mathbf{s}_2 . As γ grows, the probability that the system gives rise to two-mode events 10-01 or 01-10 is thus enlarged.

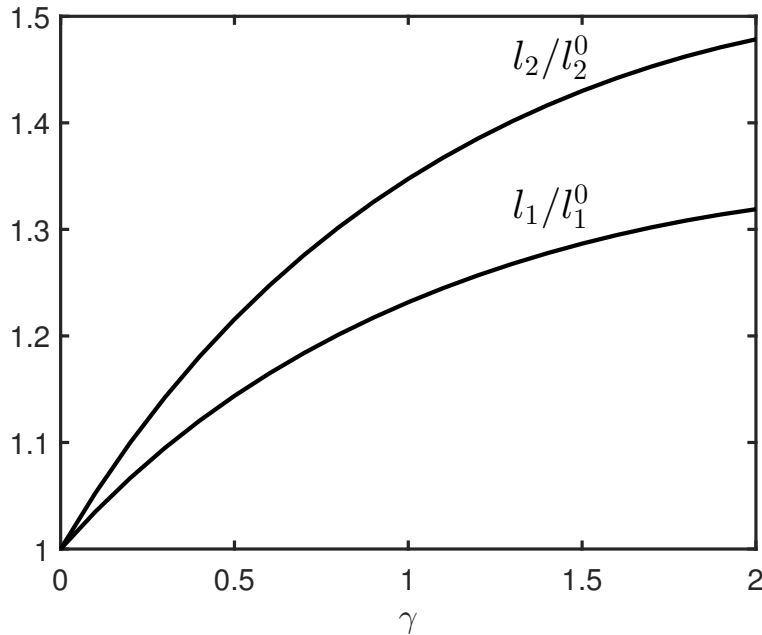


Figure 7.12: The lengths l_1/l_1^0 and l_2/l_2^0 of segments \mathbf{s}_1 and \mathbf{s}_2 , as functions of γ ($\alpha = 1, \beta = 0.5, \epsilon = 0.7$). Larger values of the ratios l_i/l_i^0 entail a higher probability of a two-mode event associated with the separate slips of both asperities.

According to Eq. (F.32), the ratio d_i/d_i^0 is the same for both segments \mathbf{s}_1 and \mathbf{s}_2 . It is shown in Fig. (7.13) as a function of γ . Evidently, an increase in γ takes both segments \mathbf{s}_1 and \mathbf{s}_2 closer to the edge CD of the sticking region. This can be

explained if one considers the already discussed correlation between the different subsets of the faces $AECD$ and $BCDF$ and the forces acting on the asperities (§7.5.2). Taking into account that wave radiation lowers the slip of the asperities, the stress transferred from one asperity to the other during a seismic event is reduced as well. Thus, the segment \mathbf{s}_1 must be closer to the edge CD , so that the value of F_2 at the beginning of mode 10 is large enough for the stress transferred by asperity 1 to asperity 2 to trigger mode 01. Analogous considerations can be made for the segment \mathbf{s}_2 on the face $BCDF$.

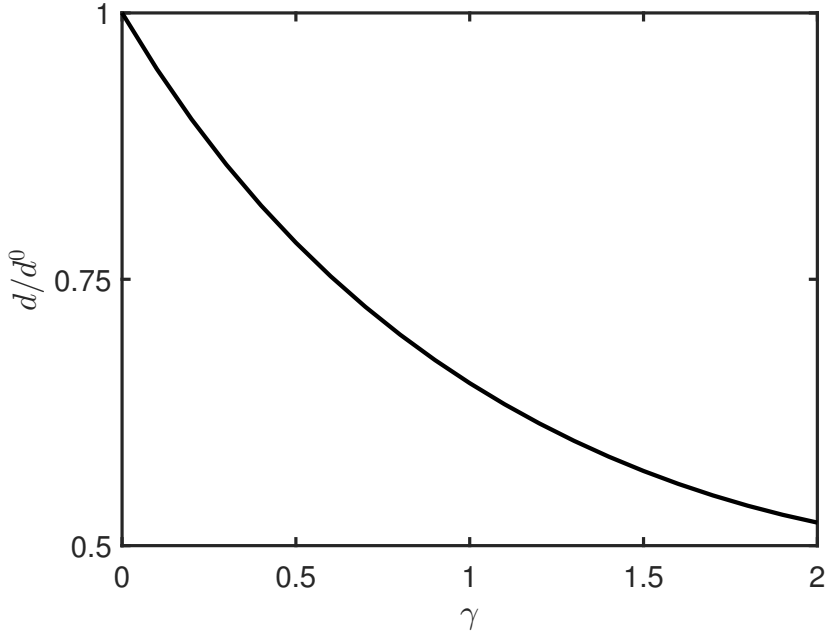


Figure 7.13: The distance d/d^0 of segments \mathbf{s}_1 and \mathbf{s}_2 from the edge CD , as a function of γ ($\alpha = 1, \epsilon = 0.7$). The smaller the distance, the more homogeneous the stress distribution on the fault at the beginning of a two-mode event associated with the separate slips of both asperities.

A direct consequence of the smaller distance between segments \mathbf{s}_1 and \mathbf{s}_2 and the edge CD is that the areas $A_{\mathbf{Q}_i}$ of the subsets \mathbf{Q}_1 and \mathbf{Q}_2 are enlarged, while the areas $A_{\mathbf{R}_i}$ of the subsets \mathbf{R}_1 and \mathbf{R}_2 are reduced. This is shown in Fig. (7.14), where the ratios $A_{\mathbf{Q}_i}/A_{\mathbf{Q}_i}^0$ and $A_{\mathbf{R}_i}/A_{\mathbf{R}_i}^0$ are plotted as functions of γ . This feature provides an additional proof that higher seismic efficiencies progressively reduce the possibility of simultaneous slip of the asperities, as pointed out in §7.3.2.

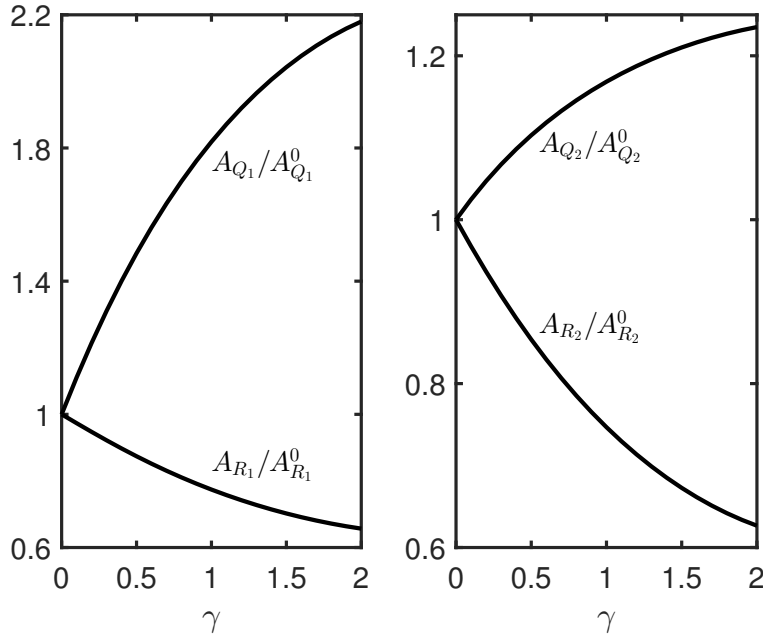


Figure 7.14: The areas $A_{\mathbf{Q}_i}/A_{\mathbf{Q}_i}^0$ and $A_{\mathbf{R}_i}/A_{\mathbf{R}_i}^0$ of the subsets $\mathbf{Q}_1, \mathbf{Q}_2, \mathbf{R}_1$ and \mathbf{R}_2 , as functions of γ ($\alpha = 1, \beta = 0.5, \epsilon = 0.7$). As the ratios $A_{\mathbf{Q}_i}/A_{\mathbf{Q}_i}^0$ increase, the possibility of simultaneous slip of asperities is reduced. The converse holds for the ratios $A_{\mathbf{R}_i}/A_{\mathbf{R}_i}^0$.

7.7 Choice of the parameters

With the same consideration as in §5.4, the coupling parameter α can be calculated as

$$\alpha = \frac{\mu A s v}{\dot{\sigma}_t} \quad (7.91)$$

where s is the tangential traction (per unit moment) imposed on an asperity by the slip of the other and $\dot{\sigma}_t$ is the tangential stress rate acting on the fault. The expression of s has been given in Eq. (5.94) and Eq. (5.95) for strike-slip and dip-slip faulting, respectively, while the proper expression for $\dot{\sigma}_t$ is provided in Appendix A.

As for the parameters β, γ and ϵ , the same considerations discussed in §6.7 hold. Finally, the effect of viscoelastic relaxation is conveyed by the product $V\Theta$, in terms of which the solutions (7.28) for mode 00 can be rewritten (as all other expressions derived from them). From Eq. (7.9), we have

$$V\Theta = \frac{K v \theta}{f_{s1}}. \quad (7.92)$$

By definition, we can write

$$U = \frac{K u_1^0}{f_{s1}} \quad (7.93)$$

where

$$u_1^0 = \frac{u_1}{\kappa_1} \quad (7.94)$$

is the slip amplitude of asperity 1 when it slips alone, in the limit case $\gamma = 0$. Accordingly, the static friction force on asperity 1 can be estimated as

$$f_{s1} = \frac{K u_1}{\kappa_1 U}. \quad (7.95)$$

Replacing this expression in Eq. (7.92), we find

$$V\Theta = \frac{\kappa_1 U v \theta}{u_1}. \quad (7.96)$$

7.8 An application: the 1964 Alaska earthquake

The 28 March 1964 M_w 9.2 Alaska earthquake was the second largest earthquake of the last century, with a seismic moment m_0 estimated between 3 and 8×10^{22} Nm (Christensen and Beck, 1994; Holdahl and Sauber, 1994; Johnson et al., 1996). The event was due to reverse dip-slip faulting at the boundary between the North American plate and the Pacific plate, with a rupture extending of about 800 km along the Alaska/Aleutian trench. A sketch of the tectonic setting is shown in Fig. (7.15).

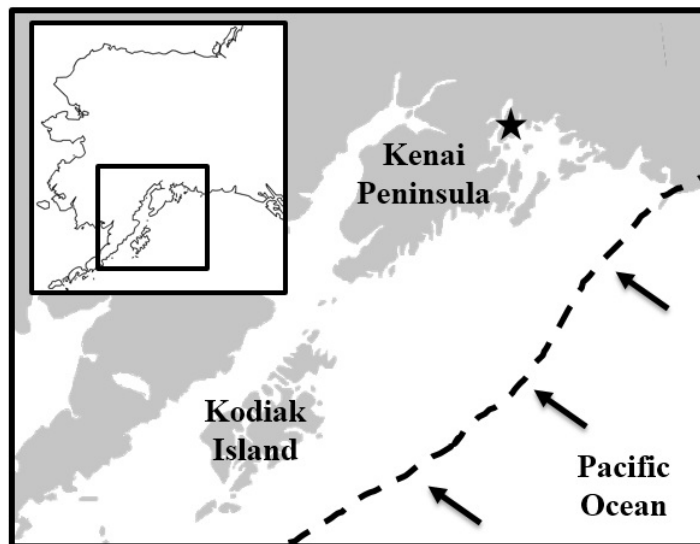


Figure 7.15: Geographic location of the 1964 Alaska earthquake. The star denotes the epicenter. Black arrows indicate the relative motion of the Pacific plate with respect to the North American plate, whereas the thick dashed line identifies the boundary between the tectonic plates.

The joint analysis of seismological, geodetic and tsunami data pointed out that the seismic event was due to the failure of two distinct asperities: the Prince William Sound and Kodiak Island asperities, which I call asperity 1 and 2, respectively. The earthquake initiated with the failure of asperity 1, followed by the failure of asperity 2. On the basis of coseismic surface deformation, Santini et al. (2003) suggested average slips $u_1 = 24$ m for asperity 1 and $u_2 = 18$ m for asperity 2. Following Dragoni and Santini (2015), an area $A = 20,000$ km² for both asperities and a distance $a = 300$ km between their centres are assumed.

It is assumed that the fault is embedded in a shear zone of width $d = 300$ km (Plafker, 1965) and average rigidity $\mu = 55$ GPa (Dziewonski and Anderson, 1981). The relative plate velocity is $v = 5.7$ cm a⁻¹ (DeMets and Dixon, 1999; Cohen and Freymueller, 2004). As a matter of fact, the velocity of the Pacific plate relative to the North American plate at the Alaska/Aleutian trench increases gradually from the northeast to the southwest. However, the difference between the area of Prince William Sound and the area of Kodiak Island is in the order of few mm per year and can be reasonably neglected. From Eq. (A.9), the tangential stress rate on the fault is $\dot{\sigma}_t \simeq 3 \times 10^{-4}$ Pa s⁻¹.

In the decades following the earthquake, significant post-seismic deformation took place, which has been ascribed to aseismic slip on the fault and viscoelastic relaxation (Zweck et al., 2002; Suito and Freymueller, 2009). The latter process shows a characteristic time $\theta \approx 30$ a.

With the data listed above, the parameters of the model are calculated. From Eq. (7.91) and Eq. (6.121), we get $\alpha \approx 0.01$ and $\beta = 0.75$. From Eq. (5.24) and taking $\epsilon = 0.7$ (e.g. Jaeger and Cook, 1976), we get $U \simeq 0.594$. I take $\gamma = 0.2$ as in Dragoni and Santini (2015), a value yielding the best fit with the observed source function of the earthquake. Thus, we have $\kappa_1 \simeq 0.87$ from Eq. (5.25). Finally, we have $V\Theta \simeq 0.037$ from Eq. (7.96).

In terms of the present model, the earthquake can be described as a two-mode event 10-01 starting from mode 00. Accordingly, the orbit of the system during mode 00 lies on the surface Σ_1 inside the subset \mathbf{H}_1 of the sticking region (Fig. 7.5). Furthermore, letting P_1 be the representative point of the system at the beginning of the earthquake, we have that P_1 belongs to segment \mathbf{s}_1 (Fig. 7.3).

From Eq. (F.13), the coordinates of P_1 are

$$X_1 = \alpha Z_1 + 1, \quad Y_1 = \beta - \alpha \kappa_1 U - \alpha Z_1, \quad Z_1 \quad (7.97)$$

with

$$Z_a \leq Z_1 \leq Z_b \quad (7.98)$$

where the extreme values Z_a and Z_b correspond to the end points (F.12) and (F.11) of \mathbf{s}_1 :

$$Z_a = \frac{\kappa_1 U - 1}{\alpha}, \quad Z_b = \frac{\beta - \kappa_1 U(\alpha + \beta)}{\alpha}. \quad (7.99)$$

Mode 10 terminates at the point P_2 with coordinates

$$X_2 = X_1 - \kappa_1 U, \quad Y_2 = Y_1, \quad Z_2 = Z_1 + \kappa_1 U, \quad (7.100)$$

where mode 01 starts. As Z_1 varies in the interval (7.98), an infinite number of points P_2 describe a segment \mathbf{r}_1 on the subset \mathbf{Q}_2 of the face $BCDF$ and parallel to the edge CD . At the end of mode 01, the system is at the point P_3 with coordinates

$$X_3 = X_2, \quad Y_3 = Y_2 - \beta \kappa_1 U, \quad Z_3 = Z_2 - \beta \kappa_1 U. \quad (7.101)$$

Again, as Z_1 varies in the interval (7.98), there is an infinite number of points P_3 defining another segment \mathbf{q}_1 parallel to the edge CD . This segment lies inside the sticking region and crosses the surface Σ for $Z_1 = Z_c$, with $Z_a < Z_c < Z_b$. What is more, it intersects the surface Σ_2 for $Z_1 = Z_d$, with $Z_a < Z_d < Z_c$, and the surface Σ_1 for $Z_1 = Z_e$, with $Z_c < Z_e < Z_b$.

7.8.1 Refinement according to the seismic history to date

The knowledge of the time interval elapsed after the 1964 earthquake provides a constraint on the state of the system that may have given rise to that event. Depending on the specific state P_1 where the 1964 earthquake begun, the state of the system at the end of the event corresponds to a particular point P_3 on the segment \mathbf{q}_1 . The coordinates of P_3 given in Eq. (7.101) can be expressed as a function of Z_1 thanks to Eq. (7.100). Owing to the intersection of \mathbf{q}_1 with the surface Σ , the point P_3 can belong to \mathbf{H}_1 , \mathbf{H}_2 or Σ , in correspondence to $Z_c < Z_1 \leq Z_b$, $Z_a \leq Z_1 < Z_c$ and $Z_1 = Z_c$, respectively. This circumstance determines which of the two asperities will fail the first at the beginning of the next earthquake produced by the fault. In the first case, the next event will start with the failure of asperity 1; in the second case, with the failure of asperity 2; in

the third case, with the simultaneous failures of the asperities.

With the values of α, β, κ_1 and U listed above, we find $Z_a \simeq -48.3$, $Z_b \simeq 35.7$, $Z_c \simeq 6.2$, $Z_d \simeq 6$ and $Z_e \simeq 6.46$. These figures suggest that only about one third of segment \mathbf{q}_1 lies inside the subset \mathbf{H}_1 of the sticking region. This would lead us to the preliminary conclusion that future events on the 1964 fault are more likely to start with the failure of asperity 2.

Let us calculate the duration T_{is} of the interseismic interval after the 1964 earthquake from Eq. (7.31) and Eq. (7.34) for states belonging to \mathbf{H}_1 and \mathbf{H}_2 , respectively:

$$T_{is} = \begin{cases} \Theta W(\gamma'_1) + \frac{1-X_3}{V}, & Z_c < Z_1 \leq Z_b \\ \Theta W(\gamma'_2) + \frac{\beta-Y_3}{V}, & Z_a \leq Z_1 < Z_c \end{cases} \quad (7.102)$$

where

$$\gamma'_1 = \frac{\alpha Z_3}{V\Theta} e^{-\frac{1-X_3}{V\Theta}}, \quad \gamma'_2 = -\frac{\alpha Z_3}{V\Theta} e^{-\frac{\beta-Y_3}{V\Theta}}. \quad (7.103)$$

The duration T_{is} is shown in Fig. (7.16) as a function of Z_1 .

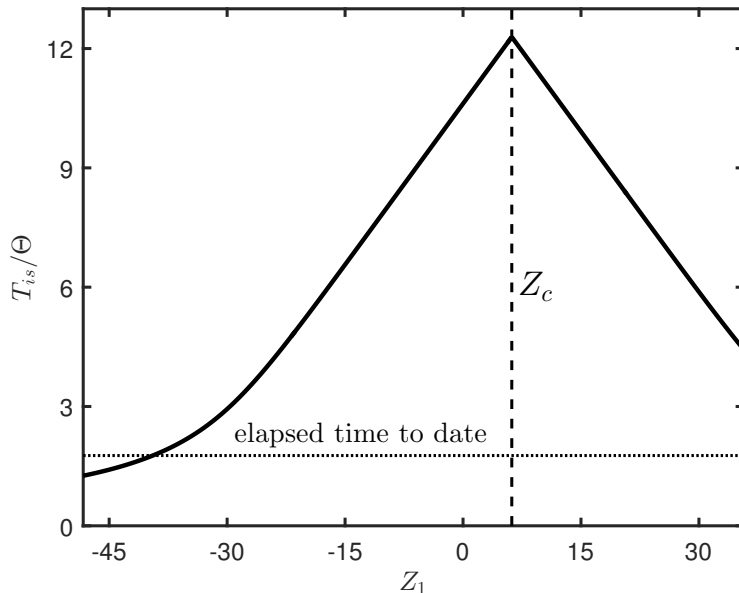


Figure 7.16: Duration of the interseismic interval after the 1964 Alaska earthquake, in units of the associated Maxwell relaxation time Θ . The variable Z_1 characterizes the initial state of the 1964 event. The elapsed time to date (dotted line) constrains the possible initial states of the 1964 earthquake and, in turn, the features of the next event on the fault. The case $Z_1 = Z_c$ corresponds to the largest future event predicted by the model, associated with a two-mode event 11-01.

The 1964 earthquake took place about 53 years ago. Hence, the states on segment \mathbf{s}_1 for which the expected interseismic time interval (7.102) is shorter than or equal to $t_{is} = 53$ years can be ruled out. Imposing the condition

$$\frac{T_{is}}{\Theta} > \frac{t_{is}}{\theta} \simeq 1.77 \quad (7.104)$$

we conclude that only the states on segment \mathbf{s}_1 in the subset $\tilde{Z}_a \leq Z_1 \leq Z_b$ are acceptable as starting states for the 1964 event, with $\tilde{Z}_a = -39.5$.

In turn, this refinement introduces a constraint on the admissible states on the segment \mathbf{q}_1 , and so on the possible future events generated by the fault. In fact, if we compare the interval $[\tilde{Z}_a, Z_c]$ with the interval $[Z_c, Z_b]$, we conclude that approximately 60% of the acceptable portion of \mathbf{q}_1 lies in \mathbf{H}_2 . Accordingly, the probability that future events on the 1964 fault start with the failure of asperity 2 has been reduced by this refinement; however, the next earthquake is still more likely to start with the failure of this asperity, according to the present model.

The refining procedure described above may be repeated again in the future, if no earthquakes were to be observed for some time. Thus, it would be possible to further constrain the admissible subsets of segments \mathbf{s}_1 and \mathbf{q}_1 .

7.8.2 Future earthquakes

The next seismic event generated by the 1964 fault is now further characterized, providing details about the sequence of slipping modes involved.

It was already mentioned that the features of the next earthquake on the 1964 fault depend upon the specific state P_3 on segment \mathbf{q}_1 . The number and the sequence of dynamic modes in the earthquake are summarized in Table (7.3) as a function of the different subintervals of Z_1 .

The value of the seismic moment M_0 released during the next event on the 1964 fault is shown in Fig. (7.17) as a function of Z_1 . The largest possible earthquake predicted by the model, corresponding to $Z_1 = Z_c$ and associated with a two-mode event 11-01, entails a seismic moment $M_0 \simeq 1.53 M_1$.

Table 7.3: Future earthquakes generated by the 1964 Alaska fault, as functions of the variable Z_1 describing the initial state of the 1964 event, with $Z_1 \in [\tilde{Z}_a, Z_b] = [-39.5, 35.7]$. The value $Z_1 = Z_c = 6.2$ corresponds to the largest possible earthquake predicted by the model. The values $Z_1 = Z_d = 6$ and $Z_1 = Z_e = 6.46$ correspond to events associated with the separate (consecutive) slips of the asperities.

Future earthquake	Initial state of the 1964 earthquake
1-mode event 01	$\tilde{Z}_a \leq Z_1 < Z_d$
2-mode event 01-10	$Z_1 = Z_d$
3-mode event 01-11-10	$Z_d < Z_1 < Z_c$
2-mode event 11-01	$Z_1 = Z_c$
3-mode event 10-11-01	$Z_c < Z_1 < Z_e$
2-mode event 10-01	$Z_1 = Z_e$
1-mode event 10	$Z_e < Z_1 \leq Z_b$

This application serves as an example of the concepts discussed in §7.4. In fact, each of the possible future seismic events on the 1964 Alaska fault predicted by the model (Table 7.3) is associated with a characteristic shape of the source function. Accordingly, the observation of the shape and the number of humps in the source function associated with the next event generated by the fault, together with the energy release, will provide information about the state of the system at the onset of that event. In turn, it will be possible to further constrain the acceptable set of states from which the 1964 event may have taken place.

7.8.3 Comparison with the purely elastic case

Assuming purely elastic coupling between the asperities, Dragoni and Santini (2015) were able to identify the particular stress states of the fault at the onset and at the end of the 1964 earthquake. Specifically, they estimated the difference between the slip deficits of the asperities to be

$$Y_1 - X_1 \simeq -0.25 \quad (7.105)$$

at the beginning of the event and

$$Y_3 - X_3 \simeq -0.12 \quad (7.106)$$

at the end of the event. In Chapter 6, it was shown that the number and sequence of dynamic modes in a seismic event produced by a two-asperity fault in the

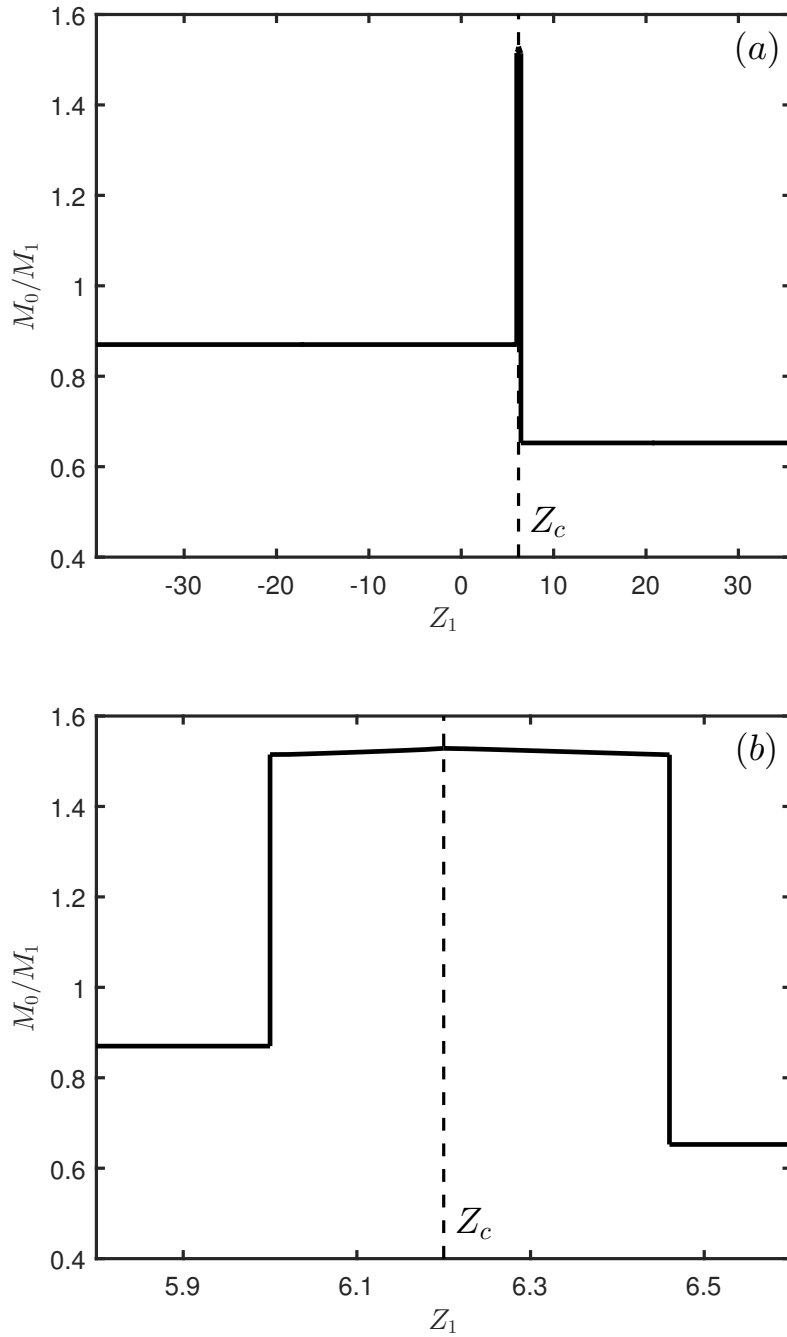


Figure 7.17: (a) Seismic moment M_0 of the next event generated by the 1964 Alaska fault, as a function of the variable Z_1 characterizing the initial state of the 1964 earthquake; (b) magnification of the narrow interval associated with events involving the simultaneous failures of both asperities. The value $Z_1 = Z_c$ corresponds to the largest possible earthquake predicted by the model, associated with a two-mode event 11-01. The values of the parameters are relevant to the 1964 Alaska earthquake ($\alpha = 0.01, \beta = 0.75, \gamma = 0.2, \epsilon = 0.7, V\Theta = 0.037$).

case of purely elastic rheology can be univocally determined from the knowledge of the difference between the slip deficits of the asperities at the beginning of the interseismic interval preceding the event; such difference is identified by the variable p defined in Eq. (6.34). From Eq. (7.106), it results

$$p = -0.12 > p_2 \quad (7.107)$$

at the end of the 1964 event, with p_2 given by Eq. (D.6) assuming $\xi = 1$. Accordingly, the next earthquake produced by the 1964 Alaska fault will be caused by the sole failure of asperity 2, i.e., it will be a one-mode event 01. The duration of the interseismic interval preceding the event can be calculated from Eq. (6.38) assuming again $\xi = 1$: it results $\Delta t \simeq 316$ a.

In the previous sections, it was shown that the presence of viscoelastic relaxation entails a broad range of states compatible with the observed slip pattern of the 1964 earthquake. Such uncertainty on the initial state of the fault is in turn reflected on the particular features of the next earthquake on the 1964 fault and on the duration of the interseismic interval preceding the event. In order to carry out a comparison with the elastic case, it is therefore necessary to determine the specific state on segment \mathbf{s}_1 that corresponds with the stress state (7.105). This can be easily achieved bearing in mind that the limit case of purely elastic coupling between the asperities corresponds to $Z = Y - X$. We conclude that, among all states on segment \mathbf{s}_1 , the elastic case studied by Dragoni and Santini (2015) is identified by $Z_1 = -0.25$.

Since $\tilde{Z}_a \leq -0.25 \leq Z_d$, the present model predicts that the next earthquake on the 1964 fault will be a one-mode event 01, in agreement with the elastic case. The duration of the interseismic interval preceding the event can be calculated from Eq. (7.102) with $Z_1 = -0.25$: it results $\Delta t \simeq 315$ a. The influence of viscoelastic relaxation on the post-seismic evolution of the 1964 fault is therefore relatively weak, according to the present model, since it causes the anticipation of the next earthquake by only about 1 a with respect to the purely elastic case.

Chapter 8

Stress perturbations on a two-asperity fault in the presence of viscoelastic relaxation

In this chapter, I consider the discrete model of a two-asperity fault in the presence of viscoelastic relaxation presented in the previous chapter and I devise a means to study the effect of stress perturbations from neighbouring faults (§2.1.2) taking place during the phase of post-seismic deformation of the fault, pointing out the main differences with respect to the case of a purely elastic rheology.

8.1 Modelling stress perturbations

Let us consider the fault model described in §7.1 and focus on the perturbations of its state caused by the coseismic slip on surrounding faults. Following Dragoni and Piombo (2015), it is assumed that:

1. the perturbations occur during an interseismic interval: this is a reasonable assumption, since faults are predominantly stationary over time;
2. the stress transfer takes place over a time interval negligible with respect to the duration of the interseismic interval;
3. at the time of the perturbation, the state of the fault is sufficiently far from the failure condition and the stress transfer is small enough that the onset of motion of either asperity is not achieved immediately.

As discussed in §2.1.2, an effective way to characterize the interaction between neighbouring faults is provided by the concept of Coulomb stress. In the present

model, the presence of two asperities with different strengths make it necessary to assign a value of Coulomb stress to each of them. By definition, the Coulomb forces associated with asperity 1 and 2 are, respectively,

$$f_1^C = -f_1 - f_{s1}, \quad f_2^C = -f_2 - f_{s2}. \quad (8.1)$$

In nondimensional form, they become

$$F_1^C = X - \alpha Z - 1, \quad F_2^C = Y + \alpha Z - \beta. \quad (8.2)$$

Of course, these forces vanish on planes Π_1 and Π_2 , respectively (§7.1.1); furthermore, their gradients

$$\nabla F_1^C = (1, 0, -\alpha), \quad \nabla F_2^C = (0, 1, \alpha) \quad (8.3)$$

are orthogonal to Π_1 and Π_2 , respectively.

Let $(X, Y, Z) \in \mathbf{H}$ be the state of the fault at the time of the perturbation. As a result of the stress transfer, the system undergoes a transition to a new state

$$(X', Y', Z') = (X, Y, Z) + (\Delta X, \Delta Y, \Delta Z). \quad (8.4)$$

Since the stress transfer takes place over a time interval short with respect to the interseismic interval (assumption 2), viscoelastic relaxation is negligible during the perturbation and the rheology can be reasonably considered as purely elastic as the perturbation takes place. Accordingly, it is possible to set

$$\Delta Z = \Delta Y - \Delta X. \quad (8.5)$$

The change of state is associated with a vector in the XYZ space,

$$\Delta \mathbf{R} = (\Delta X, \Delta Y, \Delta Z). \quad (8.6)$$

The components of $\Delta \mathbf{R}$ generally have different magnitudes and may have different signs, as a consequence of the inhomogeneity of the stress field produced by an earthquake. They can be written in terms of the tangential forces ΔF_1 and ΔF_2 exerted by the perturbing source on asperity 1 and 2, respectively: from Eq. (7.16), we have

$$\Delta F_1 = -\Delta X + \alpha \Delta Z = \alpha \Delta Y - (1 + \alpha) \Delta X \quad (8.7)$$

$$\Delta F_2 = -\Delta Y - \alpha \Delta Z = \alpha \Delta X - (1 + \alpha) \Delta Y. \quad (8.8)$$

Combining these expressions together, we get

$$\Delta X = -\frac{1+\alpha}{1+2\alpha}\Delta F_1 - \frac{\alpha}{1+2\alpha}\Delta F_2 \quad (8.9)$$

$$\Delta Y = -\frac{\alpha}{1+2\alpha}\Delta F_1 - \frac{1+\alpha}{1+2\alpha}\Delta F_2 \quad (8.10)$$

$$\Delta Z = \frac{1}{1+2\alpha}(\Delta F_1 - \Delta F_2). \quad (8.11)$$

As a result, the variations in tangential stress alter the orbit of the system.

The components of $\Delta \mathbf{R}$ can also be related to the orientation of the vector in the state space. With reference to Fig. (8.1), we have

$$\Delta X = \Delta R \cos \varphi \cos \vartheta, \quad \Delta Y = \Delta R \cos \varphi \sin \vartheta, \quad \Delta Z = \Delta R \sin \varphi. \quad (8.12)$$

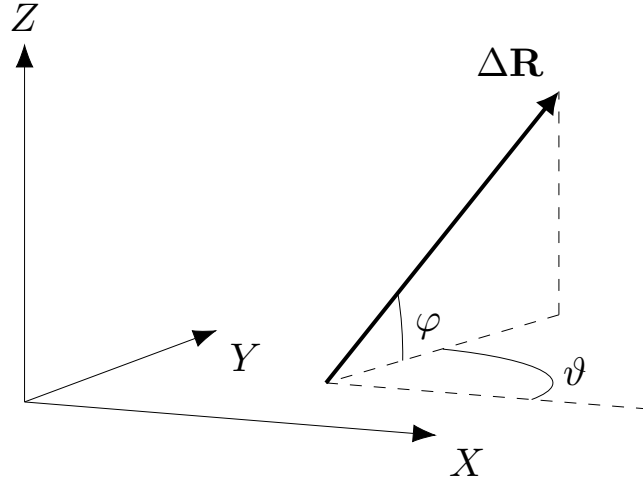


Figure 8.1: The vector $\Delta \mathbf{R}$ and its orientation in the XYZ space, characterizing the stress perturbation imposed on the system by earthquakes produced by neighbouring faults.

Introducing the assumption (8.5), the angle φ may be expressed in terms of the angle ϑ as

$$\varphi = \arctan(\sin \vartheta - \cos \vartheta). \quad (8.13)$$

In writing Eq. (8.13), it was taken into account that

$$\varphi \neq \frac{\pi}{2}, \frac{3\pi}{2} \quad (8.14)$$

or it would result

$$\Delta Z = \pm \Delta R, \quad \Delta X = \Delta Y = 0 \quad (8.15)$$

which is a meaningless circumstance. From Eq. (8.12), the tangential forces (8.7)-(8.8) can be rewritten as

$$\Delta F_1 = \frac{\alpha \sin \vartheta - (1 + \alpha) \cos \vartheta}{\sqrt{2 - \sin 2\vartheta}} \Delta R \quad (8.16)$$

$$\Delta F_2 = \frac{\alpha \cos \vartheta - (1 + \alpha) \sin \vartheta}{\sqrt{2 - \sin 2\vartheta}} \Delta R. \quad (8.17)$$

Following the variations in normal stress, the static and dynamic frictions on each asperity are altered. Letting f'_{s1} and f'_{s2} be the new static frictions on asperity 1 and 2, respectively, I define

$$\beta_1 = \frac{f'_{s1}}{f_{s1}}, \quad \beta_2 = \frac{f'_{s2}}{f_{s1}}. \quad (8.18)$$

The changes in static frictions are then

$$\Delta\beta_1 = \beta_1 - 1, \quad \Delta\beta_2 = \beta_2 - \beta \quad (8.19)$$

on asperity 1 and 2, respectively.

Since the stress perturbation does not alter the friction coefficients of rocks, it is reasonable to assume that the ratio ϵ between dynamic and static frictions remains unchanged on both asperities. Therefore, letting f'_{d1} and f'_{d2} be the new dynamic frictions on asperity 1 and 2, respectively, we have

$$\frac{f'_{d1}}{f_{s1}} = \epsilon \frac{f'_{s1}}{f_{s1}} = \epsilon\beta_1, \quad \frac{f'_{d2}}{f_{s1}} = \epsilon \frac{f'_{s2}}{f_{s1}} = \epsilon\beta_2. \quad (8.20)$$

The consequent changes in dynamic frictions are $\epsilon\Delta\beta_1$ and $\epsilon\Delta\beta_2$ on asperity 1 and 2, respectively.

8.2 Effects of the perturbation

The stress transfer resulting from earthquakes on neighbouring faults alters several parameters of the model. A first remarkable change concerns the strength of the asperities. After the perturbation, it is possible to define a new ratio

$$\beta' = \frac{f'_{s2}}{f'_{s1}} = \frac{f'_{d2}}{f'_{d1}} = \frac{\beta_2}{\beta_1} \quad (8.21)$$

which differs from the original value β given in Eq. (7.8). Moreover, the stress transfer may be so intense that the weaker asperity may become the stronger one:

that is, it may result $\beta' > 1$.

The variations in static frictions entail different conditions for the onset of motion of the asperities. Taking Eq. (8.18) into account, Eq. (7.17) is replaced by

$$F_1 = -\beta_1, \quad F_2 = -\beta_2. \quad (8.22)$$

By combination with Eq. (7.16), these conditions define the planes

$$X - \alpha Z - \beta_1 = 0 \quad (8.23)$$

$$Y + \alpha Z - \beta_2 = 0 \quad (8.24)$$

that I call Π'_1 and Π'_2 , respectively. Conversely, the planes Γ_1 and Γ_2 given in Eq. (7.20) and Eq. (7.21) are not affected by the stress perturbation, since they do not depend on frictions. In conclusion, the changes in normal stress modify the sticking region of the system, describing a new hexahedron \mathbf{H}' in the state space. The coordinates of its vertices are

$$A' = \left(0, \beta_1, -\frac{\beta_1}{\alpha}\right), \quad B' = \left(\beta_2, 0, \frac{\beta_2}{\alpha}\right), \quad C' = \left(\beta_1 + \beta_2, 0, \frac{\beta_2}{\alpha}\right) \quad (8.25)$$

$$D' = \left(0, \beta_1 + \beta_2, -\frac{\beta_1}{\alpha}\right), \quad E' = (\beta_1, 0, 0), \quad F' = (0, \beta_2, 0). \quad (8.26)$$

The volume of \mathbf{H}' is $\beta_1\beta_2(\beta_1 + \beta_2)/2\alpha$: by comparison with the characteristics of \mathbf{H} discussed in §7.1.1, we conclude that the set of states corresponding to stationary asperities is enlarged or reduced, depending on how normal stresses on the asperities are modified.

Following the changes in static frictions, the surface Σ defined in Eq. (7.76) is replaced by a new surface Σ' expressed by

$$V\Theta [W(\gamma'_1) - W(\gamma'_2)] + Y - X + \beta_1 - \beta_2 = 0, \quad (8.27)$$

where

$$\gamma'_1 = \frac{\alpha Z}{V\Theta} e^{-\frac{\beta_1 - X}{V\Theta}}, \quad \gamma'_2 = -\frac{\alpha Z}{V\Theta} e^{-\frac{\beta_2 - Y}{V\Theta}}. \quad (8.28)$$

As a result, the sticking region \mathbf{H}' is split in two subsets \mathbf{H}'_1 and \mathbf{H}'_2 ; furthermore, its faces $A'E'C'D'$ and $B'C'D'F'$ are divided into subsets $\mathbf{Q}'_1, \mathbf{s}'_1, \mathbf{R}'_1$ and $\mathbf{Q}'_2, \mathbf{s}'_2, \mathbf{R}'_2$, respectively.

As for the surfaces Σ_1 and Σ_2 , we see from their definitions (7.77) and (7.78) that they are affected by the variations of the static frictions and of the slip amplitudes of the asperities (which are a consequence of the changes in dynamic frictions). Accordingly, the surface Σ_1 is replaced by a new surface Σ'_1 given by

$$X - Y - 2\alpha Z e^{-W(\gamma'_1) - \frac{\beta_1 - X}{V\Theta}} + \beta_2 - \beta_1(1 + \alpha\kappa_1 U) = 0 \quad (8.29)$$

with γ'_1 given in Eq. (8.28). Analogously, the surface Σ_2 is replaced by a new surface Σ'_2 expressed by

$$X - Y - 2\alpha Z e^{-W(\gamma'_2) - \frac{\beta_2 - Y}{V\Theta}} + \beta_2(1 + \alpha\kappa_1 U) - \beta_1 = 0, \quad (8.30)$$

with γ'_2 given in Eq. (8.28).

Since the amount of slip that asperities undergo during a seismic event is modified by the perturbation, the seismic moment associated with an earthquake is altered as well. The variations in the final slip amplitudes U_1 and U_2 of asperity 1 and asperity 2, respectively, and in the final seismic moment M_0 associated with the different seismic events predicted by the model are listed in Table (8.1).

Table 8.1: Changes in the final slip amplitudes U_1 and U_2 of asperity 1 and 2 and in the seismic moment M_0 associated with the different seismic events predicted by the model, after a stress perturbation from neighbouring faults. The entry *e.n.* is the abbreviation for *evaluated numerically*. The unperturbed slip amplitudes and seismic moment are listed in Table (7.1).

Kind of event	ΔU_1	ΔU_2	ΔM_0
one-mode 10	$\Delta\beta_1\kappa_1 U$	-	$\Delta\beta_1\kappa_1 M_1$
one-mode 01	-	$\Delta\beta_2\kappa_1 U$	$\Delta\beta_2\kappa_1 M_1$
two-mode 10-01/01-10	$\Delta\beta_1\kappa_1 U$	$\Delta\beta_2\kappa_1 U$	$\kappa_1 M_1(\Delta\beta_1 + \Delta\beta_2)$
involving mode 11	<i>e.n.</i>	<i>e.n.</i>	<i>e.n.</i>

8.2.1 Changes in Coulomb forces

The variations in tangential stresses and static frictions discussed so far entail a change in the Coulomb forces assigned to the asperities. Combining Eq. (8.2) with Eq. (8.7) and Eq. (8.8), these changes are given by

$$\Delta F_1^C = -\Delta F_1 - \Delta\beta_1 = (1 + \alpha)\Delta X - \alpha\Delta Y - \Delta\beta_1 \quad (8.31)$$

$$\Delta F_2^C = -\Delta F_2 - \Delta\beta_2 = (1 + \alpha)\Delta Y - \alpha\Delta X - \Delta\beta_2 \quad (8.32)$$

or, exploiting Eq. (8.16) and Eq. (8.17),

$$\Delta F_1^C = \frac{(1 + \alpha) \cos \vartheta - \alpha \sin \vartheta}{\sqrt{2 - \sin 2\vartheta}} \Delta R - \Delta\beta_1 \quad (8.33)$$

$$\Delta F_2^C = \frac{(1 + \alpha) \sin \vartheta - \alpha \cos \vartheta}{\sqrt{2 - \sin 2\vartheta}} \Delta R - \Delta\beta_2. \quad (8.34)$$

The sign of ΔF_i^C ($i = 1, 2$) determines whether the perturbation brings an asperity closer to or farther from the failure; specifically, positive variations entail that slip is favoured, and vice-versa. Equations (8.33) and (8.34) clearly point out that this effect is regulated by the orientation of the vector $\Delta \mathbf{R}$ in the state space. Bearing in mind the observations concerning the orientation of the gradients ∇F_1^C and ∇F_2^C made in §8.1, we find that: ΔF_1^C is maximum when $\Delta \mathbf{R}$ is perpendicular to plane Π_1 and points toward it; it vanishes when $\Delta \mathbf{R}$ is parallel to plane Π_1 ; it is minimum when $\Delta \mathbf{R}$ is perpendicular to plane Π_1 and points away from it. Analogous considerations can be made for ΔF_2^C .

On the whole, the effect of the stress perturbation can be discussed in terms of the quantity

$$\Delta F^C = \Delta F_2^C - \Delta F_1^C = (1 + 2\alpha) (\Delta Y - \Delta X) + \Delta\beta_1 - \Delta\beta_2. \quad (8.35)$$

Let us assume that the system is at a certain state $(X, Y, Z) \in \mathbf{H}_1$ before the perturbation; accordingly, the next seismic event on the fault will start with the failure of asperity 1. If $\Delta F^C > 0$, the perturbation favours the slip of asperity 2 over the slip of asperity 1: therefore, the system is brought to a state closer to the condition for the simultaneous failures of the asperities and thus to the Σ surface. On the contrary, perturbations for which $\Delta F^C < 0$ take the system farther from the Σ surface. The opposite holds for an unperturbed state $(X, Y, Z) \in \mathbf{H}_2$.

8.2.2 Changes in the duration of the interseismic interval

As already stated, stress perturbations can anticipate or delay the occurrence of an earthquake produced by a certain asperity. This effect can be quantified in terms of the variation in the duration of the interseismic interval. Generally speaking, the perturbation vector $\Delta \mathbf{R}$ may cross the Σ surface and thus bring the system from an unperturbed state within \mathbf{H}_1 (\mathbf{H}_2) to a perturbed state within \mathbf{H}'_2 (\mathbf{H}'_1). For the sake of simplicity, only the particular case in which the perturbation

vector $\Delta \mathbf{R}$ does not cross the Σ surface is considered here. An example of a more general case will be shown in §8.3 for a real fault.

Let us first focus on the case in which the unperturbed state $(X, Y, Z) \in \mathbf{H}_1$. The time required by the orbit of the system to reach plane Π_1 , triggering the failure of asperity 1, was given in Eq. (7.31). If the stress perturbation brings the system to a state $(X', Y', Z') \in \mathbf{H}'_1$ and the static friction on asperity 1 to β_1 , the time required by the orbit to reach plane Π'_1 is

$$T'_1 = \Theta W(\gamma'_1) + \frac{\beta_1 - X'}{V} \quad (8.36)$$

with γ'_1 given in Eq. (8.28). The difference between the two times is

$$\Delta T_1 = T'_1 - T_1 = \Theta [W(\gamma'_1) - W(\gamma_1)] - \frac{\Delta F_1^C + \alpha \Delta Z}{V} \quad (8.37)$$

where Eq. (8.31) has been employed. If instead $(X, Y, Z) \in \mathbf{H}_2$, the time required by the orbit of the system to reach plane Π_2 , triggering the failure of asperity 2, was given in Eq. (7.34). If the stress perturbation takes the system to a state $(X', Y', Z') \in \mathbf{H}'_2$ and the static friction on asperity 2 to β_2 , the time required to reach plane Π'_2 is

$$T'_2 = \Theta W(\gamma'_2) + \frac{\beta_2 - Y'}{V} \quad (8.38)$$

with γ'_2 given in Eq. (8.28). The difference between the two times is

$$\Delta T_2 = T'_2 - T_2 = \Theta [W(\gamma'_2) - W(\gamma_2)] - \frac{\Delta F_2^C - \alpha \Delta Z}{V} \quad (8.39)$$

where Eq. (8.32) has been employed. Positive values of ΔT_1 and ΔT_2 correspond to a delay in the occurrence of an earthquake on asperity 1 and 2, respectively, and vice-versa.

8.2.3 Comparison with the elastic case

According to the model, rock rheology plays a critical role in the response to stress perturbations. In the case of purely elastic coupling between the asperities, Dragoni and Piombo (2015) showed that the changes in the duration of the interseismic interval prior to the failure of asperity 1 and 2 are, respectively,

$$\Delta T_1 = -\frac{\Delta F_1^C}{V}, \quad \Delta T_2 = -\frac{\Delta F_2^C}{V}. \quad (8.40)$$

Accordingly, an increase in the Coulomb force associated with a given asperity ($\Delta F_i^C > 0$) directly yields the anticipation of the slip of that asperity, and

vice-versa. What is more, the variation in the duration of the interseismic interval is proportional to the change in the Coulomb force associated with the asperity.

Conversely, in the viscoelastic case there is no straightforward connection between the sign of ΔF_i^C and the anticipation or delay of an earthquake on the associated asperity. In fact, the expressions (8.37) and (8.39) obtained for ΔT_1 and ΔT_2 indicate that the net effect depends in a non trivial way on the particular state of the fault at the time of the stress perturbation and right after it. This result points out the complex interplay between the post-seismic evolution of a fault in the presence of viscoelastic relaxation and the stress transfer from neighbouring faults.

8.3 An application: perturbation of the 1992 Landers fault by the 1999 Hector Mine earthquake

I study the effects of the 16 October 1999 M_w 7.1 Hector Mine, California, earthquake on the post-seismic evolution of the fault that generated the 28 June 1992 M_w 7.3 Landers, California, earthquake. The geometry of the two faults is shown in Fig. (8.2).

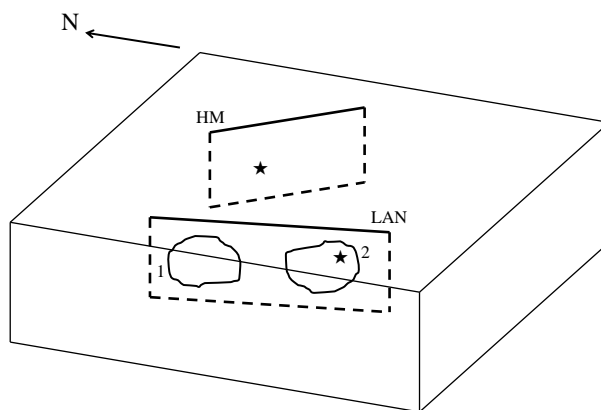


Figure 8.2: Geometry of the Landers (LAN) and Hector Mine (HM), California, faults that generated the 1992 and 1999 earthquakes, respectively. The stars indicate the hypocentres of the seismic events. The labels 1 and 2 identify the asperities on the Landers fault.

The 1992 Landers earthquake was due to right-lateral strike-slip faulting within the Mojave block, a part of the eastern California shear zone to the east of the San Andreas fault, accommodating part of the motion of the Pacific plate with respect to the North American plate (Masterlark and Wang, 2002). A sketch of the tectonic setting is shown in Fig. (8.3).

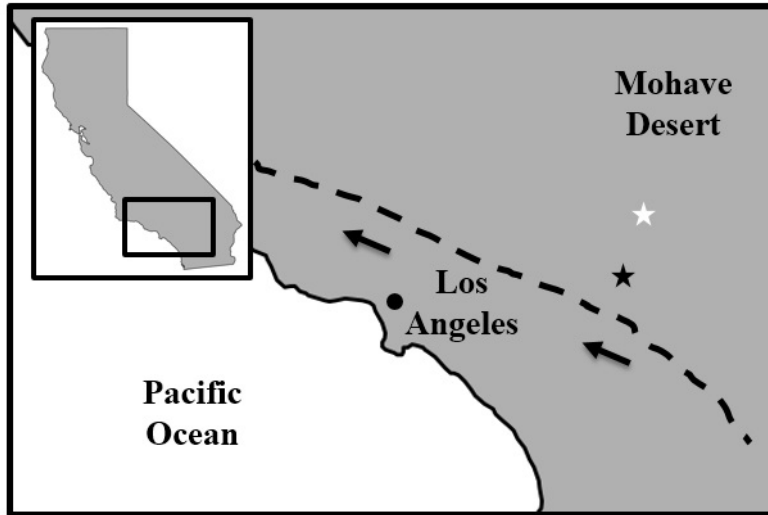


Figure 8.3: Geographic location of the 1992 Landers and 1999 Hector Mine, California, earthquakes. The black star denotes the epicenter of the former, the white one the epicenter of the latter. Black arrows indicate the relative motion of the Pacific plate with respect to the North American plate, whereas the thick dashed line identifies the boundary between the tectonic plates.

Although geodetic and seismological observations indicate a very heterogeneous slip distribution along a multiple-segment fault (Wald and Heaton, 1994), the event can be approximated as the result of the slip of two coplanar asperities (Kanamori et al., 1992): a northern one (asperity 1) and a southern one (asperity 2), with average slips $u_1 = 6$ m and $u_2 = 3$ m, respectively. The earthquake started with the failure of asperity 2, followed by the failure of asperity 1. Following Dragoni and Tallarico (2016), a common area $A = 300$ km² for both asperities and a distance $a = 30$ km between their centres are assumed. The centres of asperity 1 and asperity 2 are placed at (34.46° N, 116.52° W) and (34.20° N, 116.44° W), respectively, with a common depth of 8 km. I characterize the event by strike, dip and rake angles of 345°, 85° and 180°, respectively, an average of the values provided by Kanamori et al. (1992) for the two phases of the earthquake.

As for the shear zone containing the fault, I take an average rigidity $\mu = 30$ GPa

(Kanamori et al., 1992) and a width $d = 80$ km (Masterlark and Wang, 2002). The relative plate velocity is $v = 3 \text{ cm a}^{-1}$ (Wallace, 1990) and the tangential stress rate on the fault is $\dot{\sigma}_t \simeq 3 \times 10^{-4} \text{ Pa s}^{-1}$ (Eq. A.9).

GPS and InSAR measurements highlighted significant post-seismic deformation after the 1992 event. Multiple processes have been suggested to explain the observations, such as aseismic afterslip on or beneath the seismogenic rupture zone, poroelastic rebound and viscoelastic relaxation of the upper mantle. Even though a combination of mechanisms seems to be required to explain the geodetic measurements (Fialko, 2004), I assume viscoelastic relaxation as the predominant post-seismic process. Modelling of viscoelastic relaxation has led to several estimates of the viscosity of the lower crust at Landers. For the sake of the present application, I average the values provided by a number of authors (Deng et al., 1998; Pollitz et al., 2000; Freed and Lin, 2001; Masterlark and Wang, 2002) and assume a viscosity $\eta = 5 \cdot 10^{18} \text{ Pa s}$. The corresponding Maxwell relaxation time is $\theta = \eta/\mu \simeq 5 \text{ a}$.

With the data listed above, the parameters of the model are calculated. From Eq. (7.91) and Eq. (6.121), we get $\alpha = 0.1$ and $\beta = 0.5$. From Eq. (5.24) and taking $\epsilon = 0.7$ (e.g. Jaeger and Cook, 1976), we get $U \simeq 0.546$. I take $\gamma = 1.5$ as in Dragoni and Tallarico (2016), a value yielding modelled moment rate and seismic spectrum comparable with the observations. Thus, we have $\kappa_1 \simeq 0.52$ from Eq. (5.25). Finally, we have $V\Theta \simeq 0.007$ from Eq. (7.96).

The 1992 earthquake is modelled as a two-mode event 01-10 starting from mode 00. Accordingly, the orbit of the system during mode 00 lies on the surface Σ_2 inside the subset \mathbf{H}_2 of the sticking region (Fig. 7.6) and the state P_1 at the beginning of the earthquake belongs to segment \mathbf{s}_2 (Fig. 7.3). The coordinates of P_1 are

$$X_1 = \alpha Z_1 + 1 - \alpha\beta\kappa_1 U, \quad Y_1 = \beta - \alpha Z_1, \quad Z_1 \quad (8.41)$$

with

$$Z_a \leq Z_1 \leq Z_b, \quad (8.42)$$

where the extreme values Z_a and Z_b correspond to the end points (F.26) and (F.27) of \mathbf{s}_2 :

$$Z_a = \frac{\kappa_1 U (\alpha\beta + 1) - 1}{\alpha}, \quad Z_b = \frac{\beta(1 - \kappa_1 U)}{\alpha}. \quad (8.43)$$

At the end of mode 01, the system is at point P_2 with coordinates

$$X_2 = X_1, \quad Y_2 = Y_1 - \beta\kappa_1 U, \quad Z_2 = Z_1 - \beta\kappa_1 U, \quad (8.44)$$

where mode 10 starts. As Z_1 varies in the interval (8.42), an infinite number of points P_2 describe a segment \mathbf{r}_2 on the subset \mathbf{Q}_1 of the face $AECD$ and parallel to the edge CD . Mode 10 terminates at point P_3 with coordinates

$$X_3 = X_2 - \kappa_1 U, \quad Y_3 = Y_2, \quad Z_3 = Z_2 + \kappa_1 U. \quad (8.45)$$

Again, as Z_1 varies in the interval (8.42), there is an infinite number of points P_3 defining another segment \mathbf{q}_2 parallel to the edge CD . This segment is situated within the sticking region and crosses the surface Σ for $Z_1 = Z_c$, with $Z_a < Z_c < Z_b$. Furthermore, it intersects the surface Σ_2 for $Z_1 = Z_d$, with $Z_a < Z_d < Z_c$, and the surface Σ_1 for $Z_1 = Z_e$, with $Z_c < Z_e < Z_b$.

Every state P_1 on segment \mathbf{s}_2 , where the 1992 earthquake began, corresponds to a specific state P_3 on segment \mathbf{q}_2 , where the 1992 earthquake ended. Exploiting Eq. (8.44), we can express the coordinates (8.45) of P_3 as a function of Z_1 . Since \mathbf{q}_2 crosses the surface Σ , the state P_3 can belong to \mathbf{H}_1 , \mathbf{H}_2 or Σ , in correspondence to $Z_c < Z_1 \leq Z_b$, $Z_a \leq Z_1 < Z_c$ and $Z_1 = Z_c$, respectively. In the first case, the next event will start with the failure of asperity 1; in the second case, with the failure of asperity 2; in the third case, with the simultaneous failures of the asperities. With the values of α, β, κ_1 and U listed above, we find $Z_a \simeq -7.02$, $Z_b \simeq 3.58$, $Z_c \simeq 0.78$, $Z_d \simeq 0.71$ and $Z_e \simeq 0.92$. Accordingly, only about one fourth of segment \mathbf{q}_2 lies inside the subset \mathbf{H}_1 of the sticking region. Without any further discussion and neglecting the stress perturbation caused by the Hector Mine earthquake, we would infer that future events on the 1992 fault are more likely to start with the failure of asperity 2.

8.3.1 Stress perturbation by the 1999 Hector Mine earthquake

The 1999 Hector Mine earthquake was generated by right-lateral strike-slip faulting located at (34.59° N, 116.27° W), about 20 km northeast from the Landers fault (Jónsson et al., 2002; Salichon et al., 2004). I characterize the event averaging the data available in the SRCMOD database and assume: strike, dip and rake angles of 330° , 80° and 180° , respectively; a depth of 10 km; a seismic moment of

6.62×10^{19} Nm.

The stress transferred to the asperities at Landers is evaluated employing the model of Appendix H, taking

$$\phi_1 = 345^\circ, \quad \phi_2 = 330^\circ, \quad \psi_1 = 85^\circ, \quad \psi_2 = 80^\circ, \quad \lambda_1 = \lambda_2 = 180^\circ. \quad (8.46)$$

As a result, the normal and tangential components of the perturbing stress on asperity 1 are

$$\sigma_{1n} \simeq 0.14 \text{ MPa}, \quad \sigma_{1t} \simeq 0.39 \text{ MPa}. \quad (8.47)$$

Accordingly, the static friction on asperity 1 is reduced and right-lateral slip is favoured. As for asperity 2, the components of the perturbing stress are

$$\sigma_{2n} \simeq 0.18 \text{ MPa}, \quad \sigma_{2t} \simeq -0.17 \text{ MPa}, \quad (8.48)$$

suggesting that static friction on asperity 2 is reduced and right-lateral slip is inhibited.

Let us now introduce the effect of the perturbation in the framework of the discrete model. The changes in the tangential forces (7.16) on the asperities are

$$\Delta F_1 = -\frac{\sigma_{1t}}{f_{s1}} A, \quad \Delta F_2 = -\frac{\sigma_{2t}}{f_{s1}} A. \quad (8.49)$$

An estimate of the static friction f_{s1} on asperity 1 was provided in Eq. (7.95): accordingly, we get $f_{s1}/A \simeq 7.9$ MPa. Hence, we have

$$\Delta F_1 \simeq -0.05, \quad \Delta F_2 \simeq 0.02. \quad (8.50)$$

From Eq. (8.9) – (8.11), the components of the perturbation vector $\Delta \mathbf{R}$ are

$$\Delta X \simeq 0.043, \quad \Delta Y \simeq -0.016, \quad \Delta Z \simeq -0.059. \quad (8.51)$$

As a result, the orientation of $\Delta \mathbf{R}$ in the state space is characterized by angles $\vartheta \simeq -0.35$ rad and $\varphi \simeq -0.91$ rad. The changes in static frictions (8.19) can be calculated as

$$\Delta \beta_1 = -\frac{k_s \sigma_{1n}}{f_{s1}} A, \quad \Delta \beta_2 = -\frac{k_s \sigma_{2n}}{f_{s1}} A, \quad (8.52)$$

where k_s is the effective static friction coefficient on asperity 1. Assuming $k_s = 0.4$, we get

$$\Delta \beta_1 \simeq -0.0073, \quad \Delta \beta_2 \simeq -0.0092. \quad (8.53)$$

Finally, from Eq. (8.31) and Eq. (8.32), the changes in Coulomb forces on the asperities are

$$\Delta F_1^C \simeq 0.057, \quad \Delta F_2^C \simeq -0.012. \quad (8.54)$$

At the time of the Hector Mine earthquake, the Landers fault was at a state P_4 resulting from the post-seismic evolution of any of the possible states $P_3 \in \mathbf{q}_2$ where the 1992 event ended. The coordinates of P_4 can be calculated from the solution to the equations of mode 00 given by Eq. (7.28) and taking into account that the time interval \tilde{t} elapsed between the 1992 Landers and 1999 Hector Mine earthquakes amounts to about 7.3 years:

$$X_4 = X_3 + V \tilde{T}, \quad Y_4 = Y_3 + V \tilde{T}, \quad Z_4 = Z_3 e^{-\tilde{T}/\Theta}, \quad (8.55)$$

where

$$\frac{\tilde{T}}{\Theta} = \frac{\tilde{t}}{\theta} \approx 1.5. \quad (8.56)$$

Making use of Eq. (8.44) and Eq. (8.45), we can express the coordinates of P_4 as a function of $Z_1 \in [Z_a, Z_b]$. Accordingly, there is an infinite number of points P_4 defining a segment \mathbf{t}_2 inside the sticking region. At $T = \tilde{T}$, the perturbation vector $\Delta \mathbf{R}$ moves every state P_4 to a new state P'_4 with coordinates

$$X'_4 = X_4 + \Delta X, \quad Y'_4 = Y_4 + \Delta Y, \quad Z'_4 = Z_4 + \Delta Z \quad (8.57)$$

which can be expressed as a function of $Z_1 \in [Z_a, Z_b]$. As a result, a new segment \mathbf{t}'_2 identifies the state of the Landers fault after the Hector Mine earthquake.

In order to characterize the effect of the perturbation, let us consider the difference ΔF^C defined in Eq. (8.35): from Eq. (8.54), we get $\Delta F^C \simeq -0.069$. Since $\Delta F^C < 0$, we conclude that the stress perturbation is such that: states $P_4 \in \mathbf{H}_1$ are moved to \mathbf{H}'_1 ; the state $P_4 \in \Sigma$ enters \mathbf{H}'_1 ; states $P_4 \in \mathbf{H}_2$ are shifted towards the Σ surface and some of them enter \mathbf{H}'_1 . Specifically, we find that P'_4 belongs to \mathbf{H}'_1 , \mathbf{H}'_2 and Σ' in correspondence to $Z'_c < Z_1 \leq Z_b$, $Z_a \leq Z_1 < Z'_c$ and $Z_1 = Z'_c$, with $Z'_c \simeq 0.50$. Furthermore, the state P'_4 lies on the surfaces Σ'_1 and Σ'_2 for $Z_1 = Z'_e$ and $Z_1 = Z'_d$, respectively, with $Z'_d \simeq 0.43$ and $Z'_e \simeq 0.64$. On the whole, we can draw the preliminary conclusion that the stress perturbation is such that future events on the Landers fault starting with the slip of asperity 1 are favoured over events starting with the slip of asperity 2. A deeper discussion is provided in the next section.

8.3.2 Constraints due to the seismic history to date

I now follow a procedure similar to that presented for the 1964 Alaska fault in §7.8.1, exploiting the seismic history between 1999 and the present date in order to improve the knowledge on the state that gave rise to the 1992 Landers earthquake and on the possible future events generated by that fault. After the perturbation caused by the Hector Mine earthquake, the interseismic time T'_{is} of the Landers fault can be calculated from Eq. (8.36) and Eq. (8.38) for states P'_4 belonging to \mathbf{H}'_1 and \mathbf{H}'_2 , respectively:

$$T'_{is} = \begin{cases} \Theta W(\gamma'_1) + \frac{\beta_1 - X'_4}{V}, & Z'_c < Z_1 \leq Z_b \\ \Theta W(\gamma'_2) + \frac{\beta_2 - Y'_4}{V}, & Z_a \leq Z_1 < Z'_c \end{cases} \quad (8.58)$$

where

$$\gamma'_1 = \frac{\alpha Z'_4}{V\Theta} e^{-\frac{\beta_1 - X'_4}{V\Theta}}, \quad \gamma'_2 = -\frac{\alpha Z'_4}{V\Theta} e^{-\frac{\beta_2 - Y'_4}{V\Theta}}. \quad (8.59)$$

Since no earthquakes have been produced by the Landers fault after the occurrence of the Hector Mine event, up to year 2017, the states on segment \mathbf{s}_2 yielding an expected interseismic time (8.58) shorter than or equal to $t'_{is} \approx 17$ years can be excluded. The requirement

$$\frac{T'_{is}}{\Theta} > \frac{t'_{is}}{\theta} \approx 3.5 \quad (8.60)$$

is satisfied by states on segment \mathbf{s}_2 in the subset $\tilde{Z}_a \leq Z_1 \leq \tilde{Z}_b$, with $\tilde{Z}_a \simeq -1.17$ and $\tilde{Z}_b \simeq 2.19$.

As a consequence, the admissible states on segment \mathbf{t}_2 can be constrained. A comparison between the intervals $[\tilde{Z}_a, Z_c]$ and $[Z_c, \tilde{Z}_b]$ points out that more than one half of the acceptable subset of \mathbf{t}_2 belongs to \mathbf{H}_2 . Hence, before the stress perturbation caused by the Hector Mine earthquake, future events on the 1992 Landers fault were more likely to start with the failure of asperity 2. In turn, the refinement of \mathbf{t}_2 limits the acceptable states on the segment \mathbf{t}'_2 . From the amplitude of the intervals $[\tilde{Z}_a, Z'_c]$ and $[Z'_c, \tilde{Z}_b]$, we deduce that the acceptable subset of \mathbf{t}'_2 is almost equally divided between \mathbf{H}'_1 and \mathbf{H}'_2 . Therefore, if we consider the influence of the Hector Mine earthquake on future events generated by the 1992 Landers fault, we conclude that the stress perturbation yielded homogenization in the probability of events starting with the failure of asperity 1 or asperity 2. This result is in agreement with the observation that the perturbation vector $\Delta\mathbf{R}$ shifted the whole segment \mathbf{t}_2 towards the subset \mathbf{H}'_1 of the sticking region.

These conclusions would have to be reconsidered if new stress perturbations from neighbouring faults were to affect the post-seismic evolution of the Landers fault in the future. In addition, if no earthquakes were to be observed for some time on the Landers fault, the refining procedure discussed above could be repeated and the admissible subsets of segments \mathbf{s}_2 , \mathbf{t}_2 and \mathbf{t}'_2 could be constrained with further precision.

8.3.3 Effects of the stress perturbation on future earthquakes

The features of the next seismic event generated by the 1992 Landers fault, as predicted by the present model, are discussed, highlighting the changes due to the 1999 Hector Mine earthquake.

Every state $P_1 \in \mathbf{s}_2$ where the 1992 earthquake begun corresponds to a particular state $P_4 \in \mathbf{t}_2$ and $P'_4 \in \mathbf{t}'_2$ before and after the stress perturbation associated with the Hector Mine earthquake, respectively. Since the segment \mathbf{t}_2 intersects the surface Σ , the state P_4 can belong to $\mathbf{H}_1, \mathbf{H}_2$ or Σ (Fig. 7.4), thus affecting the asperity that will fail the first at the beginning of the next earthquake on the fault. In the first case, the next event will start with the failure of asperity 1, in the second case with the failure of asperity 2, in the third case with the simultaneous failures of the asperities. Analogous considerations hold for states P'_4 in $\mathbf{H}'_1, \mathbf{H}'_2$ and Σ' , respectively. The number and sequence of dynamic modes in the earthquake depend on the subinterval of Z_1 considered. The details are summarized in Table (8.2) for both the unperturbed and perturbed cases.

Taking these specifics into account and referring to Table (7.1) and Table (8.1), I evaluate the seismic moments M_0 and M'_0 associated with the expected future earthquake on the 1992 fault before and after the 1999 Hector Mine earthquake, respectively. In Fig. (8.4), the difference

$$\Delta M_0 = M'_0 - M_0 \quad (8.61)$$

is shown as a function of $Z_1 \in [\tilde{Z}_a, \tilde{Z}_b]$. Owing to the translation imposed to segment \mathbf{t}_2 by the perturbation vector $\Delta \mathbf{R}$, the sign of ΔM_0 changes across the different subintervals of Z_1 . The energy released by the earthquake is increased for $Z_1 \in [Z'_d, Z_d]$, while it is reduced elsewhere.

Table 8.2: Future earthquakes generated by the 1992 Landers, California, fault, as functions of the variable Z_1 describing the initial state of the 1992 event, with $Z_1 \in [\tilde{Z}_a, \tilde{Z}_b] = [-1.17, 2.19]$. The results predicted by the model before and after the stress perturbation associated with the 1999 Hector Mine, California, earthquake are shown. The values $Z_1 = Z_c = 0.78$ and $Z_1 = Z'_c = 0.50$ correspond to the largest possible earthquakes before and after the stress perturbation, respectively. The values $Z_1 = Z_d = 0.71$, $Z_1 = Z'_d = 0.43$, $Z_1 = Z_e = 0.92$ and $Z_1 = Z'_e = 0.64$ correspond to events associated with the separate (consecutive) slips of the asperities.

Future earthquake	Unperturbed condition	Perturbed condition
1-mode event 01	$\tilde{Z}_a \leq Z_1 < Z_d$	$\tilde{Z}_a \leq Z_1 < Z'_d$
2-mode event 01-10	$Z_1 = Z_d$	$Z_1 = Z'_d$
3-mode event 01-11-01	$Z_d < Z_1 < Z_c$	$Z'_d < Z_1 < Z'_c$
2-mode event 11-01	$Z_1 = Z_c$	$Z_1 = Z'_c$
3-mode event 10-11-01	$Z_c < Z_1 < Z_e$	$Z'_c < Z_1 < Z'_e$
2-mode event 10-01	$Z_1 = Z_e$	$Z_1 = Z'_e$
1-mode event 10	$Z_e < Z_1 \leq \tilde{Z}_b$	$Z'_e < Z_1 \leq \tilde{Z}_b$

Another significant effect of the stress perturbation concerns the variation in the interseismic time before the next seismic event. I consider again the post-seismic evolution from 1999 onwards and set the origin of times at the occurrence of the Hector Mine earthquake. The expected interseismic time T_{is} prior to the stress perturbation can be calculated from Eq. (7.31) and Eq. (7.34) for states P_4 belonging to \mathbf{H}_1 and \mathbf{H}_2 , respectively:

$$T_{is} = \begin{cases} \Theta W(\gamma_1) + \frac{1-X_4}{V}, & Z_c < Z_1 \leq \tilde{Z}_b \\ \Theta W(\gamma_2) + \frac{\beta-Y_4}{V}, & \tilde{Z}_a \leq Z_1 < Z_c \end{cases} \quad (8.62)$$

where

$$\gamma_1 = \frac{\alpha Z_4}{V\Theta} e^{-\frac{1-X_4}{V\Theta}}, \quad \gamma_2 = -\frac{\alpha Z_4}{V\Theta} e^{-\frac{\beta-Y_4}{V\Theta}}. \quad (8.63)$$

The interseismic time T'_{is} after the stress perturbation has been given in Eq. (8.58).

The difference

$$\Delta T = T'_{is} - T_{is} \quad (8.64)$$

is shown in Fig. (8.5) as a function of $Z_1 \in [\tilde{Z}_a, \tilde{Z}_b]$. For states $P_4 \in \mathbf{H}_1$ corresponding to $P'_4 \in \mathbf{H}'_1$ and states $P_4 \in \mathbf{H}_2$ corresponding to $P'_4 \in \mathbf{H}'_2$, this difference coincides with (8.37) and (8.39), respectively.

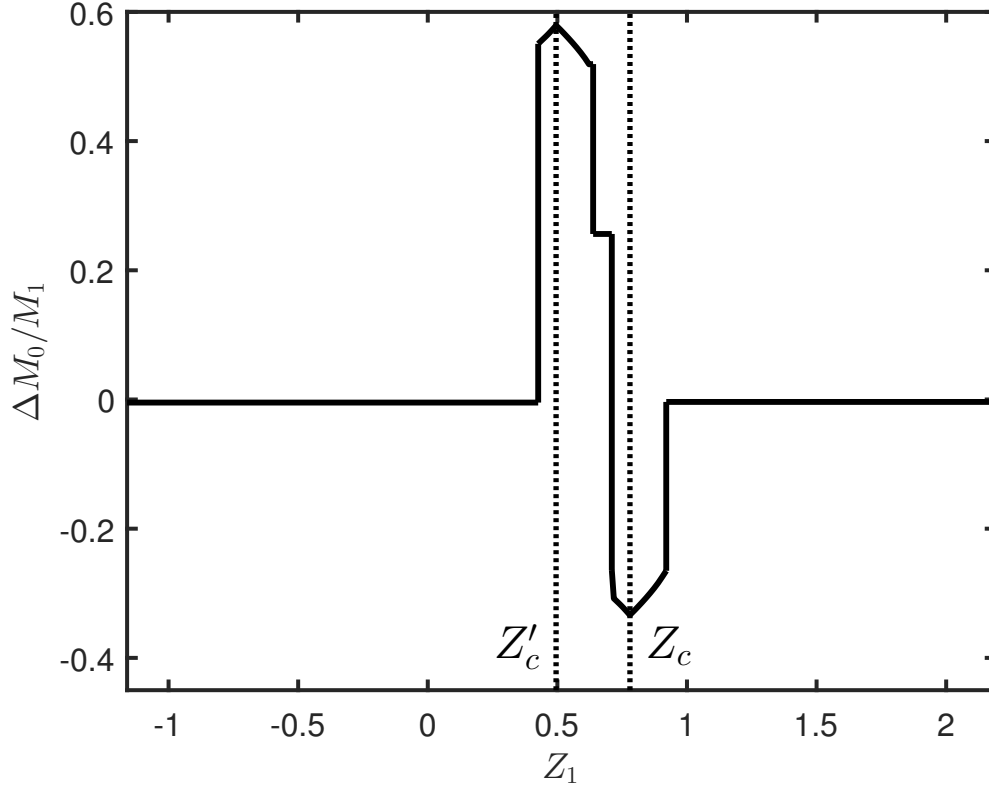


Figure 8.4: Change in the seismic moment released during the next event on the 1992 Landers, California, fault, as a result of the stress perturbation due to the 1999 Hector Mine, California, earthquake. On the horizontal axis, the variable Z_1 describing the initial state of the 1992 event. The values $Z_1 = Z_c$ and $Z_1 = Z'_c$ correspond to the largest possible earthquakes predicted by the model before and after the stress perturbation, respectively, associated with a sequence of modes 11-01.

Some peculiar features stand out. First, we notice that, for all states $P_4 \in \mathbf{H}_2$ corresponding to $P'_4 \in \mathbf{H}'_2$, that is, for $Z_1 \in [\tilde{Z}_a, Z'_c]$, the interseismic time is increased by the stress perturbation, in agreement with the inhibiting effect on asperity 2 suggested by Eq. (8.54). On the other hand, Eq. (8.54) suggests that the failure of asperity 1 is promoted, but this is not verified by all states $P'_4 \in \mathbf{H}'_1$, that is, for $Z_1 \in [Z'_c, \tilde{Z}_b]$. In fact, the interseismic time is reduced only for $Z_1 \in (0.53, \tilde{Z}_b]$, while it is increased for $Z_1 \in [Z'_c, 0.53)$. In the particular case $Z_1 = 0.53$, there is no change in the interseismic time. This is a remarkable result, showing that the presence of viscoelastic relaxation at the time of the stress perturbation entails the unpredictability of the consequent influence in terms of anticipation/delay of future earthquakes, on the basis of the sole knowledge of the change in Coulomb stress.

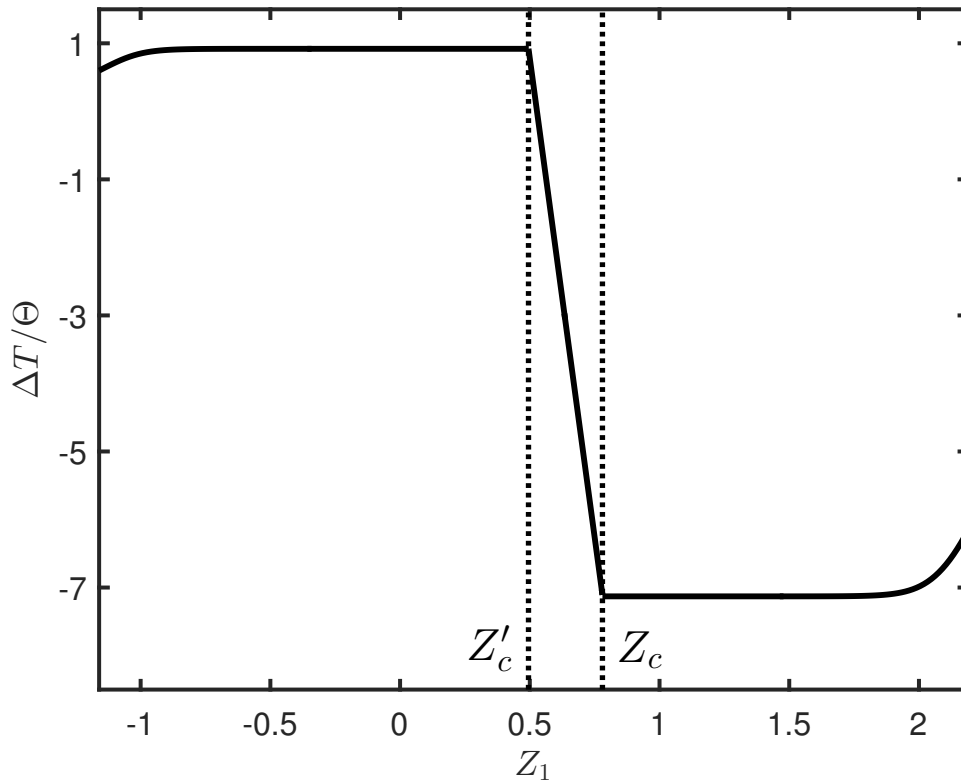


Figure 8.5: Change in the interseismic time before the next event on the 1992 Landers, California, fault, as a result of the stress perturbation due to the 1999 Hector Mine, California, earthquake. On the horizontal axis, the variable Z_1 describing the initial state of the 1992 event. The values $Z_1 = Z_c$ and $Z_1 = Z'_c$ correspond to the largest possible earthquakes predicted by the model before and after the stress perturbation, respectively, associated with a sequence of modes 11-01.

Finally, the same considerations presented in §7.8.2 for the 1964 Alaska fault hold. At the occurrence of the next earthquake produced by the Landers fault, the shape and number of humps in the source function associated with the event and the energy released will reveal more about the state of the system, thus allowing a further refinement of the specific conditions that gave rise to the 1992 event.

Chapter 9

Seismic sequences originated by a fault system

In this chapter, a particular expression of the interaction between neighbouring faults discussed in §2.1.2 is considered: the seismic sequences produced by a fault system.

I name “seismic sequence” a series of earthquakes generated by faults located in a relatively small region (in the order of 100 km) and occurring in a time interval (in the order of few months) much shorter than a typical interseismic interval, when the system is at rest. Seismic sequences are originated by fault systems that produce similar earthquakes in terms of focal mechanism and magnitude. A sequence is typically made of a small number (< 10) of larger events of medium magnitude, in general between 5 and 6, plus a greater number of smaller events. Generally speaking, the time interval elapsing between two seismic sequences in the same region is in the order of several decades at least (Rovida et al., 2011). The present definition of seismic sequence does not include the series of aftershocks following a greater event, since they may have similar features but are strongly conditioned by the main shock. Also, I only focus on the larger events of the sequence, neglecting the smaller ones. This chapter presents a generalized version of the results discussed by Dragoni and Lorenzano (2016).

9.1 The model

The fault model described in §3.4 is adopted and a system made up of n plane faults characterized by the same strike and dip angles is considered. A coordinate

system (x, y, z) is introduced, with x, y and z defined as the strike direction, the horizontal direction perpendicular to strike and depth, respectively. Notice that, in the framework of the present model, x, y and z do not represent the state variables of the system as in the previous chapters. The faults are numbered from 1 to n , according to the order in which they are encountered while moving along the strike direction from one end of the system. A sketch of the model in the case of $n = 3$ faults is shown in Fig. (9.1).

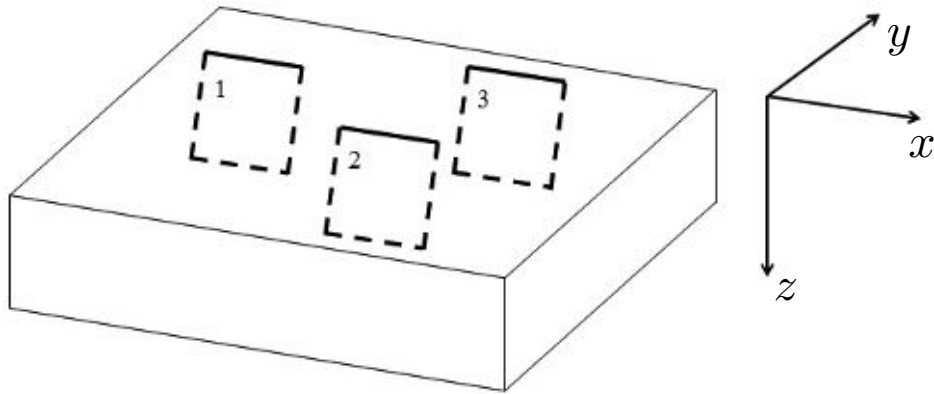


Figure 9.1: A system of $n = 3$ faults, numbered according to the order in which they are encountered while moving along the strike direction x from one end of the system.

Let A_i be the area of the i -th fault and r_{ij} be the distance between the centres of the i -th and the j -th fault. Finally, let δ be the dip angle of the faults. The following assumptions are made:

1. the fault system is subject to a strain rate $\dot{\epsilon}$ that is constant in time and uniform in space;
2. the onset of seismic events is controlled by the average values of tangential traction and static friction on fault surfaces;
3. fault slip is a step function of time and does not produce overshooting;
4. each fault slips only once during a sequence;
5. there is no simultaneous slip of two or more faults and a finite time interval elapses between the failures of any two faults;
6. the duration of a sequence is much shorter than the interval between two consecutive sequences;
7. the system is not subject to external stress perturbations.

Assumption 1 is reasonable, since the n faults are defined as belonging to the

same seismogenic region, for which the same tectonic mechanism is observed. Assumptions 2 and 3 are supported by the fact that I am not interested in the details of each event, which has a much shorter duration than the duration of the sequence, but rather in the relationship between the n events. Assumptions 4, 5 and 6 are suggested by the features of the seismic sequences that are dealt with: such sequences are made of distinct events, each one associated with the failure of a single fault of the system, and there is no reactivation of the same fault during a sequence. As a matter of fact, seismic sequences typically last for several weeks or few months, whereas the interval between two consecutive sequences may be even centuries long. As for assumption 7, it was already shown that the evolution of a fault can be altered by stress perturbations from neighbouring faults (§2.1.2). Generally speaking, contributions from external faults may be numerous during an interseismic interval, but they are smaller than contributions from faults belonging to the system, owing to greater distances and to different orientations of fault surfaces. What is more, such contributions may partially cancel each other out.

Let σ_i be the average tangential traction applied to the i -th fault in the slip direction and τ_i be the average static friction of the i -th fault. Accordingly, the Coulomb stress associated with the i -th fault is (§2.1.2)

$$x_i = \sigma_i - \tau_i, \quad i = 1, 2, \dots, n. \quad (9.1)$$

By definition, the σ_i are always positive or zero; hence, we have

$$-\tau_i \leq x_i \leq 0, \quad i = 1, 2, \dots, n. \quad (9.2)$$

An earthquake is generated by the i -th fault when $x_i = 0$. Introducing the coefficient of static friction k_s , assumed to be the same for the whole fault system, we obtain the rates of σ_i and τ_i as

$$\dot{\sigma}_i = \dot{\sigma}_t, \quad \dot{\tau}_i = k_s \dot{\sigma}_n \quad (9.3)$$

where $\dot{\sigma}_n$ and $\dot{\sigma}_t$ are the normal and tangential stress rates acting on the faults, respectively. Their expressions are calculated from the strain rate $\dot{\epsilon}$ in Appendix A, distinguishing between strike-slip and dip-slip faults. Accordingly, the rate of Coulomb stress for the whole fault system is

$$\dot{x} = \kappa \dot{\sigma} \quad (9.4)$$

where

$$\kappa = \sin \delta (k_s \sin \delta \pm \cos \delta) \quad (9.5)$$

for normal and reverse faults and

$$\kappa = 1 \tag{9.6}$$

for transcurrent faults. Then, during an interseismic intervals, the Coulomb stress of the i -th fault changes in time as

$$x_i(t) = x_{0i} + \dot{x}t \tag{9.7}$$

where x_{0i} is the Coulomb stress at an arbitrary time $t = 0$.

Owing to the presence of friction, the system of n faults represents a nonlinear dynamical system. At any instant in time, the state of the system is described by an n -dimensional vector $\mathbf{x}(t)$ whose components are the Coulomb stresses x_i . Since the system has n degrees of freedom, the phase-space is a $2n$ -manifold. The representative point of the system is enclosed within an n -dimensional parallelepiped \mathbf{S} , defined by the n inequalities (9.2). It is shown in Fig. (9.2) in the case of $n = 3$ faults.

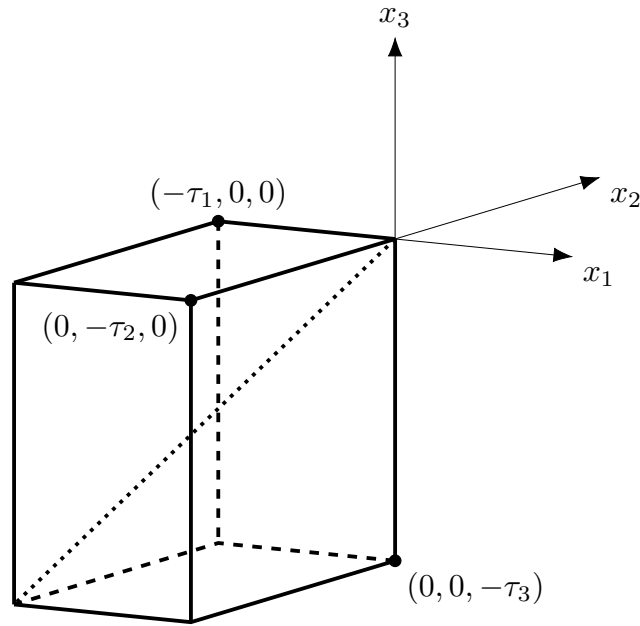


Figure 9.2: The parallelepiped \mathbf{S} enclosing all states of the system, in the case of $n = 3$ faults associated with Coulomb stresses x_i and static frictions τ_i . The dotted segment lies on line (9.8).

During the interseismic intervals, the representative point of the system \mathbf{x} moves inside \mathbf{S} along the line defined by the parametric equations (9.7), which is parallel

to the line

$$x_1 = x_2 = \dots = x_n. \quad (9.8)$$

According to assumption 5, all the components of \mathbf{x} are different from one another. Therefore, one (and only one) component will vanish first, generating the first event in the sequence. At the occurrence of an earthquake, a static stress field is applied to all faults, thus modifying the associated Coulomb stresses and causing a sudden change in the state of the system \mathbf{x} . Generally speaking, the change in Coulomb stress on the j -th fault due to the failure of the i -th fault can be written as

$$\Delta x_{ij}(t) = (\Delta\sigma_{ij} - \Delta\tau_{ij}) H(t) + \Delta x'_{ij}(t) \quad (9.9)$$

where: $\Delta\sigma_{ij}$ and $\Delta\tau_{ij}$ are the coseismic changes in tangential traction and static friction, respectively; H is the Heaviside function; $\Delta x'_{ij}$ is the overall change in Coulomb stress due to time-dependent processes, such as pore fluid diffusion, afterslip and viscoelastic relaxation. The change in static friction is a consequence of the variation in normal stress on the fault.

The coseismic components of $\Delta x_{ij}(t)$ are calculated following the model described in Appendix H, treating the i -th fault as a point-like double-couple source in an unbounded medium. As for the stress change on the i -th fault, it is given by

$$\Delta x_{ii} = -\Delta\sigma_i \quad (9.10)$$

where $\Delta\sigma_i$ is the static stress drop, which can be estimated from the average slip u_i and the fault area A_i as

$$\Delta\sigma_i = C \frac{\mu u_i}{\sqrt{A_i}}. \quad (9.11)$$

Here, C is a nondimensional constant of the order of unity determined by the geometry of the fault (Kanamori, 2001).

As far as the pore fluid diffusion is concerned, I discussed in §2.3.2 how the coseismic stress field may induce a fluid flow that changes the stress field in turn. In the particular case of coplanar faults, the effect of fluid diffusion is at least one order of magnitude smaller than the coseismic stress transfer (Appendix I). Although the evolution of a seismic sequence may be influenced by pore fluid diffusion (e.g. Convertito et al., 2013), this effect is neglected in the following, for the sake of simplicity. As for afterslip and viscoelastic relaxation, I am considering sequences of medium-size earthquakes: accordingly, it is assumed that the seismic

events do not produce appreciable afterslip nor impose significant stress to deeper ductile regions that may relax it afterwards.

For later use, I introduce the differences between the components of the state vector \mathbf{x} as

$$d_{ij}(t) = x_i(t) - x_j(t). \quad (9.12)$$

These differences form an antisymmetric matrix having $n(n - 1)$ nonvanishing components that are related by $(n - 1)^2$ equations. Therefore d_{ij} is known if we know only $n - 1$ components, for example the d_{1j} with $j = 2, 3, \dots, n$.

9.1.1 A particular case: coplanar faults

Let us consider the particular case of a system of n faults lined up in the strike direction x and belonging to the same plane (Fig. 9.3).

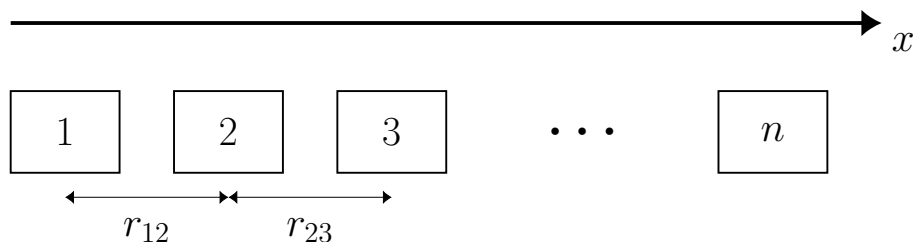


Figure 9.3: A system of n coplanar faults. The x axis is the strike direction. Distances r_{ij} between the i -th and the j -th fault are computed from the fault centres.

The main difference with respect to the more general case discussed beforehand involves the change in Coulomb stress of the j -th fault, following the failure of the i -th fault. In fact, since the faults are coplanar, there are no changes in normal stress on the fault plane; in turn, the static friction on the fault remains the same throughout the sequence. Neglecting the effect of time-dependent processes as before, Eq. (9.9) then reduces to

$$\Delta x_{ij}(t) = \Delta \sigma_{ij} H(t). \quad (9.13)$$

As a result, we can equivalently refer to stress changes or stress transfers. As discussed in Appendix H, the stress transferred to the j -th fault following an earthquake on the i -th fault is always positive in this particular framework. Thus, the j -th component of the state vector \mathbf{x} is reduced in magnitude and the failure

of the corresponding fault is anticipated in time. In conclusion, the cumulative effect of the earthquakes in the sequence is always to concentrate the events in a shorter time interval. A means for quantifying such effect will be discussed later on.

9.2 Evolution of the system

Let t_k be the occurrence times of the events in the sequence ($k = 1, 2, \dots, n$), so that the durations of the interseismic intervals are

$$\Delta t_k = t_{k+1} - t_k, \quad k = 1, 2, \dots, n-1. \quad (9.14)$$

Accordingly, the initial state of the system is expressed by $\mathbf{x}(t_1-)$. If the first event is due to the failure of the i_1 -th fault, \mathbf{x} undergoes a sudden change and its k component becomes

$$x_k(t_1+) = x_k(t_1-) + \Delta x_{i_1 k}. \quad (9.15)$$

Afterwards, \mathbf{x} changes continuously in time, as a consequence of tectonic loading: according to Eq. (9.7), we have

$$x_k(t) = x_k(t_1+) + \dot{x}(t - t_1). \quad (9.16)$$

At $t = t_2$, the second event takes place, due to the failure of the i_2 -th fault, so that \mathbf{x} undergoes another sudden change, and so on. At the end of the sequence, the state of the system is expressed by

$$x_k(t_n+) = x_k(t_n-) + \Delta x_{i_n k}. \quad (9.17)$$

Making use of the previous equations, the final state can be rewritten in terms of the initial state as

$$x_k(t_n+) = x_k(t_1-) + \dot{x} \Delta t + \sum_{j=1}^n \Delta x_{j k} \quad (9.18)$$

where

$$\Delta t = \sum_{k=1}^{n-1} \Delta t_k = t_n - t_1 \quad (9.19)$$

is the duration of the sequence, which can be written as

$$\Delta t = -\frac{x_{i_n}(t_1-)}{\dot{x}} - \frac{1}{\dot{x}} \sum_{j=1}^n \Delta x_{i_j i_n}, \quad i_j \neq i_n. \quad (9.20)$$

We see from Eq. (9.18) that the difference between the final and the initial state consists in two terms: the first one represents the effect of tectonic loading during the time interval Δt , whereas the second one reflects the cumulative effect of the earthquakes in the sequence. The latter term causes the lengthening or the shortening of the duration of the sequence, depending on the features of the stress transfer between the faults of the system. The net effect can be evaluated by calculating how much the occurrence time t_n of the last event is anticipated or delayed: this variation is due to the sum of the stresses that are transferred to the i_n -th fault from the other $n - 1$ faults. From Eq. (9.20), the duration of the sequence in the absence of interaction is given by

$$\Delta t' = \Delta t + \frac{1}{\dot{x}} \sum_{j=1}^n \Delta x_{i_j i_n}, \quad i_j \neq i_n. \quad (9.21)$$

Finally, the interseismic intervals (9.14) can be calculated as

$$\Delta t_k = -\frac{x_{i_{k+1}}(t_k^+)}{\dot{x}}, \quad k = 1, 2, \dots, n - 1. \quad (9.22)$$

The duration and the particular evolution of a seismic sequence strongly depend on the heterogeneity of stress distribution on the faults of the system. One possible way to characterize this feature is provided by the standard deviation associated with the state vector \mathbf{x} . At a given instant in time, it is defined as

$$s = \left[\frac{1}{n} \sum_{i=1}^n (x_i - \bar{x})^2 \right]^{1/2} \quad (9.23)$$

where

$$\bar{x} = \frac{1}{n} \sum_{i=1}^n x_i. \quad (9.24)$$

9.3 Retrieval of the initial and final states

According to the present model, the observation of a seismic sequence allows to retrieve the state of the system at any time during the sequence. In the following, I focus on the evaluation of the state of the system at the onset and at the end of the sequence.

Let us consider a seismic sequence made up of n earthquakes that can be ascribed to the failure of n faults belonging to the same system. Let t_1, t_2, \dots, t_n be the observed occurrence times of the events. The stress transfer matrix can be

calculated from the knowledge of the geometry of the faults and of the seismic moments associated with the events; in turn, it is possible to retrieve the Coulomb stress change matrix Δx_{ij} . Also, the Coulomb stress rate \dot{x} can be determined by means of Eq. (9.4) from the strain rate $\dot{\epsilon}$ provided by geodetic measurements.

Let us focus on the generic fault i_k that generated the k -th event in the sequence. By definition, the Coulomb stress of fault i_k at the onset of the sequence $x_{i_k}(t_1-)$ must be such that it is cancelled by the stress accumulated on the fault up to time t_k . Accordingly, we can write

$$x_{i_k}(t_1-) = -\dot{x}(t_k - t_1) - \sum_{j=1}^{k-1} \Delta x_{i_j i_k}. \quad (9.25)$$

In fact, apart from the sign, the right-hand side is the total stress accumulated on fault i_k since the beginning of the sequence. It consists of two terms: the first term is the tectonic stress concentrated on the fault from the beginning of the sequence up to time t_k , whereas the second term is the sum of stress transfers that the fault i_k has received from the faults i_1, i_2, \dots, i_{k-1} that slipped before it.

As for the final state of fault i_k , it is given by Eq. (9.18). Replacing $x_{i_k}(t_1-)$ in Eq. (9.18) with its expression (9.25), we obtain

$$x_{i_k}(t_n+) = \dot{x}(t_n - t_k) + \sum_{j=k}^n \Delta x_{i_j i_k}. \quad (9.26)$$

Bearing in mind that the Coulomb stress of fault i_k was equal to zero at $t = t_k-$, the final stress is equal to the tectonic stress accumulated in the time interval from t_k to the end of the sequence, plus the stress drop associated with the failure of fault i_k and the stress transfers from the faults $i_{k+1}, i_{k+2}, \dots, i_n$ that slipped after fault i_k .

To sum up, the Coulomb stress of fault i_k at the onset of the sequence depends only on what happened before its failure, while the Coulomb stress at the end of the sequence depends only on what happened after its failure. Notice that the retrieval of the complete state vector of the system requires the knowledge of the entire sequence. An example will be shown in §9.6 for two real cases.

9.4 The order of events

It was already mentioned that the n components of the state vector \mathbf{x} are always different from each other. As a result, they can be ordered according to their magnitudes: at any instant t in time, the set X of the $x_i(t)$ is a well-ordered set. This order controls the order of the events in the seismic sequence, as shown in the following.

Let N_n be the set of the first n natural numbers. According to the premise, a permutation α of N_n can be associated with each state \mathbf{x} of the system, expressing the order of faults in relation to the value of their Coulomb stress:

$$\alpha = \begin{pmatrix} 1 & 2 & \dots & n \\ i_1 & i_2 & \dots & i_n \end{pmatrix} \quad (9.27)$$

where

$$x_{i_1} = \max(X) \quad (9.28)$$

$$x_{i_k} = \max(X - \{x_{i_1}, x_{i_2}, \dots, x_{i_{k-1}}\}) \quad (9.29)$$

with $k = 2, 3, \dots, n$. Hence, the parallelepiped \mathbf{S} enclosing all states of the system can be divided into a number $n!$ of subsets \mathbf{S}_j , corresponding to the $n!$ permutations of N_n . During the interseismic intervals, the permutation α_j associated with the system does not change, because all the x_i increase with the same rate, according to Eq. (9.7). Therefore, the representative point \mathbf{x} remains in the same subset \mathbf{S}_j . At the occurrence of a seismic event, \mathbf{x} switches to a different subset \mathbf{S}_k , characterized by a permutation α_k .

Let us assume that, before the sequence, the permutation associated with the system is

$$\alpha_0 = \begin{pmatrix} 1 & 2 & \dots & n \\ i_1 & i_2 & \dots & i_n \end{pmatrix} \quad (9.30)$$

implying that the first event of the sequence will be generated by the i_1 -th fault. This event changes the magnitudes of all Coulomb stresses, so that the new state of the system is associated with a different permutation

$$\alpha_1 = \begin{pmatrix} 1 & 2 & \dots & n \\ j_1 & j_2 & \dots & j_n \end{pmatrix} \quad (9.31)$$

implying that the second event will be generated by the j_1 -th fault, and so on. After the $(n - 1)$ -th event, the permutation is

$$\alpha_{n-1} = \begin{pmatrix} 1 & 2 & \dots & n \\ k_1 & k_2 & \dots & k_n \end{pmatrix} \quad (9.32)$$

implying that the last event will be generated by the k_1 -th fault. To sum up, the order of events in the sequence is expressed by the permutation

$$\alpha^* = \begin{pmatrix} 1 & 2 & \dots & n \\ i_1 & j_1 & \dots & k_1 \end{pmatrix}. \quad (9.33)$$

The quantities determining α^* are the initial stress state of the fault system, the stress drops and the stress transfers associated with each event. In terms of the order of events, the number of possible sequences in a system made up of n faults is equal to $n!$. Since every fault may slip only once in a sequence (assumption 4), there are $n!$ alternatives for the initial permutation α_0 , but only $(n - 1)!$ for α_1 and $(n - k)!$ for the generic permutation α_k .

9.4.1 Subsequent evolution

After the n -th event of the sequence (i.e., at the end of the sequence), the state of the system is associated with the permutation

$$\alpha_n = \begin{pmatrix} 1 & 2 & \dots & n \\ i & j & \dots & k \end{pmatrix}. \quad (9.34)$$

Accordingly, the next sequence will start with the failure of the i -th fault after an interseismic time interval

$$\Delta T = -\frac{x_i(t_n+)}{\dot{x}} \quad (9.35)$$

where Eq. (9.7) was employed. Generally speaking, the permutation α_n does not coincide with the permutation α_0 characterizing the system at the onset of the sequence. In fact, the stress distribution on the faults is rearranged, owing to the combined effects of stress drops and stress transfers between the faults. In terms of the differences d_{ij} , we have, thanks to Eq. (9.26),

$$d_{ij}(t_n+) - d_{ij}(t_1-) = \sum_{k=1}^n (\Delta x_{ki} - \Delta x_{kj}). \quad (9.36)$$

It is noteworthy that the right-hand side of this expression is different from zero: as a matter of fact, the sum of stress transfers received by a fault during the

sequence is in general different from that received by the other faults, depending on the relative positions of the faults. In conclusion, the next sequence produced by the system will be associated with a different order of events, described by a new permutation α^* .

9.5 Discussion of the model

In this section, the particular conditions of the state of the system that are required in order to observe a seismic sequence with the features listed in §9.1 are first discussed. For the sake of providing a means to better understand the evolution of a seismic sequence, I then focus on the particular case of coplanar faults and discuss the special situation in which the process of stress redistribution within the system is governed by the stress drops.

9.5.1 Constraints on the state of the system

A first constraint on the differences d_{ij} between the components of the state vector \mathbf{x} is determined by assumption 5. Let us assume that the slip of the i -th fault entails a positive change in the Coulomb stress of the j -th fault, that is, $\Delta x_{ij} > 0$. If d_{ij} is smaller than Δx_{ij} , the failure of the i -th fault would immediately produce the failure of the j -th fault, in contrast with the hypothesis of a finite time interval elapsing between any two seismic events of the sequence. Therefore, if $\Delta x_{ij} > 0$, d_{ij} must always be larger than Δx_{ij} . Although this circumstance cannot be validated a priori (since it depends on the specific orientation and location of the j -th fault relative to the i -th fault), it represents an intrinsic property of the system, which must be verified at any time.

An additional condition on d_{ij} is set by the observed durations of seismic sequences. In fact, the d_{ij} must be small enough that a sequence is completed within a few months, if the effect of stress transfer between faults is taken into account. Therefore, in agreement with assumption 6, the stress change $\dot{x} \delta t$ that tectonic loading produces in a time $\delta t \ll \Delta T$ plus the sum of stress changes Δx_{ij} ($i \neq j$) may be assumed as an upper limit for d_{ij} , where ΔT is the interseismic time interval between two sequences. Specifically, a greater value of δt (several decades) can be assumed for lower stress rates \dot{x} , a smaller value (several years) for higher stress rates.

9.5.2 Stress drops vs. stress transfers: a special case

Let us consider a system of n coplanar faults lined up in the strike direction (§9.1.1) generating a seismic sequence made up of n distinct events whose associated stress drops $\Delta\sigma_i$ ($i = 1, 2, \dots, n$) are approximately equal to each other. Also, let us assume that the differences d_{ij} between the components of the state vector \mathbf{x} are such that, following the failure of the i -th fault, the relative magnitude of the other $n - 1$ components of \mathbf{x} does not change.

Let α_0 and α^* be the permutations describing the initial state of the system and the order of events in the sequence, respectively (§9.4). Under the assumptions introduced above, it is easy to see that the only effect of the k -th event of the sequence is simply to shift the label i_k to the last position in the permutation α_k , whereas the stress transfers $\Delta\sigma_{i_k j}$ do not change the relative positions of the other labels. Accordingly, a permutation

$$\eta = \begin{pmatrix} i_1 & i_2 & \dots & i_n \\ i_2 & i_3 & \dots & i_1 \end{pmatrix} \quad (9.37)$$

can be associated with each event, so that the permutation α_k characterizing the state of the system after the k -th event is

$$\alpha_k = \eta\alpha_{k-1}, \quad k = 1, 2, \dots, n. \quad (9.38)$$

As a result, the order of events is given by the initial permutation, i.e., $\alpha^* = \alpha_0$. The final permutation α_n is also equal to α_0 ; however, this circumstance does not imply the repetition of the order α^* in the following sequence. In fact, according to Eq. (9.36), the new sequence will start with different values of d_{ij} , entailing a different order of events.

The special case described here is based on the assumption that the rearrangement in the permutations throughout a sequence can be entirely ascribed to the stress drops $\Delta\sigma_i$, with respect to which the role of stress transfers is negligible. This case is useful as a terms for comparison with real sequences. As a matter of fact, the order implied by α_0 is generally changed during a sequence, since the d_{ij} have the same order of magnitude as the stress transfers $\Delta\sigma_{ij}$ ($i \neq j$), so that the relative magnitude of the components of \mathbf{x} is modified after each event. In addition, if an event k has a stress drop that is considerably larger than the others, the label i_k will permanently occupy the last position in the permutation,

thus altering the initial order. To sum up, the order of events is different from the initial order of stresses, i.e. $\alpha^* \neq \alpha_0$. The final permutation α_n is also different from α_0 .

9.6 Applications

In this section, two applications of the present model are presented. For a better understanding, I first focus on the simpler case of a system of coplanar, lined up faults (see §9.1.1) and study the 2012 Emilia (Italy) seismic sequence. I then move to the general case of non-coplanar faults and consider the 1997-1998 Umbria-Marche (Italy) sequence.

9.6.1 The 2012 Emilia sequence

I consider the 2012 Emilia (Italy) seismic sequence, which was made up of seven events with magnitudes between 5 and 6 (Pezzo et al., 2013). They occurred in the period between May 20th and June 3rd, 2012, and can be ascribed to a fault system of $n = 7$ faults approximately lined up in the West-East direction, with a total length of about 50 km. The faults are all of thrust type, with shallow hypocentres between 5 and 10 km in depth. The geographic location of the sequence is shown in Fig. (9.4).

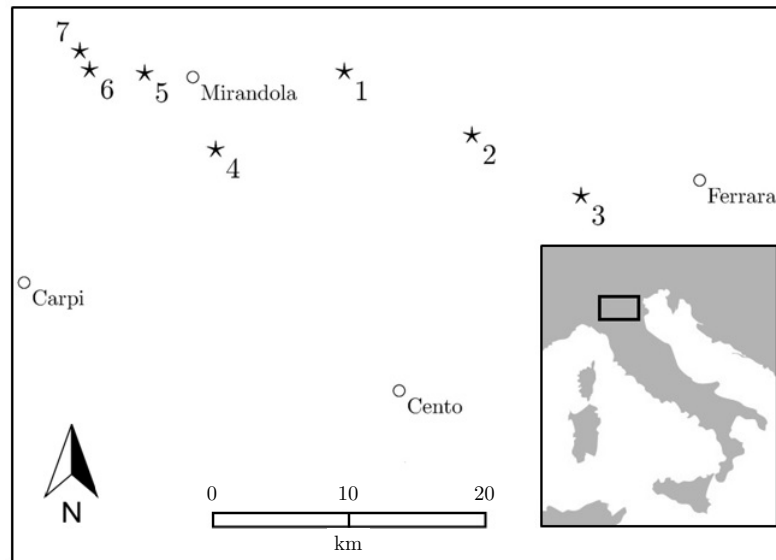


Figure 9.4: Geographic location of the 2012 Emilia (Italy) seismic sequence. Stars indicate the epicentres; numbers indicate the order of fault activation.

In studying the features of the 2012 Emilia sequence, Convertito et al. (2013) suggested that dynamic triggering caused by seismic waves might be the primary factor to explain the evolution of the sequence, in addition to the variation in permeability and pore-pressure effects due to a massive presence of fluids in the Po Plain basin. As stated in §9.1, the role of dynamic triggering and pore fluid diffusion is neglected in the present model. Although these phenomena may alter the sequence of permutations describing the evolution of the sequence, as well as the state of the system at the end of the sequence, they would not change the general conclusions of this section.

All sources are treated as pure reverse dip-slip faults with a dip angle $\delta = 40^\circ$, an average of the values given by Convertito et al. (2013). The areas and the locations of the faults are inferred by employing the distances between hypocentres along the strike direction as constraints (Caporali and Ostini, 2012; Serpelloni et al., 2012). The projection of the faults on a vertical plane is shown in Fig. (9.5).

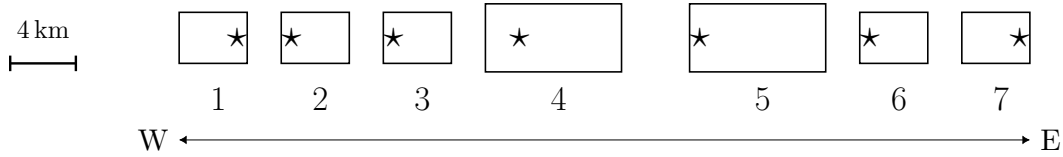


Figure 9.5: Geometry of the model for the 2012 Emilia (Italy) seismic sequence. The rectangles are the projections of faults on a vertical plane. Stars correspond to hypocenters; each fault is labelled with the corresponding index $i = 1, 2, \dots, 7$.

Accordingly, the matrix \mathbf{r} of the distances between the centres of the faults is given by

$$\mathbf{r} \text{ (km)} = \begin{pmatrix} 0 & 5 & 10 & 18 & 30 & 38 & 43 \\ 5 & 0 & 5 & 13 & 25 & 33 & 38 \\ 10 & 5 & 0 & 8 & 20 & 28 & 33 \\ 18 & 13 & 8 & 0 & 12 & 20 & 25 \\ 30 & 25 & 20 & 12 & 0 & 8 & 13 \\ 38 & 33 & 28 & 20 & 8 & 0 & 5 \\ 43 & 38 & 33 & 25 & 13 & 5 & 0 \end{pmatrix}. \quad (9.39)$$

I take $\mu = 30 \text{ GPa}$ for the rigidity of the medium and $k_s = 0.6$ as the effective coefficient of static friction. With a strain rate $\dot{\epsilon} = -3 \times 10^{-15} \text{ s}^{-1}$ (Caporali and Ostini, 2012) and a Poisson modulus $\nu = 0.25$, the rate of Coulomb stress

calculated from Eq. (9.4) is

$$\dot{x} = \kappa \dot{\sigma} \simeq 2 \text{ kPa a}^{-1} \quad (9.40)$$

where κ and $\dot{\sigma}$ are given by Eq. (9.5) and Eq. (A.3), respectively. All other data required by the application of the model are listed in Table (9.1). The origin times and the seismic moments m_i are taken from Pezzo et al. (2013) and Tramelli et al. (2014), respectively. The areas A_i take into account the analysis of Caporali and Ostini (2012) and Serpelloni et al. (2012), whereas the slips u_i are constrained according to the values of m_i and A_i . From Eq. (9.11) with $C = 1$, the values of stress drops $\Delta\sigma_i$ are in the range between 0.9 and 1.9 MPa, consistent with the range evaluated by Castro et al. (2013) from seismic spectra.

Table 9.1: Data for the seismic events of the 2012 Emilia (Italy) sequence. See Fig. (9.5) for fault numbers.

Event	Fault	Origin time (UTC)		t_i (d)	m_i (N m)	A_i (km ²)	u_i (m)
		yyyy/mm/dd	hh:mm:ss				
1	5	2012/05/20	02:03:52	0	8.9×10^{17}	60	0.49
2	6	2012/05/20	02:07:31	0.0025	5.6×10^{16}	16	0.12
3	7	2012/05/20	13:18:02	0.47	5.6×10^{16}	16	0.12
4	4	2012/05/29	07:00:03	9.2	6.3×10^{17}	60	0.35
5	3	2012/05/29	10:55:57	9.4	1.1×10^{17}	16	0.23
6	2	2012/05/29	11:00:25	9.4	7.9×10^{16}	16	0.16
7	1	2012/06/03	19:20:43	15	5.6×10^{16}	16	0.12

According to Table (9.1), the order of events is given by the permutation

$$\alpha^* = \begin{pmatrix} 1 & 2 & 3 & 4 & 5 & 6 & 7 \\ 5 & 6 & 7 & 4 & 3 & 2 & 1 \end{pmatrix}. \quad (9.41)$$

Therefore, the sequence started about in the middle of the system and propagated eastward up to the end of it (5, 6, 7); afterwards, the sequence propagated from the middle to the west end of the system (4, 3, 2, 1).

Combining the data provided in Table (9.1) with the distances r_{ij} listed above, I calculate the stress change matrix Δx_{ij} making use of Eq. (9.11) and Eq. (H.19) for the diagonal and nondiagonal components, respectively. Afterwards, it is

possible to retrieve the state of the system at any time during the sequence, together with the associated permutations, following the procedure discussed in §9.2. Specifically, at the beginning of the sequence we have

$$\alpha_0 = \begin{pmatrix} 1 & 2 & 3 & 4 & 5 & 6 & 7 \\ 5 & 4 & 7 & 1 & 2 & 3 & 6 \end{pmatrix} \quad (9.42)$$

whereas the state after the i -th event of the sequence is described by

$$\alpha_1 = \begin{pmatrix} 1 & 2 & 3 & 4 & 5 & 6 & 7 \\ 6 & 4 & 7 & 1 & 2 & 3 & 5 \end{pmatrix} \quad \alpha_2 = \begin{pmatrix} 1 & 2 & 3 & 4 & 5 & 6 & 7 \\ 7 & 4 & 1 & 2 & 3 & 6 & 5 \end{pmatrix} \quad (9.43)$$

$$\alpha_3 = \begin{pmatrix} 1 & 2 & 3 & 4 & 5 & 6 & 7 \\ 4 & 1 & 2 & 3 & 6 & 7 & 5 \end{pmatrix} \quad \alpha_4 = \begin{pmatrix} 1 & 2 & 3 & 4 & 5 & 6 & 7 \\ 3 & 1 & 2 & 6 & 7 & 4 & 5 \end{pmatrix} \quad (9.44)$$

$$\alpha_5 = \begin{pmatrix} 1 & 2 & 3 & 4 & 5 & 6 & 7 \\ 2 & 1 & 6 & 7 & 4 & 3 & 5 \end{pmatrix} \quad \alpha_6 = \begin{pmatrix} 1 & 2 & 3 & 4 & 5 & 6 & 7 \\ 1 & 6 & 7 & 2 & 4 & 3 & 5 \end{pmatrix} \quad (9.45)$$

$$\alpha_7 = \begin{pmatrix} 1 & 2 & 3 & 4 & 5 & 6 & 7 \\ 6 & 7 & 1 & 2 & 4 & 3 & 5 \end{pmatrix} \quad (9.46)$$

The initial state $\mathbf{x}(t_1-)$ and the final state $\mathbf{x}(t_7+)$ are shown in Fig. (9.6). Since the origin of times was set at the onset of the first event, we have $x_5(t_1-) = 0$.

Some peculiar features stand out. First of all, the initial (α_0) and final (α_7) permutations do not coincide; what is more, they are both different from the permutation α^* giving the order of events during the 2012 sequence. This is a direct consequence of the heterogeneous distribution of seismic moment in the fault system and of the dissimilar magnitude of the stress drops on the faults. In particular, we notice that fault 5 permanently occupies the last position in all permutations from α_1 to α_7 , as a consequence of its larger stress drop. Furthermore, the permutations α_i suggest that the stress transfers $\Delta\sigma_{ij}$ play a major role in determining the evolution of the sequence and that the rearrangement in the permutations cannot be entirely ascribed to the stress drops $\Delta\sigma_i$, as supposed in §9.5.2. In fact, Eq. (9.38) does not hold for any value of k .

The duration of the sequence is

$$\Delta t = t_7 - t_1 \simeq 15 \text{ d.} \quad (9.47)$$

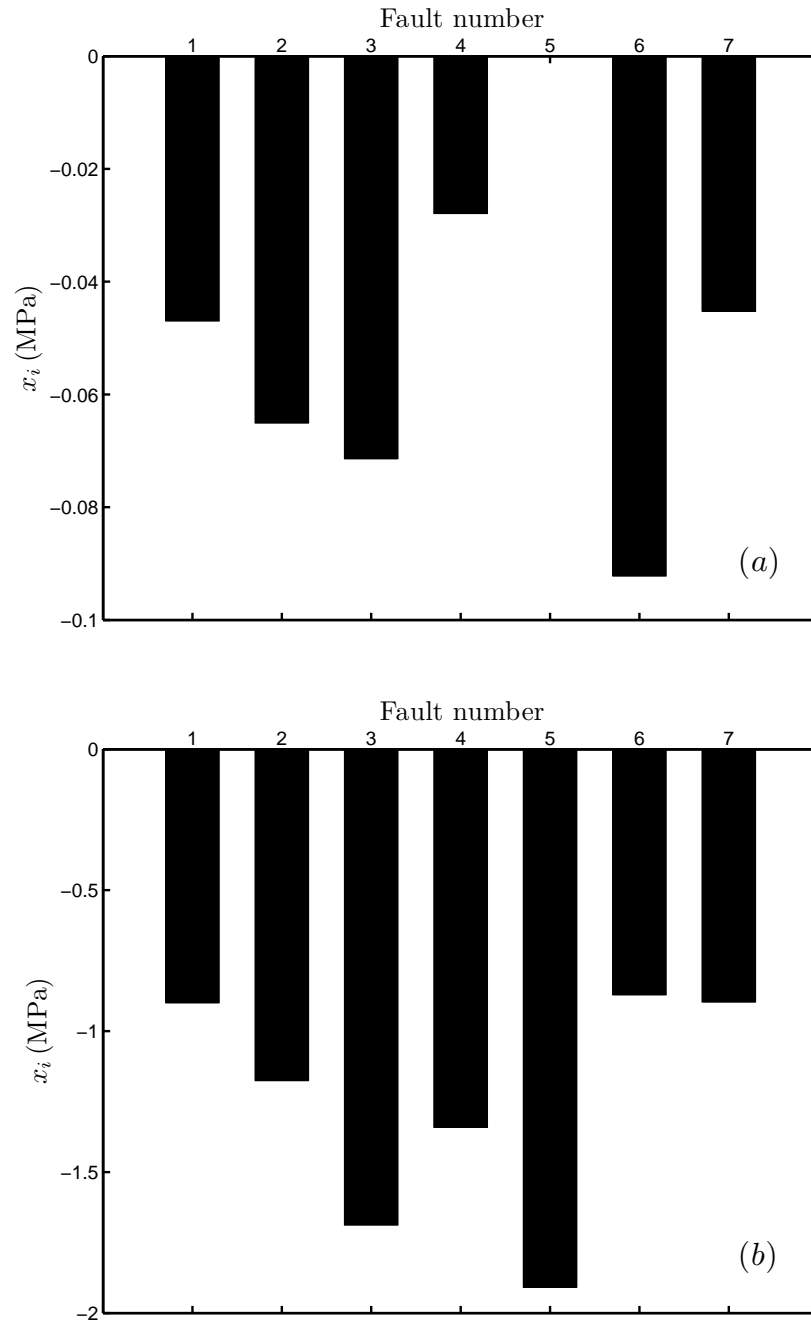


Figure 9.6: Initial (a) and final (b) states calculated from the model for the 2012 Emilia (Italy) seismic sequence. Histograms show the components of the state vector \mathbf{x} at the beginning and at the end of the sequence.

In the absence of fault interaction, it would have been

$$\Delta t' = -\frac{x_6(t_1-)}{\dot{x}} \simeq 46 \text{ a} \quad (9.48)$$

where Eq. (9.21) was employed. Hence, the process of stress transfer between the faults of the system caused a severe shortening of the duration of the seismic

sequence, with a ratio $\Delta t'/\Delta t \simeq 10^3$.

I now compare the stress states on the fault system at the beginning and at the end of the sequence. To this aim, the mean value (9.24) of the state vector \mathbf{x} and its standard deviation (9.23) at $t = t_1 -$ and $t = t_7 +$ are considered. At the beginning of the sequence, we have

$$\bar{x} \simeq -0.05 \text{ MPa}, \quad s \simeq 0.03 \text{ MPa} \quad (9.49)$$

whereas at the end of the sequence

$$\bar{x} \simeq -1.2 \text{ MPa}, \quad s \simeq 0.4 \text{ MPa}. \quad (9.50)$$

Accordingly, Coulomb stresses are more spread out at the end of the sequence than before, since the standard deviation in Eq. (9.50) is one order of magnitude larger than in Eq. (9.49). As an additional means to visualize the particular distribution of stress on the fault system before and after the seismic sequence, I consider the average values

$$\bar{d}_i = \frac{\sum_{j=1}^n |d_{ij}|}{n-1}, \quad j \neq i. \quad (9.51)$$

At the beginning of the sequence, we find

$$\bar{d}_i \simeq (20, 30, 30, 30, 60, 50, 30) \text{ kPa}, \quad (9.52)$$

whereas at the end of the sequence we have

$$\bar{d}_i \simeq (400, 400, 600, 400, 700, 400, 400) \text{ kPa}. \quad (9.53)$$

We conclude that, at the end of the sequence, the average difference between the Coulomb stress on the i -th fault and the other $(n-1)$ faults is increased by about one order of magnitude with respect to the average difference characterizing the state at the beginning of the sequence. This result confirms that the distribution of stress on the fault system is eventually made more heterogeneous by the seismic events. This feature will play an essential role in the evolution of the system during the next seismic sequence.

The permutation α_7 in Eq. (9.46) shows that, according to the present model, the next sequence will start with the failure of fault 6, i.e, at the eastern end of the fault system. It will take place after an interseismic interval

$$\Delta T = -\frac{x_6(t_7+)}{\dot{x}} \simeq 440 \text{ a} \quad (9.54)$$

where Eq. (9.35) was employed. This figure appears to be representative of typical recurrence times of moderate-size earthquakes along the Ferrara-Romagna arc: the largest event in this area before the 2012 sequence was the M_w 5.5 November 17, 1570, Ferrara earthquake (Rovida et al., 2011).

9.6.2 The 1997 - 1998 Umbria-Marche sequence

I consider the 1997-1998 Umbria-Marche (Italy) seismic sequence, which was made up of eight events with moment magnitudes between 5 and 6 (Morelli et al., 2000). The geographic location of the sequence is shown in Fig. (9.7).

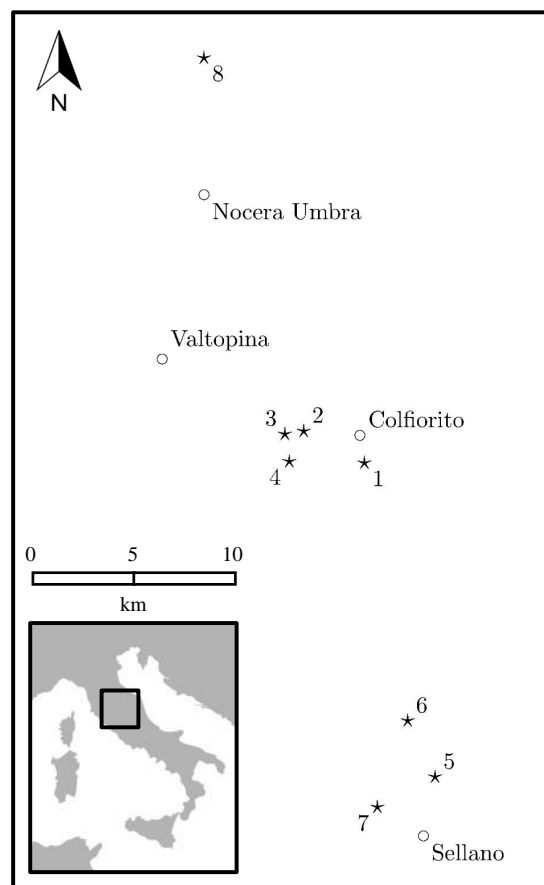


Figure 9.7: Geographic location of the 1997-1998 Umbria-Marche (Italy) seismic sequence. Stars indicate the epicentres; numbers indicate the order of fault activation.

The sequence started on 26 September 1997 and lasted for more than six months, ending on 3 April 1998. The earthquakes are ascribed to a fault system of $n = 8$ faults approximately lined up in the North West - South East direction, with a total length of about 40 km. All sources are treated as pure normal dip-slip faults with shallow hypocentres between 2 and 8 km in depth (Bindi et al., 2004).

Averaging the figures given by Morelli et al. (2000) for the eight seismic events, the dip angle of the fault system is $\delta = 40^\circ$. The geometry and the location of each fault are chosen using the models proposed by Hunstad et al. (1999), Capuano et al. (2000), Cocco et al. (2000) and Tallarico et al. (2005) as a starting point (Fig. 9.8).

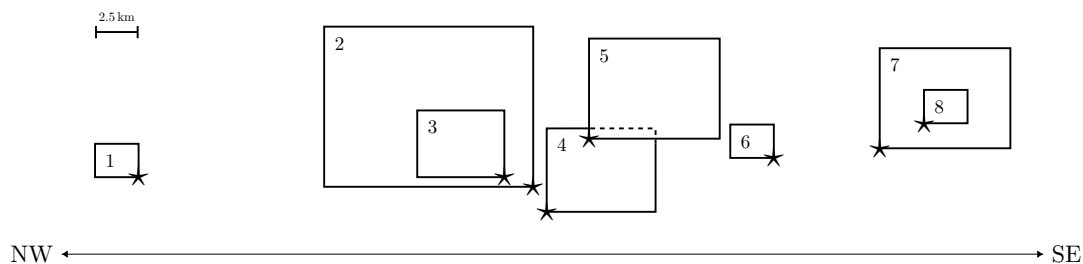


Figure 9.8: Geometry of the model for the 1997-1998 Umbria-Marche (Italy) seismic sequence. The rectangles are the projections of faults on the Earth surface. Stars correspond to epicenters; each fault is labelled with the corresponding index $i = 1, 2, \dots, 8$.

I take $\mu = 30 \text{ GPa}$ for the rigidity of the medium and $k_s = 0.6$ as the effective coefficient of static friction. With a strain rate $\dot{\epsilon} = 2 \times 10^{-15} \text{ s}^{-1}$ (Riguzzi et al., 2013) and a Poisson modulus $\nu = 0.25$, the rate of Coulomb stress calculated from Eq. (9.4) is

$$\dot{x} = \kappa \dot{\sigma} \simeq 3 \text{ kPa a}^{-1} \quad (9.55)$$

where κ and $\dot{\sigma}$ are given by Eq. (9.5) and Eq. (A.3), respectively. All other data required by the application of the model are listed in Table (9.2). The origin times and the seismic moments m_i are taken from Bindi et al. (2004), whereas the slips u_i are constrained according to the values of m_i and A_i .

From the knowledge of the UTM coordinates and depths of the hypocentres, I constrain the location of the centres of the faults according to the geometry shown in Fig. (9.8) and to the value of the dip angle of the fault system. The matrix \mathbf{r}

of the distances between the centres of the faults is then given by

$$\mathbf{r} \text{ (km)} = \begin{pmatrix} 0 & 14 & 17 & 23 & 25 & 29 & 37 & 36 \\ 14 & 0 & 4 & 10 & 12 & 15 & 23 & 23 \\ 17 & 4 & 0 & 6 & 9 & 12 & 20 & 20 \\ 23 & 10 & 6 & 0 & 6 & 6 & 14 & 14 \\ 25 & 12 & 9 & 6 & 0 & 6 & 12 & 12 \\ 29 & 15 & 12 & 6 & 6 & 0 & 8 & 8 \\ 37 & 23 & 20 & 14 & 12 & 8 & 0 & 1.8 \\ 36 & 23 & 20 & 14 & 12 & 8 & 1.8 & 0 \end{pmatrix}. \quad (9.56)$$

Table 9.2: Data for the seismic events of the 1997-1998 Umbria-Marche (Italy) sequence. See Fig. (9.8) for fault numbers.

Event	Fault	Origin time (UTC)		t_i (d)	m_i (N m)	A_i (km ²)	u_i (m)
		yyyy/mm/dd	hh:mm				
1	5	1997/09/26	00:33	0	4.0×10^{17}	36	0.37
2	2	1997/09/26	09:40	0.38	1.2×10^{18}	120	0.33
3	3	1997/10/03	08:55	7.3	8.6×10^{16}	16	0.18
4	4	1997/10/06	23:24	11	1.7×10^{17}	25	0.23
5	8	1997/10/12	11:08	16	7.8×10^{16}	6.3	0.41
6	7	1997/10/14	15:23	19	3.4×10^{17}	33	0.34
7	6	1998/03/21	16:45	180	4.0×10^{16}	6.3	0.21
8	1	1998/04/03	07:26	190	5.7×10^{16}	6.3	0.30

According to Table (9.2), the order of events is expressed by the permutation

$$\alpha^* = \begin{pmatrix} 1 & 2 & 3 & 4 & 5 & 6 & 7 & 8 \\ 5 & 2 & 3 & 4 & 8 & 7 & 6 & 1 \end{pmatrix}, \quad (9.57)$$

indicating that the sequence started approximately in the middle of the fault system (5, 2, 3, 4), migrated to its southeastern end (8, 7, 6) and finally involved its northwestern end (1). Combining the data in Table (9.2) with the distances r_{ij} reported in Eq. (9.56), the stress change matrix Δx_{ij} is computed. For the diagonal components, I make use of Eq. (9.11); for the nondiagonal components, the model of Appendix H is employed, taking

$$\phi_i = 135^\circ, \quad \psi_i = 40^\circ, \quad \lambda_i = -90^\circ \quad (9.58)$$

with $i = 1, 2, \dots, 8$. Following the procedure discussed in §9.2, it is possible to retrieve the state of the system at any time during the sequence, together with the associated permutations. Specifically, at the beginning of the sequence we find

$$\alpha_0 = \begin{pmatrix} 1 & 2 & 3 & 4 & 5 & 6 & 7 & 8 \\ 5 & 2 & 8 & 1 & 6 & 4 & 7 & 3 \end{pmatrix} \quad (9.59)$$

whereas the state after the i -th event of the sequence is described by

$$\alpha_1 = \begin{pmatrix} 1 & 2 & 3 & 4 & 5 & 6 & 7 & 8 \\ 2 & 8 & 1 & 4 & 6 & 7 & 5 & 3 \end{pmatrix} \quad \alpha_2 = \begin{pmatrix} 1 & 2 & 3 & 4 & 5 & 6 & 7 & 8 \\ 3 & 1 & 8 & 4 & 6 & 2 & 7 & 5 \end{pmatrix} \quad (9.60)$$

$$\alpha_3 = \begin{pmatrix} 1 & 2 & 3 & 4 & 5 & 6 & 7 & 8 \\ 4 & 1 & 8 & 6 & 2 & 7 & 3 & 5 \end{pmatrix} \quad \alpha_4 = \begin{pmatrix} 1 & 2 & 3 & 4 & 5 & 6 & 7 & 8 \\ 8 & 1 & 6 & 2 & 7 & 3 & 4 & 5 \end{pmatrix} \quad (9.61)$$

$$\alpha_5 = \begin{pmatrix} 1 & 2 & 3 & 4 & 5 & 6 & 7 & 8 \\ 7 & 1 & 6 & 2 & 3 & 4 & 5 & 8 \end{pmatrix} \quad \alpha_6 = \begin{pmatrix} 1 & 2 & 3 & 4 & 5 & 6 & 7 & 8 \\ 6 & 1 & 8 & 2 & 3 & 4 & 5 & 7 \end{pmatrix} \quad (9.62)$$

$$\alpha_7 = \begin{pmatrix} 1 & 2 & 3 & 4 & 5 & 6 & 7 & 8 \\ 1 & 8 & 2 & 3 & 4 & 5 & 7 & 6 \end{pmatrix} \quad \alpha_8 = \begin{pmatrix} 1 & 2 & 3 & 4 & 5 & 6 & 7 & 8 \\ 8 & 2 & 3 & 4 & 5 & 7 & 6 & 1 \end{pmatrix} \quad (9.63)$$

Figure (9.9) shows the states at the beginning ($t = t_1 -$) and at the end ($t = t_8 +$) of the sequence. Since the origin of times was set at the onset of the first event, we have $x_5(t_1 -) = 0$. In the first place, we notice that the initial (α_0) and final (α_8) permutations do not coincide and they are both different from the permutation α^* giving the order of events during the 1997-1998 sequence. As a result, the next sequence generated by the system will be associated with a different order of events. Furthermore, the permutations α_i suggest that the stress transfers within the system are such that the failure of certain faults is delayed by some of the seismic events, as a consequence of the relative positions of the faults. For example, a comparison between α_0 and α_1 clearly points out that the slip of fault 5 promoted the failure of fault 4, while it delayed the failure of fault 6.

The duration of the sequence is

$$\Delta t = t_8 - t_1 \simeq 190 \text{ d.} \quad (9.64)$$

In the absence of fault interaction, it would have been

$$\Delta t' = -\frac{x_3(t_1 -)}{\dot{x}} \simeq 790 \text{ a} \quad (9.65)$$

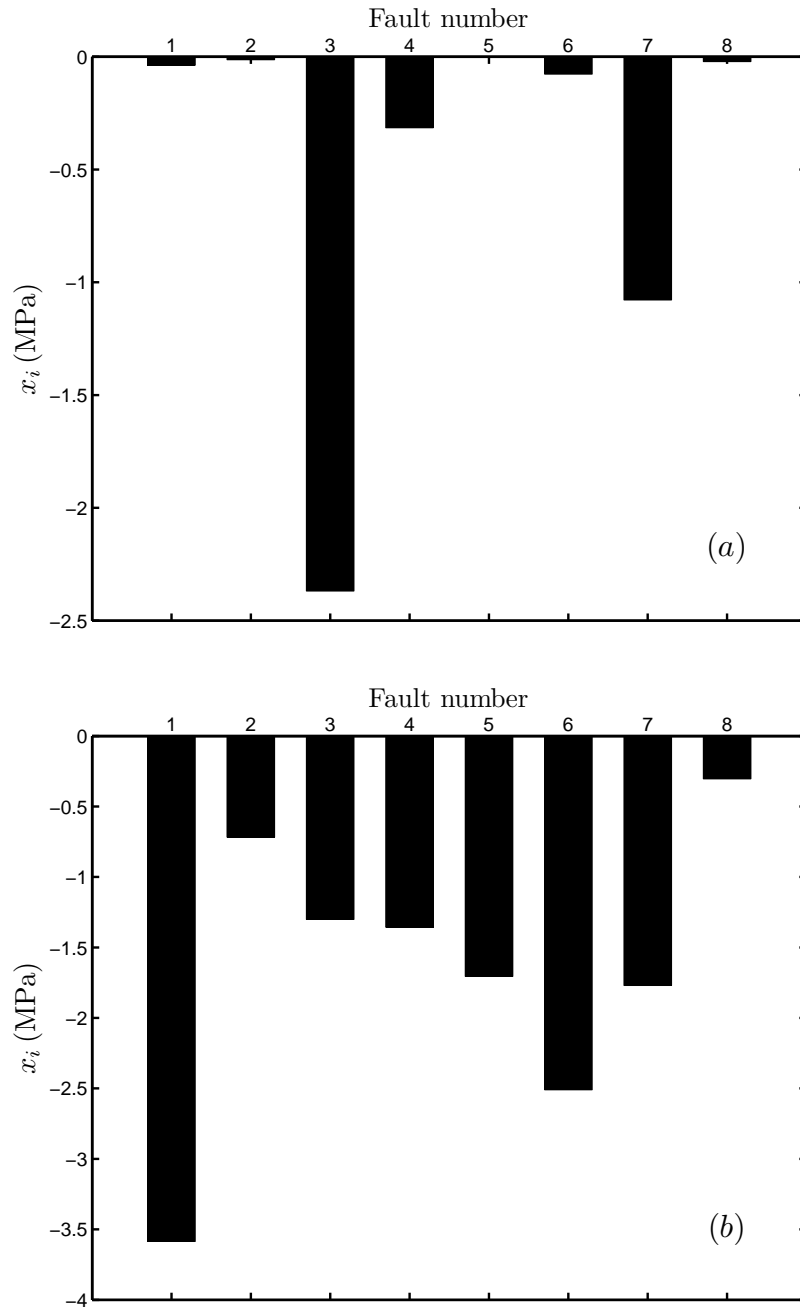


Figure 9.9: Initial (a) and final (b) states calculated from the model for the 1997-1998 Umbria-Marche (Italy) seismic sequence. Histograms show the components of the state vector \mathbf{x} at the beginning and at the end of the sequence.

where Eq. (9.21) was employed. Accordingly, the process of stress transfer between the faults of the system yielded a dramatic shortening of the duration of the seismic sequence, with a ratio $\Delta t'/\Delta t \simeq 10^3$. Interestingly, we notice that $\Delta t'/\Delta t$ is of the same order of magnitude as the ratio calculated for the 2012 Emilia sequence (§9.6.1), suggesting this might be a general feature of seismic sequences.

In order to compare the stress states on the fault system at the beginning and at the end of the sequence, let us consider the mean value (9.24) of the state vector \mathbf{x} and its standard deviation (9.23) at $t = t_1-$ and $t = t_8+$. At the beginning of the sequence, we have

$$\bar{x} \simeq -0.49 \text{ MPa}, \quad s \simeq 0.79 \text{ MPa} \quad (9.66)$$

whereas at the end of the sequence

$$\bar{x} \simeq -1.7 \text{ MPa}, \quad s \simeq 0.96 \text{ MPa}. \quad (9.67)$$

These figures point out that Coulomb stresses are slightly more spread out at the end of the sequence than before, since the standard deviation in Eq. (9.67) is larger than in Eq. (9.66). An additional way to further understand and visualize the particular distribution of stress on the fault system before and after the seismic sequence is given by considering the average values

$$\bar{d}_i = \frac{\sum_{j=1}^n |d_{ij}|}{n-1}, \quad j \neq i. \quad (9.68)$$

At the beginning of the sequence, we find

$$\bar{d}_i \simeq (0.54, 0.55, 2.1, 0.61, 0.56, 0.54, 1.0, 0.54) \text{ MPa}, \quad (9.69)$$

whereas at the end of the sequence we have

$$\bar{d}_i \simeq (2.2, 1.2, 0.86, 0.84, 0.84, 1.3, 0.86, 1.5) \text{ MPa}. \quad (9.70)$$

In agreement with the features suggested by Eq. (9.66) and Eq. (9.67), we conclude that, at the end of the sequence, the average difference between the Coulomb stress on the i -th fault and the other $(n-1)$ faults is of the same order of magnitude of the average difference characterizing the state at the beginning of the sequence. However, the variations in the differences d_{ij} entail a different order of events during the next sequence, as well as different durations of the time intervals between two subsequent events.

Finally, the permutation α_8 in Eq. (9.63) suggests that, according to the present model, the next sequence will start with the failure of fault 8, i.e, at the southeastern end of the fault system. According to Eq. (9.35), it will take place after an interseismic interval

$$\Delta T = -\frac{x_8(t_8+)}{\dot{x}} \simeq 100 \text{ a}. \quad (9.71)$$

Conclusions

A model describing different aspects of fault dynamics in the framework of discrete dynamical systems was presented.

A plane fault (or a fault system) lying in an elastic shear zone and enclosed by two tectonic plates moving at constant relative velocity was considered. As a consequence of tectonic motion, the fault is subject to a uniform and constant strain rate. It was assumed that the fault contains one or more asperities and possibly one or more weak regions. The fault was treated as a discrete dynamical system whose state is described by the state of the asperities and weak regions (or the fault segments in the fault system). The state variables are the slip deficits or the Coulomb stresses associated with the regions on the fault.

In correspondence with specific properties associated with the asperities, the weak regions or the fault segments and with the form of their interactions, five different cases were discussed. For the first four of them, the dynamics was described in terms of a number of dynamic modes, each one associated with a specific system of autonomous ordinary differential equations.

The characterization of the system as made of a finite number of asperities, weak regions or fault segments allowed a description by means of a finite number of degrees of freedom. Thus, a deeper understanding of the processes controlling the dynamics of seismic sources and the retrieval of the analytical solutions of the evolution equations were possible. In turn, the orbit of the system in the state-space was calculated: via this geometrical approach, it was possible to follow the different phases of the evolution of the system, highlight their distinctive features and predict the long-term evolution of the system.

In Chapter 4, a fault with a single asperity was considered. It was assumed

that the asperity is responsible for the majority of seismic moment release during an earthquake. From the solutions of the equations of motion, it was possible to distinguish between a loading phase and a slipping phase, associated with a seismic event on the fault. The system is characterized by the existence of a limit cycle, with earthquakes associated with a fixed recurrence time and slip amplitude. The model is capable to reproduce the typical features of the source function of an earthquake and predicts a seismic spectrum with the classical high-frequency behaviour described by Brune (1970). As an application of the model, the great 2004 Sumatra-Andaman earthquake was considered, describing the event as the result of the failure of one large asperity. The modelled source function and seismic spectrum were found to be in good agreement with the observations.

Chapter 5 was devoted to the analysis of a fault containing two mechanically different regions, namely an asperity and a stable, velocity-strengthening region. The generation of earthquakes on the fault is ascribed to the slip of the sole asperity. The dynamics of the system was studied in terms of three dynamic modes, corresponding to the evolution during interseismic intervals, seismic slip of the asperity and afterslip in the stable region. In agreement with observations, the amount of afterslip resulted to be proportional to the seismic slip of the asperity. In the absence of stress perturbations due to earthquakes on surrounding faults, the system exhibits a cycle made of a sequence of the three dynamic modes, with fixed amplitudes of seismic slip and afterslip and given recurrence time of earthquakes. An interesting feature of the model was found in its potentiality to discriminate between different sources of post-seismic deformation: in fact, the model predicts that afterslip reaches a maximum amplitude in a finite time interval, in contrast with descriptions based on indefinitely increasing time functions. The model was applied to the fault that generated the 2011 Tohoku-Oki earthquake, which was ascribed to the slip of a large asperity and was followed by a prolonged afterslip episode. The dominant part of the source function was reproduced and the surface displacement due to afterslip was described as a function of time: according to the model, post-seismic deformation was governed by afterslip in the first four months after the event, while the subsequent deformation was probably due to viscoelastic relaxation.

In Chapter 6, a fault with two asperities of different areas and strengths was considered, assuming purely elastic coupling between the asperities. The dynamics

of the system was characterized in terms of four dynamic modes: a sticking mode, associated with stationary asperities, and three slipping modes, corresponding to the slip of one or both asperities at a time. The kind of seismic event generated by the fault can be discriminated from the knowledge of the state of the system at the beginning of the interseismic interval preceding the event. Specifically, the different seismic events predicted by the model correspond with specific values of a variable related with the difference between the slip deficits of the asperities at the beginning of the interseismic interval. The difference between the asperity size affects several features of the system, such as the force rates on the asperities, the slip duration and amplitude, the corner frequency of the seismic spectrum, the set of states corresponding to stationary asperities, the probability of events involving the simultaneous slip of the asperities and the radiation of seismic energy. As an application of the model, the 2007 Pisco, Peru, earthquake was considered. This event was ascribed to the consecutive, but separate, failures of two asperities with significantly different sizes. The earthquake was modelled as a two-mode event starting with the slip of the weaker asperity, followed by the slip of the stronger one after a finite time interval. The model allowed to characterize the state of the fault at the onset of the event and to adequately replicate the observed source function and seismic moment release.

In Chapter 7, a fault with two asperities of equal areas and different frictional resistance was considered. It was assumed that the coseismic stress field due to earthquakes produced by the fault undergoes viscoelastic relaxation. In addition to the slip deficits of the asperities, the state of the fault was described in terms of a third variable: the variation of the difference between the slip deficits of the asperities resulting from viscoelasticity. The occurrence of earthquakes on the fault can be anticipated or delayed, with respect to the case of purely elastic coupling between the asperities, owing to viscoelastic relaxation, the specific effect depending on the state of the system at the beginning of an interseismic interval. The system is characterized by one sticking mode, corresponding to stationary asperities, and three slipping modes, associated with the failure of one of both asperities at a time. It was showed how the state of the system at the beginning of an interseismic interval constrains the state at the onset of the subsequent seismic event, and vice-versa. In turn, these details were related to the number and sequence of slipping modes involved in the earthquake, which determine the amount of seismic moment released, the shape of the source function and the

stress drops on the asperities. A notable result of this study is that the knowledge of the source functions of a sufficiently large number of consecutive earthquakes allows to constrain the orbit more and more precisely and, in turn, to predict its evolution with smaller uncertainty. The model was applied to the fault that generated the 1964 Alaska earthquake. The event was due to the failure of two asperities and was followed by remarkable post-seismic deformation mainly due to viscoelastic relaxation in the lithosphere. The earthquake was modelled as a two-mode event associated with the separate slips of the asperities and the subsets of the state space in which the system laid before and after the event were determined; these subsets were further constrained on the basis of the duration of the interseismic interval to date.

The fault model discussed in Chapter 7 was considered again in Chapter 8 in order to study the effect of earthquakes on neighbouring faults. The stress transfer was described in terms of a perturbation vector yielding changes to the state of the system: the specific effect on the future evolution of the fault is related with the orientation of this vector in the state space. The perturbation also causes a variation in the frictional resistances of the asperities: in turn, the amount of slip allowed to the asperities and the energy released during a subsequent seismic event are altered. Due to changes in the parameters of the system, the subsets the state space can be divided into, associated with the different seismic events that the fault can generate, are modified as well: accordingly, the probability of occurrence of the various events is altered. Following a stress perturbation, the anticipation/delay of the failure of one asperity is connected with the change in the associated Coulomb stress. In particular, the variation in the difference between the Coulomb stresses of the two asperities influences the possibility of their simultaneous slips during the next seismic event. However, the presence of viscoelastic relaxation prevents any prediction about the change in the interseismic time of the fault, which is conditioned by the particular state of the fault at the time of the stress perturbation and immediately after it. As an application, the stress perturbation imposed by the 1999 Hector Mine, California, earthquake to the 1992 Landers, California, fault was considered. Like the 1964 Alaska earthquake, the 1992 Landers earthquake was generated by the slip of two asperities and a significant post-seismic deformation was observed in the aftermath, mainly associated with viscoelastic relaxation in the lithosphere. In order to model the event, the same analysis as for the 1964 Alaska earthquake was carried out. As

for the stress transfer due to the 1999 Hector Mine earthquake, the complexity of its influence on the possible future events generated by the 1992 Landers fault was discussed in terms of the associated energy release, the sequence of dynamic modes involved and the duration of the interseismic interval.

Finally, Chapter 9 was devoted to the study of the seismic sequences generated by a system of faults with the same strike and dip angles and the same faulting mechanism. The fault system was characterized as a dynamical system whose state variables are the Coulomb stresses associated with the faults. In order to determine the conditions required for the occurrence of seismic sequences and the processes controlling the order of events in a sequence, each state of the system was associated with a permutation expressing the order of the faults in terms of the magnitudes of their Coulomb stresses. The permutation does not change as long as the system is at rest; each time a fault produces an earthquake, the stress drop on the activated fault and the stress transfers to the surrounding faults cause a change in the order of Coulomb stresses, so that the state of the system is described by a different permutation. Ultimately, the order of activation in a seismic sequence can be associated with a particular permutation of the faults: it is determined by the initial stress state of the fault system, the stress drops and the stress transfers associated with each event. It is noteworthy that the characteristics of consecutive sequences originated by the system are bound to change: in fact, the order of activation suggested by the initial stress distribution is generally changed during the sequence, owing to the different order of magnitude of the stress drops and stress transfers. As a result, the state of the system at the end of a sequence does not coincide with the initial one. In addition, the durations of the interseismic intervals between consecutive sequences and between events in a sequence are different. As an application of the model, two seismic sequences were considered: the 1997-1998 Umbria-Marche, Italy, sequence and the 2012 Emilia, Italy, sequence. The former was ascribed to a system of non-coplanar faults, whereas a system of coplanar, lined up faults was assumed for the latter. In both cases, the knowledge of the order of activation during the seismic sequence allowed the retrieval of the state of the system at any time during the sequence. The model predicts that, in the absence of external perturbations, the next sequence on both fault systems will occur after an interseismic interval of a few centuries and will be completely different from the previous one.

Of course, all discussed models present a simplified description of real fault dynamics. In the author's opinion, they nonetheless provide a useful tool for the characterization of the seismic source, enlarging the understanding of the most significant aspects of the seismic activity in an analytical framework. As a matter of fact, if we aim to a neat understanding of the physics of a process, unnecessary complications must be set apart: focusing on the essential dynamics, discrete fault models offer a deep insight into the basic mechanisms of seismic sources.

Several further developments may be object of future work, such as a model of a fault containing three or more asperities, a model describing stress perturbations due to post-seismic deformation processes, the introduction of dynamic stress triggering, and more.

Appendices

Appendix A

Stress rates in different tectonic settings

A plane fault located in a homogeneous and isotropic elastic shear zone with the features of a Hooke solid with Lamé constants λ and μ is considered. As a consequence of tectonic motion, the fault is subject to a uniform and constant strain rate $\dot{\epsilon}$. A coordinate system (x, y, z) is introduced, with x, y and z defined as the strike direction of the fault, the horizontal direction perpendicular to strike and depth, respectively. Let δ be the dip angle of the fault. I retrieve the expressions of the normal stress rate $\dot{\sigma}_n$ and the tangential stress rate (in the slip direction) $\dot{\sigma}_t$ acting on the fault, distinguishing between dip-slip faulting and strike-slip faulting.

In the case of normal and reverse faulting, plane strain is assumed, according to the Anderson model (Anderson, 1951; Sibson, 1974; Turcotte and Schubert, 2002). The nonvanishing strain components are

$$e_{yy} = \dot{\epsilon}t, \quad e_{zz} = -\frac{\lambda}{\lambda + 2\mu}e_{yy} \quad (\text{A.1})$$

where $\dot{\epsilon}$ is positive for tensile strain and negative for compressive strain. The associated stress components are

$$\sigma_{xx} = \nu\sigma_{yy}, \quad \sigma_{yy} = \frac{2\mu}{1 - \nu}e_{yy} \quad (\text{A.2})$$

where ν is the Poisson modulus. Introducing the stress rate

$$\dot{\sigma} = \frac{2\mu}{1 - \nu}\dot{\epsilon}, \quad (\text{A.3})$$

the rates of normal and tangential traction on the fault are given by

$$\dot{\sigma}_n = -\frac{\dot{\sigma}}{2}(1 - \cos 2\delta), \quad \dot{\sigma}_t = \pm\frac{\dot{\sigma}}{2}\sin 2\delta \quad (\text{A.4})$$

where the upper and lower sign in σ_t corresponds to normal and reverse faulting, respectively.

In the case of transcurrent faulting, simple shear is considered, with strain and stress components

$$e_{xy} = \dot{\epsilon}t, \quad \sigma_{xy} = 2\mu e_{xy}. \quad (\text{A.5})$$

In this case, the stress rate is

$$\dot{\sigma} = 2\mu\dot{\epsilon} \quad (\text{A.6})$$

and the rates of normal and tangential traction on the fault are given by

$$\dot{\sigma}_n = 0, \quad \dot{\sigma}_t = \dot{\sigma}. \quad (\text{A.7})$$

For both source mechanisms, a particular expression of $\dot{\sigma}_t$ can be written in the framework of the elastic rebound model of a fault, first proposed by Reid (1911). It is assumed that the fault is embedded in a shear zone of width d enclosed by two tectonic plates moving at constant relative velocity v (Fig. A.1). The tectonic velocity is parallel to the slip direction on the fault.

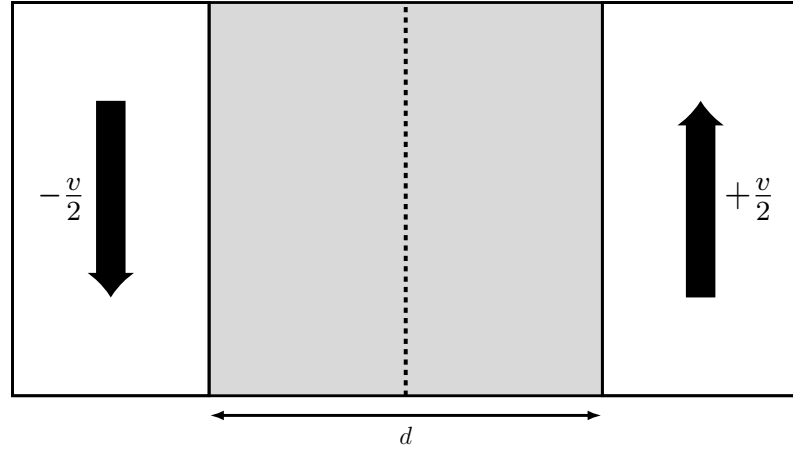


Figure A.1: The elastic rebound model of a fault. A plane fault (dashed line) is embedded in a shear zone of width d (gray patch) enclosed by two tectonic plates moving at constant relative velocity v .

According to the boundary conditions, the fault is subject to a tangential strain rate

$$\dot{\epsilon} = \frac{v}{2d} \quad (\text{A.8})$$

corresponding to a tangential stress rate

$$\dot{\sigma}_t = \frac{\mu v}{d}. \quad (\text{A.9})$$

Appendix B

Traction due to different dislocation sources

A dislocation source in a homogeneous and isotropic Poisson medium of rigidity μ is considered. The dislocation is characterized in four different ways, namely as (i) a point-like source in an unbounded medium, (ii) a point-like source in a half-space, (iii) a finite square source in an unbounded medium and (iv) a finite square source in a half-space. In each case, the tangential traction σ_t produced on the fault plane in the slip direction is calculated, as a function of the distance from the source along the strike direction.

A coordinate system (x, y, z) is introduced, with x, y and z defined as the strike direction, the horizontal direction perpendicular to strike and depth, respectively. Let n_i be the unit vector perpendicular to the fault and m_i the unit vector in the slip direction. Also, let m_0 be the scalar seismic moment of the dislocation, while δ and λ are the dip and rake angles of the fault, respectively. Given the static stress field σ_{ij} produced by the dislocation, the tangential traction in the direction of slip σ_t is given by

$$\sigma_t = \sigma_{ij} m_i n_j. \quad (\text{B.1})$$

B.1 Point-like source in an unbounded medium

Let us consider a point-like dislocation source (a double-couple of forces) in an unbounded elastic medium, located at the origin of the coordinate system. The

fault lies on the plane $y = 0$, so that

$$n_i = (0, 1, 0). \quad (\text{B.2})$$

As for the slip direction, it is given by

$$m_i = (\cos \lambda, 0, -\sin \lambda). \quad (\text{B.3})$$

The static displacement field generated by the dislocation is (Love, 1944)

$$u_i = -M_{jk}G_{ij,k} \quad (\text{B.4})$$

where M_{ij} is the moment tensor associated with the dislocation source

$$M_{ij} = m_0 (m_i n_j + m_j n_i) \quad (\text{B.5})$$

and G_{ij} is the Somigliana tensor

$$G_{ij} = \frac{1}{8\pi\mu} \left(\frac{2}{r} \delta_{ij} - \frac{2}{3} r_{,ij} \right) \quad (\text{B.6})$$

with

$$r = \sqrt{x^2 + y^2 + z^2}. \quad (\text{B.7})$$

The stress field due to the dislocation is

$$\sigma_{ij} = \mu (e_{kk} \delta_{ij} + 2e_{ij}), \quad (\text{B.8})$$

where e_{ij} is the strain field associated with the displacement field (B.4). In the case of strike-slip faulting ($\lambda = 0$) and setting $y = z = 0$, we get

$$\sigma_t = \frac{5 m_0}{12\pi|x|^3}. \quad (\text{B.9})$$

In the case of dip-slip faulting ($\lambda = \pi/2$) and setting again $y = z = 0$, we get

$$\sigma_t = \frac{m_0}{6\pi|x|^3}. \quad (\text{B.10})$$

B.2 Point-like source in a half-space

Let us consider a point-like dislocation source (a double-couple of forces) in a half space, located at $(0, 0, c)$. The unit vector perpendicular to the fault is

$$n_i = (0, -\sin \delta, -\cos \delta), \quad (\text{B.11})$$

while the slip direction is given by

$$m_i = (\cos \lambda, \sin \lambda \cos \delta, -\sin \lambda \sin \delta). \quad (\text{B.12})$$

The cases of strike-slip and dip-slip faulting correspond to $\lambda = 0$ and $\lambda = \pi/2$, respectively. The displacement, strain and stress field due to the dislocation can be calculated from the formulae provided by Okada (1992). The tangential traction $\sigma_t(x)$ is then obtained by setting $y = 0$ and $z = c$. Due to its complexity, I do not report its analytical expression and only show its trend later on.

B.3 Finite square source in an unbounded medium

Let us consider a finite square dislocation source of side L in an unbounded medium, centred at the origin of the coordinate system. The fault lies on the plane $y = 0$, so that

$$n_i = (0, 1, 0). \quad (\text{B.13})$$

As for the slip direction, it is given by

$$m_i = (\cos \lambda, 0, -\sin \lambda). \quad (\text{B.14})$$

The cases of strike-slip and dip-slip faulting correspond to $\lambda = 0$ and $\lambda = \pi/2$, respectively. The displacement, strain and stress field due to the dislocation can be calculated from the formulae provided by Rybicki (1970). The tangential traction $\sigma_t(x)$ is then obtained by setting $y = 0$ and $z = 0$. Its analytical expression is too complicated to be reported here: thus, I only show its trend later on.

B.4 Finite square source in a half-space

Let us consider a finite square dislocation source of side L in a half-space. The unit vector perpendicular to the fault is

$$n_i = (0, -\sin \delta, -\cos \delta), \quad (\text{B.15})$$

while the slip direction is given by

$$m_i = (\cos \lambda, \sin \lambda \cos \delta, -\sin \lambda \sin \delta). \quad (\text{B.16})$$

The cases of strike-slip and dip-slip faulting correspond to $\lambda = 0$ and $\lambda = \pi/2$, respectively. In order to exploit the formulae for the displacement, strain and

stress field due to the dislocation provided by Okada (1992), the lower edge of the fault is placed on the plane $y = 0$ at depth $c \geq L$ (Fig. B.1). Also, the centre of the fault is placed at $(0, 0.5 L \cos \delta, c - 0.5 L \sin \delta)$. The tangential traction $\sigma_t(x)$ is then obtained by setting $y = 0.5 L \cos \delta$ and $z = c - 0.5 L \sin \delta$. Due to its complexity, I do not report its analytical expression and only show its trend in the following.

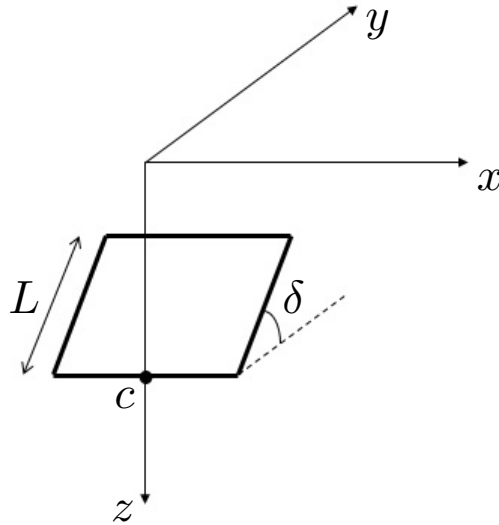


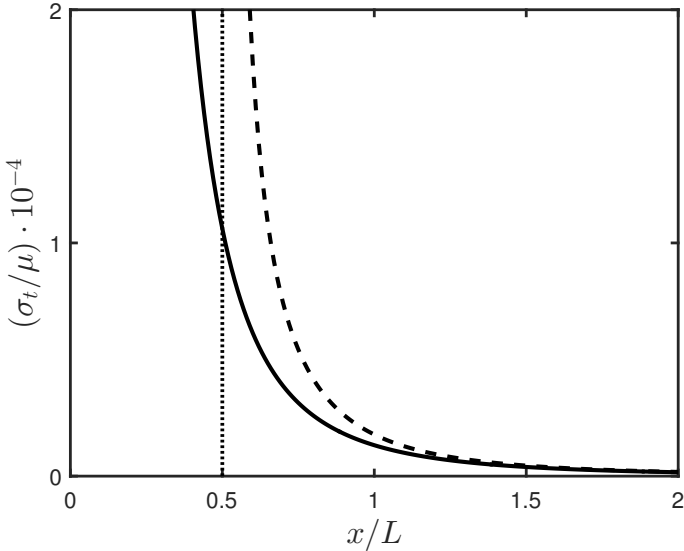
Figure B.1: Square dislocation source in an elastic half-space.

B.5 Comparison

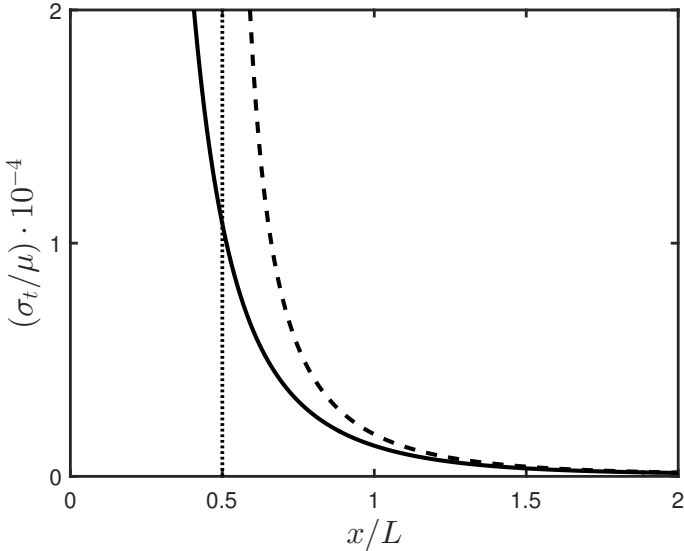
In order to compare the results corresponding to the four cases presented above, it is assumed $c = L$ and $\delta = \pi/4$ in §B.2 and §B.4. Also, all distances are expressed in units of L : accordingly, the average slip of the fault is assumed to be of the order of 10^{-4} , taking into account that a fault typically extends in width and length for tens of kilometres, whereas maximum fault slips are in the order of meters or less.

The tangential traction produced on the fault plane in the slip direction $\sigma_t(x)$ is shown in Fig. (B.2) and Fig. (B.3) in the case of strike-slip and dip-slip faulting, respectively. In both cases, a singularity appears in correspondence with the border of the finite source ($x = 0.5 L$) or, in the case of a point-like source, in correspondence with the source location ($x = 0$). Looking at the trends associated

with the different dislocation sources, the graphs clearly point out that the value of σ_t becomes essentially the same at distances $x \geq 1.5 L$. Furthermore, the elastic medium in which the fault is embedded can be indifferently treated as an infinite space or a half-space if the depth c of the dislocation source is at least comparable with the side of the fault.

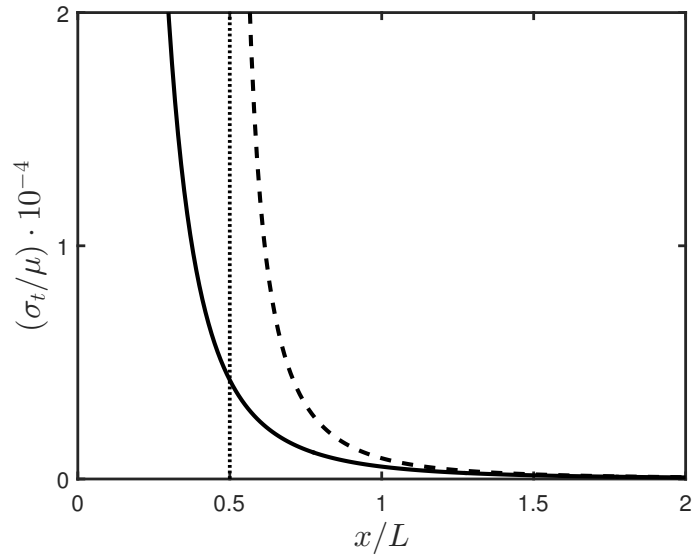


(a) Unbounded medium.

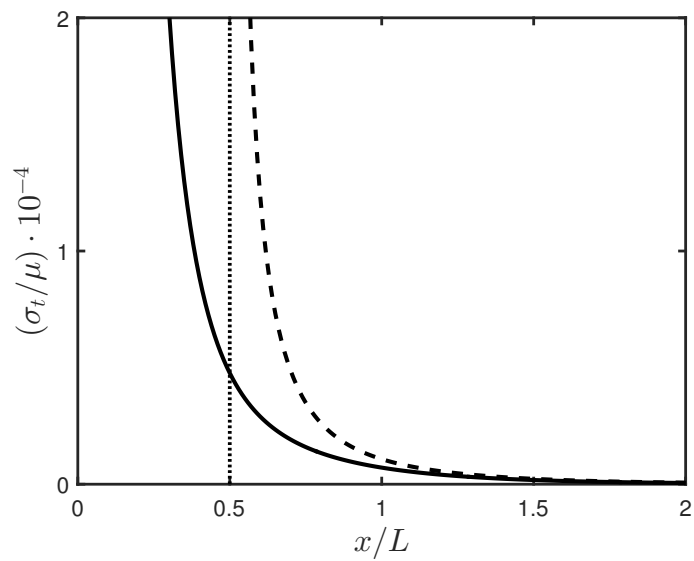


(b) Half-space.

Figure B.2: Tangential traction produced by a strike-slip dislocation in the slip direction on the fault plane, in the case of a point-like source (solid line) and a finite square source (dashed line).



(a) Unbounded medium.



(b) Half-space.

Figure B.3: Tangential traction produced by a dip-slip dislocation in the slip direction on the fault plane, in the case of a point-like source (solid line) and a finite square source (dashed line).

Appendix C

Constants in mode 11 - Chapter 6

The fault can enter mode 11 from mode 10, 01 or 00. I list the constants A , B , C and D appearing in the solution for mode 11, discriminating between these three initial conditions.

C.1 Case 10 \rightarrow 11

The initial conditions are

$$X(0) = \bar{X}, \quad Y(0) = \bar{Y}, \quad \dot{X}(0) = \bar{V}, \quad \dot{Y}(0) = 0 \quad (\text{C.1})$$

with \bar{X} and \bar{Y} satisfying the equation of line 2. The constants are

$$A = \frac{1}{\omega_0} \left(\frac{\gamma}{2} B + \frac{1}{1+\xi} \bar{V} \right) \quad (\text{C.2})$$

$$B = \frac{1}{1+\xi} [\bar{X} + \xi \bar{Y} - \epsilon(1 + \beta\xi)] \quad (\text{C.3})$$

$$C = \frac{1}{\omega_3} \left(\frac{\gamma}{2} D - \frac{\xi}{1+\xi} \bar{V} \right) \quad (\text{C.4})$$

$$D = \frac{\xi}{1+\xi} [\bar{X} - \bar{Y} - \epsilon(X_P - Y_P)] \quad (\text{C.5})$$

C.2 Case 01 \rightarrow 11

The initial conditions are

$$X(0) = \bar{X}, \quad Y(0) = \bar{Y}, \quad \dot{X}(0) = 0, \quad \dot{Y}(0) = \bar{V} \quad (\text{C.6})$$

with \bar{X} and \bar{Y} satisfying the equation of line 1. The constants are

$$A = \frac{1}{\omega_0} \left(\frac{\gamma}{2} B + \frac{\xi}{1+\xi} \bar{V} \right) \quad (\text{C.7})$$

$$B = \frac{1}{1+\xi} [\bar{X} + \xi \bar{Y} - \epsilon(1 + \beta\xi)] \quad (\text{C.8})$$

$$C = \frac{1}{\omega_3} \left(\frac{\gamma}{2} D - \frac{\xi}{1+\xi} \bar{V} \right) \quad (\text{C.9})$$

$$D = \frac{\xi}{1+\xi} [\bar{X} - \bar{Y} - \epsilon(X_P - Y_P)] \quad (\text{C.10})$$

C.3 Case 00 \rightarrow 11

The initial conditions are

$$X(0) = X_P, \quad Y(0) = Y_P, \quad \dot{X}(0) = 0, \quad \dot{Y}(0) = 0. \quad (\text{C.11})$$

The constants are

$$A = \frac{\gamma}{2\omega_0} B \quad (\text{C.12})$$

$$B = \frac{1}{1+\xi} (1 - \epsilon) (1 + \beta\xi) \quad (\text{C.13})$$

$$C = \frac{\gamma}{2\omega_3} D \quad (\text{C.14})$$

$$D = \frac{\xi}{1+\xi} (1 - \epsilon) (X_P - Y_P) \quad (\text{C.15})$$

Appendix D

Events resulting from $p = p_1$ and $p = p_2$ - Chapter 6

Here, the values p_1 and p_2 of the variable p defined in Eq. (6.34) are calculated and the kind of seismic event resulting from these stress distributions is discussed. In view of the following discussion, I recall that the maximum slip of asperity 1 during mode 10 is $\kappa_1 U$, corresponding to the slip duration T_{1b} , whereas the maximum slip of asperity 2 during mode 01 is $\beta \kappa_2 U'$, corresponding to the slip duration T_{2b} .

Let us calculate the value of p_1 . The coordinates of point P_1 , where mode 10 starts, are

$$X_1 = 1 + \alpha p, \quad Y_1 = 1 + (1 + \alpha)p. \quad (\text{D.1})$$

The coordinates of point P_2 , where mode 10 ends, are

$$X_2 = X_1 - \kappa_1 U, \quad Y_2 = Y_1. \quad (\text{D.2})$$

Since it must belong to line 2, we obtain

$$p_1 = \frac{(\beta - 1)\xi - \alpha \kappa_1 U}{\alpha + \xi + \alpha \xi}. \quad (\text{D.3})$$

Let us calculate the value of p_2 . The coordinates of point P_1 , where mode 01 starts, are

$$X_1 = \beta - (1 + \alpha')p, \quad Y_1 = \beta - \alpha'p. \quad (\text{D.4})$$

The coordinates of point P_2 , where mode 01 ends, are

$$X_2 = X_1, \quad Y_2 = Y_1 - \beta \kappa_2 U'. \quad (\text{D.5})$$

Since it must belong to line 1, we obtain

$$p_2 = \frac{(\beta - 1)\xi + \alpha\beta\xi\kappa_2 U'}{\alpha + \xi + \alpha\xi}. \quad (\text{D.6})$$

The kind of seismic event resulting from $p = p_1$ and $p = p_2$ is related to the degree of symmetry of the system, as discussed in the following.

Case $p = p_1$

If $p = p_1$, asperity 1 triggers the motion of asperity 2 after completing mode 10. The earthquake then continues with mode 01, starting at point P_2 with coordinates given in Eq. (D.2). If the orbit of mode 01 does not meet line 1 before time T_{2b} has elapsed, the slip of asperity 2 terminates at point P_3 with coordinates

$$X_3 = X_2, \quad Y_3 = Y_2 - \beta\kappa_2 U'. \quad (\text{D.7})$$

If P_3 belongs to line 1, mode 01 is followed by a second phase of mode 10. This situation corresponds to a specific value of β , namely

$$\beta = \beta_1 = \frac{(\alpha + \xi)\kappa_1}{\alpha\xi\kappa_2}. \quad (\text{D.8})$$

In the particular case in which $\beta > \beta_1$, the orbit of mode 01 reaches line 1 before time T_{2b} has elapsed and the system enters mode 11. The different cases are summarized in Table (D.1).

Table D.1: Seismic events resulting from $p = p_1$ defined in Eq. (D.3), as functions of β . The particular value $\beta = \beta_1$ is defined in Eq. (D.8).

	$\beta < \beta_1$	$\beta = \beta_1$	$\beta > \beta_1$
Seismic event	10-01	10-01-10	10-01-11-

Finally, I investigate whether the system can generate four-mode events 10-01-10-01. At the end of a three-mode event 10-01-10, the system is at point P_4 with coordinates

$$X_4 = X_3 - \kappa_1 U, \quad Y_4 = Y_3, \quad (\text{D.9})$$

where it was assumed that the orbit of mode 10 starting at P_3 did not meet line 2 before asperity 1 had stopped. The event will then continue with another phase of mode 01 if P_4 belongs to line 2. Introducing the coordinates of P_4 in the equation of line 2 and taking into account that $\beta = \beta_1$, we end up with the condition

$$\alpha = -\frac{\xi}{1 + \xi} \quad (\text{D.10})$$

which is unacceptable, since α is defined as positive. In conclusion, if seismic events involving the alternate slips of the asperities and starting with the slip of asperity 1 are considered, the system can only generate a two-mode event 10-01 and, under particular conditions related with the symmetry of the system, a three-mode event 10-01-10.

Case $p = p_2$

If $p = p_2$, asperity 2 triggers the motion of asperity 1 after completing mode 01. The earthquake then continues with mode 10, starting at point P_2 with coordinates given in Eq. (D.5). If the orbit of mode 10 does not meet line 2 before time T_{1b} has elapsed, the slip of asperity 1 terminates at point P_3 with coordinates

$$X_3 = X_2 - \kappa_1 U, \quad Y_3 = Y_2. \quad (\text{D.11})$$

If P_3 belongs to line 2, mode 10 is followed by a second phase of mode 01. This situation corresponds to a specific value of β , namely

$$\beta = \beta_2 = \frac{\alpha \kappa_1}{\xi(1 + \alpha)\kappa_2}. \quad (\text{D.12})$$

In the particular case in which $\beta < \beta_2$, the orbit of mode 10 reaches line 2 before time T_{1b} has elapsed and the system enters mode 11. The different cases are summarized in Table (D.2).

Table D.2: Seismic events resulting from $p = p_2$ defined in Eq. (D.6), as functions of β . The particular value $\beta = \beta_2$ is defined in Eq. (D.12).

	$\beta < \beta_2$	$\beta = \beta_2$	$\beta > \beta_2$
Seismic event	01-10-11-	01-10-01	01-10

Finally, I investigate whether the system can generate four-mode events 01-10-01-10. At the end of a three-mode event 01-10-01, the system is at point P_4 with coordinates

$$X_4 = X_3, \quad Y_4 = Y_3 - \beta \kappa_2 U', \quad (\text{D.13})$$

where it was assumed that the orbit of mode 01 starting at P_3 did not meet line 1 before asperity 2 had stopped. The event will then continue with another phase of mode 10 if P_4 belongs to line 1. Introducing the coordinates of P_4 in the equation of line 1 and taking into account that $\beta = \beta_2$, we end up with the same condition

given by Eq. (D.10). In conclusion, if seismic events involving the alternate slips of the asperities and starting with the slip of asperity 2 are considered, the system can only generate a two-mode event 01-10 and, under particular conditions related with the symmetry of the system, a three-mode event 01-10-01.

For the sake of simplicity, the condition

$$\beta_2 < \beta < \beta_1 \tag{D.14}$$

is assumed throughout Chapter 6. Accordingly, the stress distributions associated with $p = p_1$ and $p = p_2$ correspond to two-mode events 10-01 and 01-10, respectively.

Appendix E

Constants in mode 11 - Chapter 7

The fault can enter mode 11 from mode 10, 01 or 00. I list the constants A , B , C , D , E_1 , E_2 and E_3 appearing in the solution for mode 11, discriminating between these three initial conditions.

E.1 Case 10 \rightarrow 11

The initial conditions are

$$X(0) = \bar{X}, \quad Y(0) = \bar{Y}, \quad Z(0) = \bar{Z} \quad (\text{E.1})$$

$$\dot{X}(0) = \bar{V}, \quad \dot{Y}(0) = 0, \quad \dot{Z}(0) = -\bar{V} \quad (\text{E.2})$$

with \bar{Y} and \bar{Z} satisfying the equation (7.19) of plane Π_2 . The constants are

$$A = \frac{1}{2\omega_0} (\bar{V} + \gamma B) \quad (\text{E.3})$$

$$B = \frac{1}{2} [\bar{X} + \bar{Y} - \epsilon (X_P + Y_P)] \quad (\text{E.4})$$

$$C = \frac{1}{2\omega_2} (\bar{V} + \gamma D) \quad (\text{E.5})$$

$$D = \frac{1}{2} \left(\epsilon Z_P + \frac{\bar{X} - \bar{Y} - 2\alpha \bar{Z}}{1 + 2\alpha} \right) \quad (\text{E.6})$$

$$E_1 = \epsilon X_P + \frac{\alpha}{1 + 2\alpha} (\bar{X} - \bar{Y} + \bar{Z}) \quad (\text{E.7})$$

$$E_2 = \epsilon Y_P - \frac{\alpha}{1 + 2\alpha} (\bar{X} - \bar{Y} + \bar{Z}) \quad (\text{E.8})$$

$$E_3 = \epsilon Z_P + \frac{1}{1 + 2\alpha} (\bar{X} - \bar{Y} + \bar{Z}) \quad (\text{E.9})$$

E.2 Case 01 \rightarrow 11

The initial conditions are

$$X(0) = \bar{X}, \quad Y(0) = \bar{Y}, \quad Z(0) = \bar{Z} \quad (\text{E.10})$$

$$\dot{X}(0) = 0, \quad \dot{Y}(0) = \bar{V}, \quad \dot{Z}(0) = \bar{V} \quad (\text{E.11})$$

with \bar{X} and \bar{Z} satisfying the equation (7.18) of plane Π_1 . The constants are

$$A = \frac{1}{2\omega_0} (\bar{V} + \gamma B) \quad (\text{E.12})$$

$$B = \frac{1}{2} [\bar{X} + \bar{Y} - \epsilon(X_P + Y_P)] \quad (\text{E.13})$$

$$C = \frac{1}{2\omega_2} (-\bar{V} + \gamma D) \quad (\text{E.14})$$

$$D = \frac{1}{2} \left(\epsilon Z_P + \frac{\bar{X} - \bar{Y} - 2\alpha\bar{Z}}{1 + 2\alpha} \right) \quad (\text{E.15})$$

$$E_1 = \epsilon X_P + \frac{\alpha}{1 + 2\alpha} (\bar{X} - \bar{Y} + \bar{Z}) \quad (\text{E.16})$$

$$E_2 = \epsilon Y_P - \frac{\alpha}{1 + 2\alpha} (\bar{X} - \bar{Y} + \bar{Z}) \quad (\text{E.17})$$

$$E_3 = \epsilon Z_P + \frac{1}{1 + 2\alpha} (\bar{X} - \bar{Y} + \bar{Z}) \quad (\text{E.18})$$

E.3 Case 00 \rightarrow 11

The initial conditions are

$$X(0) = \bar{X}, \quad Y(0) = \bar{Y}, \quad Z(0) = \bar{Z} \quad (\text{E.19})$$

$$\dot{X}(0) = 0, \quad \dot{Y}(0) = 0, \quad \dot{Z}(0) = 0 \quad (\text{E.20})$$

with \bar{X}, \bar{Y} and \bar{Z} satisfying both equations (7.18) and (7.19) of planes Π_1 and Π_2 .

The constants are

$$A = \frac{\gamma}{2\omega_0} B \quad (\text{E.21})$$

$$B = \frac{1 - \epsilon}{2} (X_P + Y_P) \quad (\text{E.22})$$

$$C = \frac{\gamma}{2\omega_2} D \quad (\text{E.23})$$

$$D = \frac{\epsilon - 1}{2} Z_P \quad (\text{E.24})$$

$$E_1 = \epsilon X_P + \frac{\alpha}{1+2\alpha} (\bar{X} - \bar{Y} + \bar{Z}) \quad (\text{E.25})$$

$$E_2 = \epsilon Y_P - \frac{\alpha}{1+2\alpha} (\bar{X} - \bar{Y} + \bar{Z}) \quad (\text{E.26})$$

$$E_3 = \epsilon Z_P + \frac{1}{1+2\alpha} (\bar{X} - \bar{Y} + \bar{Z}) \quad (\text{E.27})$$

Appendix F

Details of the faces $AECD$ and $BCDF$ - Chapter 7

I provide here a description of the subsets of the faces $AECD$ and $BCDF$ of the sticking region \mathbf{H} as they appear in Fig. (7.3).

Let us first focus on the face $AECD$ and consider a seismic event starting at a point $P_1 = (X_1, Y_1, Z_1)$ on this face. Accordingly, the coordinates of P_1 verify the equation (7.18) of plane Π_1

$$X_1 = 1 + \alpha Z_1 \quad (\text{F.1})$$

and the event starts with mode 10. If the orbit of mode 10 does not intercept plane Π_2 before time T_{1b} has elapsed, the slip of asperity 1 terminates at a point P_2 with coordinates

$$X_2 = X_1 - \kappa_1 U, \quad Y_2 = Y_1, \quad Z_2 = Z_1 + \kappa_1 U. \quad (\text{F.2})$$

Combining the no overshooting condition $X_2 \geq 0$ with Eq. (F.1), we end up with the constraint

$$Z_1 \geq \frac{\kappa_1 U - 1}{\alpha}. \quad (\text{F.3})$$

Accordingly, we can define the points

$$J_1 = \left(\kappa_1 U, \beta - \kappa_1 U + 1, \frac{\kappa_1 U - 1}{\alpha} \right) \quad (\text{F.4})$$

$$K_1 = \left(\kappa_1 U, 1 - \kappa_1 U, \frac{\kappa_1 U - 1}{\alpha} \right) \quad (\text{F.5})$$

corresponding to the intersection of the face $AECD$ of \mathbf{H} with the plane

$$Z = \frac{\kappa_1 U - 1}{\alpha}. \quad (\text{F.6})$$

In order to obtain a two-mode event 10-01, one must have $P_2 \in \Pi_2$: hence, using Eq. (7.19),

$$Y_2 = \beta - \alpha Z_2. \quad (\text{F.7})$$

If the orbit of mode 01 does not meet plane Π_1 before time T_{1b} has elapsed, the slip of asperity 2 terminates at point P_3 with coordinates

$$X_3 = X_2, \quad Y_3 = Y_2 - \beta\kappa_1 U, \quad Z_3 = Z_2 - \beta\kappa_1 U. \quad (\text{F.8})$$

Imposing the no overshooting conditions

$$X_3 \geq 0, \quad Y_3 \geq 0 \quad (\text{F.9})$$

and expressing all coordinates in terms of Z_1 by means of the previous equations, we are left with the constraint

$$\frac{\kappa_1 U - 1}{\alpha} \leq Z_1 \leq \frac{\beta - (\alpha + \beta)\kappa_1 U}{\alpha}. \quad (\text{F.10})$$

In turn, this condition constrains the admissible values of X_1 and Y_1 giving rise to a two-mode event 10-01. We conclude that such a seismic event takes place from the segment \mathbf{s}_1 with end points

$$H_1 = \left(\beta - \kappa_1 U(\alpha + \beta) + 1, \beta\kappa_1 U, \frac{\beta - \kappa_1 U(\alpha + \beta)}{\alpha} \right) \quad (\text{F.11})$$

$$I_1 = \left(\kappa_1 U, \beta - \kappa_1 U(1 + \alpha) + 1, \frac{\kappa_1 U - 1}{\alpha} \right) \quad (\text{F.12})$$

lying on the line

$$\begin{cases} X + Y - \beta + \alpha\kappa_1 U - 1 = 0 \\ X - \alpha Z - 1 = 0 \end{cases} \quad (\text{F.13})$$

As a result, we can define the point

$$G_1 = \left(\beta - \alpha\kappa_1 U + 1, 0, \frac{\beta - \alpha\kappa_1 U}{\alpha} \right) \quad (\text{F.14})$$

corresponding to the intersection of line (F.13) with the edge CE of the sticking region \mathbf{H} . To sum up, the vertices of the trapezoid \mathbf{Q}_1 are the point E given in Eq. (7.23) and the points G_1, I_1 and K_1 . Finally, the vertices of the trapezoid \mathbf{R}_1 are the end points of \mathbf{s}_1 and the points J_1 and

$$J_2 = \left(\beta(1 - \kappa_1 U) + 1, \beta\kappa_1 U, \frac{\beta(1 - \kappa_1 U)}{\alpha} \right) \quad (\text{F.15})$$

defined as the intersection of the edge CD with the plane

$$Y = \beta\kappa_1 U. \quad (\text{F.16})$$

Let us now turn our attention to the face $BCDF$ and consider a seismic event starting at a point $P_1 = (X_1, Y_1, Z_1)$ on this face. Accordingly, the coordinates of P_1 verify the equation (7.19) of plane Π_2

$$Y_1 = \beta - \alpha Z_1 \quad (\text{F.17})$$

and the event starts with mode 01. If the orbit of mode 01 does not meet plane Π_1 before time T_{1b} has elapsed, the slip of asperity 2 terminates at a point P_2 with coordinates

$$X_2 = X_1, \quad Y_2 = Y_1 - \beta \kappa_1 U, \quad Z_2 = Z_1 - \beta \kappa_1 U. \quad (\text{F.18})$$

Combining the no overshooting condition $Y_2 \geq 0$ with Eq. (F.17), we end up with the constraint

$$Z_1 \leq \frac{\beta(1 - \kappa_1 U)}{\alpha}. \quad (\text{F.19})$$

Accordingly, we can define the point

$$K_2 = \left(\beta(1 - \kappa_1 U), \beta \kappa_1 U, \frac{\beta(1 - \kappa_1 U)}{\alpha} \right) \quad (\text{F.20})$$

corresponding to the intersection of the face $BCDF$ of \mathbf{H} with the plane

$$Z = \frac{\beta(1 - \kappa_1 U)}{\alpha}. \quad (\text{F.21})$$

In order to obtain a two-mode event 01-10, one must have $P_2 \in \Pi_1$: hence, using Eq. (7.18),

$$X_2 = 1 + \alpha Z_2. \quad (\text{F.22})$$

If the orbit of mode 10 does not meet plane Π_2 before time T_{1b} has elapsed, the slip of asperity 1 terminates at point P_3 with coordinates

$$X_3 = X_2 - \kappa_1 U, \quad Y_3 = Y_2, \quad Z_3 = Z_2 + \kappa_1 U. \quad (\text{F.23})$$

Imposing the no overshooting conditions

$$X_3 \geq 0, \quad Y_3 \geq 0 \quad (\text{F.24})$$

and expressing all coordinates in terms of Z_1 by means of the previous equations, we are left with the constraint

$$\frac{\kappa_1 U(\alpha\beta + 1) - 1}{\alpha} \leq Z_1 \leq \frac{\beta(1 - \kappa_1 U)}{\alpha}. \quad (\text{F.25})$$

In turn, this condition constrains the admissible values of X_1 and Y_1 giving rise to a two-mode event 01-10. We conclude that such a seismic event takes place from the segment \mathbf{s}_2 with end points

$$H_2 = \left(\kappa_1 U, \beta - \kappa_1 U(\alpha\beta + 1) + 1, \frac{\kappa_1 U(\alpha\beta + 1) - 1}{\alpha} \right) \quad (\text{F.26})$$

$$I_2 = \left(\beta(1 - \kappa_1 U - \alpha\kappa_1 U) + 1, \beta\kappa_1 U, \frac{\beta(1 - \kappa_1 U)}{\alpha} \right) \quad (\text{F.27})$$

lying on the line

$$\begin{cases} X + Y - \beta(1 - \alpha\kappa_1 U) - 1 = 0 \\ Y + \alpha Z - \beta = 0 \end{cases} \quad (\text{F.28})$$

As a result, we can define the point

$$G_2 = \left(0, \beta(1 - \alpha\kappa_1 U) + 1, \beta\kappa_1 U - \frac{1}{\alpha} \right) \quad (\text{F.29})$$

corresponding to the intersection of line (F.28) with the edge DF of the sticking region \mathbf{H} . To sum up, the vertices of the trapezoid \mathbf{Q}_2 are the point F given in Eq. (7.23) and the points G_2, I_2 and K_2 . Finally, the vertices of the trapezoid \mathbf{R}_2 are the end points of \mathbf{s}_2 and the points J_1 and J_2 .

A straightforward calculation yields the lengths l_1 and l_2 of segments \mathbf{s}_1 and \mathbf{s}_2 , respectively:

$$l_1 = |\beta + 1 - \kappa_1 U(1 + \alpha + \beta)| \sqrt{\frac{1 + 2\alpha^2}{\alpha^2}} \quad (\text{F.30})$$

$$l_2 = |\beta + 1 - \kappa_1 U(1 + \alpha\beta + \beta)| \sqrt{\frac{1 + 2\alpha^2}{\alpha^2}} \quad (\text{F.31})$$

The distances of segments \mathbf{s}_1 and \mathbf{s}_2 from the edge CD are, respectively,

$$d_1 = \alpha\kappa_1 U \sqrt{\frac{1 + \alpha^2}{1 + 2\alpha^2}}, \quad d_2 = \beta d_1. \quad (\text{F.32})$$

Appendix G

Particular events generated on segments s_1 and s_2 - Chapter 7

The aim of the present Appendix is to investigate the conditions under which states belonging to the subsets \mathbf{s}_1 and \mathbf{s}_2 of the sticking region \mathbf{H} generate n -mode events involving the separate slips of the asperities, with $n > 2$. In view of the following discussion, I recall that the slip deficit of asperity 1 is reduced by an amount $\kappa_1 U$ each time it slips alone; analogously, the slip deficit of asperity 2 is reduced by an amount $\beta \kappa_1 U$ each time it slips alone.

G.1 Three-mode events 10-01-10

At the end of a two-mode event 10-01, starting at a point $P_1 = (X_1, Y_1, Z_1)$ on the segment s_1 on the face $AECD$ of the sticking region, the system is at a point P_2 with coordinates

$$X_2 = X_1 - \kappa_1 U, \quad Y_2 = Y_1 - \beta \kappa_1 U, \quad Z_2 = Z_1 + \kappa_1 U(1 - \beta). \quad (\text{G.1})$$

The event will then continue with a third mode 10 if $P_2 \in \Pi_1$: thus, introducing the coordinates of P_2 in Eq. (7.18) and bearing in mind that

$$X_1 = 1 + \alpha Z_1, \quad (\text{G.2})$$

we get the following condition:

$$\alpha = \frac{1}{\beta - 1}. \quad (\text{G.3})$$

As $0 < \beta < 1$, this result is unacceptable, since α is defined as positive. In conclusion, if we consider seismic events involving the alternate slips of the

asperities and starting with the slip of asperity 1, the system can only generate a two-mode event 10-01. Any additional slip phase is prevented by the stronger frictional resistance of asperity 1 with respect to asperity 2.

G.2 Three-mode events 01-10-01

At the end of a two-mode event 01-10, starting at a point $P_1 = (X_1, Y_1, Z_1)$ on the segment \mathbf{s}_2 on the face $BCDF$ of the sticking region, the system is at a point P_2 with the same coordinates as given in Eq. (G.1). The event will then continue with a third mode 01 if $P_2 \in \Pi_2$: thus, introducing the coordinates of P_2 in Eq. (7.19) and bearing in mind that

$$Y_1 = \beta - \alpha Z_1, \quad (\text{G.4})$$

we get the following condition:

$$\alpha = \alpha^* = \frac{\beta}{1 - \beta}. \quad (\text{G.5})$$

Since $0 < \beta < 1$, the constraint $\alpha^* \geq 0$ is always satisfied. Accordingly, under the particular condition $\alpha = \alpha^*$, the system can give rise to three-mode events 01-10-01.

G.3 Four-mode events 01-10-01-10

At the end of a three-mode event 01-10-01, the system is at a point P_3 with coordinates

$$X_3 = X_1 - \kappa_1 U, \quad Y_3 = Y_1 - 2\beta\kappa_1 U, \quad Z_3 = Z_1 + \kappa_1 U(1 - 2\beta). \quad (\text{G.6})$$

The event will then continue with a fourth mode 10 if $P_3 \in \Pi_1$: thus, introducing the coordinates of P_3 in Eq. (7.18), bearing Eq. (F.28) in mind and taking into account that $\alpha = \alpha^*$, we end up with

$$\beta = -1, \quad (\text{G.7})$$

which is unacceptable, since β is defined as positive. In conclusion, if we consider seismic events involving the alternate slips of the asperities and starting with the slip of asperity 2, the system can only generate two-mode events 01-10 and, under particular conditions related with the degree of coupling between the asperities, three-mode events 01-10-01.

For the sake of simplicity, the condition $\alpha \neq \alpha^*$ is assumed throughout all Chapter 7. Accordingly, seismic events taking place on \mathbf{s}_2 are two-mode events 01-10 and three-mode events 01-10-01 are not considered.

Appendix H

Stress perturbations between neighbouring faults

Let us consider two plane faults, namely fault 1 and fault 2, embedded in an infinite, homogeneous and isotropic Poisson medium of rigidity μ (Fig. H.1). Following the slip of fault 1 (perturbing fault), stress is transferred to fault 2 (receiving fault). I calculate the normal traction σ_n and the tangential traction in the direction of slip σ_t transferred to the receiving fault, estimated as the average value at its centre.

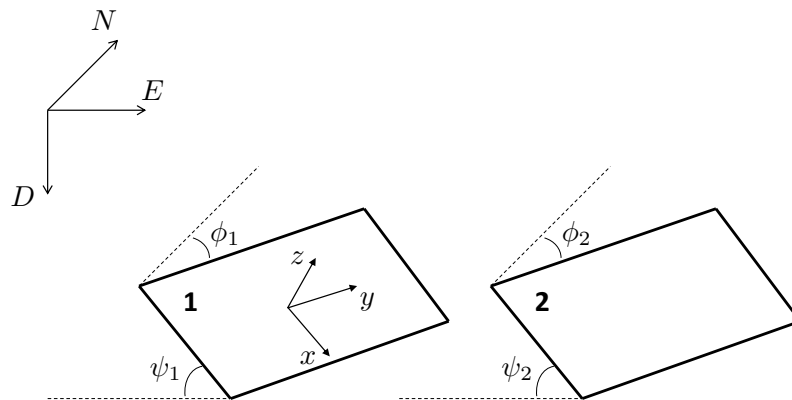


Figure H.1: Geometry of the model employed to study the stress transfer between neighbouring faults. Fault 1 is the perturbing fault, while fault 2 is the receiving fault. The coordinates (E, N, D) are the UTM coordinates and depth of the centres of the faults, respectively, whereas the axes (x, y, z) correspond with the directions of dip, strike and normal on fault 1, respectively. The angles ϕ and ψ are the strike and dip angles of the faults, respectively.

Let us define a coordinate system (x, y, z) with axes corresponding with the directions of dip, strike and normal on fault 1, respectively. Fault 1 lies on the

plane $z = 0$ and its centre is in the origin of the coordinate system. Accordingly, the unit vector perpendicular to fault 1 is $n_{1i} = (0, 0, 1)$. Let ϕ_1 , ψ_1 and λ_1 be the strike, dip and rake angles of fault 1, respectively. The slip direction of fault 1 is then given by

$$m_{1i} = (-\sin \lambda_1, \cos \lambda_1, 0). \quad (\text{H.1})$$

Fault 2 is characterized by strike and dip angles ϕ_2 and ψ_2 , respectively. Accordingly, the unit vector perpendicular to fault 2 is given by

$$n_{2i} = (\sin \Delta\psi \cos \Delta\phi, -\sin \Delta\psi \sin \Delta\phi, \cos \Delta\psi) \quad (\text{H.2})$$

where

$$\Delta\phi = \phi_2 - \phi_1, \quad \Delta\psi = \psi_2 - \psi_1. \quad (\text{H.3})$$

Let λ_2 be the preferred rake angle on fault 2, correlated with the orientation of tectonic loading: $\lambda_2 = 0^\circ$ for left-lateral strike-slip, $\lambda_2 = 180^\circ$ for right-lateral strike-slip, $\lambda_2 = -90^\circ$ for normal dip-slip and $\lambda_2 = 90^\circ$ for reverse dip-slip. The components of the corresponding slip direction m_{2i} are

$$m_{2x} = \cos \lambda_2 \sin \Delta\phi - \sin \lambda_2 \cos \Delta\psi \cos \Delta\phi \quad (\text{H.4})$$

$$m_{2y} = \cos \lambda_2 \cos \Delta\phi + \sin \lambda_2 \cos \Delta\psi \sin \Delta\phi \quad (\text{H.5})$$

$$m_{2z} = \sin \lambda_2 \sin \Delta\psi \quad (\text{H.6})$$

Let (E_i, N_i) and D_i be the UTM coordinates and depths of the centres of the faults, respectively. In the (x, y, z) reference system, the coordinates of the centre of fault 2 are identified by the following three steps:

1. placing the origin at the centre of fault 1:

$$x' = E_2 - E_1, \quad y' = N_2 - N_1, \quad z' = D_2 - D_1 \quad (\text{H.7})$$

2. clockwise rotation about the z axis by the angle ϕ_1 :

$$x'' = x' \cos \phi_1 - y' \sin \phi_1 \quad y'' = x' \sin \phi_1 + y' \cos \phi_1, \quad z'' = z' \quad (\text{H.8})$$

3. counterclockwise rotation about the y axis by the angle ψ_1 :

$$x = x'' \cos \psi_1 - z'' \sin \psi_1, \quad y = y'', \quad z = x'' \sin \psi_1 + z'' \cos \psi_1. \quad (\text{H.9})$$

The perturbing fault is treated as a point-like dislocation source (a double-couple of forces) located at the origin. This is good approximation for nonoverlapping regions (Appendix B). Let m_0 be the scalar seismic moment of the dislocation.

The i -th component of the static displacement field generated by the slip of fault 1 is

$$u_i = -M_{jk}G_{ij,k} \quad (\text{H.10})$$

where M_{ij} is the moment tensor associated with the dislocation source

$$M_{ij} = m_0 (m_{1i}n_{1j} + m_{1j}n_{1i}) \quad (\text{H.11})$$

and G_{ij} is the Somigliana tensor

$$G_{ij} = \frac{1}{8\pi\mu} \left(\frac{2}{r}\delta_{ij} - \frac{2}{3}r_{,ij} \right) \quad (\text{H.12})$$

with

$$r = \sqrt{x^2 + y^2 + z^2}. \quad (\text{H.13})$$

The components of the stress field are given by

$$\sigma_{ij} = \mu(e_{kk}\delta_{ij} + 2e_{ij}), \quad (\text{H.14})$$

where e_{ij} is the strain field associated with the displacement field (H.10). Finally, the normal traction σ_n and the tangential traction in the direction of slip σ_t on fault 2 are

$$\sigma_n = \sigma_{ij}n_{2i}n_{2j}, \quad \sigma_t = \sigma_{ij}m_{2i}n_{2j}. \quad (\text{H.15})$$

The signs of σ_n and σ_t define the effect of the stress transfer on fault 2. If $\sigma_n > 0$, the amount of compressional stress on the receiving fault is reduced, and vice-versa. If $\sigma_t > 0$, the slip of the receiving fault is promoted, and vice-versa.

Finally, the particular case in which fault 1 and fault 2 are coplanar and lined up in the strike direction is discussed. Also, it is assumed that the faults are characterized by the same dip angle and faulting mechanism. Accordingly, we have

$$\phi_1 = \phi_2, \quad \psi_1 = \psi_2, \quad \lambda_1 = \lambda_2 \quad (\text{H.16})$$

so that it results

$$\mathbf{n}_1 = \mathbf{n}_2, \quad \mathbf{m}_1 = \mathbf{m}_2. \quad (\text{H.17})$$

Under this circumstance, the tangential traction in the direction of slip is given by

$$\sigma_t = \frac{5m_0}{12\pi r^3} \quad (\text{H.18})$$

in the case of strike-slip faulting ($\lambda_i = 0, \pi$) and by

$$\sigma_t = \frac{m_0}{6\pi r^3} \quad (\text{H.19})$$

in the case of dip-slip faulting ($\lambda_i = \pm \pi/2$), where the results reported in §B.1 were employed. Since the faults are coplanar, the normal traction σ_n is always null; what is more, it is always $\sigma_t > 0$, so that the slip of the receiving fault is always promoted by the failure of the perturbing fault.

Appendix I

Poroelastic effect

Let us consider a system made up of n plane faults characterized by the same strike and dip angles (§9). The fault system is placed in a homogeneous and isotropic Poisson poroelastic medium characterized by an hydraulic diffusivity c and drained and undrained Poisson moduli ν and ν_u , respectively. Let r_{ij} be the distance between the centres of the i -th and the j -th fault. The stress field produced by a seismic event is discussed, treating each fault as a point-like dislocation source and distinguishing between strike-slip and dip-slip faulting. The solutions are provided by Carvalho and Curran (1998) and Cheng and Detournay (1998).

The stress field consists of two terms: a constant term, corresponding to the coseismic stress, and a time-dependent term, associated with pore fluid diffusion. The former was discussed in §B.1. In order to study the latter term, I introduce the nondimensional variable

$$\xi(t) = \frac{r_{ij}}{2\sqrt{ct}} \quad (\text{I.1})$$

and a coefficient

$$b = \frac{\nu_u - \nu}{(1 - \nu)(1 - \nu_u)} \quad (\text{I.2})$$

where t is time. After the failure of the i -th fault, associated with a seismic moment m_i , the j -th fault is subject to the time-dependent tangential traction

$$\Delta\sigma'_{ij}(t) = \frac{bm_i}{2\pi r_{ij}^3} f(t), \quad (\text{I.3})$$

where

$$f(t) = -\frac{2}{\sqrt{\pi}} \xi e^{-\xi^2} + 3 \frac{\text{erf } \xi}{\xi^2} - \frac{6}{\sqrt{\pi}} \frac{e^{-\xi^2}}{\xi} + \text{erfc } \xi \quad (\text{I.4})$$

for strike-slip faulting and

$$f(t) = -\frac{3}{4} \frac{\text{erf } \xi}{\xi^2} + \frac{3}{2\sqrt{\pi}} \frac{e^{-\xi^2}}{\xi} - \frac{1}{2} \text{erfc } \xi \quad (\text{I.5})$$

for dip-slip faulting. As $t \rightarrow \infty$, the traction (I.3) approaches an asymptotic value

$$\Delta\sigma_{ij}^{\infty} = \frac{bm_i}{2\pi r_{ij}^3} \quad (\text{I.6})$$

for strike-slip faulting and

$$\Delta\sigma_{ij}^{\infty} = -\frac{bm_i}{4\pi r_{ij}^3} \quad (\text{I.7})$$

for dip-slip faulting. The function $f(t)$ is shown in Fig. (I.1).

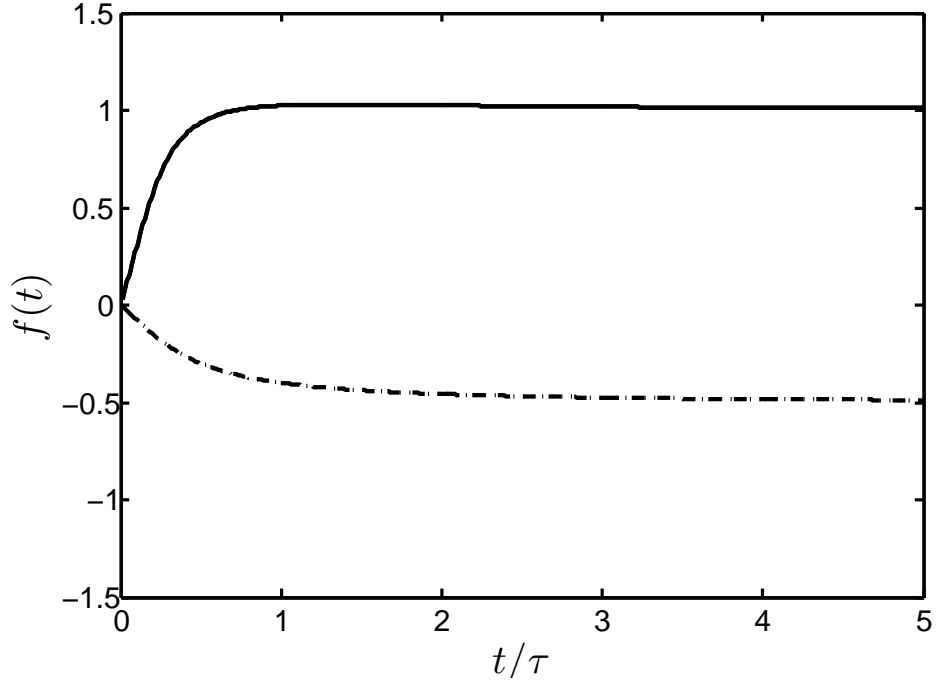


Figure I.1: Function $f(t)$ in the case of strike-slip faulting (solid line) and dip-slip faulting (dashed line). Time is in units of the characteristic diffusion time τ .

According to the choice of a Poisson solid, I take $\nu_u = 0.25$. For a typical value $\nu = 0.2$ under drained conditions (e.g. Rice and Cleary, 1976), it results $b \simeq 0.1$. Then the ratio $|\Delta\sigma_{ij}^{\infty}|/\Delta\sigma_{ij}$ between the asymptotic poroelastic stress and the coseismic stress reported in Eq. (B.9) and Eq. (B.10) is about 0.12 for strike-slip faulting and 0.15 for dip-slip faulting. These are the maximum values, which may be reached for $t \gg \tau$, where $\tau = r_{ij}^2/(4c)$ is the characteristic diffusion time. For distances of tens of km, τ is much longer than the typical duration of a seismic sequence: as a result, the poroelastic effect is at least one order of magnitude smaller than the coseismic stress transfer.

Bibliography

Amendola, A. and Dragoni, M. (2013). Dynamics of a two-fault system with viscoelastic coupling, *Nonlin. Processes Geophys.*, 20, 1 – 10, doi:10.5194/npg-20-1-2013.

Ammon, C. J., Ji, C., Thio, H. K., Robinson, D., Ni, S., Hjorleifsdottir, V., Kanamori, H., Lay, T., Das, S., Helmberger, D., Ichinose, G., Polet, J. and Wald, D. (2005). Rupture process of the 2004 Sumatra-Andaman earthquake. *Science*, 308(5725), 1133 – 1139, doi:10.1126/science.1112260.

Anderson, E. M. (1951). *The Dynamics of Faulting*, 2nd ed., Oliver and Boyd, Edinburgh.

Barbot, S., Fialko, Y. and Bock, Y. (2009). Postseismic deformation due to the M_w 6.0 2004 Parkfield earthquake: Stress-driven creep on a fault with spatially variable rate-and-state friction parameters. *J. Geophys. Res.*, 114, B07405, doi:10.1029/2008JB005748.

Belardinelli, M. E. and Bonafede, M. (1993). Modelling afterslip processes on a strike-slip fault in the framework of a non-singular crack theory. *Annali di Geofisica*, XXXVI, 25 – 36.

Belardinelli, M.E., Bizzarri, A. and Cocco, M. (2003). Earthquake triggering by static and dynamic stress changes. *J. Geophys. Res.*, 108 (B3), 2135, doi:10.1029/2002JB001779, 2003.

Bindi, D., Castro, R. R., Franceschina, G., Luzi, L. and Pacor, F. (2004). The 1997-1998 Umbria-Marche sequence (central Italy): Source, path, and site effects estimated from strong motion data recorded in the epicentral area. *J. Geophys. Res.*, 109(B4), doi:10.1029/2003JB002857.

Biot, M. A. (1941). General theory of three-dimensional consolidation. *J. Appl. Geophys.*, 12(2), 155 – 164, doi:10.1063/1.1712886.

- Bletery, Q., Sladen, A., Delouis, B., Vallée, M., Nocquet, J.-M., Rolland, L. and Jiang, J. (2014). A detailed source model for the M_w 9.0 Tohoku-Oki earthquake reconciling geodesy, seismology, and tsunami records. *J. Geophys. Res. Solid Earth*, 119, 7636 – 7653, doi: 10.1002/2014JB011261.
- Brune, J. N. (1970). Tectonic stress and the spectra of seismic shear waves from earthquakes. *J. Geophys. Res.*, 75(26), 4997 – 5009, doi:10.1029/JB075i026p04997.
- Bürgmann, R. and Dresen, G. (2008). Rheology of the Lower Crust and Upper Mantle: Evidence from Rock Mechanics, Geodesy, and Field Observations. *Annu. Rev. Earth. Planet. Sci.*, 36, 531 – 567.
- Burridge, R. and Knopoff, L. (1967). Model and theoretical seismicity. *Bull. Seismol. Soc. Am.*, 57(3), 341 – 371.
- Byerlee, J. (1978). Friction of rocks. *Pure Appl. Geophys.*, 116(4), 615 – 626, doi:10.1007/BF00876528.
- Caporali, A. and Ostini, L. (2012). Analysis of the displacement of geodetic stations during the Emilia seismic sequence of May 2012. *Ann. Geophys.*, 55(4), doi:10.4401/ag-6115.
- Capuano, P., Zollo, A., Emolo, A., Marcucci, S. and Milana, G. (2000). Rupture mechanism and source parameters of Umbria-Marche mainshocks from strong motion data. *Journal of seismology*, 4(4), 463 – 478, doi:10.1023/A:1026523703464.
- Carlson, J. M. and Langer, J. S. (1989a). Properties of earthquakes generated by fault dynamics. *Phys. Rev. Lett.*, 62(22), 2632, doi:10.1103/PhysRevLett.62.2632.
- Carlson, J. M. and Langer, J. S. (1989b). Mechanical model of an earthquake fault. *Phys. Rev. A*, 40(11), 6470, doi:10.1103/PhysRevA.40.6470.
- Carlson, J. M., Langer, J. S., Shaw, B. E. and Tang, C. (1991). Intrinsic properties of a Burridge-Knopoff model of an earthquake fault. *Phys. Rev. A*, 44(2), 884, doi:10.1103/PhysRevA.44.884.
- Carter, N.L. (1976). Steady State Flow of Rocks. *Rev. Geophys. Space. Phys.*, 14, 301 – 360, doi:10.1029/RG014i003p00301.

Carvalho, J. L. and Curran, J. H. (1998). Three-dimensional displacement discontinuity solutions for fluid-saturated porous media. *Int. J. Solids Struct.*, 35, 4887 – 4893, doi:10.1016/S0020-7683(98)00099-7.

Castro, R. R., Pacor, F., Puglia, R., Ameri, G., Letort, J., Massa, M. and Luzi, L. (2013). The 2012 May 20 and 29, Emilia earthquakes (Northern Italy) and the main aftershocks: S-wave attenuation, acceleration source functions and site effects. *Geophys. J. Int.*, 195(1), 597 – 611, doi:10.1093/gji/ggt245.

Cheng, A. H.-D. and Detournay, E. (1998). On singular integral equations and fundamental solutions of poroelasticity. *Int. J. Solids Struct.*, 35, 4521 – 4555, doi:10.1016/S0020-7683(98)00082-1.

Chlieh, M., Avouac, J. P., Hjorleifsdottir, V., Song, T. R. A., Ji, C., Sieh, K., Sladen, A., Hebert, H., Prawirodirdjo, L., Bock, Y. and Galetzka, J. (2007). Coseismic slip and afterslip of the great Mw 9.15 Sumatra–Andaman earthquake of 2004. *Bull. Seismol. Soc. Am.*, 97(1A), S152-S173, doi: 10.1785/0120050631.

Christensen, D. H. and Beck, S. L., (1994). The rupture process and tectonic implications of the great 1964 Prince William Sound earthquake. *Pure Appl. Geophys.*, 142, 29 – 53, doi:10.1007/BF00875967.

Cocco, M., Nostro, C. and Ekström, G. (2000). Static stress changes and fault interaction during the 1997 Umbria-Marche earthquake sequence. *Journal of Seismology*, 4(4), 501 – 516, doi:10.1023/A:1026507917308.

Cohen, S. C. and Freymueller, J. T. (2004). Crustal deformation in the south-central Alaska subduction zone. *Adv. Geophys.*, 47, 1 – 63, doi:10.1016/S0065-2687(04)47001-0.

Convertito, V., Catalli, F. and Emolo, A. (2013). Combining stress transfer and source directivity: The case of the 2012 Emilia seismic sequence. *Sci. Rep.*, 3, doi:10.1038/srep03114.

Delouis, B., Nocquet, J. M. and Vallée, M. (2010). Slip distribution of the February 27, 2010 Mw = 8.8 Maule earthquake, central Chile, from static and high-rate GPS, InSAR, and broadband teleseismic data. *Geophys. Res. Lett.*, 37(17), L17305, doi:10.1029/2010GL043899.

- DeMets, C. and Dixon, T. H. (1999). New kinematic models for Pacific-North America motion from 3 Ma to present, I: Evidence for steady motion and biases in the NUVEL-1A Model. *Geophys. Res. Lett.*, 26(13), 1921 – 1924, doi:10.1029/1999GL900405.
- Deng, J., Gurnis, M., Kanamori, H. and Hauksson, E. (1998). Viscoelastic flow in the lower crust after the 1992 Landers, California, earthquake. *Science*, 282(5394), 1689 – 1692, doi:10.1126/science.282.5394.1689.
- Detournay, E. and Cheng, A. H. D. (1993). Fundamentals of poroelasticity, in *Comprehensive Rock Engineering: Principles, Practice and Projects*, Vol. II, Analysis and Design Method, Pergamon Press, Oxford.
- Diao, F. Q., Xiong, X., Wang, R. J., Zheng, Y., Walter, T. R., Weng, H. H., Li, J. (2013). Overlapping post-seismic deformation processes: afterslip and viscoelastic relaxation following the 2011 Mw 9.0 Tohoku (Japan) earthquake. *Geophys. J. Int.*, 196(1), 218–229, doi:10.1093/gji/ggt376.
- Di Bernardo, M., Budd, C. J., Champneys, A. R. and Kowalczyk, P. (2008). *Piecewise-smooth Dynamical Systems - Theory and Applications*, Springer, Berlin.
- Dieterich, J. H. (1972). Time-dependent friction in rocks. *J. Geophys. Res.*, 77(20), 3690 – 3697, doi:10.1029/JB077i020p03690.
- Dieterich, J. H. (1992). Earthquake nucleation on faults with rate-and state-dependent strength. *Tectonophysics*, 211(1 – 4), 115 – 134, doi:10.1016/0040-1951(92)90055-B.
- Dieterich, J. (1994). A constitutive law for rate of earthquake production and its application to earthquake clustering. *J. Geophys. Res.*, 99, 2601 – 2618, doi:10.1029/93JB02581.
- Ding, M., and Lin, J. (2014). Post-seismic viscoelastic deformation and stress transfer after the 1960 M 9.5 Valdivia, Chile earthquake: effects on the 2010 M 8.8 Maule, Chile earthquake. *Geophys. J. Int.*, 197 (2), 697 – 704, doi:10.1093/gji/ggu048.
- Dragonì, M., Bonafede, M. and Boschi, E. (1982). Stress relaxation in the earth and seismic activity. *Riv. Nuovo Cim. (1978-1999)*, 5(2), 1 – 34, doi:10.1007/BF02740828.

Dragoni, M. and Lorenzano, E. (2015). Stress states and moment rates of a two-asperity fault in the presence of viscoelastic relaxation. *Nonlinear Process. Geophys.*, 22(3), 349 – 359, doi:10.5194/npg-22-349-2015.

Dragoni, M. and Lorenzano, E. (2016). Conditions for the occurrence of seismic sequences in a fault system. *Nonlin. Process. Geophys.*, 23(6), 419 – 433, doi:10.5194/npg-23-419-2016.

Dragoni, M. and Lorenzano, E. (2017). Dynamics of a fault model with two mechanically different regions. *Earth Planets Space*, 69(145), doi:10.1186/s40623-017-0731-2.

Dragoni, M. and Piombo, A. (2011). Dynamics of a seismogenic fault subject to variable strain rate. *Nonlin. Process. Geophys.*, 18(3), 431 – 439, doi:10.5194/npg-18-431-2011.

Dragoni, M. and Piombo, A. (2015). Effect of stress perturbations on the dynamics of a complex fault. *Pure Appl. Geophys.*, 172(10), 2571 – 2583, doi:10.1007/s00024-015-1046-5.

Dragoni, M. and Santini, S. (2010). Simulation of the long-term behaviour of a fault with two asperities. *Nonlin. Process. Geophys.*, 17(6), 777 – 784, doi:10.5194/npg-17-777-2010.

Dragoni, M. and Santini, S. (2011). Conditions for large earthquakes in a two-asperity fault model. *Nonlin. Process. Geophys.*, 18(5), 709 – 717, doi:10.5194/npg-18-709-2011.

Dragoni, M. and Santini, S. (2012). Long-term dynamics of a fault with two asperities of different strengths. *Geophys. J. Int.*, 191, 1457 – 1467, doi:10.1111/j.1365-246X.2012.05701.x.

Dragoni, M. and Santini, S. (2014). Source functions of a two-asperity fault model. *Geophys. J. Int.*, 196, 1803 – 1812, doi:10.1093/gji/ggt491.

Dragoni, M. and Santini, S. (2015). A two-asperity fault model with wave radiation. *Phys. Earth. Planet. In.*, 248, 83 – 93, doi:10.1016/j.pepi.2015.08.001.

Dragoni, M. and Tallarico, A. (2016). Complex events in a fault model with interacting asperities. *Phys. Earth Planet. Inter.*, 257, 115 – 127, doi:10.1016/j.pepi.2016.05.014.

- Dziewonski, A. M. and Anderson, D. L. (1981). Preliminary reference Earth model. *Phys. Earth Planet. In.*, 25(4), 297 – 356, doi:10.1016/0031-9201(81)90046-7.
- Fialko, Y. (2004). Evidence of fluid-filled upper crust from observations of postseismic deformation due to the 1992 Mw 7.3 Landers earthquake. *J. Geophys. Res.*, 109, 1 – 17, doi:10.1029/2004JB002985.
- Filippov, A. F. (1988). *Differential equations with discontinuous righthand sides*, Kluwer Academic Publishers, Dordrecht.
- Freed, M. and Lin, J. (2001). Delayed triggering of the 1999 Hector Mine earthquake by viscoelastic stress transfer. *Nature*, 411, 180 – 183, doi:10.1038/35075548.
- Hainzl, S., Zöller, G. and Kurths, J. (1999). Similar power laws for foreshock and aftershock sequences in a spring-block model for earthquakes. *J. Geophys. Res.*, 104(B4), 7243 – 7253, doi:10.1029/1998JB900122.
- Harris, R. A. (1998). Introduction to special section: Stress triggers, stress shadows, and implications for seismic hazard, *J. Geophys. Res.*, 103(B10), 24347 – 24358, doi:10.1029/98JB01576.
- He, C. (2003). Interaction between two sliders in a system with rate-and state-dependent friction. *Sci. China. Earth. Sci.*, 46, 67 – 74, doi:10.1360/03dz0006.
- Heki, K., Miyazaki, S. and Tsuji, H. (1997). Silent fault slip following an intraplate thrust earthquake at the Japan Trench. *Nature*, 386, 595 – 598, doi:10.1038/386595a0.
- Holdahl, S. R. and Sauber, J. (1994). Coseismic slip in the 1964 Prince William Sound earthquake: A new geodetic inversion. *Pure Appl. Geophys.*, 142, 55 – 82, doi:10.1007/BF00875968.
- Huang, J. and Turcotte, D. L. (1990a). Are earthquakes an example of deterministic chaos?. *Geophys. Res. Lett.*, 17(3), 223 – 226, doi:10.1029/GL017i003p00223.
- Huang, J. and Turcotte, D. L. (1990b). Evidence for chaotic fault interactions in the seismicity of the San Andreas fault and Nankai trough. *Nature*, 348(6298), 234 – 236, doi:10.1038/348234a0.

Huang, J., Narkounskaia, G. and Turcotte, D. L. (1992). A cellular-automata, slider-block model for earthquakes II. Demonstration of self-organized criticality for a 2-D system. *Geophys. J. Int.*, 111(2), 259 – 269, doi:10.1111/j.1365-246X.1992.tb00575.x.

Hunstad, I., Anzidei, M., Cocco, M., Baldi, P., Galvani, A. and Pesci, A. (1999). Modelling coseismic displacements during the 1997 Umbria-Marche earthquake (central Italy). *Geophys. J. Int.*, 139(2), 283 – 295, doi:10.1046/j.1365-246x.1999.00949.x.

Jaeger, J. C. and Cook, N. G. W. (1976). *Fundamentals of Rock Mechanics*. Chapman & Hall, London.

Johnson, J. M., Satake, K., Holdahl, S. R. and Sauber, J. (1996). The 1964 Prince William Sound earthquake: Joint inversion of tsunami and geodetic data. *J. Geophys. Res.*, 101, 523 – 532, doi:10.1029/95JB02806.

Jónsson, S., Zebker, H., Segall, P. and Amelung, F. (2002). Fault slip distribution of the 1999 M_w 7.1 Hector Mine, California, earthquake, estimated from satellite radar and GPS measurements. *Bull. Seismol. Soc. Am.*, 92(4), 1377 – 1389, doi:10.1785/0120000922.

Jónsson, S., Segall, P., Pedersen, R. and Björnsson, G. (2003). Post-earthquake ground movements correlated to pore-pressure transients. *Nature*, 424(6945), 179 – 183, doi:10.1038/nature01776.

Kanamori, H. (1978). Use of seismic radiation to infer source parameters. USGS Open File Report, 78, 283 – 318.

Kanamori, H. (2001). Energy budget of earthquakes and seismic efficiency. *Int. Geophys.*, 76, 293 – 305.

Kanamori, H., Thio, H., Dreger, D., Hauksson, E. and Heaton, T. (1992). Initial investigation of the Landers, California, Earthquake of 28 June 1992 using TERRAscope. *Geophys. Res. Lett.*, 19(22), 2267 – 2270, doi:10.1029/92GL02320.

Kato, T., El-Fiky, G. S., Oware, E. N. and Miyazaki, S. (1998). Crustal strains in the Japanese islands as deduced from dense GPS array. *Geophys. Res. Lett.*, 25(18), 3445 – 3448, doi:10.1029/98GL02693.

- Kenner, S. and Segall, P. (2000). Postseismic deformation following the 1906 San Francisco earthquake. *J. Geophys. Res.*, 105(B6), 13195 – 13209, doi:10.1029/2000JB900076.
- Kirby, S. H. and Kronenberg, A. K. (1987). Rheology of the Lithosphere: Selected Topics. *Rev. Geophys.*, 25, 1219 – 1244, doi:10.1029/RG025i006p01219.
- Kusznir, N. J., Vita-Finzi, C., Whitmarsh, R. B., England, P., Bott, M. H. P., Govers, R., Cartwright, J. and Murrell, S. (1991). The distribution of stress with depth in the lithosphere: Thermo-rheological and geodynamic constraints [and discussion]. *Phil. Trans. Roy. Soc. Lond. A*, 337(1645), 95-110, doi:10.1098/rsta.1991.0109.
- Lawrence, J. D. (1972). *A catalog of special curves*. Dover Publications, New York.
- Lay, T., Kanamori, H. and Ruff, L. (1982). The asperity model and the nature of large subduction zone earthquakes. *Earthquake Prediction Research*, 1(1), 3 – 71.
- Lay, T., Kanamori, H., Ammon, C. J., Nettles, M., Ward, S. N., Aster, R. C., Beck, S. L., Bilek, S. L., Brudzinski, M. R., Butler, R., DeShon, H. R., Ekström, G., Satake, K. and Sipkin, S. (2005). The great Sumatra-Andaman earthquake of 26 december 2004. *Science*, 308(5725), 1127 – 1133, doi:10.1126/science.1112250.
- Lay, T., Ammon, C. J., Hutko, A. R. and Kanamori, H. (2010). Effects of kinematic constraints on teleseismic finite-source rupture inversions: Great Peruvian earthquakes of 23 June 2001 and 15 August 2007. *Bull. Seismol. Soc. Am.*, 100(3), 969–994, doi: 10.1785/0120090274.
- Lay, T., Kanamori, H., Ammon, C. J., Koper, K. D., Hutko, A. R., Ye, L., Yue, H. and Rushing, T. M. (2012). Depth-varying rupture properties of subduction zone megathrust faults. *J. geophys. Res.*, 117, B04311, doi:10.1029/2011JB009133.
- Lorito, S., Piatanesi, A., Cannelli, V., Romano, F. and Melini, D. (2010). Kinematics and source zone properties of the 2004 Sumatra-Andaman earthquake and tsunami: Nonlinear joint inversion of tide gauge, satellite altimetry, and GPS data. *J. Geophys. Res.*, 115(B2), doi:10.1029/2008JB005974.
- Love, A. E. H. (1944). *A Treatise on the Mathematical Theory of Elasticity*, 4th ed., Dover Publications, New York.

- Maercklin, N., Festa, G., Colombelli S. and Zollo, A. (2012). Twin ruptures grew to build up the giant 2011 Tohoku, Japan, earthquake. *Sci. Rep.*, 2, 709, doi:10.1038/srep00709.
- Marone, C., Raleigh, C. B. and Scholz, C. H. (1990). Frictional behavior and constitutive modeling of simulated fault gouge. *J. Geophys. Res.*, 95(B5), 7007 – 7025, doi:10.1029/JB095iB05p07007.
- Marone, C., Scholz, C. H. and Bilham, R. (1991). On the mechanics of earthquake afterslip. *J. Geophys. Res.*, 96(B5), 8441 – 8452, doi:10.1029/91JB00275.
- Masterlark, T. and Wang, H. F. (2002). Transient stress-coupling between the 1992 Landers and 1999 Hector Mine, California, earthquakes. *Bull. Seismol. Soc. Am.*, 92, 1470 – 1486, doi:10.1785/0120000905.
- McCaffrey, R. (2009). The tectonic framework of the Sumatran subduction zone. *Annu. Rev. Earth. Planet. Sci.*, 37, 345 – 366, doi:10.1146/annurev.earth.031208.100212.
- Montagner, J. P., Juhel, K., Barsuglia, M., Ampuero, J. P., Chassande-Mottin, E., Harms, J., Whiting, B., Bernard, P., Clévéde, E. and Lognonné, P. (2016). Prompt gravity signal induced by the 2011 Tohoku-Oki earthquake. *Nat. Comm.*, 7, doi:10.1038/ncomms13349.
- Morelli, A., Ekström, G. and Olivieri, M. (2000). Source properties of the 1997–98 Central Italy earthquake sequence from inversion of long-period and broad-band seismograms. *Journal of Seismology*, 4(4), 365 – 375, doi:10.1023/A:1026587817690.
- Nakanishi, H. (1990). Cellular-automaton model of earthquakes with deterministic dynamics. *Phys. Rev. A*, 41(12), 7086, doi:10.1103/PhysRevA.41.7086.
- Nakanishi, H. (1991). Statistical properties of the cellular-automaton model for earthquakes. *Phys. Rev. A*, 43(12), 6613, doi:10.1103/PhysRevA.43.6613.
- Nason, R. and Weertman, J. (1973). A dislocation theory analysis of fault creep events. *J. Geophys. Res.*, 78, 7745 – 7751, doi:10.1029/JB078i032p07745.
- Nishimura, T. and Thatcher, W. (2003). Rheology of the lithosphere inferred from postseismic uplift following the 1959 Hebgen Lake earthquake. *J. Geophys. Res.*, 108(B8), doi:10.1029/2002JB002191.

- Nussbaum, J. and Ruina, A. (1987). A two degree-of-freedom earthquake model with static/dynamic friction. *Pure Appl. Geophys.*, 125(4), 629 – 656, doi:10.1007/BF00879576.
- Okada, Y. (1985). Surface deformation due to shear and tensile faults in a half-space. *Bull. Seismol. Soc. Am.*, 75, 1135–1154.
- Okada, Y. (1992). Internal deformation due to shear and tensile faults in a half-space. *Bull. Seismol. Soc. Am.*, 82, 1018 – 1040.
- Ozawa, S., Nishimura, T., Suito, H., Kobayashi, T., Tobita, M. and Imakiire, T. (2011). Coseismic and postseismic slip of the 2011 magnitude-9 Tohoku-Oki earthquake. *Nature*, 475, 373 – 377, doi: 10.1038/nature10227.
- Pelletier, J. D. (2000). Spring-Block Models of Seismicity: Review and Analysis of a Structurally Heterogeneous Model Coupled to a Viscous Asthenosphere, in *Geocomplexity and the Physics of Earthquakes*, 27 – 42, doi:10.1029/GM120p0027.
- Pezzo, G., Boncori, J. P. M., Tolomei, C., Salvi, S., Atzori, S., Antonioli, A., Trasatti, E., Novali, F., Serpelloni, E., Candela, L. and Giuliani, R. (2013). Coseismic deformation and source modeling of the May 2012 Emilia (Northern Italy) earthquakes. *Seismol. Res. Lett.*, 84(4), 645 – 655, doi:10.1785/0220120171.
- Piombo, A., Martinelli, G. and Dragoni, M. (2005). Post-seismic fluid flow and Coulomb stress changes in a poroelastic medium. *Geophys. J. Int.*, 162(2), 507 – 515, doi:10.1111/j.1365-246X.2005.02673.x.
- Piombo, A., Tallarico, A., and Dragoni, M. (2007). Displacement, strain and stress fields due to shear and tensile dislocations in a viscoelastic half-space. *Geophys. J. Int.*, 170(3), 1399 – 1417, doi:10.1111/j.1365-246X.2007.03283.x.
- Plafker, G. (1965). Tectonic deformation associated with the 1964 Alaska earthquake. *Science*, 148(3678), 1675 – 1687, doi:10.1126/science.148.3678.1675.
- Pollitz, F. F., Peltzer, G. and Bürgmann, R. (2000). Mobility of continental mantle: Evidence from postseismic geodetic observations following the 1992 Landers earthquake. *J. Geophys. Res.*, 105, 8035, doi:10.1029/1999JB900380.
- Ranalli, G. (1995). *Rheology of the Earth*, 2nd ed., Chapman & Hall, London.
- Reid, H. F. (1911). *The elastic-rebound theory of earthquakes*. University Press.

Rice, J. R. and Cleary, M. P. (1976). Some basic stress diffusion solutions for fluid-saturated elastic porous media with compressible constituents. *Rev. Geophys.*, 14(2), 227 – 241, doi:10.1029/RG014i002p00227.

Riguzzi, F., Crespi, M., Devoti, R., Doglioni, C., Pietrantonio, G. and Pisani, A. R. (2013). Strain rate relaxation of normal and thrust faults in Italy. *Geophys. J. Int.*, 195(2), 815 – 820, doi:10.1093/gji/ggt304.

Roeloffs, E. (1996). Poroelastic techniques in the study of earthquake-related hydrologic phenomena. *Adv. Geophys.*, 37, 135 – 195, doi:10.1016/S0065-2687(08)60270-8.

Rovida, A., Camassi, R., Gasperini, P. and Stucchi, M. (2011). CPTI11, the 2011 version of the Parametric Catalogue of Italian Earthquakes. Milano, Bologna.

Ruff, L. J. (1983). Fault asperities inferred from seismic body waves. *Earthquakes: Observation, Theory and Interpretation*, 251 – 276.

Ruff, L. J. (1992). Asperity distributions and large earthquake occurrence in subduction zones. *Tectonophysics*, 211(1), 61 – 83, doi:10.1016/0040-1951(92)90051-7.

Ruina, A. (1983). Slip instability and state variable friction laws. *J. Geophys. Res.*, 88, 10359 – 10370, doi:10.1029/JB088iB12p10359.

Rybicki, K. (1970). Dependence of the spatial distribution of aftershocks on the site of the dislocated area at the time of the main earthquake. *Publ. Inst. Geophys. Pol. Ac. Sci.*, 36, 117 – 126.

Salichon, J., Lundgren, P., Delouis, B. and Giardini, D. (2004). Slip history of the 16 October 1999 Mw 7.1 Hector Mine earthquake (California) from the inversion of InSAR, GPS, and teleseismic data. *Bull. Seismol. Soc. Am.*, 94(6), 2015 – 2027, doi:10.1785/0120030038.

Santini, S., Dragoni, M. and Spada, G. (2003). Asperity distribution of the 1964 Great Alaska earthquake and its relation to subsequent seismicity in the region. *Tectonophysics*, 367(3), 219 – 233, doi:10.1016/S0040-1951(03)00130-6.

Scholz, C. H. (1990). *The Mechanics of Earthquakes and Faulting*. Cambridge University Press, Cambridge.

Scholz, C. H. (1998). Earthquakes and friction laws. *Nature*, 391(6662), 37 – 42, doi:10.1038/34097.

Scholz, C. H. and Engelder, J. T. (1976). The role of asperity indentation and ploughing in rock friction-I: Asperity creep and stick-slip. In *Int. J. Rock. Mech. Min. Sci. Geomech. Abstr.* (Vol. 13, No. 5, pp. 149 – 154), Pergamon Press, Oxford.

Serpelloni, E., Anderlini, L., Avallone, A., Cannelli, V., Cavaliere, A., Cheloni, D., D'Ambrosio, C., D'Anastasio, E., Esposito, A., Pietrantonio, G., Pisani, A. R., Anzidei, M., Cecere, G., D'Agostino, N., Del Mese, S., Devoti, R., Galvani, A., Massucci, A., Melini, D., Riguzzi, F., Selvaggi, G. and Sepe, V. (2012). GPS observations of coseismic deformation following the May 20 and 29, 2012, Emilia seismic events (northern Italy): data, analysis and preliminary models. *Ann. Geophys.*, 55(4), doi:10.4401/ag-6168.

Sibson, R. H. (1974). Frictional constraints on thrust, wrench and normal faults. *Nature*, 249(5457), 542 – 544, doi:10.1038/249542a0.

Silverii, F., Cheloni, D., D'Agostino, N., Selvaggi G. and Boschi, E. (2014). Post-seismic slip of the 2011 Tohoku-Oki earthquake from GPS observations: implications for depth-dependent properties of subduction megathrusts. *Geophys. J. Int.*, doi: 10.1093/gji/ggu149.

Simons, M., Minson, S. E., Sladen, A., Ortega, F., Jiang, J., Owen, S. E., Meng, L., Ampuero, J.-P., Wei, S., Chu, R., Helmberger, D. V., Kanamori, H., Hetland, E., Moore, A. W. and Webb, F. H. (2011). The 2011 magnitude 9.0 Tohoku-Oki earthquake: Mosaicking the megathrust from seconds to centuries. *Science* 332, 1421 – 1425, doi: 10.1126/science.1206731.

Sladen, A., Tavera, H., Simons, M., Avouac, J. P., Konca, A. O., Perfettini, H., Audin, L., Fielding, E. J., Ortega, F. and Cavagnoud, R. (2010). Source model of the 2007 Mw 8.0 Pisco, Peru earthquake: Implications for seismogenic behavior of subduction megathrusts. *J. Geophys. Res.*, 115(B2), BO2405, doi:10.1029/2009JB006429.

Steady, S., Gombert, J. and Cocco, M. (2005). Introduction to special section: Stress transfer, earthquake triggering, and time-dependent seismic hazard, *J. Geophys. Res.*, 110(B5), doi:10.1029/2005JB003692.

Stein, R. S. (1999). The role of stress transfer in earthquake occurrence, *Nature*, 402(6762), 605 – 609, doi:10.1038/45144.

Stesky, R. M., Brace, W. F., Riley, D. K. and Robin, P. Y. (1974). Friction in faulted rock at high temperature and pressure. *Tectonophysics*, 23(1 – 2), 177 – 203, doi:10.1016/0040-1951(74)90119-X.

Stewart, H. B. and Thompson, J. M. (1986). *Nonlinear dynamics and chaos*. NY: John Wiley & Sons, Hoboken.

Strogatz, S. (2014). *Nonlinear Dynamics and Chaos: With Applications*, 2nd ed., Westview Press, Boulder.

Suito, H. and Freymueller, J. T. (2009). A viscoelastic and afterslip postseismic deformation model for the 1964 Alaska earthquake. *J. Geophys. Res.*, 114(B11), doi:10.1029/2008JB005954.

Sun, T., Wang, K., Iinuma, T., Hino, R., He, J., Fujimoto, H., Kido, M., Osada, Y., Miura, S., Ohta, Y. and Hu, Y. (2014). Prevalence of viscoelastic relaxation after the 2011 Tohoku-oki earthquake. *Nature*, 514, 84 – 87, doi:10.1038/nature13778.

Tallarico, A., Santini, S. and Dragoni, M. (2005). Stress changes due to recent seismic events in the Central Apennines (Italy). *Pure Appl. Geophys.*, 162(12), 2273 – 2298, doi:10.1007/s00024-005-2779-3.

Tramelli, A., Convertito, V., Pino, N. A., Piochi, M., Troise, C. and De Natale, G. (2014). The 2012 Emilia, Italy, Quasi-Consecutive Triggered Mainshocks: Implications for Seismic Hazard. *Seismol. Res. Lett.*, 85(5), 970 – 976, doi:10.1785/0220140022.

Turcotte, D. L. (1997). *Fractals and Chaos in Geology and Geophysics*, 2nd ed., Cambridge University Press, Cambridge.

Turcotte, D. L. and Schubert, G. (2002). *Geodynamics*, 2nd ed., Cambridge University Press, Cambridge.

Twardzik, C., Madariaga, R., Das, S. and Custòdio, S. (2012). Robust features of the source process for the 2004 Parkfield, California, earthquake from strong-motion seismograms. *Geophys. J. Int.*, 191(3), 1245 – 1254, doi:10.1111/j.1365-246X.2012.05653.x.

Wald, D. J. and Heaton, T. H. (1994). Spatial and Temporal Distribution of Slip for the 1992 Landers, California, Earthquake. *Bull. Seismol. Soc. Am.*, 84, 668 – 691, doi:10.1785/0120000728.

Wallace, R. E. (1990). The San Andreas fault system, California. U.S. Geol. Surv. Prof. Pap., 1515.

Wang, H. (2000). Theory of linear poroelasticity with applications to geomechanics and hydrogeology. Princeton University Press, Princeton.

Wang, K., Hu, Y. and He, J. (2012). Deformation cycles of subduction earthquakes in a viscoelastic Earth. *Nature* 484, 327 – 332, doi:10.1038/nature11032.

Wang, X. and Liu, P. L. F. (2007). Preliminary study of the August 15 2007 Peru Earthquake and Tsunami.

Weatherley, D. and Abe, S. (2004). Earthquake statistics in a block slider model and a fully dynamic fault model. *Nonlinear Process. Geophys.*, 11(5/6), 553 – 560.

Wei, S., Graves, R., Helmberger, D., Avouac, J.-P. and Jiang, J. (2012). Sources of shaking and flooding during the Tohoku-Oki earthquake: A mixture of rupture styles. *Earth Planet. Sci. Lett.*, 333 – 334, 91 – 100, doi:10.1016/j.epsl.2012.04.006.

Zweck, C., Freymueller, J. T. and Cohen, S. C. (2002). The 1964 great Alaska earthquake: present day and cumulative postseismic deformation in the western Kenai Peninsula. *Phys. Earth Planet. In.*, 132(1), 5 – 20, doi:10.1016/S0031-9201(02)00041-9.

Online databases

Finite-Source Rupture Model Database (SRCMOD): <http://quake-rc.info/SRCMOD/>.

Acknowledgments

I would like to thank all the people who contributed in some way to the achievement of this thesis. First and foremost, I would like to thank my supervisor, Prof. Michele Dragoni, for the constant support and for all the stimulating discussions we had. I owe my deepest gratitude also to Dr. Antonello Piombo and Prof. Andrea Tallarico for their generous cooperation and for all the suggestions provided.

I am grateful to Prof. Mario Di Bernardo, Dr. Martin Homer, Dr. Mike Jeffrey, Dr. Petri Piironen and Dr. Christian Camilo Erazo Ordoñez for their continuous support and encouragement during my visit at the University of Bristol (UK). I would also like to offer my special thanks to Prof. Stefano Santini, Prof. Laura Gardini, Prof. Gian Italo Bischi and Prof. Stefano Lenci for their kind assistance in organizing this experience abroad.

My sincere thanks go to my colleagues in Bologna, Dr. Antonio Petrucci, Dr. Francesco Pintori, Dr. Glaucio Gallotti, Dr. Liang Wang, Dr. Katharina Maria Elsen, Dr. Massimo Valeri, Dr. Mathieu Poret, Dr. Valentina Agresti and Dr. Federico Fabiano, for their invaluable friendship and support even at difficult times.

I would also like to thank Prof. Alberto Armigliato, Dr. Filippo Zaniboni, Dr. Gianluca Pagnoni, Dr. Maria Ausilia Paparo, Dr. Sara Bruni and Dr. Maddalena Errico for their understanding and for sharing information and advice. My greatest appreciation also goes to Mrs. Maria Paola Buccella, Mr. Massimo Bacchetti and Mrs. Caterina Pultrone for their cordiality and helpfulness.

Finally, I would like to express my gratitude to Prof. Andrea Morelli and Prof. Aldo Zollo for making themselves available to review this thesis.